A COMPARATIVE POLARIMETRIC STUDY OF THE 43 GHZ AND 86 GHZ SIO MASERS TOWARD THE SUPERGIANT STAR VY CMA

A thesis submitted in fulfilment of the
requirements for the degree of

DOCTOR OF PHILOSOPHY

of

RHODES UNIVERSITY

by

LAURA RICHTER

April 2012

Abstract

The aim of this thesis is to perform observational tests of SiO maser polarisation and excitation models, using component-level comparisons of multiple SiO maser transitions in the 43 GHz and 86 GHz bands at milliarcsecond resolution. These observations require very long baseline interferometric imaging with very accurate polarimetric calibration. The supergiant star VY CMa was chosen as the object of this study due to its high SiO maser luminosity, many detected SiO maser lines, and intrinsic scientific interest.

Two epochs of full-polarisation VLBA observations of VY CMa were performed. The Epoch 2 observations were reduced using several new data reduction methods developed as part of this work, and designed specifically to improve the accuracy of circular polarisation calibration of spectral-line VLBI observations at millimetre wavelengths. The accuracy is estimated to be better than 1% using these methods.

The Epoch 2 images show a concentration of v=1 and v=2 J=1-0 SiO masers to the east and northeast of the assumed stellar position. The v=1 J=2-1 masers were more evenly distributed around the star, with a notable lack of emission in the northeast. There is appreciable spatial overlap between these three lines.

The nature of the overlap is generally consistent with the predictions of hydrodynamical circumstellar SiO maser simulations. Where the v=1 J=1-0 and J=2-1 features overlap, the v=1 J=2-1 emission is usually considerably weaker. This is not predicted by current hydrodynamical models, but can be explained in the context of collisional pumping in a low density environment.

Six observational tests of weak-splitting maser polarisation models were performed, including intercomparisons of linear polarisation in the v=1 J=1-0 and J=2-1 lines, linear polarisation versus saturation level, linear polarisation versus distance from the star, circular polarisation in the v=1 J=1-0 and J=2-1 lines, circular versus linear polarisation and modeling of $\sim 90°$ electric-vector position angle rotations.

The polarisation model tests generally do not support non-Zeeman circular polarisation mechanisms. For the linear polarisation tests, the results are more consistent with models that predict similar linear polarisation across transitions. The scientific importance of these tests is described in detail and avenues for future work are described.

Acknowledgements

I acknowledge the financial support of the NRF, Fuchs Foundation, Atlantic Philanthropies and SKA South Africa.

Thank you to my supervisors, Professor Jonas and Professor Kemball, for many years of help and guidance. Thank you to the Rhodes University Physics and Electronics Department. I have countless great memories of the department, since being late for my first undergraduate lecture in 1999. Special thanks to Anthony who got me started on Linux and spoiled me for all other system administrators. Also to Dr Haggard - I always felt welcome to pop down to your office to ask you questions about whatever (about physics or strikes!). Thanks also to the financial aid office at Rhodes, and especially to John Gillam.

Thank you to Prof Kemball for organising and sponsoring several trips to the University of Illinois. Special thanks to the Kemball family - for meals and company and making me feel welcome in Urbana.

Thank you to my fellow postgrads who have passed through room 48, in its various stages of refinement (from the days where we were the storage room, to the current glory of new flooring and aircon). It was a fun place to weep over AIPS! And especially thanks to Kim - we did it!

Thank you to my mother, for having me at home for the last two years, encouraging me over the many years of my thesis, and proofreading along the way. Thank you to my brother, for gchat tech support sessions and for introducing me to regular expressions.

Thank you to my digsmates from over the years (Muts, Minz, Sna, Danai, Mary) - for bearing with me working on my thesis when there were so many more fun things I was missing. Also to all the friends who were in and out of 37 New Street and Gray Rose over the years, they were good years!

I would also like to remember the people who are no longer with us. Dr Nathanson, who was always the best person to turn to for encouragement and help and advice. My grandfather, who would always ask me puzzled questions about what I actually *do* every day. My grandmother, the tireless helper and supporter.

Finally, thank you to the creator of the cosmos that we marvel at, and the creator of this soul who lives in it.

Contents

List of Tables

List of Figures

Chapter 1

Introduction

This thesis describes full-polarisation Very Long Baseline Interferometry (VLBI) observations of Silicon Monoxide (SiO) masers towards the supergiant star VY Canis Majoris (VY CMa). A number of different vibrationally-excited J=1-0 and J=2-1 SiO maser lines in several isotopomers were observed nearly simultaneously, towards this high-luminosity stellar maser source, in order to investigate the excitation conditions of the masers and to use the masers as probes of the circumstellar environment.

The high resolution VLBI images presented in this thesis enable component-level comparisons of SiO maser properties across multiple transitions. Component-level comparison of the emission provides important observational tests of both SiO maser excitation models and SiO maser polarisation radiative transfer models. Specifically, comparison of the relative distribution of v=1 and v=2, J=1-0 and J=2-1 SiO maser features informs models of the pumping mechanism maintaining the maser, a question which has not yet been fully settled for SiO masers (e.g. Soria-Ruiz et al. 2004). In addition, comparison of the polarisation of the v=1 J=1-0 and J=2-1 maser features provides several key tests of maser polarisation theory, that have not yet been performed at component-level with high resolution images (e.g. Watson 2009).

The magnetic field in the SiO maser emission region can potentially be derived from measurements of the maser polarisation, but requires interpretation in terms of a maser polarisation transport theory. Currently, the two main polarisation theories provide orders of magnitude different magnetic field estimates from the same observed levels of SiO maser circular polarisation (e.g. Elitzur 2002; Watson 2002, and references therein). The observational tests performed in this thesis will be used to constrain maser polarisation models.

Magnetic field estimates for the target source VY CMa can then be derived from the measured maser polarisation (e.g. Barvainis et al. 1987; Kemball & Diamond 1997), providing new evidence regarding the magnetic fields strength around late-type evolved stars, an open area of significant astrophysical importance.

1.1 Nature and role of magnetic fields in late-type stars

The relative dynamical influence of magnetic fields is a key factor in a number of open questions regarding post-AGB (Asymptotic Giant Branch) stellar evolution.

Magnetic fields have been invoked to explain various observed characteristics of late-type evolved stars, such as asymmetric mass loss (García-Segura et al. 2005), localised features such as arcs observed

in the circumstellar material (Soker & Clayton 1999; Soker 2000b), and as the origin of circumstellar disks around late-type stars (Matt et al. 2000). The role of magnetic fields in the death of massive stars is also an open question (Heger et al. 2003).

Magnetic fields have also been invoked to explain various characteristics of planetary nebulae. The main unresolved planetary nebulae problems that involve magnetic fields, are (Balick & Frank 2002):

- Many planetary nebulae and proto-planetary nebulae display disks or tori, the origin of which is uncertain. Magnetic fields may play a role in shaping these disks.
- Collimated outflows are observed in a subset of planetary nebulae and proto-planetary nebulae. The mechanism driving the collimation is unknown, and magnetic fields have been proposed as a collimating agent.
- A small subset of planetary nebulae display multiple lobes. It has been proposed that these morphologies arise through precessing or disrupted flow collimation, possibly due to magnetic instabilities.

Reviews of the shaping of planetary nebulae, and discussions of unresolved issues in planetary nebulae studies, are provided by Balick & Frank (2002) and Frank et al. (2007).

There is no definitive model for magnetic field generation in isolated late-type stars (Balick & Frank 2002). A number of generation models have been proposed, falling into the categories of global dynamic dynamos, or convective turbulence.

Global dynamic dynamo models have been developed by Pascoli (1997) and Blackman et al. (2001), and have been proposed as sources of fields of up to 400 G in strength (Blackman et al. 2001). However, these theoretical models require some means to sustain the dynamo (e.g. Soker 1998; Nordhaus et al. 2007). A binary companion or large planet could provide the necessary angular momentum (e.g. Soker 1998; Nordhaus & Blackman 2006), but for isolated stars it is unclear how a dynamo could be sustained. One possibility is that convection resupplies the differential rotation (Nordhaus et al. 2007).

Alternatively, a weak magnetic field can be created through turbulent dynamos in the convective envelope of a slowly rotating star (Soker 2000a; Soker & Zoabi 2002). Although these fields will not have a global dynamic role, they can lead to the formation of magnetic cool spots on the stellar surface (Soker 1998). Localised magnetic fields of up to ~ 10 G can form above magnetic cool spots on the surface of AGB stars (Soker 2002), and a simulation of magnetic fields created through dynamo action in multiple convective cells in the supergiant Betelgeuse produces fields of up to ~ 500 G in localised regions of the stellar surface (Dorch 2004).

A summary of the various proposed late-type star magnetic field models and their possible roles in shaping the circumstellar envelope is given in Blackman (2009).

1.2 Observations of magnetic fields

Observational evidence of the strength and morphology of the magnetic field is required to test the magnetic field models for late-type evolved stars. There are a number of methods available to measure the magnetic fields of late-type evolved stars and their environments, primarily through linear and circular polarisation observations of several different emission mechanisms.

Detections of magnetic fields have been made towards planetary nebulae and protoplanetary nebulae, using the linear polarisation of continuum submillimetre images, which traces dust alignment due to a magnetic field (Greaves 2002; Sabin et al. 2007). Linear polarisation of molecular line emission can also trace the magnetic field through the Goldreich-Kylafis effect (Goldreich & Kylafis 1981), which has been observed in 620.701 GHz $5_{32} - 4_{41}$ H_2O maser emission towards VY CMa (Harwit et al. 2010).

Optical spectropolarimetry has recently uncovered magnetic fields of magnitudes $\sim$ 100 G in an active giant (Aurière et al. 2008), a few Gauss in several rapidly rotating giants (Konstantinova-Antova et al. 2009), $\sim$ 1 G in the supergiant Betelgeuse (Aurière et al. 2010) and $\lesssim$ 1 G in eight massive late-type supergiants (Grunhut et al. 2010). These detections make use of broad bandpass, high spectral resolution observations of hundreds of optical spectral lines, which were analysed with the least-squares deconvolution technique to find composite circular polarisation profiles (Donati et al. 1997). Magnetic fields of a few kiloGauss have also been detected in the central stars of planetary nebulae, through observations of Zeeman profiles in blended He II and Balmer lines (Jordan et al. 2005).

The magnetic field detections listed above are based on optical and infrared observations. Towards the end of its lifetime the rate of mass loss from a star increases considerably, and can be as high as $\sim 10^{-3}$ $M_\odot$ yr^{-1}. During this stage a star can shed an appreciable fraction of it's mass through the stellar wind (Iben & Renzini 1983). The ejected matter surrounds the star, forming a dusty circumstellar envelope which obscures the star at optical and infrared wavelengths (Iben & Renzini 1983). Habing (1996) provides a review of the circumstellar envelopes that form around AGB stars.

In this stage maser observations make a particularly important contribution towards efforts to measure magnetic fields. Due to the modest dust cross-section at radio wavelengths, maser emission is visible within the dusty circumstellar envelopes that surround late-type evolved stars.

OH maser emission has been used to derive magnetic field estimates for evolved stars (e.g. Reid et al. 1979; Chapman & Cohen 1986; Szymczak et al. 1998; Etoka & Diamond 2004) and protoplanetary nebulae (e.g. Bains et al. 2003, 2004; Szymczak & Gérard 2004; Gómez et al. 2009) through direct detection of Zeeman patterns. Magnetic fields have been derived from the observed circular polarisation of H_2O masers in circumstellar envelopes of evolved stars (e.g Vlemmings et al. 2002, 2005; Richards et al. 2004), in water-fountain sources (Vlemmings et al. 2006), and in protoplanetary nebulae (Vlemmings & van Langevelde 2008). Circular polarisation measurements of SiO maser emission have also been used to measure the magnetic fields of late-type, evolved stars (e.g. Barvainis et al. 1987; Kemball & Diamond 1997).

The high brightness temperature of maser emission makes it observable with VLBI, so that circumstellar maser emission can also be imaged at high resolution, unmatched by other observational techniques. Observations of polarised maser emission therefore provide one of the most promising methods to measure the magnetic fields in the inner atmospheres of late-type evolved stars.

1.3 Astronomical masers around late-type evolved stars

Astronomical maser emission was first discovered by Weaver et al. (1965) in the 1665 MHz OH line, although it was not identified as maser emission at the time. Masers have subsequently been observed in a wide variety of astronomical environments, including comets, star formation regions, the interstellar

medium, supernova remnants, the nuclei of active galaxies, in the atmospheres of late-type stars and in protoplanetary nebulae (Reid 2002).

Maser emission requires a population inversion in the energy levels of the molecules in a gas, which leads to stimulated emission. Maser emission then results when the stimulated emission is amplified, dependent on appropriate density conditions in the gas and a pumping mechanism to maintain the population inversion.The physics of astronomical maser emission is covered in detail in the book, "Astronomical Masers," by Elitzur (1992).

Late-type evolved stars are often observed to display maser emission from rotational transitions of one or more of molecules SiO, H_2O and OH, with the characteristics of the masers varying between different categories of such stars (e.g. Mira variables, OH/IR stars, semiregular variables, supergiants) (Habing 1996). The masers are located in the circumstellar envelope that forms around the star during the final stages of stellar evolution.

Within the circumstellar envelope, the SiO masers are located closest to the star, in the near circumstellar envelope (Elitzur 1980). H_2O masers are located further from the star, in a region accelerated by radiation pressure on dust, and OH satellite line masers are located further still, in a region characterised by a constant velocity outflow (Reid 2002). OH main line masers are located closer to the H_2O maser region (Chapman & Cohen 1986).

This simple "onion" model of maser species distributions is explained by excitation temperature and molecular distribution arguments (Elitzur 1992, pg. 225). While the onion model is broadly appropriate to a large number of observations, it is a simplification, and high resolution images show that the OH maser emission region overlaps with the outer H_2O maser emission region, which can be attributed to density inhomogeneities in the circumstellar environment (Richards et al. 2008).

1.4 Circumstellar masers as probes of magnetic fields

As discussed above, OH, H_2O and SiO masers have all been used to measure magnetic fields in the circumstellar envelopes of late-type stars. These three maser species sample the magnetic field over a range of distances from the star (Reid & Moran 1981).

The OH molecule is paramagnetic (Elitzur 1992, pg. 161) and circumstellar OH masers often show appreciable line splitting. The magnetic fields of late-type stars have been estimated from observed Zeeman patterns to range from about a third of a milliGauss to about ten milliGauss in the satellite line OH maser region (e.g. Reid et al. 1979; Szymczak & Cohen 1997; Trigilio et al. 1998; Szymczak et al. 2001) and the main line OH maser region (e.g. Chapman & Cohen 1986; Szymczak et al. 1998; Richards et al. 2004).

The molecules H_2O and SiO are both non-paramagnetic (Elitzur 1992, pg. 191) and fall into the weak-splitting regime. The Zeeman splitting of these spectral lines is smaller than the line widths, for plausible magnetic field values, and fully separated Zeeman patterns are not visible. For both of these maser molecules, the magnetic field strength can be estimated through analysis of circular polarisation observations, subject to a theory of maser polarisation (e.g. Kemball & Diamond 1997; Vlemmings et al. 2002).

The polarisation of maser emission in the weak field regime has been investigated in two series of papers by Elitzur (e.g. Elitzur 2002, and references therein), and by Watson and a number of

co-authors (e.g. Watson 2002, and references therein). Elitzur developed an analytic model of maser polarisation, while Watson et al. developed numerical models of polarised maser radiation, which they explored over a range of physical conditions.

In the Elitzur model, the circular polarisation is created through the Zeeman effect, and can be used to derive the magnetic field value in the envelope, if maser polarisation has reached its stationary state and field line curvature is not significant (Elitzur 2002). In the Watson et al. models, circular polarisation can be created either through the Zeeman effect alone, or through the Zeeman effect with modifications due to saturation, or through a change in quantisation axis as the maser propagates, termed non-Zeeman circular polarisation (Watson 2002).

H_2O masers appear to be mostly unsaturated, and have weak or undetectable linear polarisation (e.g. Vlemmings et al. 2005; Richards et al. 2011). Under these conditions it is unlikely that the circular polarisation observed towards H_2O masers is caused by non-Zeeman effects (Watson 2009). This supports a Zeeman interpretation of H_2O maser circular polarisation, which implies magnetic fields of between about 15 mG and 4 G in the H_2O maser region, with typical values of around 100 mG (e.g. Nedoluha & Bowers 1992; Vlemmings et al. 2001, 2002, 2005).

For typical AGB star conditions in the H_2O maser region, the thermal pressure is estimated to be $\sim 10^{-5.2}$ dyne.cm^{-2}, and the ram pressure is estimated to be $\sim 10^{-4.1}$ dyne.cm^{-2}. For a representative H_2O maser magnetic field estimate of 300 mG, the magnetic energy density is $\sim 10^{-2.4}$ dyne.cm^{-2} (Reid 2007). In this case, the magnetic energy pressure will dominate over the thermal and ram pressure in the H_2O maser region (Reid 2007). The high magnetic field estimates derived from H_2O masers have been explained as tracing particularly high density clumps of gas, with frozen-in field lines (Vlemmings et al. 2002). If this is the case, the magnetic field estimates provided by H_2O maser observations would reflect the field in the clumps only, and be higher than that in the ambient gas. Vlemmings et al. (2002) also note that their observations are biased towards the detection of the highest magnetic fields, and will not be representative of the entire H_2O maser region. Nonetheless, Vlemmings (2007) argues that the magnetic field strength in the envelope is large enough to have a global dynamic influence on the envelope shape.

The interpretation of SiO maser polarisation is more contentious than that of H_2O masers. Circumstellar SiO masers are probably at least partially saturated (Nedoluha & Watson 1994), and are strongly linearly polarised (e.g. Kemball & Diamond 1997). In this parameter regime it is unclear whether the observed circular polarisation is created by Zeeman or non-Zeeman effects. Anisotropic pumping is an additional consideration for the SiO maser observations.

In a number of observational papers, the circular polarisation of SiO masers has been interpreted as due to the Zeeman effect alone, which implies typical circumstellar magnetic fields of a few Gauss, up to a few tens of Gauss in some cases (Barvainis et al. 1987; Kemball & Diamond 1997). This implies a magnetic energy density of more than $\sim 10^{-0.5}$ dyne.cm^{-2} (Reid 2007). In the SiO maser region of a typical AGB star circumstellar envelope, the thermal pressure is $\sim 10^{-2.7}$dyne.cm^{-2}, and the ram pressure is $\sim 10^{-2.5}$dyne.cm^{-2} (Reid 2007). As for the H_2O maser case, the magnetic energy density derived from the Zeeman interpretation is considerably greater than the thermal and ram energy densities.

Such large magnetic fields may be caused by amplification of the tangential magnetic field due to shock compression around pulsating stars (Hartquist & Dyson 1997). However, if the large SiO

magnetic field values are representative of the ambient magnetic field in the envelope, then the magnetic field may play a dominant role in the mass loss from the star and shaping of the envelope (e.g. Soker 1998; Matt et al. 2000; García-Segura et al. 2005).

On the other hand, if the SiO maser circular polarisation is caused by the non-Zeeman mechanism explored in the Watson models, then the observed levels of circular polarisation could be created in the presence of magnetic fields of only a few tens of milliGauss (Nedoluha & Watson 1994; Wiebe & Watson 1998). If the magnetic field is of this order, the magnetic energy density is less than the thermal and kinetic energy densities in the SiO maser region.

As SiO masers are the maser species formed closest to the star, the magnetic field values determined from SiO masers are key to investigating the stellar magnetic field. Unfortunately, the present lack of certainty as to how to interpret observed levels of polarisation is limiting their usefulness as probes of the magnetic field. This thesis aims to observationally constrain SiO maser polarisation models, in order to ascertain how SiO maser polarisation observations can be used to derive circumstellar magnetic field values. Several such observational tests are performed in the thesis. The main tests entail component-level comparisons of the circular and linear polarisation of coincident SiO maser spots in the v=1 J=1-0 and J=2-1 SiO transitions.

1.5 SiO masers as probes of the circumsteller envelope

The SiO masers observed towards late-type evolved stars are formed between the stellar photosphere and the dust formation point, a region termed the near circumstellar envelope or extended atmosphere. VLBI maps of the SiO masers show the emission to be located in many distinct compact features, distributed in a broken ring located a few stellar radii from the central star (e.g. Diamond et al. 1994), just outside the near-infrared molecular layer (e.g. Cotton et al. 2006). High resolution VLBI observations of the morphology, variability, and the relative location of emission from multiple SiO maser transitions provide information about the envelope conditions and dynamics of this inner region.

VLBI maps of SiO masers have provided evidence of the dominant expansion of the near circumstellar envelope (e.g. Diamond & Kemball 1999, 2003), with periods of infall (e.g. Boboltz et al. 1997; Diamond & Kemball 2003; Chen et al. 2006), as shocks propagate through the envelope and material falls back towards the central star. SiO maser maps have also revealed localised ballistic infall, as well as evidence of localised mass loss (Diamond & Kemball 2003; Gonidakis et al. 2010).

Velocity gradients are often observed in circumstellar SiO maser features, and have been interpreted in various contexts as evidence of bulk motion associated with non-radial stellar pulsations (Matsumoto et al. 2008), localised mass ejection (Cotton et al. 2009a), alignment with a magnetic field (Cotton et al. 2008), and stellar rotation of the binary R Aquarii (e.g. Hollis et al. 2001; Cotton et al. 2004, 2006). Spoke-like features directed away from the star are frequently observed, with velocity gradients approaching the stellar velocity with the distance from the star. These spokes have been interpreted as a selection effect from maser amplification in a decelerating outflow (Yi et al. 2005).

Observations of quasi-periodic SiO maser polarisation variability have also recently been used to detect possible planetary companions orbiting two Mira variables (Wiesemeyer et al. 2009).

Hydrodynamical models of the near circumstellar envelope have been coupled to SiO maser models, and used to create simulated SiO maser distributions for comparison with VLBI images. These models

have reproduced many features of SiO maser maps (e.g. Humphreys et al. 1996, 2002; Gray et al. 2009). Among the first successes of the earlier models was reproducing the sparse ring geometry of the maser emission, located a few stellar radii from the photosphere, and the variation in ring diameter with stellar phase (Humphreys et al. 1996, 2002).

However, a number of observed characteristics of SiO maser maps are not reproduced by these models. One area of discrepancy is in the relative distribution of SiO masers in different transitions (e.g. Soria-Ruiz et al. 2004), which is influenced by the pumping mechanism used in the models. Both radiative and collisional pumping mechanisms have been explored for circumstellar SiO masers (e.g. Bujarrabal 1994; Lockett & Elitzur 1992), and SiO maser hydrodynamical models have incorporated both, with varying levels of importance (e.g. Humphreys et al. 1996; Gray et al. 2009).

Many comparative VLBI observations have been made of SiO maser emission from transitions J=1-0 and J=2-1 in the bands v=0 through v=3 (e.g. Colomer et al. 1996; Cotton et al. 2004; Yi et al. 2005; Soria-Ruiz et al. 2007; Imai et al. 2010). In some cases the observations support the model pumping mechanism predictions, such as the smaller ring diameter of the v=1 J=1-0 masers, compared to the ring diameter of the v=2 J=1-0 masers (e.g. Desmurs et al. 1999; Yi et al. 2000). However, the presence of the v=0 J=1-0 SiO maser line at a similar radius to the v=1 and v=2 J=1-0 masers is not predicted by the pumping mechanism used in the models (Soria-Ruiz et al. 2005).

In other cases the observational evidence itself appears in conflict: the v=1 J=2-1 and J=1-0 masers have been observed to be located in similar regions (e.g. Phillips et al. 2003; Colomer et al. 1996), and in entirely different regions (Soria-Ruiz et al. 2004, 2007) of the envelope. Earlier models of these lines predict the v=1 J=2-1 maser to be located at a comparable radius, or a slightly greater radius, than the v=1 J=1-0 emission (Gray & Humphreys 2000; Humphreys et al. 2002), while an updated version of the model shows that the v=1 J=2-1 maser ring can have the larger radius (Gray et al. 2009). Some of the observational discrepancies can also be explained as the effect of line overlaps (Soria-Ruiz et al. 2004, 2005).

The simultaneous observations of a number of SiO maser transitions reported in this thesis provide further information with which to constrain the maser excitation models.

1.6 Thesis outline

The target source for this project was chosen to be late-type supergiant star VY CMa, because it is an intense and prolific SiO maser source. VY CMa was one of the earliest objects detected in v=1 J=1-0 and v=1 J=2-1 SiO maser emission (Kaifu et al. 1975; Snyder & Buhl 1975). To date, VY CMa has been observed to display SiO maser emission in the ground state v=0 up to v=4, from angular momentum transitions as high as J=15-14. A review of the properties of VY CMa is given in Chapter 2, with particular emphasis on the observations of the circumstellar envelope. VY CMa is embedded in a chemically rich (Ziurys et al. 2007) complex red reflection nebula, which is home to many small scale features such as arcs and bright knots (e.g. Smith et al. 2001).

Circumstellar SiO maser emission is reviewed in Chapter 3, with a detailed discussion of SiO maser polarisation. A summary of the development of the polarisation models is presented, and several observational tests of the polarisation models are proposed.

The science goals of this thesis require component-level comparisons of SiO maser emission from

multiple SiO transitions. In order to resolve milliarcsecond scale SiO maser spots, the emission must be observed using the technique of VLBI. The theory of VLBI and the techniques necessary to calibrate spectral line polarimetric VLBI data are described in Chapter 4.

Two epochs of full-polarisation VLBI observations were performed for this thesis, each of multiple J=1-0 (43 GHz) and J=2-1 (86 GHz) SiO maser transitions. The observations were performed with the Very Large Baseline Array[1] (VLBA), a dedicated VLBI array of ten 25 m antennas located across the United States of America. The VLBA has both 43 GHz and 86 GHz receiver systems, and is capable of observing multiple lines within each of these two bands simultaneously. The longest VLBA baseline is 8611 km at 43 GHz and 6156 km at 86 GHz, corresponding to resolutions of 0.17 mas and 0.12 mas respectively (Romney 2010). The VLBA observations are described in Chapter 5, along with the practical details of calibrating and imaging the VLBA data.

The polarisation model observational tests discussed in Chapter 3 require high precision measurement of the linear and circular polarisation. To this end, a number of innovative data reduction techniques were developed to optimise the polarisation calibration. These new techniques are also described in Chapter 5.

The SiO maser images are presented in Chapter 6, and maser feature information is extracted from the images. The results are discussed in Chapter 7. The implications of the relative spatial distribution of the different maser transitions imaged is discussed in terms of maser excitation models. The polarisation model observational tests suggested in Chapter 3 are also performed using the Epoch 2 data, and the results are discussed.

The thesis is concluded in Chapter 8 with a summary of the main results and suggestions for future work.

[1] www.vlba.nrao.edu

Chapter 2

VY Canis Majoris

VY CMa is a late-type evolved star in the Canis Majoris constellation, located in the HII region Sharpless 310 (Moran et al. 1973). Described by Herbig (1970) as a "remarkable late-type, nebulous, irregular variable star," it has been extensively studied at a wide range of wavelengths. It is particularly bright at infrared wavelengths, and is one of the strongest sources in the sky at wavelengths longer then 5μm (Hyland et al. 1969). The first published observation of VY CMa was by Perrine (1923), where he noted the red nebula surrounding the star. Since then numerous observations have shown it to be a supergiant star located in an extended circumstellar envelope.

In recent years advances in image resolution and spectral resolution have enabled more detailed studies of the circumstellar envelope. These studies have shown the envelope to be host to many small-scale features. Many new molecules have also been detected towards VY CMa, tracing different regions of the envelope. Models of the circumstellar environment must now incorporate the observed asymmetries in the nebula and the varied small-scale structure embedded in it.

VY CMa was chosen as the object of this study, in spite of its complex circumstellar environment, because it is a particularly strong SiO maser emitter and displays SiO emission in an extremely wide range of transitions. This made it the most promising candidate for a study that requires the comparison of multiple SiO maser transitions. This chapter provides a literature review of VY CMa, to provide a context for the interpretation of the SiO maser results presented later as part of this thesis.

The chapter begins with a summary of the basic stellar properties of VY CMa. A review of observations of the circumstellar envelope is then given, separated into sections on integrated total power observations and imaging observations.

This is followed by three sections on selected scientific implications of the published observations: the evidence for and possible cause of an asymmetric circumstellar envelope geometry, the nature and extent of the mass-loss from the star, and the evolutionary stage of the star.

This literature review is a summarised and updated version of a similar literature review that appeared in Richter (2005).

2.1 Stellar properties

The main stellar properties of VY CMa are reviewed in this section. A representative selection of the stellar parameters reviewed are listed in Table 2.3 at the end of the section.

Spectral class	Reference
M3-4e	Joy (1942)
M5 Ibp	Wallerstein (1958)
M3-6 Ib	Hyland et al. (1969)
M5 Ia	Humphreys (1974)
M4 I	Massey et al. (2006)
M2.5 I	Massey et al. (2006)
M5e Ibp	Samus et al. (2009)

Table 2.1: Spectral classification of VY CMa.

Position

According to the Hipparcos Catalogue, VY CMa is located at right ascension $07^h\ 22^m\ 58.3315^s$, declination $-25°\ 46'\ 03.174''$ (J2000), with annual parallax of 1.78 mas and proper motion of 9.84 mas/yr and 0.75 mas/yr in right ascension and declination (Perryman et al. 1997).

Wright et al. (1990) first noted that observations of SiO, H_2O and OH maser emission were offset from the optical position. Zhang et al. (2012) discuss this, comparing the Hipparcos position to recent phase-referenced H_2O (Choi et al. 2008b) and SiO (Zhang et al. 2012) maser positions. They find a discrepancy of tens of mas between the Hipparcos optical position and their SiO maser position. They propose that the optical position will not provide accurate proper motion measurements, due to dust scattering in the nebula. Alternatively, inhomogeneities in the VY CMa stellar surface may cause the star to appear asymmetrical and impact proper motion measurements (Zhang et al. 2012).

The Zhang et al. (2012) position, determined from VLBA observations of SiO masers, is right ascension $07^h\ 22^m\ 58.3259^s \pm 0.0007$, declination $25°\ 46'\ 03.070'' \pm 0.010$ (J2000), with a proper motion of -2.21 ± 0.06 mas/yr and 2.29 ± 0.30 mas/yr in right ascension and declination.

Spectral classification

VY CMa is designated as an irregular variable supergiant of late spectral type by the General Catalogue of Variable Stars (Kukarkin et al. 1971). It is an oxygen-rich star (Hyland et al. 1972), first classified as an M-type star in the literature by Joy (1942).

VY CMa's spectral classification varies slightly in the literature. Several examples are given in Table 2.1. The discrepancy between the two Massey et al. (2006) classifications listed in the table is a result of using different regions of the TiO bands for the fit. The M4 I classification was based on bands further to the blue, which are less affected by veiling but are also influenced by excess flux due to scattering (Massey et al. 2006).

Wallerstein has monitored the optical spectrum of VY CMa since the 1960s and found it to remain qualitatively constant in spectral structure over this time (Wallerstein & Gonzalez 2001).

Stellar diameter

The diameter of VY CMa has been estimated using observations of near and mid-infrared interferometric visibilities, combined with dust shell models (e.g. Danchi et al. 1994; Monnier et al. 1999b, 2000, 2004). Most of the calculated diameters are close to 20 mas. Models of high resolution Keck

Distance	Technique	Reference
1500	Association with nearby objects	Herbig & Zappala (1970)
1500 ± 500	Association with nearby objects	Lada & Reid (1978)
1350 ± 150	Star-count methods	Armandroff & Herbst (1981)
1900	Assumed luminosity of spectral type	Rowan-Robinson & Harris (1983)
1900	OH maser phase lag	Herman & Habing (1985)
660	Assumed luminosity	Loup et al. (1993)
2100	Kinematic distance from stellar radial velocity	Le Sidaner & Le Bertre (1996)
1400 ± 140	H_2O maser proper motion	Marvel (1996)
2860	Galactic rotation model	Yuasa et al. (1999)
1140^{+110}_{-90}	Astrometric H_2O maser monitoring	Choi et al. (2008b)
1200^{+130}_{-100}	Astrometric SiO maser monitoring	Zhang et al. (2012)

Table 2.2: Distance to VY CMa, determined using a variety of techniques.

aperture-masking observations combine with IOTA data give a stellar diameter of $18.7 \pm 0.3 \pm 0.4$ mas (Monnier et al. 2004).

Inner dust shell radius

The inner dust-shell radius around VY CMa has been estimated through spectral energy distribution (SED) model fitting (Rowan-Robinson & Harris 1983; Le Sidaner & Le Bertre 1996), and through model fits to infrared interferometric visibilities (Danchi et al. 1994; Monnier et al. 2000). The interferometric measurements give an inner dust-shell radius of 40 to 50 mas.

All of these publications, except for Monnier et al. (2000), note significant discrepancies between the model fits and the data. This is probably due to asymmetries in the inner dust shell, or due to time variability (Monnier et al. 2000, 2004).

Distance

The distance to VY CMa has been estimated using several different techniques, with results ranging from 0.66 kpc to 2.86 kpc. The distances and the techniques used to derive them are listed in Table 2.2. The most frequently cited value of the VY CMa distance in the literature is 1.5 kpc; this is the early value provided by Herbig & Zappala (1970) and Lada & Reid (1978) from VY CMa's velocity coincidence with the association containing τ CMa and the cluster NGC 2362. Marvel (1996) determines a similar distance of 1.4 ± 0.14 kpc from modeling the proper motion of H_2O masers.

However, recent astrometric monitoring points to a significantly lower distance. Phase-referenced observations of H_2O masers using the VERA array gives a distance estimate of $1.14^{+0.11}_{-0.09}$ kpc (Choi et al. 2008b). Phase referenced VLBA observations of SiO masers give a distance estimate of $1.20^{+0.13}_{-0.10}$ kpc (Zhang et al. 2012). These distances agree to within the reported uncertainties, and are the highest precision VY CMa distance measurements to date.

Surface temperature

The surface temperature of VY CMa is somewhat uncertain. Hyland et al. (1969) propose a temperature of 2500 - 3000 K, based on observations of optical and infrared spectra. Monnier et al. (2004)

estimate an effective temperature of 2600 K from K-band Keck data. Massey et al. (2006) derive several temperature estimates from optical and near-infrared spectra, ranging from 3450 K to 3705K. This is significantly higher than previous temperature estimates, but it is a more typical value for an ordinary red supergiant star (Massey et al. 2006). A fit of the red and near-infrared TiO bands to the MARCS stellar atmosphere models (Gustafsson et al. 2003) gives a temperature of 3650 K, which Massey et al. (2006) consider their most reliable estimate. Massey et al. (2006) argue that the discrepency between this temperature and earlier temperature estimates may be due to earlier authors overestimating the stellar radius, either by including part of the dust shell in the radius figure, or through the presence of an H_2O molecular layer around VY CMa which causes the photosphere to appear larger than it is.

Luminosity

VY CMa has long been known to be a highly luminous star. Luminosity values of between 2×10^5 $L_\odot$ and 5×10^5 $L_\odot$ have been derived, assuming a distance of 1.5 kpc to the star (Lada & Reid 1978; Monnier et al. 1999b; Humphreys et al. 2007). Choi et al. (2008b) use their more precise distance value of 1.14 kpc to revise the luminosity estimate for VY CMa to a value of 3×10^5 $L_\odot$. Massey et al. (2006) estimate luminosity from the effective temperature, also using the MARCS model. This yields a lower luminosity 0.6×10^5 $L_\odot$. They later acknowledged that the luminosity value given by their model cannot be correct, given that the circumstellar envelope alone is more luminous than this. They suggested that the erroneous luminosity value they calculated may be the result of the quantity of dust, and the properties of the dust, which surrounds the star (Massey et al. 2008).

Initial mass

A number of estimates of the initial stellar mass of VY CMa have been derived from its position on the Hertzsprung-Russel diagram. de Jager (1980, pg 293) estimate a zero-age main-sequence mass of 20 $M_\odot$ for VY CMa, and Wittkowski et al. (1998) propose a mass of between 30 and 40 $M_\odot$.

Choi et al. (2008b) use their luminosity estimate and adopt the Massey et al. (2006) temperature to place VY CMa on the Hertzsprung-Russel diagram in a position consistent with an evolved star of initial mass 25 $M_\odot$. When they adopt a lower temperature of 3000 K, they find that the position of VY CMa on the Hertzsprung-Russel diagram is not within the theoretically allowed region (Choi et al. 2008b).

Systemic velocity

The systemic velocity of VY CMa and the expansion velocity of its circumstellar envelope have been derived from numerous spectral line observations.

Spectral lines from SiO, SO, CO, HCN and SO and H_2O and a variety of other molecules observed towards VY CMa yield systemic velocity estimates ranging from 16 to 25 km/s (Zuckerman & Dyck 1986; Nercessian et al. 1989; Sahai & Wannier 1992; Nyman et al. 1992; Stanek et al. 1995; Neufeld et al. 1999; Harwit & Bergin 2002; Milam et al. 2007, 2008; Ziurys et al. 2009). Observations of the OH maser emission profile yield a stellar velocity of 21.1 km/s (Bowers et al. 1983) and measurements of the KI halo give a stellar velocity of 21 km/s (Smith 2004).

Parameter	Value	Reference
Right ascension	$07^h\ 22^m\ 58.3259^s$ (J200)	Zhang et al. (2012)
Declination	$-25°\ 46'\ 03.070''$ (J2000)	Zhang et al. (2012)
Spectral type	M5	Wallerstein (1958); Samus et al. (2009)
Diameter	18.7 mas	Monnier et al. (2004)
Inner dust shell radius	50 mas	Danchi et al. (1994); Monnier et al. (2000)
Distance	1.14 kpc	Choi et al. (2008b)
Surface temperature	3650 K	Massey et al. (2006)
Luminosity	3×10^5 $L_\odot$	Choi et al. (2008b)
Initial mass	25 $M_\odot$	Choi et al. (2008b)
Systemic velocity	21 km/s	Bowers et al. (1983); Smith (2004)

Table 2.3: A selection of stellar parameter estimates for VY CMa.

The expansion velocity of the circumstellar envelope has also been derived from spectroscopy of molecules in the envelope. Because different molecules are located in different regions of the envelope, they trace regions that are expanding at different velocities. This is discussed in greater detail in the next section, where observations of chemical compounds in the circumstellar envelope are discussed.

2.2 Circumstellar envelope: Integrated observations

This section reviews non-imaging observations of the VY CMa circumstellar envelope, separated into continuum observations, non-imaging visibility observations, SED observations, and spectral line observations. The observations of thermal spectral lines are presented for separate wavelength bands. Spectral line observations of maser emission are discussed in separate sections for the three maser species OH, H_2O and SiO.

2.2.1 Radio and submillimetre continuum observations

The radio and sub-mm continuum observations of VY CMa primarily trace emission from circumstellar dust (Shinnaga et al. 2004b). Observations in the frequency range 1.44 GHz to 394 GHz are reported in the radio continuum emission catalogue of Wendker (1995) with a spectral index of approximately -2.7, if the 200 mJy reading at 85.7 GHz is disregarded. Wendker (1995) suggests in the catalogue remarks that this anomolously high value may be a flare. Knapp et al. (1995) detect radio continuum emission of 0.26 mJy at the low frequency of 8.4 GHz, and suggested that the emission could be due to dust or an extended chromosphere. Shinnaga et al. (2004b) detect continuum emission from VY CMa, with fluxes of 270 ± 40 mJy, 340 ± 10 mJy, 7.8 ± 2.6 Jy at 216, 301 and 658 GHz respectively, giving a spectral index of approximately -3 in this frequency range (Shinnaga et al. 2004b,a). The continuum readings in the 1000 to 15000 GHz region reported by Le Sidaner & Le Bertre (1996) give a spectral index closer to -2.5 (Shinnaga et al. 2004b).

2.2.2 Visibility observations

Mid-infrared interferometric observations of VY CMa have been used to measure the dust shell around the star (Monnier et al. 2000).

Sutton et al. (1977) observed VY CMa at 11.106 μm with a spatial heterodyne interferometer and found that the visibility data was not well fit by a circular model of uniform brightness. Further 11.5 μm visibility plots by Sudol et al. (1999) are consistent with the Sutton et al. (1977) result. More recently, Monnier et al. (2000) observed VY CMa with the Infrared Spatial Interferometer and also found that a spherically symmetric model is not appropriate to this mid-infrared visibility data.

2.2.3 SED observations

The earliest reported mid-infrared SED observation of VY CMa displayed the 9.7μm silicate feature often observed towards oxygen-rich stars (e.g. Merrill & Stein 1976). However, this feature is no longer visible in more recent SED observations published by Monnier et al. (1998), who undertook a long-term study of the 8-13μm mid-infrared spectral variability. They found the VY CMa spectrum to be relatively flat and stable over the four year period of the observations, with the silicate feature absent.

Monnier et al. (1999a) subsequently compared the mid-infrared spectrum at three epochs: the Merrill & Stein (1976) observations, 1986 IRAS observations and the Monnier et al. (1998) observations. Comparison of the data sets confirmed the disappearance of the silicate feature, with the intermediate IRAS data having a weaker silicate peak than that seen in 1976. The disappearance of the silicate feature may be due to a significant increase in optical depth in the envelope, and possibly a change in chemical composition (Monnier et al. 1999a). The silicate feature is also absent from subsequent mid-infrared SED observations of Monnier et al. (2000).

2.2.4 Spectral line observations

The optical spectrum of VY CMa has been monitored by Wallerstein & Gonzalez (2001) over a 43 year period, and found to remain much the same. Optical spectral lines have been detected from TiO, ScO, YO, VO, H, Na, KI, Ca, RbI, Ti, Cr, Fe, and Ba (Wallerstein 1958; Hyland et al. 1969; Wallerstein 1971; Herbig 1974; Wallerstein 1978, 1986; Wallerstein & Gonzalez 2001). A number of features in the spectrum still remain unidentified (Wallerstein & Gonzalez 2001).

Smith (2004) published high-resolution echelle spectra of the KI emission with the ESO New Technology Telescope. He used eight slit positions across the nebula around VY CMa. Bright KI emission was detected throughout the circumstellar envelope, emitted by the circumstellar gas itself rather than reflected emission from the star. The complexity of the circumstellar environment is visible in the KI spectra, which provide a promising future means to explore the envelope kinematics (Smith 2004).

More recently, Smith et al. (2009) published high resolution near-infrared Phoenix-slit CO spectra, taken with the Gemini South telescope at sixteen different positions across the VY CMa nebula. They found that most of the CO emission arises from individual dense clouds, rather than a homogeneous steady wind. Although individual bright CO components are distributed asymmetrically around the star, the overall distribution of diffuse CO and CO features is more isotropic. The CO emission is brighter to the south and west of the star. The individual bright CO components are also concentrated to the south and west, while the north and east show smoother CO emission (Smith et al. 2009).

The molecules Ammonia (NH_3) and SiO were first detected in the atmosphere of VY CMa in the mid-infrared (McLaren & Betz 1980; Geballe et al. 1979). The excitation temperatures of SiO

and the shape of the spectra lead Geballe et al. (1979) to conclude that the mid-infrared SiO emission originates about 150 mas ($\sim$ 15 R_*) from the star, in an expanding, accelerating region of the envelope.

The far-infrared spectrum of VY CMa is dominated by H_2O emission (Polehampton et al. 2010). Neufeld et al. (1999) detected forty-one far-infrared thermal H_2O lines, and an OH absorption feature, with the Infrared Space Observatory (ISO). The H_2O lines they observed were predominantly from the ground state, but included two transitions from the $v_2 = 1$ vibrationally excited state. The line profiles indicate that the emission originates in a region of outflow, with a relatively low outflow velocity of 25 km/s. This implies that the far-infrared H_2O emission arises from a region where the terminal velocity has been reached, or is close to being reached (Neufeld et al. 1999).

Polehampton et al. (2010) observed the far-infrared spectrum of VY CMa with the ISO and detected numerous H_2O lines, along with CO, OH, H_3O^+ and NH_3 lines. Fits to the far-infrared water lines up to an energy of 2000 K yield a column density lower limit of $7 \times 10^{19} cm^{-2}$ for H_2O (Polehampton et al. 2010). Even this lower limit value is two orders of magnitude higher than the CO column density, implying that the oxygen in the envelope of VY CMa is predominantly locked into H_2O, rather than CO, molecules (Polehampton et al. 2010).

Many molecules have been detected in the VY CMa circumstellar envelope in the radio and submillimetre bands, among them H_2O. Emission from a number of observed H_2O lines appears to originate in the near circumstellar envelope, including vibrationally excited thermal 336 GHz and 557 GHz emission (Harwit & Bergin 2002; Menten et al. 2006). Observations of masing H_2O lines are discussed in more detail in a subsequent section.

The number of molecules observed towards VY CMa has increased significantly in recent years following the detection of a number of unexpected molecules by Ziurys et al. (2007). The detections reported by Ziurys et al. (2007) were made during a submillimetre spectral survey of VY CMa, and include NaCl, PN, HNC, and HCO+, PS and SiS, which were detected for the first time towards VY CMa.

The chemical complexity uncovered by Ziurys et al. (2007) prompted further searches for additional molecules. Table 2.4 lists the compounds that have been detected in radio and submillimetre observations of the VY CMa circumstellar envelope. A number of these lines have been imaged, and are discussed in more detail in Section 2.3.

The spectral line profiles of the molecules detected by Ziurys et al. (2007) reveal three distinct kinematic components in the circumstellar envelope: a spherical outflow, a blueshifted outflow and a redshifted outflow. Ziurys et al. (2009) model these three regions, with the spherical outflow having an expansion velocity of 20 km/s, the redshifted outflow having an expansion velocity of 42 km/s, and the blushifted outflow having an expansion velocity of 38 km/s.

The accelerating region of the spherical outflow close to the star is traced by NaCl, which has a narrow line profile of about 14-19 km/s (Milam et al. 2007; Ziurys et al. 2007). The more extended regions of the spherical outflow are traced by SiO and PN, which have line widths of about 40 km/s (Ziurys et al. 2007). The SO and SO_2 emission have two-peaked profiles, similar to the OH maser emission discussed later in this section, with emission arising out of the blueshifted and redshifted flows (Ziurys et al. 2007). The SO and SO_2 blueshifted emission is of very similar shape and probably arises from an outflow directed nearly towards us. The redshifted emission, on the other hand, most likely arises from an outflow away from us at a large angle from the line of sight (Ziurys et al. 2007).

Molecule	Reference
OH	Neufeld et al. (1999), Eliasson & Bartlett (1969)*, Morris & Bowers (1980)* Harvey et al. (1974)*†, Masheder et al. (1974)*†
SO	Omont et al. (1993), Sahai & Wannier (1992), Muller et al. (2007)†
SO_2	Omont et al. (1993), Ziurys et al. (2007)
CO	Zuckerman & Dyck (1986), Nyman et al. (1992), Stanek et al. (1995)† Kemper et al. (2003), Muller et al. (2007)†, Smith et al. (2009)
^{28}SiO	Buhl et al. (1974)*, Geballe et al. (1979), Miyoshi et al. (1994)*† Shinnaga et al. (2003)†, Shinnaga et al. (2004b)*†, Shibata et al. (2004)*†
^{29}SiO	Geballe et al. (1979), Gonzalez-Alfonso et al. (1996)*
^{30}SiO	Geballe et al. (1979), Gonzalez-Alfonso et al. (1996)
CS	Bujarrabal et al. (1994), Ziurys et al. (2007), Ziurys et al. (2009)
CN	Bachiller et al. (1997), Ziurys et al. (2007), Ziurys et al. (2009)
H_2S	Omont et al. (1993)
H_2O	Menten & Melnick (1989)*, Menten & Melnick (1991)*, Harwit & Bergin (2002), Menten et al. (2006)*, Menten et al. (2008)*
H_3O^+	Phillips et al. (1992), Polehampton et al. (2010)
HCO^+	Ziurys et al. (2007), Ziurys et al. (2009)
HCN	Nercessian et al. (1989), Ziurys et al. (2007), Ziurys et al. (2009)
$H^{13}CN$	Nercessian et al. (1989)
HNC	Ziurys et al. (2007), Ziurys et al. (2009)
NaCl	Milam et al. (2007), Ziurys et al. (2007)
NS	Ziurys et al. (2007)
PN	Ziurys et al. (2007), Milam et al. (2008)
SiS	Ziurys et al. (2007)
PO	Tenenbaum et al. (2007)
AlO	Tenenbaum & Ziurys (2009)
AlOH	Tenenbaum & Ziurys (2010)

Table 2.4: Chemical compounds observed in radio and submillimetre observations of VY CMa. The abundances of many of these molecules relative to H_2 are given in Ziurys et al. (2007).
† Emission is imaged.
* Maser emission.

First time detections of the molecules PO and AlO and AlOH were also recently reported (Tenenbaum et al. 2007; Tenenbaum & Ziurys 2009, 2010). The observations show that all three molecules reside in the spherical outflow. AlO and AlOH are located in the inner, accelerating region also inhabited by NaCl (Tenenbaum & Ziurys 2009, 2010) and PO is located further from the star, like the PN molecule, and has a similar abundance to PN (Tenenbaum et al. 2007).

As can be seen in Table 2.4, VY CMa displays emission from a large number of carbon molecules. This is suprising for an oxygen rich star, where the bulk of carbon is expected to be locked into CO molecules (Nercessian et al. 1989; Ziurys et al. 2009). The high abundance of HCN and the presence of HCO^+ in the envelope is also noted by Ziurys et al. (2007) to be unexpected. When the HCN molecule was first detected towards VY CMa by Nercessian et al. (1989), the authors modelled the envelope chemistry in an attempt to account for the unforseen HCN abundance. Their models require that large quantities of HCN, NH_3 and CH_4 be formed in the inner layers of the envelope, perhaps through chromospheric UV radiation or through shocks (Nercessian et al. 1989). Ziurys et al. (2009) model the abundances of the six carbon molecules they observed towards VY CMa and also find that they can be formed from a combination of photodissociation and shock dissociation.

OH, H_2O and SiO maser emission are often observed in the envelopes of late-type evolved stars (Habing 1996), and maser emission from all three of these molecules has been observed toward VY CMa. Single dish observations of the maser emission are described in more detail in seperate sections below.

2.2.5 OH maser obsevations

VY CMa is a type IIb OH maser source, which displays maser emission in the two OH main lines at 1665 MHz and 1667 MHz, stronger maser emission in the 1612 MHz satellite line, and absorption in the 1720 MHz satellite line (Turner 1970).

The first detection of OH towards VY CMa was the 1612 MHz satellite line OH maser, by Eliasson & Bartlett (1969). The spectrum displays blueshifted and redshifted peaks, typical of OH maser satellite lines around late-type evolved stars, and extends over about 80 km/s (Eliasson & Bartlett 1969; Masheder et al. 1974). This geometry can be explained as emission from the front and back of an expanding circumstellar envelope (Reid & Muhleman 1978). In a constant velocity expanding envelope the velocity coherence is greatest along the line of sight, at the front and back of the envelope. This leads to preferential maser amplification in these regions, and explains the two-peaked profile commonly observed towards OH/IR stars (Reid et al. 1977).

The 1612 MHz satellite line OH maser was observed almost daily for 200 days by Herman & Habing (1985) and found to be highly variable, with large random changes over a period of days. Herman & Habing (1985) explain these variations in terms of the changing output of unsaturated maser emission.

Cohen et al. (1987) measured the circular polarisation of the 1612 MHz OH spectrum, finding a maximum of 36% at a velocity resolution of 0.06 km/s and 22% at 1 km/s. The observations imply a magnetic field of about 2 mG in the OH maser region. The fact that circular polarisation is observed throughout the velocity range of the spectra lead Cohen et al. (1987) to conclude that magnetic fields of these levels are found throughout the 1612 MHz OH maser region.

The main line OH maser spectra both consist of intense blueshifted maser spikes on top of a broad emission plateau (Morris & Bowers 1980). The 1667 MHz plateau is about 70 km/s in extent, while

the 1665 MHz plateau is narrower, about 50 km/s in extent. The 1665 MHz emission also displays a redshifted region of maser spikes about the plateau, but at a much weaker level that the blueshifted emission (Morris & Bowers 1980). Three observations of the 1667 MHz emission over the period of just over six months show strong variation in the spikes of emission, but a constant plateau (Morris & Bowers 1980).

2.2.6 H_2O maser observations

The first H_2O maser emission detected towards VY CMa was the 6_{16} - 5_{23} rotational transition of ortho-H_2O at 22 GHz (Knowles et al. 1969). Single dish spectra of the 22 GHz H_2O maser emission towards VY CMa typically have a three featured structure, with a main central region of emission and more compact redshifted and blueshifted components on either side of it (e.g. Cox & Parker 1979; Gomez Balboa & Lepine 1986).

Fourier analysis of the single dish H_2O maser light curve revealed a period of 350 days present in all three maser features, which may be linked to infrared pumping of the H_2O masers (Gomez Balboa & Lepine 1986). Short term variability with a period of 10.3 days has also been observed in two of the strongest maser peaks in the central component (Wu Zheng et al. 1998). Shintani et al. (2008) monitored the 22 GHz H_2O masers every one to two months for a period of three years with the VERA Iriki telescope and found that eight of the seventeen observed maser spots showed variation in velocity and flux density, but the periodicity was difficult to determine. The short term variations are possibly caused by shock waves forming periodically and moving through the envelope material, altering the molecular collision rate and hence the maser pumping (Wu Zheng et al. 1998).

Maser emission has also been detected in a number of submillimetre H_2O lines. These include the ground state lines at 321 GHz (Menten & Melnick 1991), and 325 GHz (Yates et al. 1995), and the vibrationally excited v_2 lines at 96 GHz, 232 GHz (Menten & Melnick 1989) and 658 GHz (Menten & Young 1995). Possible maser emission has also been observed from the vibrationally excited v_2 lines at 232 GHz (Menten & Melnick 1989) and 294 GHz (Menten et al. 2006).

The maser emission from the 96 GHz and 658 GHz v_2 H_2O lines appears to be arising from the near circumstellar envelope (Menten & Melnick 1989; Menten & Young 1995). The observed 325 GHz para-H_2O maser emission, on the other hand, has a similar profile to the 22 GHz emission and possibly arises in the same region of the envelope. The 22 GHz and 325 GHz transitions have similar excitation temperatures, so the coincidence of these masers is to be expected (Yates et al. 1995)

A recent survey of submillimetre water masers with the Atacama Pathfinder Experiment telescope detected water masers at 475 GHz, 471 GHz, 439 GHz, 437 GHz, 325 GHz, 321 GHz, as well as the common 22 GHz line (Menten et al. 2008). The spectrum shapes were different from line to line, with no discernable trend from lower to higher excitation energies. The narrow line widths confirm that this H_2O emission arises in a region where the terminal velocity has not yet been reached (Menten et al. 2008).

2.2.7 SiO maser observations

The first SiO maser observation towards VY CMa was the 86 GHz v=1 J=2-1 line detected by Buhl et al. (1974). Since then a large number of SiO maser lines have been detected, as summarised in Table 2.5. This is an updated version of a similar table presented in Richter (2005). Many of the

ν [MHz]	v	J' - J"	Ref
$^{28}Si^{16}O$			
43423.76	0	1 - 0	4,8*
86846.96	0	2 - 1	2
43122.03	1	1 - 0	1,5,6*
86243.37	1	2 - 1	3,5,10*,11
129363.24	1	3 - 2	5,11
172481.15	1	4 - 3	5
215595.95	1	5 - 4	3,5,9*
258707.39	1	6 - 5	3
301814.33	1	7 - 6	7
344916.25	1	8 - 7	7
560325.75	1	13 - 12	12
650956.12	1	15 - 14	12
42820.48	2	1 - 0	1,5,6*
85640.46	2	2 - 1	11
128458.89	2	3 - 2	2
171275.28	2	4 - 3	5
214088.54	2	5 - 4	5
256898.39	2	6 - 5	5
299703.91	2	7 - 6	7
342504.38	2	8 - 7	7
42519.34	3	1 - 0	5
170070.35	3	4 - 3	5
211077.87	4	5 - 4	5

References:

1. Buhl et al. (1974)
2. Buhl et al. (1975)
3. Jewell et al. (1987)
4. Jewell et al. (1991)
5. Cernicharo et al. (1993)
6. Miyoshi et al. (1994)*
7. Humphreys et al. (1997)
8. Shinnaga et al. (2003)*
9. Shinnaga et al. (2004b)*
10. Shibata et al. (2004)*
11. Kang et al. (2006)
12. De Beck et al. (2011)

* Interferometric observations

ν [MHz]	v	J' - J"	Ref
$^{29}Si^{16}O$			
42879.82	0	1 - 0	3
85759.20	0	2 - 1	2
214385.76	0	5 - 4	2
127748.69	1	3 - 2	1
170328.32	1	4 - 3	1
255478.49	1	6 - 5	2
84575.29	2	2 - 1	2
253703.47	2	6 - 5	2
335880.67	3	8 - 7	4
$^{30}Si^{16}O$			
42373.34	0	1 - 0	5
84746.17	0	2 - 1	2,5
211853.47	0	5 - 4	2
168323.35	1	4 - 3	2
167160.94	2	4 - 3	2

References:

1. Cernicharo et al. (1991)
2. Cernicharo & Bujarrabal (1992)
3. Cho et al. (1996)
4. Gonzalez-Alfonso et al. (1996)
5. Cho & Ukita (1998)

Table 2.5: Observed SiO maser lines for the isotopes $^{28}Si^{16}O$ (left), $^{29}Si^{16}O$ and $^{30}Si^{16}O$ (right). The first column shows the transition frequencies, from Müller et al. (2005). The next three columns are the vibrational level v of the maser transition, between rotational levels J' and J". The reference for the observation is given in the last column of each table.

Transition	Maximum Polarisation	Profile Averaged Polarisation	Reference
v=0 J=1-0	37%		McIntosh & Predmore (1996)
	60%		McIntosh & Rislow (2009)
v=0 J=2-1*	45%		Shinnaga et al. (1999)
v=1 J=1-0	4%	3.8%	Barvainis & Predmore (1985)
		3%	McIntosh & Predmore (1991)
	8%		McIntosh et al. (1994)
	1.4%		McIntosh & Predmore (1996)
v=1 J=2-1	15%		Troland et al. (1979)
		8.6%	Barvainis & Predmore (1985)
		3%	McIntosh & Predmore (1991)
	9.7%		McIntosh et al. (1994)
	3%		Shinnaga et al. (1999)
		4.5%	Glenn et al. (2003)
v=1 J=3-2		25%	McIntosh & Predmore (1991)
v=2 J=1-0	11%	5.3%	Barvainis & Predmore (1985)

Table 2.6: Linear polarisation of VY CMa SiO maser spectra.The second column gives the maximum linear polarisation observed in a component of the spectrum and the third column is the linear polarisation averaged over the full spectrum.
*Not conclusively maser emission.

Transition	Maximum Polarisation	Reference
v=1 J=1-0	6.5%	Barvainis et al. (1987)
	4.1%	McIntosh et al. (1994)
v=1 J=2-1	< 3%	Troland et al. (1979)
	0.8%	McIntosh et al. (1994)

Table 2.7: Circular polarisation of VY CMa SiO maser spectra. The second column gives the maximum circular polarisation observed in a component of the spectrum.

SiO maser lines have been observed numerous times so only references from first detections and first images are included in the table.

The triple-peaked structure of the 43 GHz v=1 J=1-0 spectrum, first observed by Snyder & Buhl (1975), prompted Van Blerkom & Auer (1976) and Zhou & Kaifu (1984) to produce a model of an almost edge-on rotating disk around VY CMa. These models used various expansion velocities and the effects of free-fall and deceleration in the atmosphere to reproduce the SiO lines profile. However, many subsequent single-dish observations of a number of SiO maser transitions have not shown this clear triple-peaked structure (e.g. Kang et al. 2006). The triple peaked structure may therefore have been due to coincidental maser distribution, rather than an underlying disk geometry.

Long-term single dish monitoring of the v=1 and 2 J=1-0 SiO maser spectra show the emission to be variable (Martinez et al. 1988; Alcolea et al. 1999; Pardo et al. 2004), as is the v=1 J=2-1 emission (Glenn et al. 2003; Kang et al. 2006). The variability displayed by supergiant SiO masers is much more complex than that of Mira variables (Pardo et al. 2004). A 22.5 km/s spike in the spectrum is visible throughout the 6 year period of the Alcolea et al. (1999) monitoring, and the 11 year period of the Pardo et al. (2004) monitoring. The masers do not seem to display short term variability, with Pijpers et al. (1994) showing that the v=1 J=1-0 maser profile remained constant over the course of

a month.

The linear and circular polarisation of the v=1 to v=2 SiO maser spectra have been measured on a number of occasions. The results are summarised in Tables 2.6 and 2.7. The linear polarisation of the v=1 J=2-1 and the v=0 J=1-0 SiO maser lines was monitored over two to three year periods by Glenn et al. (2003) and McIntosh & Rislow (2009). Both studies note maser components that remain stable over the duration of the observations.

Barvainis et al. (1987) use their 6.5% measurement of the maximum circular polarisation in the v=1 J=1-0 spectrum to estimate a magnetic field level of $\sim$ 65 G in the near circumstellar envelope of VY CMa, using the Deguchi & Watson (1986) model to interpret the polarisation. McIntosh et al. (1994) also note that their measurement of 4.1% circular polarisation from the v=1 J=1-0 line implies magnetic fields of tens of Gauss, if interpreted with the Zeeman maser polarisation model (McIntosh et al. 1994).

2.3 Circumstellar envelope: Imaging observations

This section reviews the published images of VY CMa. A number of the images discussed in the text are reproduced in an image gallery, in Figures 2.1 to 2.6. The images are discussed per wavelength band, working roughly from the most large scale images to the most small scale images.

2.3.1 Optical observations

HST images of VY CMa and it's surrounding nebula have been published by Kastner & Weintraub (1998) and Smith et al. (2001), who observed VY CMa with the Faint Object Camera and WFPC2 respectively. The images provided by Kastner & Weintraub (1998) show the star to be embedded in the eastern side of a clumpy elongated nebula, which extends to the west and southwest. The observed emission region is about 3 arcseconds in width. The bright knot that may be taken to be the star is shown to be purely scattered light, implying that the central star is obscured by the dusty envelope (Kastner & Weintraub 1998).

The WFPC2 images provide a sharp increase in resolution, and reveal an intensely complex circumstellar environment (Smith et al. 2001). Smith et al. (2001) provide a sketch of the main features observed in their HST images of the nebula, which is shown in the image gallery, in the left panel of Figure 2.1. The observed emission is about 10 arcseconds in extent, and embedded with many small scale features such as arcs, condensations and bright knots. These features provided the first evidence for localised mass ejections from the star, which are discussed further in Section 2.5.

Subsequent WFPC2 HST images by Humphreys et al. (2007) were used in conjunction with the Smith et al. (2001) images to determine the proper motion of the ejecta and to develop a three-dimensional picture of their kinematics. Polarimetric HST observations by Jones et al. (2007) also display the arcs and other features visible in the total intensity HST maps. These observations are discussed in more detail in Section 2.5.

2.3.2 Mid-infrared observations

Smith et al. (2001) imaged VY CMa at 4.7 μm, 8.4 μm and 9.8 μm with the ESO 3.6 m telescope. The 9.8 μm image is reproduced in the right panel of Figure 2.1. All three of the images are elongated

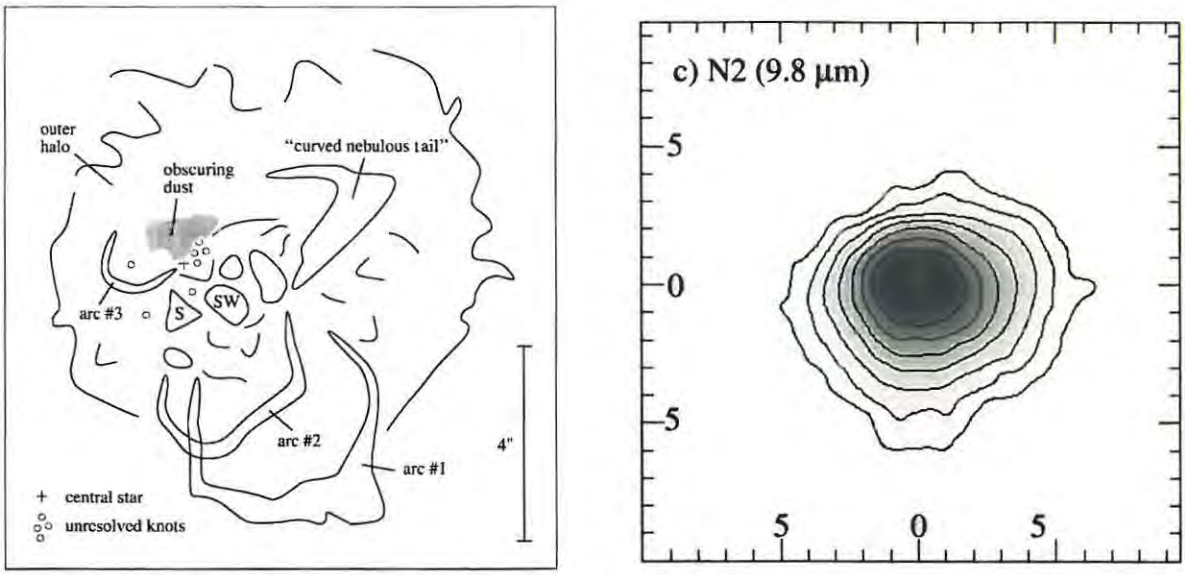

Figure 2.1: Optical and mid-infrared images of VY CMa from Smith et al. (2001). Left: Diagram of the features observed in optical near-infrared images of the nebula, using the HST and ESO 3.6 m telescope. Right: Mid-infrared image of VY CMa from the ESO 3.6 m telescope.

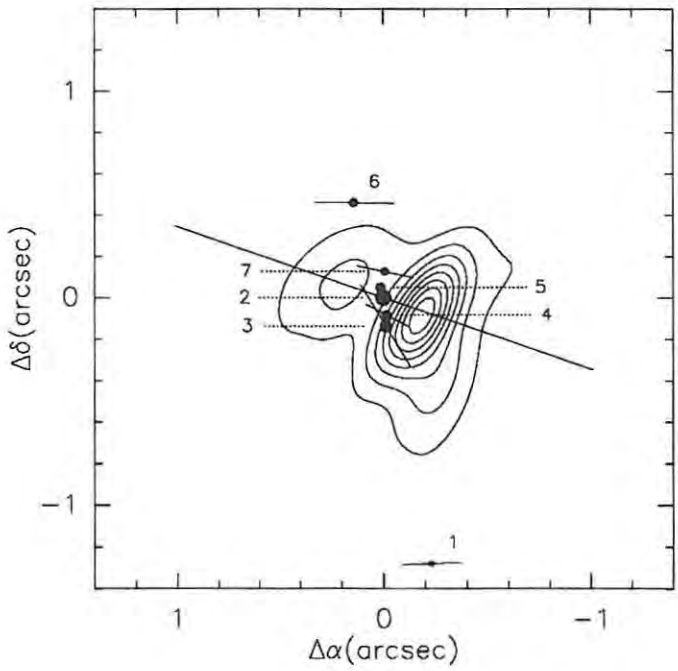

Figure 2.2: Shinnaga et al. (2004b) image of the bipolar v=0 J=1-0 thermal SiO emission (Shinnaga et al. 2003), overlayed with the seven v=1 J=5-4 SiO maser spots (Shinnaga et al. 2004b). The linear polarisation level and direction are illustrated by the vectors over each maser spot (Shinnaga et al. 2004b).

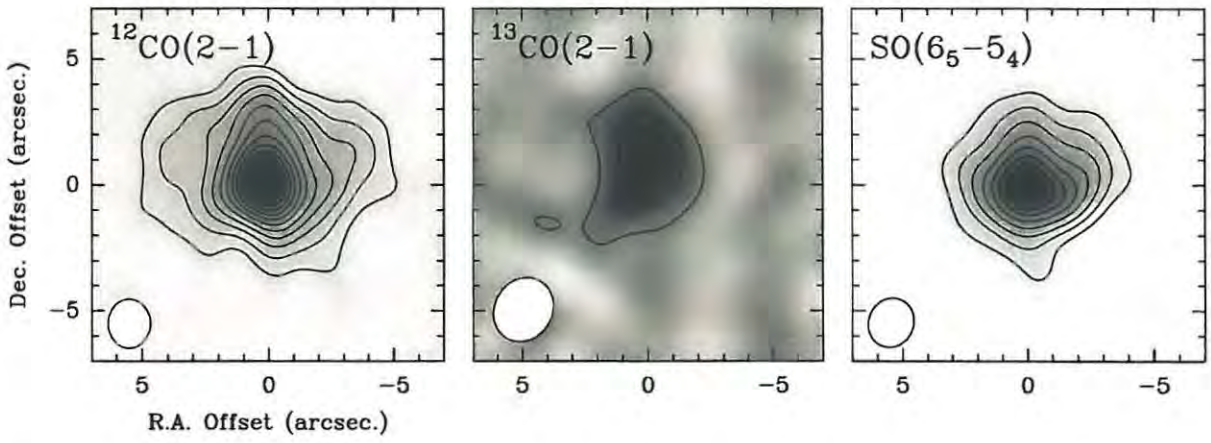

Figure 2.3: SMA images of thermal emission from ^{12}CO(2-1), ^{13}CO(2-1) and SO($6_5 - 5_4$) (Muller et al. 2007).

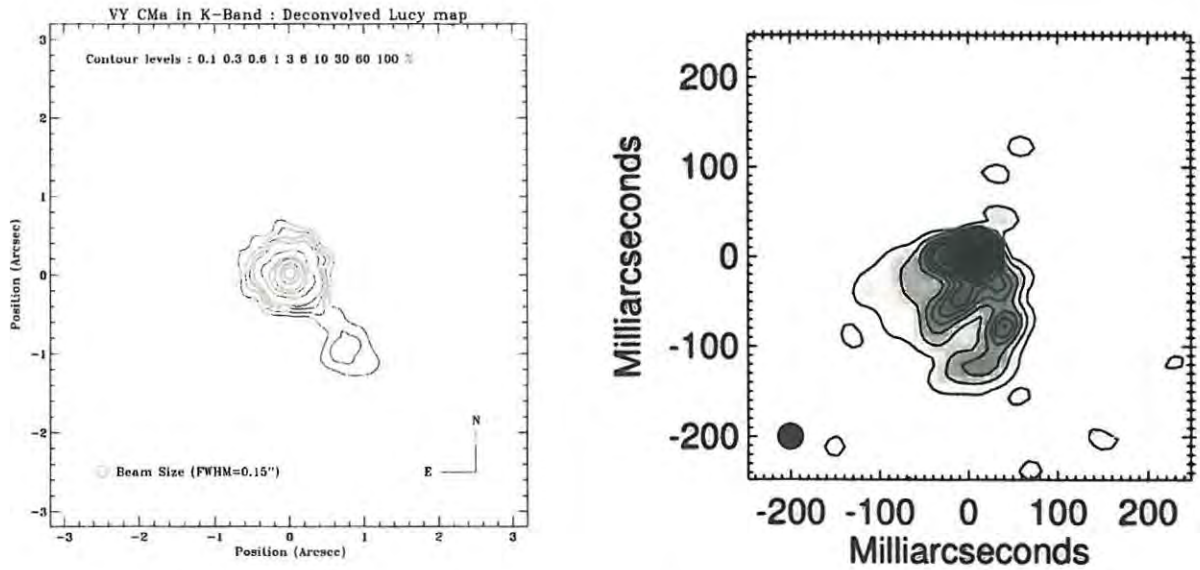

Figure 2.4: Near-infrared images of VY CMa. Left: 2.2 μm ESO image of VY CMa from Cruzalebes et al. (1998). Right: 1.65 μm near-infrared Keck aperture-masking image of VY CMa from Monnier et al. (1999b).

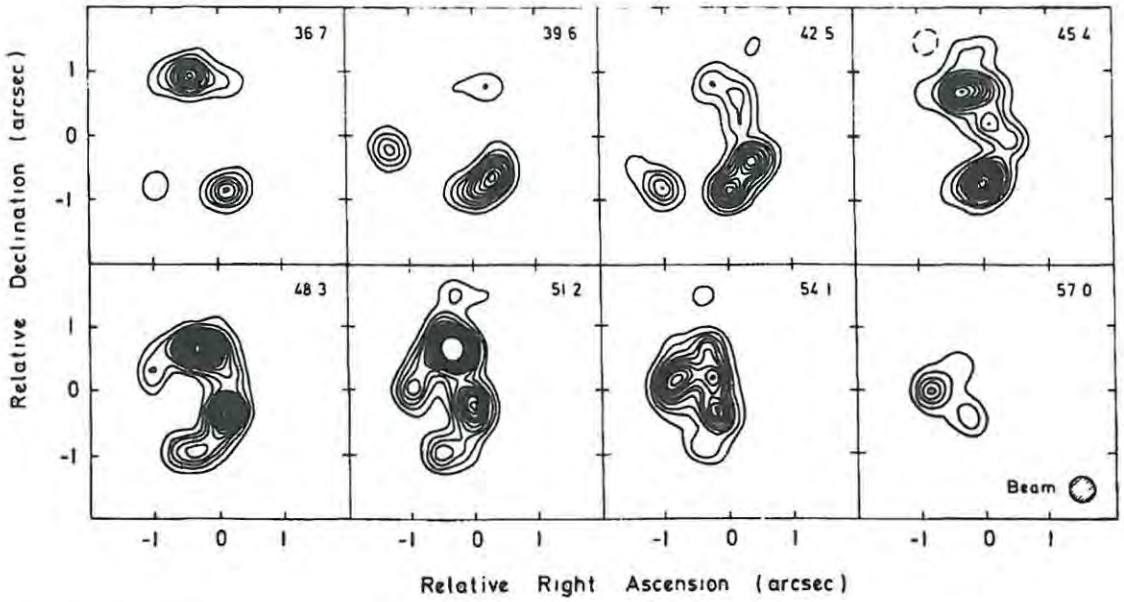

Figure 2.5: MERLIN Map of 1612 MHz OH maser emission towards VY CMa, by Cohen (1987). The velocity of each panel is shown in the top right of the panel. The velocity range of this figure is limited to the red-shifted region of the double-peaked OH maser spectrum.

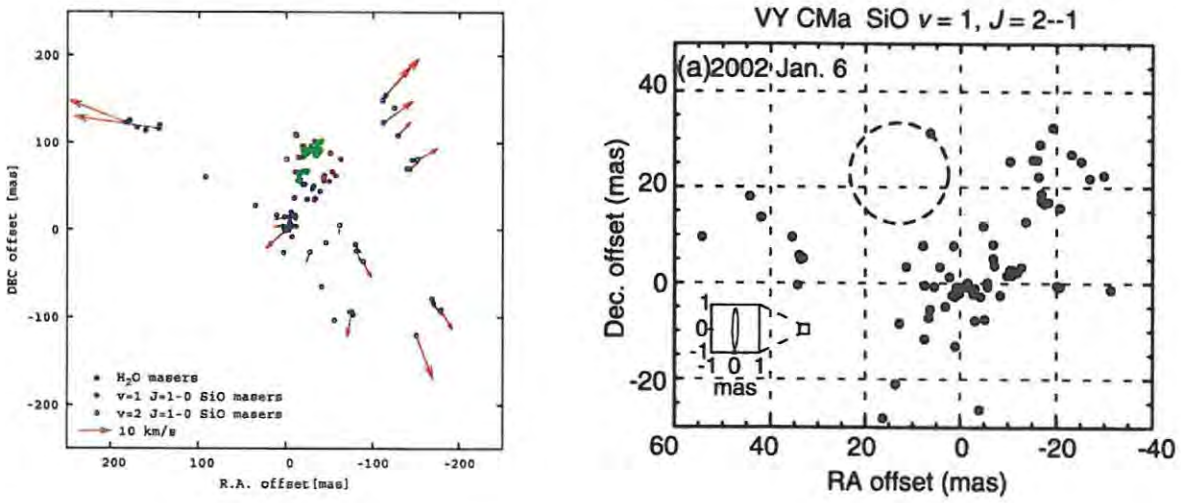

Figure 2.6: Maser maps of VY CMa. Left: VERA phase referenced image of the 22 GHzH_2O masers (blue) and 43 GHz v=1 J=1-0 (purple) and v=2 J=1-0 (green) SiO masers towards VY CMa (Choi et al. 2008a). The red arrows show the proper motion of the H_2O masers. Right: Single baseline VLBI image of the 86 GHz v=1 J=2-1 SiO masers towards VY CMa (Shibata et al. 2004).

in the east-west direction, although Smith et al. (2001) caution that this may be due to errors in the point-spread function subtraction. The ratios of the three observed mid-infrared emission observations were used to derive the dust grain size in this emission region, which is around 0.3 μm (Smith et al. 2001).

2.3.3 Submillimetre observations

Shinnaga et al. (2003) imaged the v=0 J=1-0 thermal SiO emission with the VLA. The image is reproduced in Figure 2.2. The emission has a bipolar structure and extends over approximately 1.5 arcseconds. It is elongated along a roughly east-northeast to west-southwest axis, with the south-western lobe being the brighter of the two, as shown in the figure. The linear polarisation was also mapped, and found to be aligned with the bipolar axis (Shinnaga et al. 2003).

Further SMA imaging of thermal molecular lines was perfomed by Muller et al. (2007), of the ^{12}CO (2-1), ^{13}CO (2-1) and SO ($6_5 - 5_4$) lines, and by Fu et al. (2011) of the SiS (J=13-12), PN (J=5-4), SO_2 ($4_{2,2} - 3_{1,3}$), SO_2 ($10_{3,7} - 10_{2,8}$), SO_2 ($15_{2,14} - 15_{1,15}$) and SO_2 ($16_{1,15} - 15_{2,14}$) lines.

The Muller et al. (2007) images are reproduced in Figure 2.3. Muller et al. (2007) found that the emission arises in distinct kinematic components, which they modelled using a dense central component, an extended envelope, and a high velocity bipolar flow. The modelled bipolar outflow has a wide opening angle of 120° with our viewing angle being into the bipolar flow with inclination angle of 15°. The expanding envelope was modelled as having a velocity of 15 km/s and the bipolar flow a velocity which increases from 15 km/s to 45 km/s at the outer boundary (Muller et al. 2007). Smith et al. (2009) suggest that the high velocity CO component observed by Muller et al. (2007) is the combined effect of the many individual fast moving dense cloudlets they observed in their high resolution Phoenix-slit CO spectra.

Fu et al. (2011) found no evidence for bipolarity in their SO_2 images. Instead, they model their images with four independent kinematic components: an slow spherical wind near the star, and three fast outflow components far from the star. They argue that the outflow components are the result of independent localised mass-loss events, about 500 years ago. Two of these components can be identified with the red- and blue-shifted outflows also observed by Ziurys et al. (2007), Muller et al. (2007) and Ziurys et al. (2009) (Fu et al. 2011).

2.3.4 Near-infrared observations

Several interferometric maps have been made of the near-infrared emission from VY CMa. The near-infrared radiation is emitted primarily by the stellar photosphere and the warm layers of molecular gas above the photosphere (Wittkowski et al. 2007a).

Near-infrared observations of VY CMa have been performed with adaptive optics systems at the European Southern Observatory (ESO) 3.6 m telescope at 1.25 μm by Monnier et al. (1999b) and Smith et al. (2001), at 1.65, 2.12 and 2.14 μm by Smith et al. (2001), and at 2.2 μm by Cruzalebes et al. (1998). The Cruzalebes et al. (1998) images have an angular resolution of 150 mas, those of Monnier et al. (1999b) have a resolution of $\sim$ 90 mas, and the Smith et al. (2001) images have a similar resolution to the Monnier et al. (1999b) images. The emission is visibly asymmetric in the higher reolution ESO images, with a clear lack of emission in the northeast.

A distinct clump of near-infrared emission, located approximately 1.3 arcseconds to the southwest of VY CMa, is visible in these images (Cruzalebes et al. 1998; Monnier et al. 1999b; Smith et al. 2001). It was first observed by Cruzalebes et al. (1998), and the original image is reproduced in the left panel of Figure 2.4. The clump has a diameter of approximately 0.9 arcseconds (Cruzalebes et al. 1998) and is close to two orders of magnitude brighter than any other feature in the circumstellar envelope at 1.25 μm (Monnier et al. 1999b).

This feature is also visible in the optical Smith et al. (2001) HST images, and is labelled "SW" (for southwestern clump) in the left panel of Figure 2.1. The higher resolution provided by the HST images show this southwestern knot to be one of many bright condensations located one to two arcseconds from the star. The condensations are each collections of numerous bright knots. The most prominent of the condensations are the southwestern clump originally observed in the near-infrared ("SW" in the left panel of Figure 2.1), and a second clump to the south of the star ("S" in the left panel of Figure 2.1). Unlike the southwestern clump, the southern clump is not visible at near infared wavelengths (Smith et al. 2001).

Monnier et al. (1999b) propose that the southwestern clump of emission may be stellar radiation escaping through a hole in the dust shell. The position of the clump is consistent with the path of the "rotating hole" proposed by Wallerstein (1978) (Monnier et al. 1999b), but so is the position of the southern clump (Smith et al. 2001).

Wittkowski et al. (1998) observed VY CMa in the near-infrared using speckle-masking interferometry, and found the emission to be elongated. Gaussian fits of the maps at 0.8 μm, 1.28 μm and 2.17 μm gave FWHM dimensions and position angles of 60 x 83 mas at 153°, 80 x 116 mas at 176° and 138 x 205 mas at 160° respectively. The corresponding image resolutions were 46 mas, 73 mas and 124 mas.

The following year Monnier et al. (1999b) published higher resolution Keck I aperture-masking maps of VY CMa at wavelengths 1.65 μm, 2.26 μm and 3.08 μm. The images were reconstructed with a 30 mas beam at 1.65 μm and 2.26 μm, and a 40 mas beam at 3.08 μm. The Keck I 1.25 μm image from Monnier et al. (1999b) is reproduced in the right panel of Figure 2.4. All of the Keck I maps are dramatically one-sided, with almost no emission observed to the north and northeast of the maps (Monnier et al. 1999b).

The Monnier et al. (1999b) maps also display a bright knot of emission 65 mas to the southeast of the star, visible in Figure 2.4. The proximity of the clump to the $\sim$ 50 mas inner dust shell radius suggests that it may be a recently formed clump of dust (Monnier et al. 1999b).

A subsequent K-band Keck aperture-masking observation of VY CMa was performed by Monnier et al. (2004), in conjunction with the Infrared-Optical Telescope Array (IOTA) interferometer. This provided a further increase in resolution, to approximately 20 mas. This image has a similar structure to the Monnier et al. (1999b) Keck images, being highly asymmetric and concentrated to the south of the star. The bright southeastern knot is also present in these images. When the Keck and IOTA data are combined to reconstruct the image, the southeastern knot emission looks like it may be part of a larger arc of emission extending to the south (Monnier et al. 2004).

2.3.5 OH maser observations

The earliest interferometric maps of the 1612 MHz satellite line OH masers towards VY CMa were made by Masheder et al. (1974), Moran et al. (1977) and Reid & Muhleman (1978). The maser emission was found to extend over approximately 2.5 arcseconds (Masheder et al. 1974; Moran et al. 1977; Reid & Muhleman 1978) and is observed to be somewhat elongated in a north-south direction in two of the published maps (Masheder et al. 1974; Moran et al. 1977). The Reid & Muhleman (1978) map does not display any obvious elongation. Reid & Muhleman (1978) contend that the differences between the Masheder et al. (1974), Moran et al. (1977) and Reid & Muhleman (1978) 1612 MHz OH maps is due to the different baseline lengths and imaging techniques used in each case. Reid & Muhleman (1978) were the first to image the 1612 MHz masers using the CLEAN technique, which avoided the simplifying assumptions necessary for Masheder et al. (1974) and Moran et al. (1977) to image the masers.

The blueshifted emission in the maps by Masheder et al. (1974), Moran et al. (1977) and Reid & Muhleman (1978) tends to be clustered towards the middle of the redshifted components. The maser spot at 4.6 km/s is particularly strong in the cross-correlated data, but not particularly strong in the autocorrellation spectrum, suggesting that this spot may be an amplification of the stellar radiation (Moran et al. 1977). By this reasoning the star is positioned behind the 4.6 km/s feature, near the centre of the map (Moran et al. 1977).

Connected element maps of the 1612 MHz OH masers have been made with the VLA (Bowers et al. 1983) and MERLIN (Cohen 1987). The Bowers et al. (1983) VLA map shows maser emission from what appear to be the front and back of the star, and a broken shell of emission around the star. The Cohen (1987) MERLIN map only spans a region of the red-shifted region of the spectrum, and appears as a broken clumpy ring of emission. The Cohen (1987) map is reproduced in Figure 2.5. Cohen (1987) notes that given the velocity coherence and excitation condition requirements of maser radiation, and the turbulent environment in which they are formed, the incomplete nature of the shells observed towards VY CMa and other late-type OH maser stars is to be expected.

The VLA map shows a systematic displacement in the positions of the intensity maxima of the maps at velocities lower than and greater than the stellar velocity (Bowers et al. 1983). Bowers et al. (1983) interpret these position offsets to be evidence of a thick disk or ellipsoid geometry, where the plane of the disk is highly inclined with respect to the plane of the sky. In this model the intersection of the disk with the plane of the sky will form a line at a position angle of approximately 140°, and the projected polar axis of the disk will be at approximately 49° (Bowers et al. 1983).

Three sets of interferometric maps of the main line OH emission have been made, by Harvey et al. (1974), Reid & Muhleman (1978) and Benson & Mutel (1982). None of these maps span the full velocity range of the emission observed by Morris & Bowers (1980). The Harvey et al. (1974) and Benson & Mutel (1982) velocity ranges are particularly small, covering less than 20 km/s over the main blueshifted feature.

Both the Reid & Muhleman (1978) and Benson & Mutel (1982) maps show the 1667 MHz masers to be distributed over approximately 250 mas, in a region elongated in the northeast-southwest direction. The 1667 MHz masers observed by Harvey et al. (1974) extend over a region of width approximately 450 mas. The 1665 MHz masers are distributed over approximately 500 mas, 350 mas and 300 mas in the Harvey et al. (1974), Reid & Muhleman (1978) and Benson & Mutel (1982) maps respectively.

Morris & Bowers (1980) suggest that the OH main line maser emission arises in a similar region to the thermal SiO emission, in a region of the envelope where terminal velocity has been reached.

Benson & Mutel (1982) observed a Zeeman doublet in the 1665 MHz spectrum, which flared up over a couple of years before their VLBI observations. The VLBI image confirmed that the two doublet features were located in the same region of the map, removed from the rest of the emission. A magnetic field value of 1 mG was derived from the Zeeman doublet (Benson & Mutel 1982).

2.3.6 H_2O maser observations

The first interferometric imaging of 22 GHz H_2O maser emission towards VY CMa was an early VLBI experiment that took place in 1974 and 1976 using telescopes at Haystack, NRAO and the US Navel Research Laboratory (Rosen et al. 1978). Subsequent H_2O maser maps have been made with the VLA (Bowers et al. 1993), MERLIN (Yates & Cohen 1994; Richards et al. 1998), the VLBA (Marvel 1996; Vlemmings et al. 2002) and VERA (Choi et al. 2008b,a).

The Yates & Cohen (1994) MERLIN observation was performed with just three antennas and shows a band of roughly north-northwest to south-southeast maser emission with detached maser features in the east-northeast to west-southwest direction. Yates & Cohen (1994) suggest that the band of emission is a disk, with ejected matter along a polar axis. The other maps each show a distribution of H_2O masers elongated along a roughly east to west or east-northeast to west-southwest axis. The VERA map published by Choi et al. (2008a) is shown in the left panel of Figure 2.6. This H_2O maser map was aligned to the SiO maser emission through phase referencing, and the relative alignment of the maser species is shown in the figure. The total intensity line widths and line shapes of the individual maser features mapped by Vlemmings et al. (2002) show the H_2O masers to be unsaturated or weakly saturated.

The extent of the imaged 22 GHz H_2O maser emission ranges from approximately 40 mas, close to the inner dust shell radius, to approximately 400 mas from the star (Yates & Cohen 1994; Richards et al. 1998; Marvel 1996). The inner boundary of the maser emission is set by the increasing density of the circumstellar material closer to the star (Cooke & Elitzur 1985). Richards et al. (1998) derive a mass-loss rate of 9.5×10^{-3} $M_\odot$ yr^{-1} from the quenching density, using an inner boundary of 75 mas and expansion velocity of 7.8 km/s at the inner boundary derived from a spherical expanding shell model fit to the masers (Richards et al. 1998). This mass-loss rate value is more than an order of magnitude higher than other estimates of the mass-loss rate, implying that the H_2O masers may be located in regions of enhanced density (Richards et al. 1998).

Investigations of the H_2O maser proper motion by Marvel (1996), Richards et al. (1998) and Choi et al. (2008a) show that most of the maser features are moving away from the assumed stellar position and confirmed that the H_2O masers reside in an accelerating region of the circumstellar envelope. The proper motion modeling by Richards et al. (1998) implies an outer boundary of 360 mas and an outer boundary velocity of 31.7 km/s. The model utilised by Marvel (1996) gave a mean expansion velocity of 12.8 km/s, assuming a distance of 1.5 kpc to the star. The proper motion velocity vectors from the Choi et al. (2008a) observations are shown in the left panel of Figure 2.6.

Vlemmings et al. (2002) observed the 22 GHz H_2O maser with the VLBA and correlated the data in full polarisation mode. This enabled them to measure the circular polarisation of seven of the maser spots, which ranged from 0.2 to 0.6%. The circular polarisation values imply a magnetic field of ~ 175

to $\sim$ 200 mG, depending on the model used to interpret the polarisation. They did not detect any linear polarisation (Vlemmings et al. 2002).

2.3.7 SiO maser observations

VLBI imaging of the v=1 and 2 J=1-0 and J=2-1 transitions shows emission extending over a region approximately 60 to 100 mas in extent (Miyoshi et al. 1994; Miyoshi 2003; Shibata et al. 2004; Richter et al. 2007; Choi et al. 2008a; Zhang et al. 2012). The SiO maser emission is localised in many individual features with sizes of the order of a milliarcsecond. The lifetime of a single maser feature is around several hundred days. Glenn et al. (2003) observed the characteristic lifetime of the individual components of the VY CMa v=1 J=2-1 SiO maser spectrum to be 645 days.

As dust forms in the circumstellar envelope, silicon is incorporated into silicate dust, which depletes the abundance of SiO molecule in the envelope. The SiO maser emission is therefore expected to cease outside of the dust shell boundary (Elitzur 1992, pg 283). The cessation of SiO maser emission is not abrupt, and simultaneous observations of SiO masers and the dust shell show some overlap, and variability in the extension of the masers into the dust shell with stellar phase (Wittkowski et al. 2007b). However, as expected, most of the v=1 and 2 J=1-0 and J=2-1 SiO maser emission observed towards VY CMa in VLBI maps falls roughly within the $\sim$ 50 mas dust formation radius.

Images of the SiO masers around supergiant VY CMa do not all show as obvious a ring distribution as is observed towards Mira variables. Instead the maps show clumps of maser spots located around the star (Miyoshi et al. 1994; Miyoshi 2003; Shibata et al. 2004; Richter et al. 2007; Choi et al. 2008a; Zhang et al. 2012). The v=1 J=2-1 SiO masers observed by Shibata et al. (2004), for example, do not display a ring structure at all, and instead are located to the south and west of the star, for the stellar position assumed by the authors. The Shibata et al. (2004) v=1 J=2-1 image is reproduced in the right panel of Figure 2.6, and the assumed stellar position is shown on the figure. The beam size used to restore these images was $\sim 1.7 \times 0.24$ mas. The SiO maser emission is located at radii of 2-4 R_* from the star, assuming the stellar position shown in the figure (Shibata et al. 2004).

Choi et al. (2008a) provide phase referenced VERA images of the v=1 and 2 J=1-0 SiO masers and the 22 GHz H_2O masers, as described in the previous section. The phase referenced image of the three maser species is reproduced in the left panel of Figure 2.6. In the phase referenced image, the two SiO maser lines show emission from similar regions, with the SiO masers located towards the centre of the larger H_2O maser region.

Zhang et al. (2012) recently published four epochs of phase-referenced VLBA images of v=1 J=1-0 SiO masers, which they use to determine proper motions for the maser features over the 1.5 years spanned by their observations. The maser spots show a slow expansion over this period. They model six spoke-like maser features with ballistic orbits, and suggest they they are predominantly on the far side of the star, decelerating in the direction away from the star (Zhang et al. 2012). Zhang et al. (2012) also observed the v=1 J=1-0 SiO masers with the VLA. They used the relatively low resolution (50 mas beam) VLA SiO maser map to align the VLBA maps with near-simultaneous observations of a weak 43 GHz radio photosphere toward VY CMa.

On a larger scale, SMA images of the higher frequency v=1 J=5-4 SiO spectral line shows seven maser spots, falling within 400 mas of the star, shown in Figure 2.2. The image shows two outlying features falling outside of a central group. The two outlying features are located to the northeast

and southwest of the central group of components and may be located outside the near circumstellar envelope. At this larger distance from the star, the conditions necessary for maser emission for these two spots may be supplied by shock excitation in a bipolar outflow (Shinnaga et al. 2004b). However, the positional uncertainties of the two outlying spots are large, so their offset between the central spots may not be significant (Shinnaga et al. 2004b). The presence of this high angular momentum v=1 J=5-4 line indicates that there are very dense clumps of gas close to the star, with densities of about 10^{10} cm^{-3} (Cernicharo et al. 1993).

The average linear polarisation electric vector position angle (EVPA) of the v=1 J=5-4 SiO maser emission from the seven maser spots is 72° ± 4°, with strong support for the hypothesis that the EVPA of all seven spots is the same (Shinnaga et al. 2004b). The maser spots display levels of linear polarisation ranging from less than 10%, up to 63% (Shinnaga et al. 2004b).

2.4 Axisymmetric envelope geometry

Over the many years that VY CMa has been observed, numerous astronomers have attributed characteristics of their observations to the presence of a disk around the star, with an accompanying flow from the polar regions. In this section the evidence for an axisymmetric geometry is collated, and the mechanisms that could lead to it are discussed.

2.4.1 Evidence for an axisymmetric geometry

A bipolar geometry can clearly be observed in the Shinnaga et al. (2003) thermal SiO image, which is reproduced in Figure 2.2 of the previous section. The emission appears to trace a bipolar outflow with a east-northeast west-southwest axis, with aligned linear polarisation. This bipolar structure, on the scale of a several hundred milliarcseconds, is also aligned to the linear polarisation of the much smaller scale v=1 J=4-5 SiO maser emission. The correlation may imply that the larger scale structure of the envelope, traced by the thermal SiO emission, is linked to that of the near circumstellar envelope, traced by the SiO maser emission (Shinnaga et al. 2004b).

The geometry of the 22 GHz H_2O maser emission also shows some support for a bipolar geometry. The H_2O maser emission observed by Yates & Cohen (1994) with MERLIN shows what appears to be east-northeast to west-southwest bipolar ejections, orthogonal to an equatorial disk, as described above. Richards et al. (1998) also suggest that the H_2O maser emission is located in a dense equatorial belt, perpendicular to a polar outflow. This geometry may also be supported by the Choi et al. (2008a) 22 GHz H_2O maser maps, shown in Figure 2.6, which appears to have distinct clumps of maser emission located to the northeast and southwest of the star, although a northwestern region of emission is present too.

On a larger scale, VLA observations of the 1612 MHz OH masers show a separation between blueshifted and redshifted emission, along a northeast-southwest direction (Bowers et al. 1983). Bowers et al. (1983) attribute this to a disk of material around the star, with a northeast-southwest polar axis.

The spectra from various molecules observed towards VY CMa show evidence for high velocity red and blueshifted flows, which have also been interpreted as evidence for a a bipolar outflow from the star, with a possible equatorial density enhancement (e.g. Muller et al. 2007).

Near-infrared images of VY CMa are elongated in a nearly north-south direction, with position angle of around 170° (Wittkowski et al. 1998). Wittkowski et al. (1998) suggest the elongation could be tracing either a north-south bipolar outflow in the presence of an east-west equatorial disk, or it could be the disk itself, projected onto the plane of the sky.

Higher resolution near-infrared images show emission strongly concentrated in the south of the star (Monnier et al. 1999b, 2004). Several explanations were put forward for the one-sided emission. One possibility is the existance of a roughly east-west equatorial density enhancement, where the southern emission eminates from a polar region (Monnier et al. 1999b). Alternatively, the southern emission could be forward scattering from an equatorial disk, where the southern region is tilted towards us (Monnier et al. 1999b).

The HST images of Kastner & Weintraub (1998) and Smith et al. (2001) also suggest a flattened equatorial distribution of dust around VY CMa. Kastner & Weintraub (1998) note the roughly northeast-southwest axis of symmetry in the HST images. The emission to the west-southwest can be interpreted as a forward facing lobe of emission along the polar axis. Emission from the rear polar lobe is presumably attenuated by the equatorial disk (Kastner & Weintraub 1998). Smith et al. (2001) also attribute the mid-infrared elongation at a position angle of around 120° to 130° to an equatorial disk.

A thick disk model is also proposed by Herbig & Zappala (1970) and Efstathiou & Rowan-Robinson (1990), based on the infrared spectral energy distribution. The disk modelled by Herbig & Zappala (1970) has an opening angle somewhere in the range of 10° to 30°. The flared disk model of Efstathiou & Rowan-Robinson (1990) has an opening angle of 45° and is inclined at 43° below the line of sight, so that we are veiwing the star just inside the disk.

Smith et al. (2009) also use their high resolution CO spectra to model the envelope with a flared slow equatorial density enhancement, which is imbedded in a less dense, faster halo. They propose that many high velocity localised mass ejections are randomly distributed throughout the axisymmetric envelope, explaining the arcs and knots observed in the envelope by HST images (Smith et al. 2001) and the dense cloudlets traces by the CO observations (Smith et al. 2009).

In summary, there is evidence at multiple wavelengths and resolutions for some manner of equatorial density enhancement around VY CMa, and a bipolar outflow. The most consistent picture of this, across multiple wavelength observations, is of a density enhancement having a position angle on the plane of the sky of somewhere between about 120° and 170°. A rough sketch of a possible geometry is given in Figure 2.7. The figure shows a relatively thin disk. In the flared geometries proposed by Efstathiou & Rowan-Robinson (1990), Muller et al. (2007) and Smith et al. (2001), the disk increases in width with distance from the star and our viewing angle is inside the disk.

The axisymmetic geometry could be caused by a large scale equatorial density enhancement, as pictured above, or by the combined effect of a number of smaller scale features concentrated in a particular plane. The possible causes of the axisymmetric geometry are discussed in the following section.

2.4.2 Possible causes of an axisymmetric geometry

An equatorial density enhancement could be created by several mechanisms. One possibility is the presence of a binary companion, which perturbs the extended envelope of VY CMa as it moves through

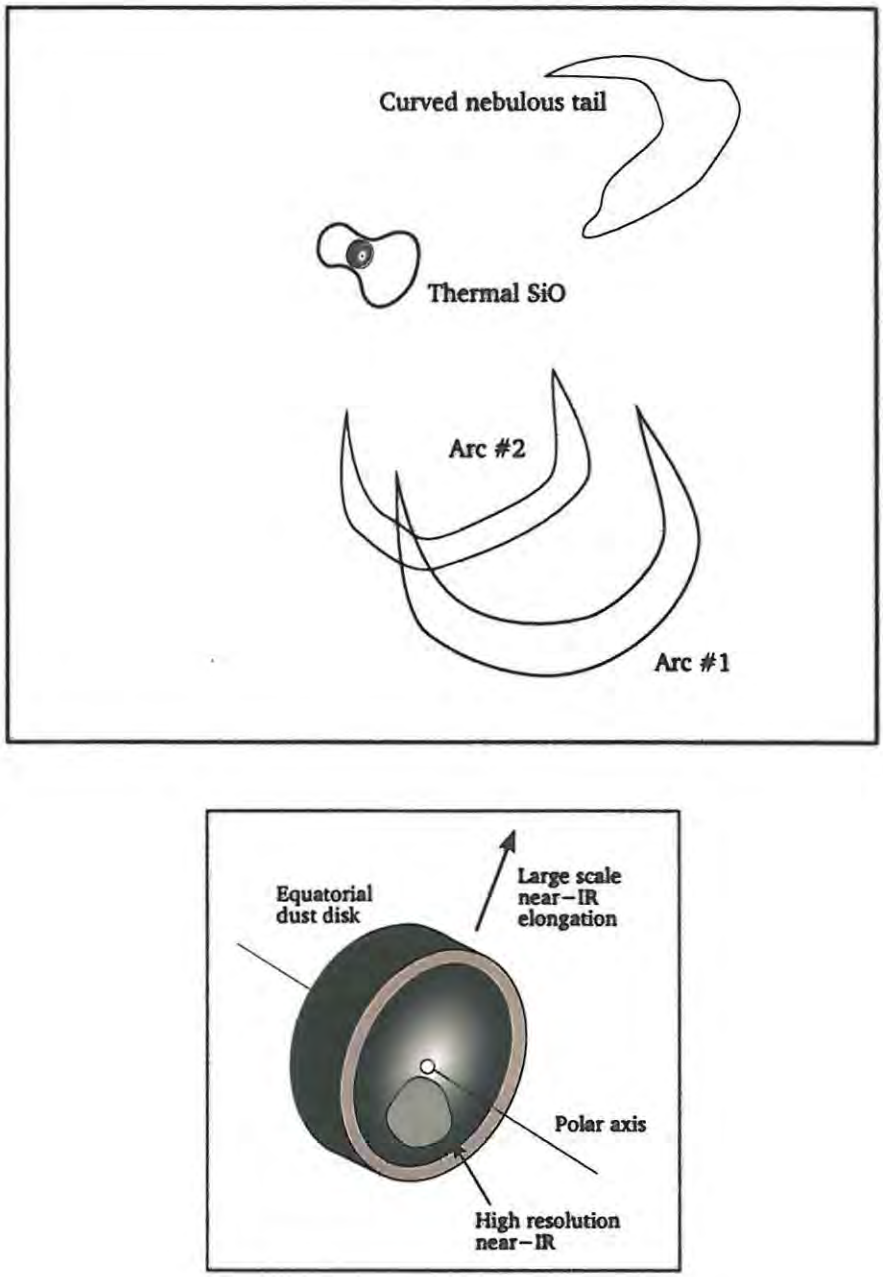

Figure 2.7: A sketch of the possible circumstellar envelope geometry. The top figure shows: an equatorial disk around the central star, the bipolar thermal SiO emission (Shinnaga et al. 2003) and the main features observed in large scale HST images of the nebula (Smith et al. 2001). The bottom figure is a close-up of the equatorial disk, and shows: the polar axis, the direction of the near infrared elongation (Wittkowski et al. 1998), and the southern emission visible in high resolution near-infrared images (Monnier et al. 1999b).

it (Cruzalebes et al. 1998; Smith et al. 2001; Muller et al. 2007). Early observers did consider VY CMa to be a multiple star system, based on observations of the bright knots in the nebulosity (Wallerstein 1958).

However, this belief was overturned by Herbig (1972) who used optical polarisation observations to show that the bright knots are structures within the circumstellar material. Wallerstein (1978) instead explains the presence of one of the bright knots as a hole in the dusty envelope surrounding VY CMa. Light from the central star escapes through the hole, leading to the bright spot observed in the infrared (Wallerstein 1978). Monnier et al. (1999b) extrapolate the path of the proposed hole to the present day knots observed in the nebula. If the knot is a rotating hole, then the rotation rate implied by it's extrapolated motion is too high for that of an isolated red supergiant. The high rotation rate of the knot could therefore also be evidence for a companion star. A low mass binary companion at a distance of about 400 mas from VY CMa would give an orbital period of about 2700 years, which is a rotational period that has been derived for VY CMa (Monnier et al. 1999b).

However, no direct spectral evidence for a large binary companion has been found (Smith et al. 2001) and no companion has been observed in high resolution imaging (Wittkowski et al. 1998). If VY CMa does have a companion it would have to be a low mass star in order to have escaped detection so far (Smith et al. 2001).

A second possible origin of an equatorial density enhancement is that it is the remnant of a protostellar disk (Richards et al. 1998; Kastner & Weintraub 1998; Monnier et al. 1999b). As a very large star, VY CMa may have evolved rapidly enough that it retained part of the pre-main sequence disk as it moved off the main sequence (Richards et al. 1998; Kastner & Weintraub 1998).

A third explanation of a disk geometry is through the effect of rotation (Wittkowski et al. 1998). The expansion of a star as it becomes a supergiant and the intense mass-loss accompanying the red supergiant stage both act to decrease the rotation of the star. Red supergiant stars have therefore been assumed to be at most very slow rotators, unable to form axisymmetric geometries on the basis of angular momentum alone (Heger & Langer 1998). The presence of a binary companion could cause the prerequisite rotation, but no appropriate binary has been observed, as discussed above. It therefore seems unlikely that rotation is playing a major role in sculpting the envelope geometry. However, Heger & Langer (1998) put forward a mechanism whereby red supergiant star envelopes are spun up as they move away from the Hyashi line, towards the blue. The increase in rotation is due to the contraction of the envelope and the convective zone retreating to higher layers of the star, taking angular momentum with it (Heger & Langer 1998). If the star is rotating at a significant level, this could lead to enhanced equatorial mass-loss, due to the von Zeipel theorem (Maeder & Meynet 2008).

A further explanation for the envelope geometry is through localised mass ejections from giant convective cells. The discrete geometric structures in the envelope, the arcs and knots, may have been created through convection effects in the outer layers of the star (Smith et al. 2001, 2009). Although the redshifted and blueshifted flows observed in the molecular line emission have been interpreted as bipolar emission, in the context of a disk model (e.g. Muller et al. 2007), an alternative interpretation is that the flows are independent of one another. Rather than being part of a global bipolar outflow, they may be associated with the arcs observed in the HST images (shown in Figures 2.1 and 2.7) (Ziurys et al. 2007). Arc #1, has been shown to be blueshifted with respect to the stellar velocity, and the curved nebulous tail and Arc #2 have been shown to be redshifted (Smith 2004; Humphreys

et al. 2005; Smith et al. 2009). On this basis these features have been linked with the blueshifted and redshifted components of the outflow, which are then assumed to be two independent flows in the directions of the curved nebulous tail and Arc #1. Ziurys et al. (2009) model the flows as two cones, each with an opening angle of 45°. The redshifted flow is directed at an angle of 45° from the line of sight, and the blueshifted flow at 20° from the line of sight. They proposed that these outflows may have been created by enhanced mass-loss above a few giant convective cells. Enhanced mass-loss above convective cells can be caused by localised ejections of matter as new convective cells form, or by enhanced dust formation over the cooler regions of convective cells (Schwarzschild 1975), which leads to increased radiation pressure and hence increased mass-loss (Frank 1995).

The complexity of the envelope around VY CMa has been attributed to magnetic as well as convective activity (e.g. Smith et al. 2001; Ziurys et al. 2007; Smith et al. 2009). The magnetic field around a supergiant star could either be associated with localised effects, such as convective cells, or it could be caused by a global internal dynamo. Magneto-hydrodynamical simulations of Betelgeuse show that a surface magnetic field of 500 G can be maintained through localised dynamos, formed by giant convective cells, amplifying a weak seed magnetic field. The local dynamos created by the few giant convective cells can create a global magnetic field (Dorch 2004). Alternatively, a large scale global dynamo could be created between a rapidly rotating core and a slowly rotating stellar envelope (Blackman et al. 2001). Magnetic fields as high as 400 G could be produced at the surface through the dynamo proposed by Blackman et al. (2001), which is strong enough to produce flares and local ejections of material on the stellar surface (Blackman et al. 2001).

Magnetic fields can form cool spots on the surface of the star, which lead to enhanced mass-loss (Soker & Clayton 1999). Soker & Clayton (1999) studied cool magnetic spots on AGB stars, and concluded that mass-loss is increased over these spots as dust forms faster and closer to the stellar surface over the spots. Soker (1998) models a slowly rotating AGB star and finds that cool magnetic spots form preferentially in the equatorial regions, which leads to axisymmetric mass-loss from these stars. Further modeling by Soker (2000b) of slowly rotating AGB stars with high mass-loss shows that under these conditions a dense, slowly moving region can be formed in the equator. Concentrated localised mass-loss above cool magnetic spots can also lead to structures in the envelope such as the arcs and condensations observed by Smith et al. (2001) (Soker 2000b). A global dipole magnetic field at the stellar surface can also create an equatorial disk, by structuring the circumstellar wind, leading to preferential mass-loss in the equatorial regions (Matt et al. 2000).

What role the magnetic field plays in shaping the envelope depends on the strength and geometry of the field. The levels of magnetic field in the envelope can be investigated through the polarisation of maser emission, as mentioned in Section 2.2. The magnetic field levels derived from the maser emission are located at different distances from the star: the magnetic field of tens of Gauss derived from SiO masers (McIntosh et al. 1994; Barvainis et al. 1987) is located in the near-circumstellar envelope, less that $\sim$ 50 mas from the star (e.g. Miyoshi et al. 1994), the $\sim$ 200 mG field derived from H_2O maser emission (Vlemmings et al. 2002) is located about 150 mas from the star (Vlemmings et al. 2002), and the $\sim$ 1 mG field derived from OH maser observations (Benson & Mutel 1982; Cohen et al. 1987) is located at about 1.6 arcseconds (Vlemmings et al. 2002). If the magnetic field drops off with distance from the star following to a solar or dipole relation, these magnetic field levels imply magnetic fields of hundreds to thousands of Gauss at the stellar surface (Reid & Moran 1981; Vlemmings et al. 2002).

Vlemmings et al. (2002) calculate the magnetic field pressure in the H_2O maser region, from the ~ 200 mG magnetic field estimate, to be about twenty times the thermal pressure. This is sufficiently high to shape the stellar wind (Vlemmings et al. 2002). However, it is possible that the H_2O maser emission arises from regions of enhanced magnetic field. The average magnetic field of the envelope may well be much lower than that in the spots, so that the thermal pressure still exceeds the magnetic pressure in most of the envelope (Vlemmings et al. 2002; Soker & Kastner 2003).

The large magnetic field values derived from SiO maser emission imply magnetic energy densities of two orders of magnitude greater than the thermal and kinematic energy densities (Reid 2007). It is possible that such large fields are created by shock compression in the circumstellar envelope (Hartquist & Dyson 1997). However, the interpretation of the SiO maser polarisation is contentious, with different SiO maser polarisation models implying order of magnitude different magnetic field levels from typically observed SiO maser circular polarisation (e.g. Nedoluha & Watson 1994; Elitzur 1996; Wiebe & Watson 1998). This is discussed in detail in Chapter 3.

2.5 Mass-loss

An extra-ordinary feature of VY CMa is it's dramatic mass-loss rate. The mass-loss rate can be estimated from models of mid- and far-infrared observations of circumstellar dust (e.g. Jura & Kleinmann 1990; Marshall et al. 1992; Danchi et al. 1994; Le Sidaner & Le Bertre 1996; Josselin et al. 2000; Harwit et al. 2001; Smith et al. 2001; Muller et al. 2007), optical observations (e.g. Smith et al. 2001), from models of the CO emission (e.g. Zuckerman & Dyck 1986; Loup et al. 1993; Stanek et al. 1995; Decin et al. 2006) and OH maser maps (e.g. Bowers et al. 1983; Booth et al. 1984). The derived mass-loss rates vary from 4.4×10^{-6} $M_\odot$ yr^{-1} to 4.7×10^{-4} $M_\odot$ yr^{-1}, with most estimates clustering around 1 to 3×10^{-4} $M_\odot$ yr^{-1}. The unusually low mass-loss estimate of 4.4×10^{-6} $M_\odot$ yr^{-1} by Loup et al. (1993) may be the result of the low distance value of 660 pc used in fitting for the mass-loss value, or due to the assumed CO abundance. The mass-loss figures derived from near-infrared emission are typically higher than those derived from CO emission as the near-infrared emission arises closer to the star, where the mass-loss rate appears to be higher than average (Decin et al. 2006).

Many of these mass-loss rate derivations assume that the circumstellar envelope is symmetric and that the mass-loss is homogenous. As discussed in the previous sections, observations of VY CMa at multiple wavelengths show significant deviations from spherical symmetry, and images of the circumstellar envelope are clearly not homogeneous.

Over the past few years many high resolution images and spectroscopic studies of VY CMa have revealed that the mass-loss around this star is not a constant isotropic outflow. Instead, the mass-loss appears to be occurring in sporadic localised outbursts, with significant changes in the mass-loss intensity over the past centuries.

One of the early indications of this was through the HST optical images of the nebula around VY CMa shown in the left panel of Figure 2.1, which show many localised features in the circumstellar envelope (Smith et al. 2001). Smith et al. (2001) use their HST images to estimate an average mass-loss rate of 3×10^{-4} $M_\odot$ yr^{-1} over the past 1200 years, with lower mass-loss prior to that. High resolution optical and near-infrared long slit echelle spectra of VY CMa paint a similar picture, with strong KI emission tracing many local structures embedded in a diffuse halo of KI (Smith 2004; Humphreys et al.

2005).

Decin et al. (2006) investigated mass-loss from asymptotic giant branch (AGB) and supergiant stars by modeling CO rotational line profiles. Their models demonstrated the variability of mass loss. When applied to VY CMa CO spectra, their model implies an 80 to 100 year period of heavy mass-loss (3.2×10^{-4} $M_\odot$ yr^{-1}) about 1000 years ago, preceeded by about 800 years of low mass loss (1×10^{-6} $M_\odot$ yr^{-1}). This is consistent with the results of Smith et al. (2001), who also suggest a drop in the heavy mass-loss rate about 1000 years ago, with the most siginficant mass-loss decrease in the southwest of the star. Decin et al. (2006) calculate that the mass-loss rate averaged over the entire circumstellar envelope is 5.1×10^{-5} $M_\odot$ yr^{-1}, but the mean value within 100 R_* is a higher value closer to 0.75×10^{-4} $M_\odot$ yr^{-1} (Decin et al. 2006).

The high resolution CO spectra observed by Smith et al. (2009) show strong variations over the large-scale nebula. This implies that the emission is not tracing a steady wind, but many dense cloudlets, a conclusion supported by the HST images (Smith et al. 2001; Humphreys et al. 2007; Jones et al. 2007). The observed variability in the mass-loss rate is therefore not simply a change in the spherical time averaged rate of mass ejection, but an increase in many individual localised mass-loss events (Smith et al. 2009). Although the overall mass-loss from the stellar surface is not isotropic, the distribution of the localised ejecta around the star is close to isotropic (Smith et al. 2009). Smith et al. (2009) confirm the Smith et al. (2001) and Decin et al. (2006) inferences of a surge in mass-loss about 1000 years ago. Smith et al. (2009) find that the mass-loss increased around 1000 years ago, peaked around 600 years ago, and slowly dropped off to the initial mass-loss rate. During the intense mass loss period 1000 to 600 years ago they estimate the mass-loss rate to be approximately 2×10^{-3} $M_\odot$ yr^{-1}.

A pair of papers by Humphreys et al. (2007) and Jones et al. (2007) provide a remarkable three-dimensional view of the features in the VY CMa envelope. Humphreys et al. (2007) observed VY CMa with the HST, using identical observation parameters to the Smith et al. (2001) observation six years earlier. This allowed them to compare the two HST images, as well as the Humphreys et al. (2005) spectra, to determine the three-dimensional structure of the ejecta. Jones et al. (2007) complemented this with HST polarisation images of the star, which were also used to determine the three-dimensional structure and confirm the results of the Humphreys et al. (2007) paper.

The arcs identified in the Smith et al. (2001) HST images of the star are particularly interesting in terms of mass-loss models, as the structure of the arcs implies that they were produced through localised ejections of matter, rather than long-term streams of radiatively driven mass-loss. The arcs appear to be randomly located in the circumstellar envelope, not aligned with any axis (Smith et al. 2001). Smith et al. (2001) suggest that these localised ejections are caused by convective and magnetic effects, as they are too massive to have been ejected by radiation pressure (Smith et al. 2001). The HST polarisation images confirm that the arcs and several other features in the nebula are distinct geometric features, rather than density enhancements (Jones et al. 2007). The arcs are shown in the Smith et al. (2001) figure reproduced the diagram in Figure 2.7. The feature labels used in this section refer to Figure 2.1 and Figure 2.7.

The Humphreys et al. (2005) high resolution spectra show the emission from the northwest arc (labelled the "Curved nebulous tail") to be highly redshifted, showing the arc to be expanding moving away from the star with a velocity of around 50 km/s relative to the star, moving across our line of sight. Assuming a distance of 1.5 kpc to the star, the curved nebulous tail appears to have formed

about 400 years ago (Humphreys et al. 2005). If the distance to VY CMa is the smaller value of 1.14 kpc, the lifetime of the arc is reduced, becoming closer to 300 years. Humphreys et al. (2007) estimate the arc lifetime to be 500 years, also assuming a 1.5 kpc distance, and find that the effect of post-ejection radiation pressure could reduce the lifetime estimate to about 400 years. The two southern arcs are both probably moving towards us, with the arc closer to the star (labelled "Arc 2") having been ejected about 460 years ago, and the southernmost arc ("Arc 1") about 800 years ago (Humphreys et al. 2007).

The KI emission from the southernmost arc (labelled "Arc 1") was shown by Smith (2004) to follow a quasi-Hubble law. If the expansion across the arc follows a Hubble law, with velocity proportional to distance from the star, it is evidence that the material was ejected in a single event (Smith 2004; Humphreys et al. 2005). Smith et al. (2009) report that the curved nebulous tail also shows a Hubble-like flow, implying that it too was formed by a single ejection of mass.

Evidence for localised mass-loss was also found in recent SMA imaging of SO_2 emission towards VY CMa, which revealed three independent fast moving components (Fu et al. 2011). Fu et al. (2011) propose that these components are the result of independent mass-loss events during an episode of enhanced mass-loss about 500 years ago. SMA images of CO also point to a period of enhanced mass-loss about 500 years ago (Muller et al. 2007).

Overall, careful mapping of the various features in the nebula show them to be moving in different directions with no preferential direction, and having been ejected at times ranging from around 1700 years ago to as recent at 157 years ago (Humphreys et al. 2007). Humphreys et al. (2007) argue that this evidence points to localised mass-loss without any alignment to a particular axis.

The evolutionary path followed by a red supergiant is determined to a large degree by it's mass-loss (Decin et al. 2006; Smith et al. 2009). The localised variable nature of the mass-loss around VY CMa must therefore be taken into account when modeling the future evolutionary path of this star.

2.6 Evolutionary status

VY CMa is widely considered to be an evolved star, though there has been debate on this point. Some early papers classified it as a protostar (e.g. Herbig 1970), and Humphreys et al. (2005) note that if VY CMa is a late-type star, it seems to be in an evolutionary stage unlike any other observed late-type star.

VY CMa's classification as an evolved star is supported by the presence of the OH 1612 MHz spectral line (Hyland et al. 1969), the near-infrared CO spectrum (Hyland et al. 1972) and it's high luminosity, which places it in on the evolutionary path of a red supergiant with initial mass around 25 $M_{\odot}$ (Choi et al. 2008b). The exact period of late stage evolution that the star is undergoing is unknown. It may be in the early stages of expelling it's envelope, or it may be further along the stellar evolutionary path (Smith et al. 2001).

A number of authors have suggested that VY CMa may be the precursor to a star like IRC +10420 (Wittkowski et al. 1998; Smith et al. 2001; Fransson et al. 2002). Both stars display bright knots in their circumstellar envelopes, and the arcs of ejected material around VY CMa may evolve into shells, like those observed surrounding IRC +10420 (Smith et al. 2001). IRC +10420 is a supergiant star with high levels of mass loss, surrounded by a dusty envelope and a possible circumstellar disk. If

the mass loss is high enough, IRC +10420 will lose it's envelope to become a Wolf-Rayet star (Jones et al. 1993). Wolf-Rayet stars are formed when mass loss from the star is extensive enough that just a bare core of nucleur processed material remains. The intense mass loss required for the star to become a Wolf-Rayet is likely to occur for supergiants with initial mass of between 20 $M_{\odot}$ and 60 $M_{\odot}$ (Chiosi & Maeder 1986). The large mass and intense mass loss rate of VY CMa supports the proposition that VY CMa too is on the path of becoming a Wolf-Rayet star (Wittkowski et al. 1998). Alternatively, if the mass loss is not sufficiently high for this to happen, VY CMa will evolve into either a yellow hypergiant or a blue supergiant (Smith et al. 2009). Smith et al. (2009) comment on the emerging picture of VY CMa's sporadic localised mass loss, noting that the numerous ejecta may be an indication that the star is approaching and possibly exceeding the Hayashi limit for convective stability.

Fransson et al. (2002) propose that both VY CMa and IRC +10420 will end their lives as a Type IIn supernova. Type IIn supernovas were first identified as a distinct class of Type II supernovae by Schlegel (1990). Their observational characteristics can be explained through the interaction of the exploding star with a dense, clumpy, cloud of circumstellar material (e.g. Chugai et al. 1995). Smith et al. (2009) investigate whether VY CMa could be the progenitor of a Type IIn supernova, using high resolution observations of CO profiles in the circumstellar envelope. As discussed in the previous section, considerable evidence, including the CO profiles, shows that the mass loss from VY CMa is localised and episodic. In this environment, the dense regions of ejected material would form a barrier to a supernova explosion, very possibly resulting in a type IIn supernova (Smith et al. 2009). If VY CMa explodes in it's present state, the dense circumstellar envelope interacting with the exploding star could lead to a supernova luminosity as high as $3 \times 10^8 L_{\odot}$ (Smith et al. 2009). If VY CMa is surrounded by a disk-like envelope, the supernova expansion would be faster in the polar regions where it encounters less resistance. This mechanism could explain the asymmetric Hα profiles of Type IIn supernovae (Fransson et al. 2002).

Chapter 3

SiO maser polarisation

SiO maser emission around late-type evolved stars is located within a few stellar radii of the central star (Elitzur 1980; Wittkowski et al. 2007b). Observations of these masers therefore provide information about the conditions in the innermost regions of the circumstellar envelope. SiO masers have been used to investigate the kinematics and dynamics of circumstellar envelopes, revealing periods of expansion and periods of infall, as well as localised infall (e.g. Boboltz et al. 1997; Diamond & Kemball 2003; Gonidakis et al. 2010).

Furthermore, the polarisation of circumstellar SiO maser emission provides a potential probe of the magnetic field in this region. Because of their proximity to the stellar surface, magnetic field information derived from the SiO maser emission may be used to infer information about the morphology and strength of the magnetic field at the stellar surface itself (Reid & Moran 1981). This will address questions surrounding the origin of magnetic fields in late-type evolved stars, and the consequent effect of magnetic fields on AGB mass-loss and post-AGB evolution. The presence of a stellar magnetic field may also influence the circumstellar envelope material by leading to localised mass loss (Soker & Clayton 1999; Soker & Zoabi 2002), and may dynamically shape the envelope (García-Segura et al. 2005). The role of the magnetic field in these processes still requires investigation, and SiO masers provide one of the few observational means to do so.

In order for magnetic field information to be derived from the observed polarisation of SiO maser emission, a maser polarisation radiative transfer model is required. The theory of SiO maser polarisation transport has been considered in several papers, with two main competing sets of models. The first has been put forward by M. Elitzur (Elitzur 2002, and references therein) and the second by W.D. Watson (Watson 2002, and references therein). The Elitzur and Watson theories were each developed over a series of papers and include a variety of factors that will be discussed in this chapter. The two approaches make significantly different predictions about the magnetic field levels implied by typical SiO maser observations however. It is therefore important to know which model is appropriate to the data, in order to allow magnetic field information to be derived from the maser polarisation observations. An overarching goal of this thesis is to perform observational tests to discriminate between the two theoretical SiO maser polarisation models.

This chapter provides a background to the SiO maser polarisation theories and discusses observational tests that can be used to discriminate between the two models. The basic theory of maser propagation is given in Section 3.1, as a framework for the later discussion. SiO maser emission is then considered in Section 3.2, including a section on how this emission is maintained through a

pumping mechanism in Section 3.3. The theory of SiO maser polarisation is subsequently introduced in Section 3.4, focusing on polarisation created by a magnetic field in the maser region. The two maser models of Elitzur and Watson are then reviewed in detail, followed by a separate section on polarisation caused by anisotropic pumping. The main results of the two models are then summarised. In the final two sections, proposed observational tests of the two models are presented, and existing implementations of the observational tests are reviewed.

3.1 Maser theory

This section provides an outline of basic maser physics relevant to this thesis, as a foundation for the discussion of the polarisation of Silicon Monoxide (SiO) maser emission. It is primarily based on the presentation in the monograph by Elitzur (1992). The notation used in these sections also follows the formalism developed by Goldreich & Keeley (1972) and Goldreich, Keeley, & Kwan (1973), in their foundational work on maser polarisation theory. Following Goldreich, Keeley, & Kwan (1973), the maser emission is treated semi-classically in that the molecules are modeled in a quantum mechanical framework, and the radiation field is modeled in a classical framework. This method is justified by the fact that the radiation wavelength is much greater than the maser particle sizes (Goldreich et al. 1973; Elitzur 2002). The semi-classical method separates the theory of maser emission into two interrelated aspects: the maser radiation and the masing particles.

3.1.1 Radiation propagation

Electromagnetic waves interact with matter in three ways: absorption, spontaneous emission and stimulated emission. Masers are the result of stimulated emission, where an incoming photon interacts with an atom or molecule which is already in an excited state. The incident photon incites the molecule to drop to a lower energy level and emit another photon in the process. This results in two coherent photons of the same frequency, from the original one, so the incident radiation is amplified by the maser process. In the language of radiative transfer, maser radiation occurs when the absorption coefficient is negative. In this case the radiation is amplified, rather than attenuated, by the medium it passes through (Reid & Moran 1981; Elitzur 1992, pg. 22,23).

The radiative transfer equation describes the interaction between radiation and the matter it passes through

$$\frac{dI_\nu}{dl} = -\kappa_\nu I_\nu + \epsilon_\nu \tag{3.1}$$

where I_ν is the intensity of the radiation, which varies with distance l along the path length, κ_ν is the absorption coefficient, ϵ_ν is the emission coefficient and the ν denotes frequency dependence (Reid & Moran 1981, Elitzur 1992, pg. 12, Wilson et al. 2009, pg. 8).

Spectral line emission and absorption is included in the equation of radiative transfer by way of the Einstein coefficients. Consider a transition between upper energy level u with a level population N_u and lower energy level l with level population N_l, as shown in Figure 3.1. The Einstein coefficient for absorption is B_{lu}, for stimulated emission is B_{ul} and for spontaneous emission is A_{ul}. The effects of absorption and stimulated emission can be incorporated into a line absorption coefficient κ_ν in the

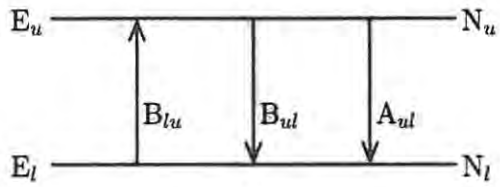

Figure 3.1: Transitions take place between energy levels u (upper) and l (lower) with energies E_u and E_l and number densities N_u and N_l respectively. The transitions are described by the Einstein coefficients: B_{lu} for absorption, B_{ul} for stimulated emission and A_{ul} for spontaneous emission.

equation of radiative transfer

$$\kappa_\nu = [\,(N_l B_{lu} - N_u B_{ul})\, h\,\nu_0\,\phi(\nu)\,]\,/4\pi$$

where $\phi(\nu)$ is the line profile (Reid & Moran 1981, Elitzur 1992, pg. 25, Wilson et al. 2009, pg. 321). Spontaneous emission contributes an emission coefficient ϵ_ν to the radiative transfer equation

$$\epsilon_\nu = [\,N_u\, A_{ul}\, h\,\nu_0\,\phi(\nu)\,]\,/4\pi$$

where the line profiles $\phi(\nu)$ are the same for both absorption and emission for radio astronomy observations (Reid & Moran 1981, Elitzur 1992, pg. 21, Wilson et al. 2009, pg. 321). Substituting these coefficients into Equation 3.1 gives

$$\frac{dI_\nu}{dl} = \frac{h\,\nu_0}{4\pi}\,\phi(\nu)\,[\,(N_u B_{ul} - N_l B_{lu})\, I_\nu - N_u A_{ul}\,] \tag{3.2}$$

(Goldreich & Keeley 1972; Wilson et al. 2009, pg. 321,322). The units of BI_ν and A are both s^{-1}. The intensity I_ν of maser emission can be calculated by solving the above radiative transfer equation using Einstein coefficients and level populations appropriate to the physical situation being modelled. The level populations are determined through the rate equations presented in the following section, coupling the radiation and particle components of the problem.

3.1.2 The maser particles

In what follows, we adopt the approach of Goldreich & Keeley (1972) and Elitzur (1992) in describing the level populations of the masing molecule.

Again considering Figure 3.1, the number densities of levels u and l are regulated through the effects of absorption, spontaneous emission and stimulated emission between these two lines, through collisions that cause transfers between the two lines, as well as through interactions with the other energy levels of the masing particle. The interactions with other energy levels can be modeled by phenomenological pump rates Λ and decay rates Γ (Elitzur 1992, pg. 21-23, 72-73).

The rate equations for the level populations in the presence of this line emission are

$$\frac{\partial N_u}{\partial t} = \Lambda_u - \Gamma N_u - N_u A_{ul} - \bar{J}\left(N_u B_{ul} - N_l B_{lu}\right) - \left(N_u C_{ul} - N_l C_{lu}\right)$$

$$\frac{\partial N_l}{\partial t} = \Lambda_l - \Gamma N_l + N_u A_{ul} + \bar{J}\left(N_u B_{ul} - N_l B_{lu}\right) - \left(N_u C_{lu} - N_l C_{ul}\right) \tag{3.3}$$

(Goldreich & Keeley 1972; Elitzur 1992, pg. 72) where $\bar{J}$ is the intensity over the full line profile, averaged over angle. The rate coefficients C_{ul} and C_{lu} (s^{-1}) represent the effects of collisions which cause u-l inter-level transitions, where C_{ul} is the the rate at which inelastic collisions transfer particles from level u to level l and *vice versa* for C_{lu}. The number density N is the total number density of the masing particle, and $N_{ul} = N_u + N_l$. The pump rates Λ ($cm^{-3}s^{-1}$) are for population gains to level u and l respectively, from outside the u l system. The decay rate Γ (s^{-1}) is the inverse of the lifetime for radiative or collisional transitions out of levels u and l and it is assumed to be equal for the two levels (Goldreich & Keeley 1972; Elitzur 1992, pg. 72).

The population densities are assumed to be in a steady state so the time derivatives in Equations 3.3 can be set to zero and the level populations N_u and N_l can then be calculated (Elitzur 1992, pg. 72).

The level population equation (Equation 3.3) and the radiative transfer equation (Equation 3.2) are coupled, with the intensity from the radiative transfer equation being averaged into $\bar{J}$ in the level population equation, and the number densities N_u and N_l in the radiative transfer equation effecting the emission and absorption coefficients in the radiative transfer equation. In order for the maser action to take place, the population inversion between levels N_u and N_l must be maintained by a pumping mechanism, which overpopulates N_u or depopulates N_l.

3.2 SiO maser emission

SiO is one of several molecules observed to emit maser radiation in the envelopes of late-type evolved stars. The first observation of SiO maser emission was of the v=1 J=2-1 line, observed towards the Orion Nebula (Snyder & Buhl 1974). This initial tentative detection was followed by a detection of the v=1 J=3-2 SiO transition towards Orion (Davis et al. 1974) and a detection of the v=1 J=1-0 SiO line towards Orion and the M-type star W Hya (Thaddeus et al. 1974). Detections of transitions from the second vibrational level soon followed (Buhl et al. 1974) and today SiO maser emission has been observed towards numerous late-type stars between many rotational levels, within different vibration bands (e.g. Gray et al. 1999).

SiO is a simple rotor molecule, so energy level transitions are limited by a $\Delta J = \pm 1$ selection rule. Transitions may take place in the same vibrational state, or between different vibrational states. The $\Delta v = \pm 1$ vibrational transitions are the most significant (Elitzur 1992, pg. 280). The most commonly imaged SiO maser transitions around late-type stars are between rotational levels J=1-0 and J=2-1, in the first vibrational state v=1, corresponding to line frequencies near 43 GHz and 86 GHz respectively.

Of all of the masing molecules typically observed around late-type stars, SiO masers originate closest to the central star. SiO masers are located in the extended atmosphere of a star, a fact first recognised by Elitzur (1980). They are located between the stellar surface and the dust formation point, although they can overlap with the dust formation region around stellar minimum (Wittkowski

et al. 2007b). The conditions for SiO maser emission to be present are a molecular density in the range 10^9 to 10^{10} cm^{-3} (Lockett & Elitzur 1992). Very Large Baseline Interferometry (VLBI) maps of this emission have been made toward a number of target stars, typically showing a broken clumpy ring of SiO maser emission a few stellar radii from the central star. The earliest VLBI observations of SiO masers were provided by Moran et al. (1979), Miyoshi et al. (1994), Diamond et al. (1994) and Greenhill et al. (1995). Subsequent VLBI imaging has been performed by a number of authors, including a series of multi-epoch observations of AGB stars by Cotton et al. (2004, 2006, 2009a,b, 2010a,b).

Maser emission saturates when the stimulated emission rate R becomes much greater than the decay rate Γ. The level of saturation is difficult to estimate, as it is dependent on the unknown beaming angle of the maser radiation. Plambeck et al. (2003) estimate a stimulated emission rate of $R \sim 30$ s^{-1} for SiO v=1 J=1-0 masers from the star-forming region Orion, which have typical intensities of ~ 1 Jy.beam^{-1} in a 0.2 mas beam. They assumed a beaming angle of 10^{-2} sr for the masers. This value of the stimulated emission rate is significantly larger than the radiative decay rate from the v=1 to v=0 level, which is $\Gamma \sim 5$ s^{-1}, and the collisional decay rate of ~ 1 s^{-1}. The condition $R \gg \Gamma$ is therefore met, for the assumed beaming angle, and Plambeck et al. (2003) consider the maser emission they observed to be saturated.

The values given by Plambeck et al. (2003) of an intensity of ~ 1 Jy.beam^{-1} in a 0.2 mas beam at a wavelength of 7 mm equate to a brightness temperature of $\sim 2 \times 10^{10}$K for these masers. The equation given by Plambeck et al. (2003) for the rate R can be simplified in terms of this brightness temperature T_B and their assumed beam solid angle $d\Omega$

$$R = 23 \left(\frac{\mathrm{T}_B}{2 \times 10^{10}\mathrm{K}} \right) \left(\frac{d\Omega}{10^2 \mathrm{sr}} \right) \tag{3.4}$$

for the v=1 J=1-0 SiO maser line (Kemball et al. 2009), and for the v=1 J=2-1 SiO maser line

$$R = 110 \left(\frac{\mathrm{T}_B}{2 \times 10^{10}\mathrm{K}} \right) \left(\frac{d\Omega}{10^2 \mathrm{sr}} \right) \tag{3.5}$$

Individual SiO masers spots around late-type stars have brightness temperatures of a similar order to the 2×10^{10}K value given for SiO masers towards Orion, being at most about an order of magnitude higher than this (e.g. Kemball & Diamond 1997). The stimulated emission rate for v=1 J=1-0 SiO masers around late-type stars is therefore likely to be similar to the Plambeck et al. (2003) estimate, assuming a similar beaming angle to that used in Plambeck et al. (2003). Kemball et al. (2009) adopt a value of $R \sim 23$ s^{-1} for SiO masers towards TX Cam.

Assuming comparable decay rates and beaming angles to those given by Plambeck et al. (2003), the SiO masers around late-type evolved stars are therefore likely to be saturated (Kemball et al. 2009). On the other hand, Watson (2009) argues that the level of saturation is moderate, with $10 > R/\Gamma \gtrsim 1$. In the absence of observational evidence for the maser beaming angle, the level of saturation is uncertain.

3.3 SiO maser pumping

For maser emission to occur in a particular transition, the population of the higher energy level must be greater than the population of the lower level, which in turn requires a pumping mechanism to maintain. The pumping mechanism which causes the circumstellar SiO population inversion is still a matter of debate. Two main types of pumping mechanisms have been investigated by numerous authors since the discovery of SiO maser radiation: radiative pumping and collisional pumping (e.g. Bujarrabal & Nguyen-Q-Rieu 1981; Bujarrabal 1994; Lockett & Elitzur 1992). Whether the primary pumping mechanism is radiative or collisional is still an open question, with the most recent models implying that both mechanisms are at work, and that the two pumping mechanisms may be coupled (Gray et al. 2009). What follows is a synopsis of the development of our understanding of SiO maser pumping.

The earliest attempt to model SiO maser pumping was made by Geballe & Townes (1974), shortly after the first SiO maser detection by Snyder & Buhl (1974). They proposed two potential pumping mechanisms. The first was based on the coincidence of the 1-0 R0 and 3-2 R18 infrared SiO transitions. The second mechanism was based on the emission of infrared radiation by hot SiO molecules, and the radiation being subsequently absorbed in cooler circumstellar regions. Both of these proposed mechanisms have been called into question by later authors. Deguchi & Iguchi (1976) pointed out that the first mechanism is specific to a few lines in the v=1 vibrational level and does not explain the observations of v=2 J=1-0 maser emission which were published after the paper by Geballe & Townes (1974). Since then, SiO maser lines from many transitions have been observed, so a pumping mechanism that is tailored to the frequencies of particular transitions is unlikely to be correct. Deguchi & Iguchi (1976) also point out that the second mechanism is unlikely because it places unrealistic requirements on the distribution of hot and cold clouds in the circumstellar envelope.

Kwan & Scoville (1974) first proposed radiative and collisional pumping mechanisms for SiO masers. Their radiative pumping mechanism requires that the population inversion be maintained by radiative pumping of vibrational level v+1 relative to level v. The rotational level inversion needed for the maser action is created through the cascade from the v+1 to the v level (Kwan & Scoville 1974; Elitzur 1980). This class of pumping mechanisms is an indirect $\Delta v = 2$ pump, with the v=1 rotational level population inversion created through absorptions from the v=0 to v=2 vibrational levels (Kwan & Scoville 1974). This requires a high transition probability for the forbidden $\Delta v = 2$ transition, which is unlikely (Deguchi & Iguchi 1976). On the other hand, the collisional pumping proposed by Kwan & Scoville (1974) utilises collisional cross-sections which are a few orders of magnitude too high (Deguchi & Iguchi 1976). When the correct cross-sections are used, the collisional pumping mechanism proposed by Kwan & Scoville (1974) is also not effective (Deguchi & Iguchi 1976).

In light of the flaws in the previous pumping mechanism theories, Deguchi & Iguchi (1976) proposed a new radiative pumping mechanism based on anisotropic radiation trapping. Circumstellar SiO masers reside in environments with large radial velocity gradients, so the opacity is different in the radial and tangential directions. The stellar radiation providing the pump photons is also anisotropic, directed radially away from the central star. These anisotropies can lead to SiO population inversions over a range of optical depths and velocity gradients (Deguchi & Iguchi 1976). This pumping mechanism is a $\Delta v = 1$ pump, which has a much greater pump rate than the $\Delta v = 2$ pump proposed by Kwan & Scoville (1974).

A collisional pumping mechanism was investigated by Elitzur (1980). SiO masers are located close to the stellar photosphere, in a region where vibrational transitions are largely collisionally excited. This fact motivated the development of the collisional pumping model, together with the view that the optical depths required by some radiative pumping models were implausibly high. For collisional pumping to take place, the density of the gas must not be so great as to thermalise the masing molecules. Elitzur (1980) considered collisions with the molecule H_2, and found that the masers are quenched at a density of 10^{12} cm^{-3} for optically thin vibrational transitions.

Bieniek & Green (1983) subsequently calculated collisional cross-sections for the first three vibrational states of SiO. The resultant cross-sections were much larger that the cross-section estimates employed in earlier studies of SiO masers. Lockett & Elitzur (1992) utilised the new cross-sections in a study of both radiative and collisional pumping methods. They found that collisional pumping produced the strongest masers, with the least need to fine-tune the physical parameters to permit maser emission. SiO masers have been observed in a wide range of late-type stars and in many transitions. The fact that collisional pumping is less dependent on specific physical conditions can therefore be used to argue for collisional pumping as the general mechanism at work in creating SiO maser emission (Elitzur 1992, pg. 294). Using the Bieniek & Green cross-sections, Lockett & Elitzur found that the molecular density must lie approximately between $10^9 - 10^{10}$ cm^{-3} for SiO maser action to take place via either of the pumping mechanisms.

In contrast, a later model developed by Bujarrabal (1994) finds the dominant pumping method to be radiative, with a minor collisional component. Their model uses non-local treatment of radiative transfer, rather than the large velocity gradient (LVG) approximation used in most other maser models. Bujarrabal et al. (1996) modified the earlier Bujarrabal (1994) model to include the effects of line overlaps between two rovibrational transitions of SiO and H_2O. The inclusion of the line overlap in the model reproduces the observed relative weakness in the v=2 J=2-1 SiO maser line. Soria-Ruiz et al. (2004) used the Bujarrabal et al. (1996) line overlap model to explain their observations of v=1 and 2 J=1-0 and J=2-1 SiO masers towards IRC +10011 and χCyg. In both radiative and collisional maser pumping models, transitions in the v=2 vibrational state produce maser emission under higher density conditions than transitions in the v=1 state. Regions of SiO maser emission from the v=1 and v=2 states are therefore unlikely to overlap. The J=1-0 and J=2-1 masers in the same vibrational state, on the other hand, occur under very similar physical conditions and therefore should arise from the same physical locations (Soria-Ruiz et al. 2004). However, observationally the J=1-0 and J=2-1 SiO masers do not overlap as expected, and the v=1 and v=2 J=1-0 maser distributions are more similar than the v=1 J=1-0 and J=2-1 lines. (Soria-Ruiz et al. 2004). The inclusion of the H_2O line overlap remedies these theoretical discrepancies. The effect of the line overlap is to couple the v=1 and v=2 J=1-0 lines and create differences between the v=1 J=1-0 and v=1 J=2-1 lines, in terms of the gas density and distance from the star where the lines will be masing. The v=2 J=2-1 line is also suppressed when the line overlap is included (Soria-Ruiz et al. 2004).

Doel et al. (1995) published an SiO maser model which coupled SiO maser calculations with a model of the circumstellar environment where the masers are located. They concluded that SiO maser pumping is predominantly collisional for Mira variables and supergiant stars, but predominantly radiative for OH/IR stars. This model included 200 rovibrational levels from v=0 to v=4; this was dramatically more that the original 18 used by Kwan & Scoville (1974).

Pumping models generally assume a blackbody spectrum for the pumping radiation. Rausch et al. (1996) first considered the effects of pumping by a photospheric line spectrum. The efficiency of the pump depends on the ratio of the intensities of different spectral lines. These ratios are significantly altered by the adoption of a photospheric spectrum, which is crowded with absorption lines. The use of a photospheric line spectrum can greatly increase the efficiency of the pump, but the efficiency is strongly dependent on the velocity difference between the photosphere and the masing gas (Rausch et al. 1996).

A series of circumstellar SiO maser models which couple a hydrodynamical model of the shocked circumstellar envelope of long-period Mira variables with an SiO maser radiative transfer model have been developed (Humphreys et al. 1996; Gray & Humphreys 2000; Humphreys et al. 2002; Gray et al. 2009). Humphreys et al. (1996) make use of the maser excitation model developed in Doel et al. (1995), using predominantly collisional maser pumping. They use Monte-Carlo techniques to produce simulated SiO maser images. These models give good agreement with high resolution observations of SiO masers around late type stars. The Humphreys et al. (1996) model reproduces the ring-like distribution of maser emission a few stellar radii from the star, and predicts the presence of maser emission from transitions between higher rotational levels. The ring distribution is attributed to radial velocity gradients in the SiO maser environment: low tangential velocity gradients and high radial velocity gradients lead to greater tangential amplification (Diamond et al. 1994; Humphreys et al. 1996). However, although the ring distribution of emission can be produced by this predominantly collisional model, the ring can also be explained by radiative pumping. The observed ring distribution of maser emission, and the tangential linear polarisation of the masers, have both been argued to support a radiative pumping scheme (Desmurs et al. 2000).

Gray & Humphreys (2000) extend the Humphreys et al. (1996) model to multiple epochs, tracking the changing stellar phase of TX Cam. This extension was motivated by an animation of the TX Cam v=1 J=1-0 SiO maser emission (Diamond & Kemball 1999). Gray & Humphreys (2000) found that the three modeled transitions, v=1 J=1-0, v=2 J=1-0 and v=1 J=2-1, behave morphologically in a similar manner over the course of the stellar period. The ring of v=1 J=1-0 masers is however found to be about double the thickness of the rings of the other two transitions, implying the population inversion necessary for v=1 J=1-0 maser emission occurs over a wider range of physical conditions.

Gray et al. (2009) provide of a review of the hydrodynamical models of SiO maser emission published to date, beginning with the Gray et al. (1995a) and Humphreys et al. (1996) papers. He also presents an updated version of the model, which makes use of more recent information about conditions in circumstellar envelopes, such as those provided by the infrared observations of Wittkowski et al. (2007b). This updated model reproduces many of the characteristics of the earlier models and shows that both radiative and collisional pumping are occurring, and are possibly coupled due to the circumstellar envelope dynamics (Gray et al. 2009).

3.4 SiO maser polarisation

As mentioned in the introduction, observations of SiO maser polarisation are a promising probe of the magnetic field in the near-circumstellar envelope of late-type stars. SiO is a non-paramagnetic molecule. For non-paramagnetic molecules the Zeeman splitting of the spectral lines invariably falls

into the weak splitting regime. In this regime the maser polarisation is difficult to interpret as there are conflicting theoretical models for the relationship between the observed polarisation of the emission and the inferred magnetic field (Elitzur 2002; Watson 2002). This limits the usefulness of polarisation observations, absent greater theoretical clarity. The two main weak-splitting maser polarisation models will be referred to respectively as the Elitzur model (Elitzur 1991, 1993, 1996), and the Watson model (e.g. Watson & Wyld 2001, and references therein). The primary goal of this thesis is to provide observational tests of the two conflicting polarisation models. The two main weak-splitting maser polarisation theories are therefore discussed in some detail later in this section.

This section begins with the a description of the basic mechanism for the generation of polarised maser emission in the presence of a magnetic field, following Elitzur (1992). This is followed by an outline of maser polarisation theory, presented in terms of the maser molecules and radiation propagation, following the format of Section 3.1.

Maser polarisation in the weak-splitting regime was first considered by Goldreich, Keeley, & Kwan, in a paper that has become the foundation of further work on maser polarisation (Goldreich, Keeley, & Kwan 1973, hereafter GKK). The GKK model is discussed in Section 3.4.4. This is followed by a summary of the progress made in developing the weak-splitting maser polarisation theory since the early paper by GKK. The Watson and Elitzur weak-splitting maser polarisation models are discussed, as well as maser polarisation caused by anisotropic pumping. Finally, Section 3.4.9 discusses ways to test the maser polarisation models using observational studies.

3.4.1 Maser polarisation in a magnetic field

In a medium where emitting particles are randomly oriented, the aggregate radiation from the particles will be randomly polarised, leading to an overall unpolarised radiation field. This randomness is removed when there is a quantisation axis in the medium - some means to align the particles, so that more particles radiate one particular polarisation configuration than another. One possible quantisation axis is along a magnetic field. When the magnetic field is strong enough that the particles are precessing around the magnetic axis, the magnetic field becomes a good quantum axis and the overall radiation may be polarised (Elitzur 1991).

Every angular momentum level J of a molecule has 2J+1 magnetic sub-levels denoted by the quantum number m, which are degenerate in the absence of a magnetic field (Elitzur 1992, pg. 161). In the presence of a magnetic field, the precession of the molecule around the magnetic axis adds a small amount of energy to each sub-level, which breaks the degeneracy, as shown in Figure 3.2. This energy shift is $B\,\mu_B\,g\,m$, where B is the magnetic field value, μ_B is the Bohr magneton, and g is the Lande factor (Cook 1977, pg. 17, Elitzur 1992, pg. 161).

The shift in the energy of the magnetic sub-levels leads to a shift in frequency of transitions between two such levels, termed Zeeman splitting. The selection rule that governs these transitions is $\Delta m = -1, 0, +1$ (Cook 1977, pg. 17-19). Lines arising from $\Delta m = 0$ transitions are termed π-components, and those arising from from $\Delta m = \pm 1$ are termed σ-components. The electric field of π-components oscillates along the magnetic field direction, while the electric field of σ-components are circularly polarised in the plane perpendicular to the magnetic field (Cook 1977, pg. 19-21, Elitzur 1992, pg. 162).

Open shell molecules are paramagnetic, and have relatively large magnetic moments. The Zeeman

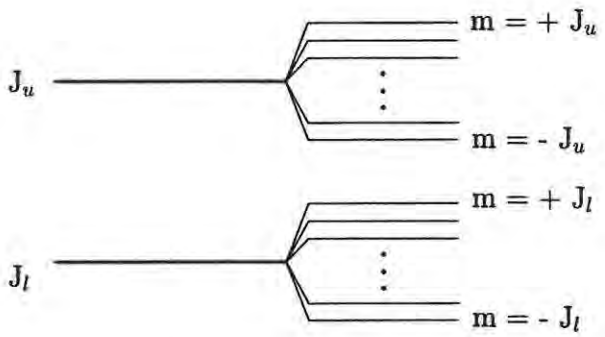

Figure 3.2: Zeeman splitting of the energy levels u and l. Level u is split into $2J_u+1$ m-levels given by m = -J_u, -J_u+1, ..., J_u-1, J_u, and similarly for level l, for $u, l \geq 1$. No Zeeman shifting occurs for level J=0.

shifts can be large enough to offset the individual Zeeman components in frequency, so that a spectral line from a transition between two angular momentum levels such as u and l in Figure 3.2 can be split into a Zeeman pattern, a number of distinct spectral lines from transitions between the different m levels (Elitzur 1992, pg. 161-162,170). OH is a paramagnetic molecule, and Zeeman patterns are observed in OH maser emission from star forming regions, where magnetic fields are at the level of up to tens of milliGauss (e.g. Fish & Reid 2007).

On the other hand, closed shell molecules such as SiO are non-paramagnetic, and have much smaller magnetic moments. In the presence of the same magnetic field, the Zeeman splitting of a non-paramagnetic molecule like SiO will be three orders of magnitude less than a paramagnetic molecule like OH (Elitzur 1992, pg. 161-162).

The Zeeman shifts of non-paramagnetic molecules are not large enough to create distinct spectral lines for different Δm transitions. The different Zeeman components of one line will overlap in frequency, so that photons produced in one Δm transition can stimulate photons of any Δm transitions between the same two J lines. This is termed the weak-splitting regime. The overall observed polarisation of the maser emission will be determined by the mixture of Δm polarisations of a particular line (Elitzur 1991). It is this mixing of polarisation characteristics in the radiative transfer that makes the polarisation of radiation in the weak-splitting regime more difficult to interpret.

3.4.2 Radiation propagation

The original radiative transfer equation, Equation 3.1, describes the change in radiation intensity as electromagnetic waves pass through matter. In order to formulate the radiative transfer equation in terms of intensity, the electromagnetic waves must be assumed to have random phases. This is not the case for polarised waves, where the phase relationships between different waves define the polarisation state. The equation of radiative transfer must therefore be reformulated for polarised radiation (Elitzur 2002).

Following GKK, we consider a monochromatic plane wave, propagating in the z direction. The electric field vector $\mathbf{E}$ can be decomposed into left and right circularly polarised components

$$\mathbf{E} = Re(E^R(z,t)\ \mathbf{e^R} + E^L(z,t)\ \mathbf{e^L}) \tag{3.6}$$

where

$$E^P(z,t) = \mathcal{E}^P(z,t)\ e^{-i(\omega t + \phi_P(z,t))} \tag{3.7}$$

The subscript P denotes either right circular polarisation (R) or left circular polarisation (L) and $\mathbf{e^R}$ and $\mathbf{e^L}$ are right and left circularly polarised unit vectors. The polarisation $\mathbf{P}$ and current density $\mathbf{J}$ can be decomposed in a similar fashion, with amplitudes $\mathcal{P}^P$ and $\mathcal{J}^P$. The wave motion along the propagation direction z is given by the wave equation, in terms of $\frac{D(\mathcal{E}^P)^2}{Dz}$ and $\frac{D}{Dz}\mathcal{E}^R\mathcal{E}^L \exp(-i\Delta\phi)$.

The polarisation state of the electromagnetic wave can be fully described by the real valued Stokes parameters I, Q, U and V (Chandrasekhar 1960, pg. 25-28). The first parameter I is the total intensity, the parameters Q and U describe the level and position angle of linear polarisation and parameter V describes the level and sense of circular polarisation (Thompson et al. 2001, pg. 98).

The Stokes parameters are defined in terms of the mean amplitudes of orthogonally-polarised components of the wave. For R and L polarisation modes, the Stokes parameters of the incident radiation are defined by

$$\begin{aligned} I &\equiv <(\mathcal{E}^R)^2> + <(\mathcal{E}^L)^2> \\ Q &\equiv <2\,\mathcal{E}^R\mathcal{E}^L> \cos\Delta\phi \\ U &\equiv <2\,\mathcal{E}^R\mathcal{E}^L> \sin\Delta\phi \\ V &\equiv <(\mathcal{E}^R)^2> - <(\mathcal{E}^L)^2> \end{aligned} \tag{3.8}$$

where the angle $\Delta\phi$ is the phase difference between the R and L components of the electric field vector, and the angular brackets denote a time average, or expectation value (after Cohen 1958).

The radiative transfer equation for the full four Stokes parameters can then be written in the form

$$\frac{d\mathbf{S}}{dz} = \mathbf{R}.\mathbf{S} \tag{3.9}$$

where $\mathbf{S}$ is a vector of the Stokes parameters, $\mathbf{S} = (I, Q, U, V)$ and $\mathbf{R}$ is a matrix determined by the transition being described. When the maser is unsaturated and isotropically pumped, the matrix $\mathbf{R}$ is diagonal (Elitzur 1991).

Deguchi & Watson (1990), for example, derived the following radiative transfer equation for polarised maser radiation

$$\frac{d}{dz}\begin{pmatrix} I(\omega) \\ Q(\omega) \\ U(\omega) \\ V(\omega) \end{pmatrix} = \begin{pmatrix} A & B & F & C \\ B & A & E & G \\ F & -E & A & D \\ C & -G & -D & A \end{pmatrix} \begin{pmatrix} I(\omega) \\ Q(\omega) \\ U(\omega) \\ V(\omega) \end{pmatrix} \tag{3.10}$$

where the matrix elements A through G are real frequency dependent functions of the density matrix elements described below, and the dipole matrix elements.

3.4.3 The maser particles

Maser emission arises from a large system of many masing molecules, such as SiO. The macroscopic development of a large system of many molecules can be related to the molecular properties via the

density matrix, ρ.

The density operator of state Ψ is defined as $\hat{\rho} = \overline{|\Psi><\Psi|}$. The time evolution of the density operator is given by the equation of motion

$$\frac{d\hat{\rho}}{dt} = \frac{1}{i\hbar}[\hat{H}, \hat{\rho}] \tag{3.11}$$

where H is the Hamiltonian (pg. 125 Yariv 1982).

If we consider the maser line shown in Figure 3.2, between angular momentum levels J_u and J_l, then each of the J levels contains $2J_a + 1$ $(a = u, l)$ magnetic sub-levels (Elitzur 1991). In this case, the density matrix equation of motion is solved by considering

$$\frac{d\rho_{ul}}{dt} = \frac{1}{i\hbar}[\hat{H}, \hat{\rho}]_{ul} + \text{relaxation terms} \tag{3.12}$$

for transitions between energy states u and l, where the relaxation terms describe ensemble effects specific to the physical problem being solved (pg. 126 Yariv 1982). GKK adapted the density matrix equation of motion to be applicable to a maser transition

$$\frac{d\rho}{dt} = -i[H\rho - \rho H] - \mathbf{\Gamma}\rho + \mathbf{\Lambda} \tag{3.13}$$

where $\mathbf{\Gamma}$ and $\mathbf{\Lambda}$ are diagonal matrices containing phenomenological decay and excitation terms respectively. For maser emission to take place the upper level must be overpopulated relative to the lower level, as a result of excess excitation to the upper level, or excess decay from the lower level, as discussed earlier (Section 3.3).

The density matrix has the useful basic quantum mechanical property that the average value of an observable A is given by $\overline{< A >} = tr(\rho A)$. The macroscopic polarisation of the maser radiation can therefore be extracted from the density matrix

$$\mathbf{P}(z,t) = \int_{-\infty}^{\infty} tr[\rho(z,t;v)\,\mathbf{d}]\,dv \tag{3.14}$$

where $\mathbf{d}$ is the dipole moment (GKK, Deguchi & Watson 1990). The full polarisation level-populations are derived from the density matrix equation to arrive at the rate equations for the level populations, in the same form as Equation 3.3.

The system is then assumed to be steady state, yielding

$$\begin{aligned} 0 &= \Lambda_{um} - \Gamma_{um}N_{um} - 3g_u B_{ul} \sum_{p,k} J^p\, c_p(u,m;l,k)(N_{um} - N_{lk}) \\ 0 &= \Lambda_{lm} - \Gamma_{lm}N_{lm} + 3g_u B_{ul} \sum_{p,k} J^p\, c_p(u,k;l,n)(N_{uk} - N_{ln}) \end{aligned} \tag{3.15}$$

These rate equations are now in terms of the angular momentum levels J_u and J_l, and are dependent on the magnetic sub-levels m and n. The dependence on the magnetic sublevels appears through the coefficients $c_p(u,m;l,n)$, which are the squares of the appropriate $3j$ coefficients for vector coupling (Elitzur 1991). The effect of spontaneous emission and collisions have not been included in these equations.

Modeling maser polarisation requires solving for both the level population equations with the density matrix equation of motion (Equation 3.13 reduced to Equation 3.15), and solving for the Stokes parameters via the radiative transfer equation (Equation 3.10).

3.4.4 The foundation of maser polarisation theory

As noted above, the foundational paper on maser polarisation is by Goldreich, Keeley, & Kwan (1973). The authors solved the density matrix equation of motion in several limiting cases, defined by the relative values of the stimulated emission rate R (s^{-1}), the decay rate Γ (s^{-1}), the Zeeman splitting $g\Omega$ (Hz) and the spectral width of the line $\Delta\omega$ (Hz). As pointed out in a review by Watson (2002), these solutions are an idealisation, dealing with the specific case of a linear maser, weak continuum seed radiation, a constant magnetic field, a J=1-0 transition, m-isotropic pumping, one-dimensional masers, a homogeneous environment, and the solutions were determined at the line centre only.

GKK only solved the maser equations for certain limiting cases, so their solutions do not provide a continuous function of maser polarisation over a range of maser intensities, or levels of saturation (Watson 2002). It is also important to note that GKK used different methods to solve for the polarisation in the saturated and unsaturated regimes. In the saturated regime they found stationary states of the polarisation, where the polarisation is constant along the maser path. In the unsaturated regime they looked for eigenvectors of the matrix $\mathbf{R}$ (see Equation 3.9) in the radiative transfer equation (Elitzur 1993).

In the weak-splitting case pertinent to SiO maser polarisation, GKK showed that the masers will be unpolarised when the maser is unsaturated ($R \ll \Gamma$). When it is saturated ($R \gg \Gamma$), the maser emission is linearly polarised in two cases. In these cases GKK solved for the linear polarisation; the solutions depend on the angle Θ between the magnetic field and the line of sight. The Stokes U value is chosen to be zero by construction, so the total linear polarisation is given by (Q/I),

- $\Delta\omega \gg g\Omega \gg R$ (GKK's Case 2a)

$$\begin{aligned} (Q/I) &= -1 & \Theta &< 35^\circ \\ (Q/I) &= (3\sin^2\Theta - 2)/3\sin^2\Theta & 35 &< \Theta < 90^\circ \end{aligned} \tag{3.16}$$

- $\Delta\omega \gg R \gg g\Omega$ (GKK's Case 3a)

$$(Q/I) = \frac{1}{3}$$

SiO maser emission probably falls in the $g\Omega \gg R$ or $g\Omega > R$ regime (Kemball et al. 2009; Watson 2009). As the linear polarisation is fully described here by the Stokes parameter Q, the linear polarisation position angle will be either parallel to or perpendicular to the magnetic field.

Since the early paper by GKK, work has been done to extend their solutions to other transitions and to intermediate cases such as partial saturation. Other explanations for high polarisations have also been investigated (such as anisotropic pumping, which was not considered by GKK), as well as non-Zeeman mechanisms producing circular polarisation.

This work in the case of weak-splitting has been undertaken separately by the two main groups referenced earlier. Elitzur has investigated the polarisation analytically, and found stationary solutions of the equations. The Watson model has been developed using numerical solutions of the radiative transfer equations in all four Stokes parameters. A key difference between the two approaches is that the Watson model claims that the GKK solutions, which were formulated in the limiting cases mentioned above, are only applicable under those limits (Nedoluha & Watson 1993). The highly saturated $R \gg \Gamma$ limit, they claim, is not applicable to observed maser emission as it is only attained for implausibly high R/Γ. The limiting solutions should therefore not be applied to observational data, in this view (Watson 2009). Elitzur, on the other hand, maintains that only the GKK solutions, which are the stationary solutions, will propagate, and that the maser emission rotates into the stationary solutions well before saturation (Elitzur 1996, 2002).

The next two sections outline the work done in the area of weak-splitting maser polarisation by each of these two groups, in approximate chronological order.

3.4.5 The Watson model

The earliest follow-up work to the GKK paper was a series of papers which looked at non-magnetic causes of linearly polarised maser radiation, specifically for the case of SiO maser emission. The first paper in this series (Western & Watson 1983c) set up the radiative transfer equations for linearly polarised maser emission in several possible maser region geometries. These equations were used in the subsequent papers to perform the numerical integrations required to solve for the maser polarisation. Western & Watson (1983a) then showed that linear polarisation arises in saturated two- and three-dimensional masers due to competition between maser rays along different axes through the maser. They consider spherical, shell and disk geometries and find linear polarisations of up to 33%. Their calculations are representative of any maser feature geometry where one dimension is smaller than the others (Western & Watson 1983a). Notably, they found that a shell geometry would lead to radial linear polarisation for thick shells, but as the shell becomes thin the direction of the overall linear polarisation changes to become tangential to the shell. The thinner the shell, the greater the degree of linear polarisation, with a maximum polarisation of 33% (Western & Watson 1983a). Small anisotropies in the maser pumping to different m levels are also amplified in maser feature geometries where one dimension is smaller than the others, and were found to create very high linear polarisation (Western & Watson 1983b). Anisotropic pumping is discussed separately in Section 3.4.7.

In the following year, Western & Watson (1984) published numerical simulations of the transfer equations of a one-dimensional maser as a function of maser intensity, in order to compare them to the GKK solutions which only dealt with the limiting situations of highly saturated or unsaturated masers. This paper looked at the J=2-1 as well as the J=1-0 transition. For the J=1-0 transition, their solutions approached the GKK idealisation in the high saturation limit. For the J=2-1 line, however, very high polarisations ($\approx 70°$) were only obtained for $R \gtrsim 10^5\ \Gamma$. This led them to conclude that the GKK mechanism cannot be responsible for the very high SiO maser linear polarisations sometimes observed towards late-type evolved stars in higher J transitions.

Deguchi et al. (1986) extended these calculations to include velocity gradients and spontaneous emission in the maser gas in the $g\Omega \gg R$ (GKK Case 2a) regime. They used the LVG approximation to solve the radiative transfer equations. The solutions provided by this different treatment confirm

the results of Western & Watson (1984), that although the J=1-0 and J=2-1 transitions have the same polarisation solutions for the limit of high optical depth, high levels of polarisation $\geq 50\%$ are only created for much higher intensities in the J=2-1 transition than in the J=1-0 transition. They also found that spontaneous emission reduced the maximum linear polarisation, although in a later study by Nedoluha & Watson (1990a), spontaneous emission was found to have a relatively insignificant effect.

Deguchi & Watson (1990) re-worked the one-dimensional maser polarisation equations to be more appropriate to deal with higher J transitions. They found that in the GKK Case 3a (for $\Theta = 90°$) effectively no linear polarisation is created in transitions higher than the J=1-0 transition. Why should the J=1-0 line polarisation be any different to that of all other higher momentum lines? They suggested that it is because J=1-0 is the only transition where one of the J levels involved has a single magnetic substate.

The numerical investigations up to this point had been undertaken under certain assumptions about the relative strength of the Zeeman splitting, the stimulated emission rate and the decay rate: $g\Omega \gg R$ (Western & Watson 1984; Deguchi et al. 1986; Deguchi & Watson 1990), $(g\Omega)^2/\Gamma \gg R \gg g\Omega$ (Deguchi & Watson 1990), or $R \gg (g\Omega)^2/\Gamma$ (Deguchi & Watson 1990). Nedoluha & Watson (1990a) solved the radiative transfer equations without making these approximations. This complicates the solution, as off-diagonal terms in the density matrix cannot be neglected. Because they avoided many of the idealisations used in earlier investigations, this study involved a Stokes U component, as well as Stokes Q. This describes a linear polarisation position angle which is not necessarily parallel or perpendicular to the magnetic field, unlike the case $g\Omega \gg R$ and $g\Omega \gg \Gamma$ where the linear polarisation will always be perpendicular or parallel to the magnetic field. In the $R > (g\Omega)^2/\Gamma$ regime, the level of linear polarisation drops to zero.

The Nedoluha & Watson (1990a) study included v=1 J=1-0, J=2-1 and J=3-2 lines. The level of linear polarisation versus saturation was found to be similar for the J=2-1 and J=3-2 transitions. For the J=1-0 transition the linear polarisation levels were much higher, as compared to the J=2-1 and J=3-2 linear polarisation at the same level of saturation. This is consistent with the results of Western & Watson (1984) and Deguchi & Watson (1990) for the $g\Omega \gg R$ and $(g\Omega)^2/\Gamma \gg R \gg g\Omega$ cases.

Also in 1990, Nedoluha & Watson undertook a numerical study of SiO and H_2O maser polarisation, using the equations of radiative transfer given in Deguchi & Watson (1990). They found that in the intermediate intensity regime where $g\Omega$ is of the order of R, intensity-dependent circular polarisation is produced that is not due to the standard Zeeman effect. In the radiative transfer equation given by Equation 3.10, the standard Stokes V Zeeman term is the $C \times I$ term and the terms with coefficients D and G are termed non-Zeeman terms. These non-Zeeman terms are appreciable in the $g\Omega \sim R$ regime (Nedoluha & Watson 1990b). Physically, the non-Zeeman circular polarisation is being created by the rotation of the linear polarisation along the maser path, due to the changing quantisation axis as the maser saturates, changing the optical axes (Nedoluha & Watson 1994). Because this circular polarisation is created in part by non-Zeeman mechanisms, the standard methods of deriving magnetic field estimates from circular polarisation measurements are inappropriate in this regime. The consequence of this is that, to quote Nedoluha & Watson (1990b), "the actual magnetic fields are 'order-of-magnitude' uncertain."

Nedoluha & Watson (1994) undertook an extensive study of this intensity-dependent circular

polarisation and applied their results to circumstellar SiO polarisation. They found that even in light of the intensity dependent modifications to Zeeman circular polarisation, a magnetic field of at least about 10 mG is required in SiO maser regions to explain the observed circular polarisation. Under a Zeeman interpretation, similar levels of polarisation would imply magnetic field strengths of 10 to 100 G (Nedoluha & Watson 1994).

In response to a stability analysis presented in Elitzur's 1993 paper, Watson (1994) performed a comparable stability analysis of the radiative transfer equations. He found that the solutions are stable to linear perturbations in intensity and angle between the magnetic field and the line of sight. He therefore claimed that Elitzur's stability analysis and all of the results based upon it are erroneous (Watson 1994). He further claimed that Elitzur's attack on his numerical studies is unjustified and that Elitzur's points about ensemble averaging issues are incorrect. Wallin & Watson (1995) furthered Watson's stability analysis by calculating the time dependent radiative transfer for polarised maser radiation. They found that instability is not a significant factor in determining the polarisation, using a range of parameters applicable to SiO maser radiation. These points are a fundamental difference between the two models discussed here.

McIntosh & Predmore (1993) published single-dish observations of the v=1 J=1-0, J=2-1 and J=3-2 SiO maser lines towards Mira. They found that the average linear polarisation across the J=2-1 and J=3-2 lines was $17 - 23\%$ higher than that of the J=1-0 line. They proposed Faraday rotation in the maser medium as an explanation for the observations. In order to investigate the possible effect of Faraday rotation, Wallin & Watson (1997) performed numerical calculations of Faraday depolarisation in SiO masers. Their calculations showed that Faraday depolarisation is not a plausible explanation of the trend. For Faraday depolarisation to be a potential explanation of the differences in linear polarisation, it should be accompanied by appreciable differences in polarisation position angle between the different transitions.

Wiebe & Watson (1998) explored non-Zeeman circular polarisation caused by rotating optical axes due to changes in the magnetic field angle or Faraday rotation along the maser path. This case is distinct from the non-Zeeman circular polarisation created in the intermediate intensity regime, discussed earlier. Wiebe & Watson (1998) considered the particular case of SiO maser emission in the atmospheres of late-type giant stars. They modeled the atmosphere of a late-type star with turbulent magnetic and velocity fields and anisotropic pumping of the masing SiO molecules, but they did not include the velocity gradients one would expect in the near-circumstellar envelope where SiO masers are formed. Their calculations revealed non-Zeeman circular polarisation in the $g\Omega \gg R$ regime, in the presence of changing magnetic field directions. This non-Zeeman circular polarisation mimics the anti-symmetric S-shape typical of Zeeman circular polarisation. Their model produced levels of non-Zeeman circular polarisation similar to those observed in SiO masers towards late-type stars, in the presence of a magnetic field of only 10 to 30 mG. The Zeeman interpretation of the same levels of circular polarisation would predict a magnetic field of 10 to 100 G (Wiebe & Watson 1998). They conclude that if many maser features in a circumstellar environment display circular polarisation much greater than the average value of $m_l^2/4$, then the circular polarisation is probably due to the Zeeman effect rather than the non-Zeeman effect investigated in this paper (Wiebe & Watson 1998).

Until this time, the only circular polarisation mechanism considered in the Watson model was created by non-Zeeman effects. Watson & Wyld (2001) investigated the standard Zeeman circular

polarisation for the original GKK limit $R \ll g\Omega \ll \Delta\omega$ (GKK Case 2a). Because GKK did not consider frequency dependence in their calculations, their results are only applicable at the line centre and their study therefore excluded circular polarisation. Watson & Wyld (2001) remedied this by considering the Stokes parameters away from the line centre. The GKK Case 2a $R \ll g\Omega \ll \Delta\omega$ inequalities are satisfied for 1720 MHz OH masers and probably satisfied by 22 GHz H_2O masers. They may not be entirely applicable to SiO masers, where the Zeeman splitting is an order of magnitude less than that of H_2O masers, in the presence of the same magnetic field, and the condition $R \ll g\Omega$ may not be satisfied.

In the $R \ll g\Omega$ regime the non-Zeeman terms are not significant and are neglected in the Watson & Wyld (2001) analysis. For unsaturated masers, the thermal line circular polarisation relationship is applicable

$$\mathrm{V}/(\partial I/\partial v) = pB\ \cos\Theta \tag{3.17}$$

where V is the Stokes V parameter, and $\partial I/\partial v$ is the derivative of the total intensity with Doppler velocity, B is the magnitude of the magnetic field, Θ is the angle between the magnetic field and the line of sight and p is the Zeeman splitting coefficient for the observed transition (Watson & Wyld 2001). Observed circumstellar masers are usually at least partially saturated, so Watson & Wyld (2001) considered how appropriate Equation 3.17 is to saturated maser emission. They found that unless the maser emission is completely unsaturated, the dependence of the quantity $\mathrm{V}/(\partial I/\partial v)$ on $\cos\Theta$ is non-linear, and could be increased by a factor of 2.5 for high levels of saturation.

Watson & Wyld (2001) concluded that although it is not ideal, in the absence of observational information about saturation levels and angle between the magnetic field and the line of sight, the best way to estimate the magnetic field strength from circular polarisation is to use Equation 3.17 and remove the $\cos\Theta$ factor.

The Watson model has also separately investigated the effects of anisotropic pumping, which is discussed in Section 3.4.7.

A review of the main elements of the Watson model is given by Watson (2009) and a longer review of the development of these models is given by Watson (2002).

3.4.6 The Elitzur model

Most of Elitzur's contribution to the theory of maser polarisation is laid out in a four-part series of papers (Elitzur 1991, 1993, 1996, 1998) and in his book on astrophysical masers (Elitzur 1992).

The first paper in Elitzur's four part series on maser polarisation examined the radiative transfer equation for all four Stokes parameters, Equation 3.9, for strong and weak Zeeman splitting. He considered the radiation in what he terms the B-frame, the frame of the magnetic field. This gives three intensity components I^p, one for each of the Δm=p transitions (p=-1,0,1). Each of the I^p have distinct polarisation characteristics, as mentioned in Section 3.4.1. From symmetry requirements he finds that $\mathrm{I}^{-1}=\mathrm{I}^{+1} \equiv \mathrm{I}^1$, which reduces the problem to two symmetry modes, I^0 and I^1 (Elitzur 1991).

For the weak-splitting case, Elitzur (1991) reproduced the GKK Case 2a solutions, assuming an isotropically pumped maser with independent pumping to the different magnetic sublevels. The solutions were found through application of the transverse condition, that the component of the electromagnetic wave along the line of sight is zero. This method makes no reference to the angular momentum levels of the transition, which generalises the GKK solutions to all angular momentum

transitions. This paper claims that for dominant rays, the polarisation of an isotropically pumped maser is determined by the particle aspect of the maser problem alone, and the radiative transfer has no effect (Elitzur 1991). In the case of anisotropic, m-dependent pumping, the polarisation is dependent on the ratio of the pump rates of the levels involved. Anisotropic pumping is discussed in more detail in Section 3.4.7.

The two main conclusions of the 1991 paper were that the GKK solutions apply to all angular momentum transitions, as long as the radiation from the maser is beamed, and that the maser polarisation properties are the same in the saturated and unsaturated regimes. Elitzur cautioned that his result is the maximum polarisation, which would be decreased by the effects of magnetic field line curvature, or by Faraday rotation.

The only point at which the Elitzur (1991) solutions were at odds with the GKK solutions was the polarisation of unsaturated masers in the weak-splitting limit. According to GKK, in this regime the magnetic field does not produce any polarisation, whereas Elitzur found that the stable GKK polarisation solutions can be achieved for unsaturated masers, as long as the amplification is sufficient that the maser emission is beamed.

This conflict was addressed in Elitzur's second paper in the series (Elitzur 1993), which revisited maser polarisation as an eigenvector problem, and provided a stability analysis of the solutions. This paper considered the stationary states of the polarisation, where the normalised Stokes parameters are constant along the path. This can be expressed as

$$\frac{dq}{dz} = \frac{du}{dz} = \frac{dv}{dz} = 0 \tag{3.18}$$

where $q = \frac{Q}{I}$, $u = \frac{U}{I}$ and $v = \frac{V}{I}$. Equation 3.18 can be reformulated to give

$$\frac{dI}{I} = \frac{dQ}{Q} = \frac{dU}{U} = \frac{dV}{V} \equiv \lambda \, dl$$

where λ is an unknown factor which may vary with position (Elitzur 1993). This is equivalent to an eigenvalue equation of the form

$$\frac{d\mathbf{S}}{dz} = \lambda \, \mathbf{S} \tag{3.19}$$

This is simply the radiative transfer equation, Equation 3.9, where λ is the eigenvalue of the matrix $\mathbf{R}$ (Elitzur 1993).

GKK used the stationary state method (Equation 3.18) to find the polarisation in the saturated regime and the eigenvalue method (Equation 3.19) to find the polarisation in the unsaturated regime. Elitzur's 1993 paper shows that these two methods are equivalent. The solutions in the two saturation regimes should therefore be the same, supporting the results of Elitzur's 1991 paper. Elitzur claims that the reason that GKK predicted no polarisation in the weak-splitting unsaturated regime was that they took limiting solutions too early on in the polarisation analysis. In the unsaturated regime the effect of this is to eliminate terms which constrain the polarisation (Elitzur 1993).

The 1993 paper also considers the difference between the many polarisation modes present in the emission, and the radiation ensemble average of the modes. The individual modes will rotate into the stationary solutions at a rate proportional to their distance from the stationary solution. Instabilities will also hinder the growth of polarisation modes differing from the stationary solution

(Elitzur 1993). Elitzur's stability analysis showed that stable polarisation growth is also only possible for maser emission propagating at an angle of at least 35° from the magnetic field direction.

In the 1993 paper Elitzur highlighted the fact that although individual polarisation modes will rotate towards the stationary eigenvalue solutions, the ensemble average will not necessarily be equal to the stationary solution. Because the observed Stokes parameters are derived from the ensemble averages of many polarisation modes, they will only become equal to the stationary solution when all of these individual modes have rotated into the stationary solution, a state which is realised when the intensity reaches J_s/τ_s, where J_s and τ_s are the intensity and optical depth when the maser saturates (Elitzur 1993). Finally, the 1993 paper examined the stability of the polarisation solutions and spontaneous decays. He concluded that the background radiation provided by spontaneous decays does not have a significant effect on maser polarisation.

In an additional paper Elitzur responds to criticism of the first two papers in his series (Elitzur 1995). He reasserts that his solutions are in complete agreement with those of GKK. He also addresses what he believes to be problems with the numerical solutions of the Watson model, which are discussed in Section 3.4.8.

Up to this point in the literature, weak Zeeman splitting was always reduced to the limiting situation where the ratio of the Zeeman splitting $\Delta\nu_B$ to the Doppler linewidth $\Delta\nu_D$, approaches zero. In the third paper in his series (Elitzur 1996), Elitzur generalises his polarisation solutions to arbitrary values of the parameter x_B, the ratio of the two linewidths, defined as

$$x_B = \frac{\Delta\nu_B}{\Delta\nu_D} = 14\, g\, \lambda\, \frac{B}{\Delta v_5} \tag{3.20}$$

where g is the Lande factor, λ is the transition wavelength, B is the magnetic field strength and Δv_5 is the Doppler width in units of km/s. This extension of his theory gives rise to several results, including the presence of circular polarisation in the weak-splitting regime. The derived circular polarisation is proportional to the ratio x_B, which is in turn proportional to the wavelength of the transition. Consequently the circular polarisation should decrease for increasing transition frequency. The non-zero x_B formulation given in Elitzur (1996) also rendered the earlier (Elitzur 1993) stability analysis unnecessary, as none of the unstable solutions are reproduced in this new formulation. Another result of this paper is that the requirement for the onset of linear polarisation becomes $J/J_s \gtrsim x_B > (S_0/J_s)^{\frac{1}{2}}$, where S_0 is the intensity of the seed radiation.

The circular polarisation predicted in Elitzur (1996) can be used to estimate the magnetic field strength. In the Zeeman profile of a maser spot, the peak normalised Stokes V, $v_{peak} = V/I$, is related to the splitting parameter x_B by

$$x_B = \frac{3\sqrt{2}}{16}\, v_{peak}\, \cos\Theta \tag{3.21}$$

where Θ is the angle between the magnetic field and the maser propagation direction. Equations 3.20 and 3.21 can be combined to solve for the magnetic field strength from the known circular polarisation v_{peak}, if the line specific parameters such as Δv_5 are either known or can be estimated.

The final paper in the four-part series investigated the detailed circular polarisation line profiles of maser radiation (Elitzur 1998). Analysis of the shape of the circular polarisation spectral profiles can provide information about several physical parameters of the maser emission, such as the level of saturation, the Zeeman splitting and the Doppler line width. Such analysis requires spectrally-resolved

Zeeman Stokes V profiles. Unfortunately observations of SiO maser circular polarisation frequently fail to meet this criterion, due to intrinsic low levels of Zeeman splitting for this non-paramagnetic molecule, and due to observational spectral resolution limits. Analysis of circular polarisation profiles is however possible for OH (e.g. Hoffman et al. 2005) and H_2O masers (e.g. Sarma et al. 2008).

Elitzur summarised the main aspects of his maser polarisation theory in a conference review paper published in 2002 (Elitzur 2002). He noted that according to the GKK Case 2a linear polarisation solution, $(Q/I) = -1 + 2/3 \sin^2 \Theta$, which he derived himself through the transverse condition, the linear polarisation is only dependent on Θ, the angle between the magnetic field and the line of sight. It is not dependent on the level of Zeeman splitting x_B. He notes that the polarisation (Q/I) is zero at $\sin^2 \Theta = 2/3$ ($\Theta = 55°$), and changes sign on either side of it. This may explain the widespread 90° polarisation position angle flips observed in VLBI SiO maser maps. The magnetic field direction may change over a maser feature, and as it passes through an angle of $\Theta = 55°$ the linear polarisation changes sign and the position angle flips.

Only a very limited range of Θ will give polarisations greater than 33%, so these high linear polarisations are not expected to be common, according to Elitzur's model. When linear polarisation greater than 33% is observed it is parallel to the projected magnetic field direction, and can be used to map the magnetic field (Elitzur 2002).

The 2002 review paper also discussed an external criticism that has been made regarding Elitzur's maser polarisation theory. Although the stationary solution has been theoretically identified, how the polarisation evolves into that stationary solution must also be shown. The only way to properly demonstrate this would be with a full evolving simulation of many maser particles and the corresponding maser radiation (Elitzur 2002). In a more recent review paper on maser theory by Elitzur (2007), he again mentioned this as the open maser polarisation problem. He emphasised that numerical models of weak-splitting maser polarisation which do not propagate phase information are problematic, as the polarisation information is contained in the phase relationships between different modes (Elitzur 2007).

3.4.7 Anisotropic pumping

The linear polarisation of SiO masers is often very high. Troland et al. (1979) observed fractional linear polarisations of a few tens of percent in the v=1 J-2-1 line observed towards several variable stars with the NRAO 11m telescope. An extensive single dish study of v=1 J=2-1 line emission from 57 SiO maser sources by Herpin et al. (2006) found fractional linear polarisations ranging from a few percent up to 70% in individual spectral line components. VLBI maps of SiO maser emission also reveal high levels of linear polarisation, and the measured polarisations are not reduced by spatial blending as they are in single dish spectra. The first VLBI observation of SiO maser polarisation was towards TX Cam, and showed a median linear polarisation of 25% from the many maser spots, with some spots being almost 100% polarised (Kemball & Diamond 1997).

Bujarrabal & Nguyen-Q-Rieu (1981) first proposed anisotropic pumping as a means to explain the linear polarisation of the SiO maser emission. This was followed by a series of Watson model papers which provided a quantitative analysis of anisotropic pumping as a potential origin of the high levels of linear polarisation (e.g. Western & Watson 1983b, 1984; Nedoluha & Watson 1990a).

Anisotropic pumping of masers can arise when the infrared radiation which pumps the masing gas,

or the infrared radiation escaping the maser gas, has an anisotropic distribution (Watson 2002). The magnetic states are then populated or depopulated to different degrees by the direction dependent incident radiation or escaping radiation. The population inversion becomes m-dependent and the pump mechanism is referred to as anisotropic. Both collisional and radiative pumping schemes can be anisotropic (Western & Watson 1983b; Watson 2009):

- Radiative pumping schemes where the infrared radiation pumping the maser is directional leads to an anisotropic population inversion. Radiation in the radial direction from a central star falls into this category.
- Collisional pumping schemes where radiation from excited molecules escapes preferentially in specific directions will also be anisotropic.

SiO masers observed towards late-type stars are natural candidates for anisotropic pumping, as they are located close to the star in environments with radial incident radiation and large velocity gradients in the maser gas. The large velocity gradients result in infrared radiation escaping in a primarily radial direction (Watson 2002).

Western & Watson (1983b) showed that masers in a model SiO circumstellar maser environment with pumping due in part to direct radiation from the central star, can produce high levels of amplified linear polarisation from small anisotropies. Collisional pumping was also shown to create the magnetic substate population inversion necessary to create the linear polarisation, because of preferential radial infrared de-excitation. In the absence of a magnetic field, anisotropic pumping will lead to tangential linear polarisation for radiative pumping mechanisms and radial linear polarisation for collisional pumping mechanisms. Western & Watson (1983b) also showed that increasing saturation decreases the m-anisotropic population inversion, and accordingly the level of resulting linear polarisation.

Western & Watson (1984) investigated how anisotropic pumping could be combined with the effect of a magnetic field to create higher levels of polarisation than can be created by the magnetic field alone. Magnetic fields of only about 10 to 100 milligauss and small anisotropies are found to create linear polarisations as high as 80%, as the small magnetic field enhances the effect of m-anisotropies. The combined effect of magnetic field and anisotropic pumping leads to the highest levels of linear polarisation for tangential masers in the presence of a radial magnetic field (Western & Watson 1984).

This was followed by a study by Nedoluha & Watson (1990a), which showed that the polarisation of anisotropically pumped maser emission is dependent on the intensity of the background radiation in the $g\Omega \sim R$ regime, like that of the isotropically pumped emission in the same study. Nedoluha & Watson (1990a) commented that axially symmetric anisotropic pumping can produce Stokes Q and U, but it cannot produce any Stokes V that would not be present in the absence of anisotropic pumping. Circular polarisation observed towards an anisotropically pumped maser source is therefore still either due to the effect of magnetic fields (Nedoluha & Watson 1990a), or due to the propagation of linear polarisation through the anisotropic medium (Nedoluha & Watson 1990b).

If linear polarisation is being created by anisotropic pumping, then the levels of linear polarisation depend on the anisotropy parameter, which is the ratio of the anisotropy in the angular distribution of incident radiation to the population inversion of the two angular momentum levels involved in the transition. This anisotropy parameter could be as high as unity for SiO maser emission (Nedoluha & Watson 1990a). Anisotropic pumping creates the highest linear polarisation when the pumping

direction is parallel to the magnetic field and perpendicular to the direction of propagation. For calculations with the pumping direction parallel to the magnetic field, polarisations of up to 100% are achieved when the anisotropy parameter is almost equal to one, and when there is a large angle between the direction of propagation and the direction of the magnetic field (Nedoluha & Watson 1990a).

As is typical of the Watson models, anisotropic pumping is shown to result in similar polarisation characteristics for the J=2-1 and higher frequency transitions, and distinctly different characteristics for the J=1-0 transition. This is illustrated by evaluating the linear polarisation magnitude over a range of R/Γ saturation values, for $g\Omega/\Gamma = 100$ (Nedoluha & Watson 1990a). On this basis Nedoluha & Watson (1994) invoked anisotropic pumping to explain the unexpected observed trend of increasing linear polarisation with increasing transition frequency. They show, in the $g\Omega \gg R$ limit, that it is plausible for the linear polarisation created by anisotropic pumping to be ranked in order of decreasing fractional linear polarisation as J=3-2 > J=2-1 > J=1-0, if the different transitions are at different levels of saturation.

Elitzur took anisotropic pumping into consideration in his first and third maser polarisation papers (Elitzur 1991, 1996). According to his models, m-isotropic maser polarisation approaches the stationary solution limit as it becomes more saturated. The same is true for anisotropic pumping, and the limit polarisation now depends on the ratio of the pumping to the two p-modes I^0 and I^1 mentioned in Section 3.4.6 (Elitzur 1991). The ratio is given by $\mathcal{R}_{01} = \mathrm{I}^0/\mathrm{I}^1$ and is equal to one for isotropic pumping. The polarisation solutions were calculated for the saturated and unsaturated regimes, with the unsaturated solution tending towards the saturated limit. The GKK Case 2a solutions are then generalised to be

$$\begin{aligned} (Q/I) &= 1 && \Theta \leq \Theta_B \\ (Q/I) &= -1 + 2/[\sin^2\Theta(1 + 2/\mathcal{R}_{01})] && \Theta \geq \Theta_B \end{aligned}$$

where Θ_B is given by the relation $\tan^2\Theta_B = \mathcal{R}_{01}/2$, which reduces to $\Theta_B = 35°$ for the isotropic case of $\mathcal{R}_{01} = 1$ (Elitzur 1991).

Asensio Ramos et al. (2005) proposed that anisotropic pumping could lead to what was termed dichroic masing. Dichroic masing occurs when two adjacent energy levels are not inverted but, because of anisotropic pumping, particular magnetic sublevels of the upper energy level may have higher populations than some magnetic sublevels of the lower energy level. For example, in an SiO v=1 vibrational level, the population of the J=2 line may be less that that of the J=1 line, so the populations are not inverted. But the population of the m=1 level of the J=2 line may be larger than the population of the m=0 level of the J=1 line. So for transitions between those two specific sub-levels, the populations are inverted and masing action can occur. Emission between particular m levels is amplified, and this can result in net polarisation.

When no magnetic field is present, radiation from a central star creates dichroic masers that are linearly polarised tangential to a ring around the star. In the presence of magnetic fields the Hanle effect will rotate the polarisation angle. The polarisation angle can flip 90° in the presence of a strong field, as the magnetic field inclination angle changes from less than, to greater than, the van Vleck angle of 55°. However, strong magnetic fields were shown in this paper to inhibit the dichroic maser effect, so observed polarisation angle flips are unlikely to be caused by this mechanism. Changes in linear polarisation position angle can also be caused by a change in radiative anisotropy factor in the

medium, due to a local change in temperature or optical depth. If the direction of the anisotropy changes from mainly radial to mainly tangential, this could result in a 90° polarisation flip (Asensio Ramos et al. 2005). The Asensio Ramos et al. mechanism also predicts greater levels of maser action at lower angular momentum J levels.

The investigation of dichroic masing by Asensio Ramos et al. (2005) only considered the completely unsaturated regime. Saturation will lead to an inhibiting of the linear polarisation caused through anisotropic pumping, as the magnetic substate population differences are reduced (Western & Watson 1983b).

3.4.8 Summary and discussion

The weak-splitting maser polarisation work done by Elitzur can be summarised into two main contributions:

- He unified the GKK theory for saturated and unsaturated masers, and found that the polarisation of unsaturated masers will evolve rapidly into the saturated limit.
- He first recognised and described the Zeeman circular polarisation that is created when the line splitting parameter x_B, though very small, is not identically equal to zero.

Under the Watson model, the weak-splitting maser polarisation solutions have been investigated over a range of saturation levels, Zeeman splitting levels, and angles between the magnetic field and maser propagation direction. The Watson model for weak-splitting maser polarisation can be summarised in terms of linear polarisation, circular polarisation and anisotropic pumping:

- In terms of linear polarisation, the Watson model found that the polarisation approaches the GKK limit as the intensity increases. For transitions higher than J=1, the high polarisation GKK limits of $\gtrsim$ 70% are only reached for extremely high levels of saturation, $R \gtrsim 10^5\ \Gamma$. They concluded that very high levels of linear polarisation must be created by other means. For intermediate intensities, where $g\Omega \sim R$, the linear polarisation becomes intensity dependent and the position angle of the linear polarisation relative to the magnetic field will depend on intensity.
- In terms of circular polarisation, the Watson model predicts that the magnetic field estimates resulting from the standard Zeeman equation, Equation 3.17, can be overestimated if the maser is saturated, by up to a factor of about two or three. A second factor identified in the Watson model can also influence the levels of circular polarisation: non-Zeeman terms resulting from the rotation of the optical axis along the maser path. This rotation can arise in the intermediate intensity $g\Omega \sim R$ regime where the linear polarisation position angle is intensity dependent, or through changes in the optical axis due to Faraday rotation, or changing magnetic field direction along the maser path in the case $g\Omega \gg R$. The non-Zeeman circular polarisation can be large and cannot easily be related to the magnetic field values. However, if a large number of SiO maser features display circular polarisation at a level much greater than the average $m_l^2/4$, then the circular polarisation is probably not due to non-Zeeman terms from changes in the optical axes (Wiebe & Watson 1998).

- In terms of anisotropic pumping, the Watson model predicts that anisotropic pumping can result in very high levels of linear polarisation. Anisotropic pumping cannot itself create circular polarisation.

There are long-standing theoretical differences between the Watson weak-splitting maser polarisation models and the Elitzur weak-splitting maser model. Elitzur claims that the numerical solutions of the Watson model are at odds with his analytical solutions. In light of his finding that his solutions are compatible with the GKK solutions, he further claims that the Watson model results are at odds with the GKK solutions (Elitzur 1995). Elitzur claims that the fundamental problem with the numerical studies of maser polarisation is that they don't take into account the statistical nature of the radiation field (Elitzur 1995). Because the polarisation characteristics of maser radiation emerge out of the phase relationships between waves from different Δm transitions, Elitzur requires that phase must be taken into account when modeling maser polarisation. The numerical simulations performed in the Watson models make use of the radiative transfer equations in all four Stokes parameters. The Stokes parameters are intensities, so the phase information is lost in this formulation (Elitzur 2007).

Watson et al., on the other hand, believe that their model solutions are entirely in agreement with those of GKK. They claim that where Elitzur's work is in conflict with theirs, it is either because of errors or omissions (Watson 1994) or because the calculations are too simplistic (Watson 2002).

Elitzur's concerns about the statistical nature of the radiation field were addressed in a recent study by Dinh-v-Trung (2009a,b), who performed numerical simulations of the random broad-band maser radiation field for partially saturated isotropically pumped masers. This work uses the ensemble averages of the emerging maser radiation to find the Stokes parameters. Their simulation shows that linear polarisation occurs for $\Theta = 30°$, a direct contradiction of the stability analysis in Elitzur (1993) which predicts that stable maser propagation is not possible for $\Theta < 35°$. For weak saturation, the level of linear polarisation predicted by the Dinh-v-Trung (2009b) simulation is low, $\sim 1.5\%$, which is also supportive of the Watson model over the Elitzur model.

Western & Watson's 1984 paper, amongst others, highlighted a significant observational disagreement with Elitzur's theory. The Western & Watson (1984) claim that higher J lines only reach high levels of linear polarisation for very high levels of saturation seemed to be in agreement with GKK, who had different solutions in the saturated and unsaturated regimes. This is at odds with the Elitzur model finding that the stationary solutions are applicable for all levels of rotational transitions (Elitzur 1991, 1993). In Elitzur's 1991 paper he commented on the Western & Watson (1984) and Deguchi et al. (1986) findings, claiming that the discrepancy is due to their using initial conditions that are not consistent with the GKK solutions. In response to Elitzur's accusations, Nedoluha & Watson (1994) claimed that Elitzur's solutions rely on incorrect simplifications and are therefore invalid.

Gray (2003) compared the two contending weak-splitting maser models to the multi-level maser model he developed with several co-authors (e.g. Field & Gray 1988; Gray & Field 1995). He compared the level population equations derived from his model to Elitzur and Watson's theories, attempting to reduce his equations to theirs. He finds that by making some approximations it is possible to reduce his equations to Watson's level population equations (Watson 1994) and consequently concludes that his theoretical work is in agreement with Watson's theory and therefore not in agreement with Elitzur's theory.

However, this conclusion assumes that the difference between the two weak-splitting polarisation theories lies in how they deal with the level populations. The difference between the Elitzur and Watson models is not in the level population equations, rather in their fundamental treatment of radiation statistics, and the level populations in Watson's 1994 paper are just a particular formulation of the standard level population equations given in Equation 3.15.

3.4.9 Observational tests

Numerous observations of SiO masers towards late-type stars have been made, both by single dish telescopes and interferometric arrays. These observations can be used to test the predictions of the maser polarisation models. Potential determinative observational tests are discussed in this section, categorised by those that require linear polarisation observations, circular polarisation observations, and tests that require both circular and linear polarisation observations. The tests are summarised in Table 3.1. Several of these tests have already been been performed using single dish and interferometric studies of SiO maser emission, and their results are discussed in Section 3.4.10.

The theoretical basis for this section is provided above. The observational tests proposed here are also specific to the observations included in this thesis: VLBI observations of SiO maser emission from the 43 GHz J=1-0 and 86 GHz J=2-1 transitions in two vibrationally excited states.

Linear polarisation observations

Maser polarisation can become linearly polarised either through the presence of a magnetic field in the maser medium, introducing a quantisation axis, through m-anisotropic pumping of the masers, or through non-axisymmetric maser feature geometries. Observational tests of the maser polarisation models provided by the linear polarisation include:

1. **Comparison of the degree of linear polarisation in the v=1 J=1-0 43 GHz J=2-1 86 GHz transitions.**
   Elitzur's model predicts the same levels of linear polarisation for all SiO maser lines. For the same level of saturation, the Watson model predicts higher levels of linear polarisation for the J=1-0 line. If the saturation level of the two transitions are similar, anisotropic pumping models also predict higher levels of linear polarisation for the J=1-0 line.

2. **Comparison of saturation level and linear polarisation level.**
   In the Elitzur model the polarisation solution is applicable for unsaturated and saturated maser emission, as long as the maser emission has evolved into the stationary solution. In the Watson model, the levels of linear polarisation will increase with saturation level.

   On the other hand, anisotropic pumping models predict reduced linear polarisation for higher levels of saturation. If the masers are anisotropically pumped, the most saturated spots are therefore expected to be the least linearly polarised. The Nedoluha & Watson (1990a) anisotropic pumping model shows the linear polarisation level declining as the maser saturates, with the decrease occurring at higher saturation levels for the v=1 J=2-1 line than for the v=1 J=1-0 line. The comparison of linear polarisation as a function of maser saturation can therefore be performed for both of these lines to look for evidence of this effect.

3. **Comparison of linear polarisation with distance from the star.**
   Radiative m-anisotropic pumping of SiO masers from stellar radiation will be strongest at the inner boundary of the maser ring, closest to the star (Western & Watson 1983b; Desmurs et al. 2000). The linear polarisation created by anisotropic pumping is therefore expected to be strongest closest to the star (Kemball et al. 2009).

4. **Electric vector position angle rotation.**
   For polarisation created by a magnetic field, the linear polarisation is either parallel or perpendicular to the projected field direction in the $R \ll g\Omega$ regime. In this regime, observations of 90% flips in the linear polarisation can be interpreted as being evidence of changes in magnetic field direction along a maser feature, with the flip occurring as the magnetic field passes through the critical angle of 55° (Elitzur 2002). The rotation of the polarisation position angle around a 90% flip can be compared to the GKK linear polarisation solution in Equation 3.16, by modeling the variation of the angle Θ between the magnetic field and the line of sight, along the maser feature (Kemball et al., 2011b).

   The linear polarisation position angle can also provide evidence of anisotropic pumping. In the absence of a magnetic field, when radiation from a central star pumps a thin shell, the anisotropic nature of the pump will lead to tangential linear polarisation. In the absence of a magnetic field, a collisionally pumped thick maser shell will display radial linear polarisation (Western & Watson 1983b). The linear polarisation created by anisotropic pumping can also rotate due to the presence of a magnetic field, but only up to angles of about 45° (Asensio Ramos et al. 2005).

   Polarisation position angle rotation can also arise in the $R \sim g\Omega$ regime, where the angle is dependent on saturation level (Nedoluha & Watson 1990a). In the $R \ll g\Omega$ regime, linear polarisation position angle rotation of $< 90\%$ can be caused by a changing projected magnetic field direction along a maser feature, or by Faraday rotation (Watson 2009). Faraday rotation is discussed in more detail below, as it is a possible factor in several of the observational tests proposed in this section.

Faraday rotation along the maser path may reduce the levels of linear polarisation and alter the interpretation of the polarisation. Elitzur (1991) first proposed that Faraday depolarisation could lead to higher levels of linear polarisation at higher J levels, as Faraday rotation scales with wavelength. However, substantial Faraday rotation would be accompanied by a significant rotation of the linear polarisation position angle. Single dish polarisation observations of SiO maser emission towards Mira show changes in linear polarisation position angle with transition frequency of at most 9° (McIntosh & Predmore 1993). Numerical calculations of Faraday rotation in the weak-splitting maser polarisation regime also show that these levels of position angle rotation are too low for the linear polarisation levels to be explained by Faraday rotation (Wallin & Watson 1997). Many VLBI observations of SiO maser emission show the linear polarisation to be ordered, with position angles predominantly tangential to the star. This also argues against a large degree of Faraday rotation along the maser path.

Test	Polarisation	Watson	Elitzur	Anisotropic
1.	L	•	•	•
2.	L	•	•	•
3.	L			•
4.	L	•	•	•
5.	C	•	•	
6.	L&C	•		

Table 3.1: Summary of the observational tests of the Elitzur and Watson maser polarisation models. The first column is the test number, as given in the text. The second column shows if the test requires linear or circular polarisation measurements, or both. The next three columns show if the test is linked to the Elitzur model, the Watson models, or anisotropic pumping models.

Circular polarisation

Maser emission can become circularly polarised through standard Zeeman splitting in the presence of a magnetic field. Alternatively, it can become circularly polarised through non-Zeeman effects in the intermediate intensity regime or in the presence of turbulent magnetic field directions or Faraday rotation (Watson 2009). Circular polarisation by weak Zeeman splitting is modeled by both Elitzur and Watson, but non-Zeeman circular polarisation is only a feature of the Watson model. Observational tests based on the circular polarisation observations include:

5. **Comparison between the degree of circular polarisation in the v=1 J=1-0 43 GHz transition and the J=2-1 86 GHz transition.**
   Standard Zeeman splitting in the presence of a magnetic field is present in both the Elitzur and Watson models, and is proportional to the wavelength of the line. In the absence of saturation effects, for the J=1-0 line at 43 GHz the circular polarisation caused by standard Zeeman splitting should be double that of the J=2-1 line at 86 GHz for both Elitzur and Watson models.

   Under the Elitzur model the circular polarisation is not saturation dependent, as long as $J/J_s > \frac{3}{4}$, where J is the maser intensity, and J_s the saturation intensity (Elitzur 1996). Under the Watson model, the standard Zeeman circular polarisation can be increased by a factor of a few due to saturation (Watson & Wyld 2001).

   Unlike Zeeman circular polarisation, the non-Zeeman circular polarisation of the Watson model is not significantly dependent on the angular momentum level of the transition.

Linear and circular polarisation observations

Observational tests that require both linear and circular polarisation observations include:

6. **Correlation between levels of linear polarisation and circular polarisation.**
   In the Watson model, circular polarisation can be created by the change in direction of linear polarisation, when the maser emission falls in the $g\Omega \sim R$ regime, when the magnetic field direction changes along the line of sight, or when Faraday rotation is significant, as mentioned above (Watson 2009). If the circular polarisation is created by this mechanism, then the circular polarisation levels will be be correlated to the linear polarisation levels (Watson 2009). Observations

of a correlation between levels of circular polarisation and linear polarisation would therefore support the Watson model.

However, work by Wiebe & Watson (1998) shows that statistical variations in the emission region properties can destroy this correlation in some cases, so lack of correlation is not necessarily evidence against non-Zeeman circular polarisation. Wiebe & Watson (1998) instead suggest testing for source ensemble correlations. If many maser features display circular polarisation at a level much greater than the average value of $m_l^2/4$, then the circular polarisation is unlikely to be caused by non-Zeeman effects (Wiebe & Watson 1998).

3.4.10 Observations

This section describes published results relevant to the observational tests listed above. Most of the tests have been applied in the context of single dish observations. Ideally the polarisation characteristics of the maser emission should be measured for individual maser components for these tests, using VLBI images of the maser region. There are two reasons for this:

- The characteristics of the maser emission, such as levels of linear and circular polarisation, intensity and velocity, vary sharply between the individual maser features in the near-circumstellar envelope. Single dish antennas measure spectra of the compound emission from the many individual maser features. Individual features may also overlap in frequency. The spatial and frequency blending reduces the measured polarisation levels.
- Two of the tests given above entail comparing the levels of polarisation of different maser transitions. This comparison should be made between maser spots which are co-located in the two transitions, to ensure that the physical conditions of the masing material are the same for both transitions. This is only possible in VLBI imaging, for which the individual maser spots are resolved.

The observations necessary for tests #1 and #5 have been performed using single dish observations, and those necessary for tests #3, #4 and #6 have been performed using VLBI observations. Test #2 has been performed with both single dish and VLBI observations. The prior observations are described below, along with their implications as tests of the polarisation models.

Test #1: Linear polarisation at v=1 J=1-0 versus v=1 J=2-1

Observational test #1 has been performed in several single dish studies, which are summarised in Table 3.2. Barvainis & Predmore (1985) compared SiO maser lines towards a number of sources, looking at the profile averaged linear polarisation and comparing the linear polarisation of different individual features where features could be paired across transitions. They observed similar levels of profile averaged linear polarisation in the different transitions. Only the emission towards VX Sgr showed a trend of increasing fractional polarisation with increasing transition frequency for the strongest three features in the line spectrum. Of all of the sources observed, VX Sgr also displayed the clearest correspondence between spectral features between the three observed lines.

McIntosh & Predmore (1991) observed SiO masers towards seven late-type stars, while McIntosh & Predmore (1993) and McIntosh et al. (1994) observed Mira and VY CMa. McIntosh & Predmore (1991)

Paper	Sources	Lines	Trend
Barvainis & Predmore (1985)	8	v=1 J=1-0	$m_l \uparrow$ J $\uparrow$
		v=2 J=1-0	(VX Sgr)
		v=1 J=2-1	
McIntosh & Predmore (1991)	7	v=1 J=1-0	$m_l \uparrow$ J $\uparrow$
		v=1 J=2-1	
		v=1 J=3-2	
McIntosh & Predmore (1993)	1	v=1 J=1-0	$m_l \uparrow$ J $\uparrow$
		v=1 J=2-1	
		v=1 J=3-2	
McIntosh et al. (1994)	1	v=1 J=1-0	
		v=1 J=2-1	

Table 3.2: Published fractional linear polarisation comparisons between different SiO maser transitions.

and McIntosh et al. (1994) compared the linear polarisation levels over specified velocity intervals in the spectra, and McIntosh & Predmore (1993) compared the polarisation of a particular feature that was visible in all of the spectra. The fractional linear polarisation of the v=1 J=1-0, J=2-1 and J=3-2 lines observed by McIntosh & Predmore (1991) and McIntosh & Predmore (1993) showed a general trend of increasing linear polarisation with increasing angular momentum of the transition. No linear polarisation trend with rotational transition was observed by McIntosh et al. (1994). All of these observations made use of the Five College Radio Astronomy Observatory 13.7 m antenna.

A trend of increasing linear polarisation with increasing angular momentum is at odds with both the Elitzur and Watson model predictions. It is possible that these observed trends are chance characteristics of the spectral lines, and that the velocity regions matched over frequency are from spatially separate maser components. Alternatively, the observed trend is possible in terms of the Watson anisotropic pumping model. Although anisotropic pumping is expected to produce lower levels of linear polarisation for higher angular momentum transitions, if the emission from the different lines is at different levels of saturation the opposite trend can occur (Nedoluha & Watson 1994). A decrease in linear polarisation with wavelength is also characteristic of Faraday rotation. Faraday rotation has been argued to be an unlikely explanation of the trend, as discussed in the previous section. The primary evidence against Faraday rotation is the lack of significant polarisation position angle rotation accompanying the observed decrease in polarisation level in higher frequency transitions (McIntosh & Predmore 1993; Wallin & Watson 1997).

The linear polarisation trend may also be explained if there are fewer maser spots at higher frequencies, or if maser features are narrower at higher frequencies. If this is the case the effect of spatial and frequency blending would be less at the higher frequencies, and the fractional linear polarisation would be greater. Two simultaneous VLBI images of the v=1 J=1-0 and v=1 =2-1 lines have shown fewer spots for the v=1 =2-1 line (Phillips et al. 2003; Soria-Ruiz et al. 2005), but this trend is not universal. This test will benefit from VLBI observations, where the maser emission is resolved and the linear polarisation comparison can be made on a component-by-component basis.

Test #2: Linear polarisation versus saturation

A trend of higher linear polarisation for the weaker maser features has been noted for late-type stars R Aquarii (Allen et al. 1989; Hall et al. 1990; Boboltz 1997), R Cassiopeia (McIntosh et al. 1989) and R Leo (Clark et al. 1984). This trend is inconsistent with both the Elitzur and Watson models. Instead, this trend supports an anisotropic pumping model for the maser polarisation. Nedoluha & Watson (1990a) explicitly link this trend to their anisotropic pumping models, which predict a drop in linear polarisation levels for saturated maser emission in the $g\Omega > R > \Gamma$ regime.

McIntosh et al. (1989) suggest that this trend could instead be caused either by Faraday depolarisation, which is higher for the longer maser path lengths of higher intensity masers, or through spatial blending of the polarisation if the higher intensity masers come from less uniform regions of the envelope. The trend may also be a signal-to-noise effect, where the errors in measurements of weaker intensity maser features are relatively larger than those of high intensity masers (Boboltz 1997). Boboltz (1997) takes this possibility into account and concludes that the trend he observes is significant even in light of the larger errors for weak masers.

Test #3: Linear polarisation with distance from the star

Kemball et al. (2009) presented time-series images of polarised SiO maser emission around TX Cam, and found that the total linear polarisation $P = \sqrt{Q^2 + U^2}$ is strongest at the inner boundary of the maser shell. This is indicative of m-anisotropic pumping from the star. However, shock compression of the magnetic field in the inner layers of the near-circumstellar envelope may also lead to stronger linear polarisation closer to the star (Kemball et al. 2009).

Test #4: Linear polarisation position angle

The linear polarisation position angles of SiO maser emission around the late-type evolved stars TX Cam, IRC +10011, R Aquarii and W Hydrae are observed to be predominantly tangential (e.g. Kemball & Diamond 1997; Desmurs et al. 2000; Cotton et al. 2006, 2008; Kemball et al. 2009), but this dominant tangential pattern is not observed in all late-type star images (e.g. Cotton et al. 2004, 2008, 2009b). In some instances the emission shows a combination of tangential and linear position angles (e.g. Boboltz 1997; Cotton et al. 2006). Kemball et al. (2009) recently published a series of 43 v=1 J=1-0 SiO maser maps of TX Cam, with each observation about two weeks apart. The linear polarisation of the maser spots is predominantly tangential over the 43 images. The images showed for the first time that the linear polarisation position angle of most of the maser features remains constant over the feature lifetime.

Tangential linear polarisation is consistent with both the Elitzur and Watson models, where the linear polarisation is either parallel or perpendicular to the projected magnetic field. The exception to this is the Watson model prediction that in the $R \sim g\Omega$ regime the linear polarisation position angle will vary with saturation level. The order observed in the linear polarisation position angles indicates either that the emission is very likely not operating in this regime. If the linear polarisation is caused by a magnetic field, then the tangential polarisation is indicative of a radial magnetic field (Kemball & Diamond 1997).

Tangential linear polarisation is also characteristic of anisotropically pumped maser emission, where

the maser pump is provided by a central star. Desmurs et al. (2000) argue for this explanation for the tangential linear polarisation they observed towards TX Cam and IRC +10011.

A number of VLBI images of SiO masers have shown the 90% EVPA flips (e.g. Kemball & Diamond 1997) that can be explained under the GKK polarisation solution as transitions across the critical 55° angle between the magnetic field and the line of sight (Elitzur 2002). Kemball et al. (2011b) recently published a detailed analysis of a 90% EVPA rotation observed in a v=1 J=1-0 SiO maser feature around TX Cam. The variation of the angle Θ between the magnetic field and the line of sight was modeled as a second order polynomial. The observed EVPA rotation across the feature was found to be consistent with the GKK polarisation solution in Equation 3.16.

Test #5: Circular polarisation at v=1 J=1-0 versus at v=1 J=2-1

The comparison between circular polarisation levels at v=1 J=1-0 and v=1 J=2-1 has only been made for a single observation of VY CMa with the Five College Radio Astronomy Observatory 13.7 m antenna (McIntosh et al. 1994). The circular polarisation was measured for four velocity regions in the spectrum. The circular polarisation of the v=1 J=2-1 line varied from less than 0.1% up to 0.8%, and the v=1 J=1-0 polarisation varied between 0.7% and 4.1%. In each velocity region the v=1 J=1-0 polarisation was significantly higher than the v=1 J=2-1 polarisation. For one of the four features the v=1 J=1-0 circular polarisation was found to be double that of the v=1 J=2-1 circular polarisation, as expected from standard Zeeman splitting, under the Elitzur and Watson models.

Test #6: Linear polarisation versus circular polarisation

McIntosh et al. (1994) looked for evidence of a circular-linear polarisation correlation in their single dish spectra of VY CMa. The four velocity regions they considered in the spectra did not show any clear relationship between the circular and linear polarisation. This test has also been performed for VLBA images of v=1 J=1-0 SiO maser emission towards R Aquarii (Boboltz 1997) and TX Cam (Kemball & Diamond 1997). In both cases no correlation was found between the levels of circular and linear polarisation of the maser features.

Cotton et al. (2011) recently compared the fractional linear and circular polarisation of v=1 and v=2 J=1-0 SiO maser emission towards IK Taurii and found that for both lines the average fractional circular polarisation is much larger than the average value of $m_l^2/4$. This rules out non-Zeeman circular polarisation for these masers, according to the test proposed by Wiebe & Watson (1998).

Chapter 4

Radio Interferometry

Interferometry has a long history of use in stellar astronomy. The first published astronomical use of an interferometer was the Michelson interferometer, which was used to measure stellar diameters at optical wavelengths (Michelson 1920; Michelson & Pease 1921). An overview of the development of astronomical interferometry at optical and radio wavelengths is provided by Quirrenbach (2009). Interferometry has become an increasingly important tool in studies of late-type, evolved stars, providing high resolution radio and sub-millimetre wavelength images of molecular line emission in circumstellar envelopes and thermal emission from dust, and allowing the measurement of the diameters of nearby evolved stars in the optical.

At optical wavelengths, both multiple-aperture interferometers and interferometric techniques for use with single apertures have been developed (Labeyrie 1978). The techniques of speckle interferometry (Labeyrie 1970), and aperture-masking interferometry (Rhodes & Goodman 1973; Haniff et al. 1987) fall into the latter category. Interferometric techniques have also been extended to infrared wavelengths, pioneered by McCarthy & Low (1975). Reviews of early optical stellar interferometric methods are provided by Brown (1968) and Labeyrie (1978), and a more recent review of optical and infrared interferometry is provided by Monnier (2003).

A few early examples of late-type, evolved star results provided by optical and infrared interferometry include the measurement of stellar diameters (e.g. Michelson & Pease 1921; Gezari et al. 1972; McCarthy et al. 1977; Haniff et al. 1995), the wavelength dependence of the Mira variable diameter measurements (e.g. Labeyrie et al. 1977), an effective temperature scale for giants (e.g. di Benedetto & Rabbia 1987), the detection of bright spots on the supergiant star Beutelgeuse (e.g. Buscher et al. 1990), and the measurement of the radii of circumstellar dust shells (McCarthy & Low 1975; Sutton et al. 1977).

Many advances in optical and infrared interferometry have since been made, as a number of new interferometers have been constructed, including, as examples, the Infrared Spatial Interferometer[1] (ISI), the Infrared-Optical Telescope Array[2] (IOTA) and the Very Large Telescope Interferometer[3] (VLTI). The interferometric capabilities of large single aperture telescopes have also been developed.

Some examples of the scientific results that have resulted from these developments include the

[1] www.isi.ssl.berkeley.edu
[2] tdc-www.harvard.edu/IOTA
[3] www.eso.org/sci/facilities/paranal/telescopes/vlti/index.html

measurement of inner dust shell radii of a number of late-type, evolved stars (Danchi et al. 1994), mid-infrared photospheric diameter variability (Weiner et al. 2003), and dust shell asymmetries (Weiner et al. 2006), using the ISI, and circumstellar dust measurements with the VLTI (Rajagopal et al. 2007). IOTA has produced images of near-infrared water shells around late-type, evolved stars (Ragland et al. 2008; Pluzhnik et al. 2009). Aperture-masking interferometry at the Keck[4] I telescope has provided long-term monitoring of Mira variable diameters as a function of pulsation period (Woodruff et al. 2008), high resolution images of the circumstellar envelopes around late-type, evolved stars (e.g. Monnier et al. 1999b), and high resolution evidence of the proper motion of dust clumps (e.g. Tuthill et al. 2000). Developments in polarimetric optical interferometry have enabled a distinction to be drawn between dust-scattered and thermal emission around Mira-type variables (Ireland et al. 2005).

Although astronomical interferometry was originally pioneered at optical wavelengths, the technical development of interferometry proceeded much faster at radio wavelengths. The instrumentation needed for the longer wavelengths of radio astronomy is technologically easier to construct, and the longer wavelengths of radio astronomy are comparatively less affected by propagation through the atmosphere (Kellermann & Moran 2001). Heterodyne down-conversion is also possible at radio wavelengths, due to the low receiver quantum noise limits (Thompson et al. 2001, pg. 39-40). For these reasons, radio interferometry led in developing new techniques, such as the use of closure phase (Jennison 1958), which was later adopted in the optical (Rogstad 1968; Baldwin et al. 1986), as well as aperture synthesis (Ryle & Hewish 1960), earth rotation synthesis (Ryle & Neville 1962), and self-calibration, which has subsequently been used in optical interferometry (Baldwin et al. 1996; Meimon et al. 2009).

The first radio wavelength interferometer was the sea interferometer, developed by Pawsey et al. (1946), shortly followed by the first two-element radio interferometer constructed by Ryle & Vonberg (1946), which consisted of two dipole antennas. A history of the development of radio interferometry is given in Thompson et al. (2001, pg. 12) and Kellermann & Moran (2001).

Thermal continuum radio emission from stars is weak (Ryle & Elsmore 1973), so the early development of radio interferometry provided relatively few results from observations of stars. Some of the earlier evolved star results that arose out of radio interferometry were from observations using the Very Large Array[5] (VLA, Napier et al. 1983). These included the resolution of free-free emission from the stellar wind around P Cygni at 4.9 GHz (White & Becker 1982), and imaging the free-free emission from the bipolar nebula MWC 349 (White & Becker 1985). The high brightness temperature of circumstellar maser emission made it an ideal target for interferometric observations, and circumstellar OH and H_2O maser emission has been observed towards many evolved stars with the VLA, the Multi Element Radio-linked Interferometer Network[6] (MERLIN) and the Australia Telescope Compact Array[7] (ATCA) (e.g. Norris et al. 1982; Johnston et al. 1985; Chapman & Cohen 1986; Bowers & Johnston 1990; Chapman et al. 1994). Reid & Menten (1997) also developed a novel technique of imaging radio photospheres of stars using the intense circumstellar H_2O masers as phase reference sources to detect the weaker stellar continuum emission.

[4] www.keckobservatory.org
[5] www.vla.nrao.edu
[6] www.merlin.ac.uk
[7] www.narrabri.atnf.csiro.au

Millimetre-wavelength molecular spectral line observations provide a further means to image circumstellar matter. The Hat Creek Millimeter-Wave Interferometer[8] (Welch et al. 1977), the IRAM interferometer[9], and the ATCA have imaged a number of molecular emission lines towards AGB stars, which have been used to investigate the chemistry and morphology of the circumstellar envelopes (e.g. Bieging et al. 1984; Dayal & Bieging 1995; Lucas & Guélin 1999; Lindqvist et al. 1999; Wong et al. 2004; Bieging 2006). Molecular lines have also been interferometrically imaged in planetary nebulae and protoplanetary nebulae and used to study the morphology and development of these objects (e.g. Jackson & Nguyen 1988; Bieging et al. 1991).

In order to increase the angular resolution of radio interferometers, the technique of Very Long Baseline Interferometry (VLBI) was developed. In connected-element interferometers, the antennas are physically connected by waveguides, optical fibres or other means, and the signals detected at each antenna are correlated in real-time. In VLBI arrays, the antennas are spaced hundreds or thousands of kilometres apart. In order to correlate the signals from such widely spaced antennas, each antenna is equipped with an independant local oscillator, and data are recorded for off-line correlation (Kellermann & Moran 2001), or near realtime correlation is performed over a wide area network (WAN) if possible (Szomoru et al. 2006). The development of VLBI is recounted by Moran (1998) and an overview of the technique and its applications is given in Middelberg & Bach (2008).

Early VLBI experiments also targeted circumstellar maser emission, from the molecules OH (e.g. Reid et al. 1977; Reid & Muhleman 1978), H_2O (e.g. Moran et al. 1977) and SiO (e.g. Moran et al. 1979; Lane 1982; McIntosh et al. 1989). VLBI observations of maser emission provide a unique high resolution probe of late-type, evolved stellar envelopes. Very Large Baseline Array (VLBA, Napier 1995) observations of SiO maser emission around late-type, evolved stars show the emission to be located only a few stellar radii from the star (e.g. Diamond et al. 1994), where it can be used to trace the kinematics of the circumstellar envelope (Gonidakis et al. 2010). VLBA obserations of H_2O maser proper motion have also been used to investigate the kinematics of circumstellar envelopes (e.g Marvel 1996), and VLBA observations of H_2O maser emission led to the observational discovery of water fountain sources, AGB objects with high-velocity collimated jets (e.g. Imai et al. 2002).

VLBI observations of the linear and circular polarisation of circumstellar maser emission have been used to derive estimates of the magnetic field strength and orientation in the circumstellar envelope (e.g. Reid et al. 1979; Kemball & Diamond 1993, 1997; Vlemmings et al. 2001, 2002). The observed polarisation of OH, H_2O and SiO maser emission imply a possible power law relation between magnetic field strength and distance from the stellar surface (Reid et al. 1979; Reid & Moran 1981; Vlemmings et al. 2002).

This thesis describes full-polarisation VLBA observations of SiO masers towards the supergiant star VY CMa, a high luminosity SiO maser source. In order to perform the observational tests of the SiO maser polarisation models described in Chapter 3, the polarisation of the 43 GHz and 86 GHz maser emission must be compared at component-level. This requires the high angular resolution implicit in VLBI observations, as well as accurate calibration of the circular polarisation.

The 86 GHz band is the highest frequency band available at the VLBA, and the performance of the array deteriorates at these high frequencies, consistent with array design specifications (Romney 2010). Routine calibration methods are not sufficiently accurate for the high quality polarisation

[8] www.mmarray.org

[9] www.iram-institute.org/EN/plateau-de-bure.php

measurements required by the scientific goals of this thesis, so a number of new reduction techniques were developed and applied in order to provide high-accuracy polarisation calibration to account for the low signal-to-noise ratio (SNR) of the 86 GHz data.

This chapter outlines the theory of spectral line polarimetric VLBI, with particular emphasis on calibration techniques. This precedes the practical details of the data reduction given in Chapter 5. A similar theoretical background was included in a previous VLBI study of SiO masers towards VY CMa by Richter (2005).

4.1 Radio interferometry

The theory and techniques of radio interferometry are covered in detail in "Interferometry and Synthesis in Radio Astronomy", by Thompson et al. (2001), and in the proceedings of the NRAO synthesis imaging summer schools (e.g. Perley et al. 1989; Zensus et al. 1995).

Radio interferometer arrays consist of multiple radio antennas, considered here to observe and track the same source at the same time. The signals received by the antennas are correlated for all permutations of antenna pairs, to yield the complex visibility as a function of baseline. Each pair of antennas in the array can be treated as a single two-element interferometer.

Consider two identical radio antennas simultaneously observing a monochromatic signal from a cosmic source. The electric field $\mathcal{E}(t)$ from the source passes through the Earth's atmosphere, is detected at each antenna and passes through the receiver systems, as a voltage signal $V(t)$. The voltage signals from the two antennas are cross-correlated by a correlator to yield a correlator output function $r_{mn} =< V_m(t)V_n(t)^* >$ for antennas (m, n) (Swenson & Mathur 1968), where the angular brackets denote a time average. The position vector between antennas m and n is the interferometer baseline.

Assuming that the source radiation is completely incoherent, quasi-monochromatic, spatially compact and in the far-field, the correlator output is related to the mutual coherence function of the incident electric field $\widehat{\Gamma}$, after Swenson & Mathur (1968)

$$r(u, \nu_0) = \int_{-\infty}^{\infty} \widehat{P}(l, u, \Delta\nu)\, \widehat{\Gamma}(l, \nu_0)\, e^{j2\pi lu} dl \tag{4.1}$$

where the correlator output is a function of frequency ν_0 and the baseline vector u, in units of wavelengths and projected onto the plane orthogonal to the source centre direction. The mutual coherence function reduces to the brightness distribution $< \mathcal{E}\,\mathcal{E}^* >$ of the source under certain conditions, and is a function of the direction cosine l in this one-dimensional formulation (Swenson & Mathur 1968). Equation 4.1 is equivalent to the result of the more general van Cittert-Zernike Theorem (Born & Wolf 1999, pg. 547).

The function $\widehat{P}(l, u, \Delta\nu)$ includes the effects of the bandwidth pattern, the antenna pattern and the interference pattern (Swenson & Mathur 1968), and it can also be considered to include propagation effects corrupting the electromagnetic radiation from the source.

Equation 4.1 can be extended to the two-dimensional case by expressing the baseline vectors in (u, v) components in the plane orthogonal to the direction towards the source. The correlator output then takes the form $r(u, v, \nu_0)$, and the two-dimensional source brightness distribution is expressed as

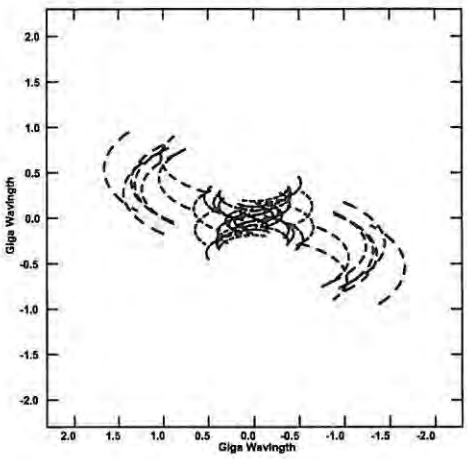

Figure 4.1: Typical (u, v) coverage of a data set used in this thesis, for a VLBA observation of the source VY CMa. The axes are baseline length, in units of wavelength, in the plane orthogonal to the source direction.

a function of two direction cosines, $\widehat{\Gamma}(l, m, \nu_0)$ (Thompson et al. 2001, pg. 71-73, 597). The coordinates l and m are direction cosines measured with respect to the u and v axes respectively. The coordinates (u, v) are measured in the east and north directions respectively, with u increasing in the direction of east on the plane of the sky (Thompson 1989; Thompson et al. 2001, pg. 70). The parameters (u, v) can equivalently be considered as spatial frequencies, and the correlator output as a spatial frequency spectrum of the brightness distribution (Swenson & Mathur 1968). We do not consider wide-field imaging in this thesis, and therefore neglect the visibility coordinate along the w-axis (Cornwell et al. 2005).

For spectroscopic observations the correlator output is measured as a function of frequency as well as (u, v) coordinates. The correlator used at the VLBA is an FX correlator, where the time domain antenna signals are Fourier transformed into the frequency domain before cross-multiplication, channel by channel, in antenna pairs, to provide correlator output in the form of cross-power spectra $r(u, v, \nu)$ (D'Addario 1989; Thompson et al. 2001, pg. 290).

Equation 4.1 can be inverted to produce an image of the intensity distribution of the source. In order to do this the $\widehat{P}(l, u, \Delta\nu)$ term must be removed from the data. For the VLBI observations performed in this thesis the imaged field of view is small compared to the width of the individual antenna patterns and $\Delta\nu \ll \nu_0$, which reduce the beamwidth and antenna pattern components of $\widehat{P}$ to scalar quantities. The interference pattern is removed from further consideration through the addition of an instrumental delay into the signal path, which corrects for the geometric delay between arrival times of the source radiation at different antennas (Swenson & Mathur 1968). The effect on the signal of propagation through the atmosphere and telescope can be removed in software after correlation, through a calibration process, later described.

The mathematical framework used to describe the propagation of the electromagnetic wave is described in the next section. This is followed in Section 4.3 by the specific propagation effects encountered by an electromagnetic wave observed by an array of radio telescopes, and a description

of the calibration techniques required to remove the propagation effects in Section 4.4.

After calibration, under the approximations described above, Equation 4.1 reduces to a Fourier transform which can be inverted to find the sky-plane intensity distribution of the source. For VLBI arrays the observed visibilities sparsely sample the (u,v) plane. This is shown in Figure 4.1, which depicts a typical example of the (u,v) coverage for a VLBA data set used in this thesis. The sparse sampling leads to image artifacts on inversion, which are corrected for through deconvolution techniques. The imaging of the calibrated data is discussed in Section 4.5.

4.2 Radio interferometric polarimetry

The VLBI observations performed in this thesis were made in full-polarisation mode, where the antennas in the array have dual-polarisation receptors that detect two nominally orthogonal components of the electric field vector and the correlation is performed for all polarisation pairs. Full polarisation correlation is necessary in order to allow inversion of the source brightness distribution in full Stokes parameters $\{I,Q,U,V\}$.

The propagation of the polarised source electric field vector through the atmosphere and telescope optics and instrumentation can be described by a series of Jones matrices (Jones 1941). Hamaker et al. made use of Jones matrices to develop a matrix formalism of radio interferometry (Hamaker et al. 1996; Sault et al. 1996; Hamaker & Bregman 1996; Hamaker 2000, 2006). The matrix formalism is particularly efficient and concise for polarimetric interferometry and will be used in this chapter.

The electric field can be described by a two-component vector

$$\mathcal{E} = \begin{pmatrix} \mathcal{E}^R \\ \mathcal{E}^L \end{pmatrix}$$

where R and L represent the right and left circular polarised components. The VLBA antennas have left- and right-circularly polarised receptors, so left and right circular polarisation bases are used throughout this chapter, and the Hamaker et al. (1996) formalism adapted accordingly. Symbols used in all references were also modified as needed to provide consistent, uniform notation throughout this chapter.

The propagation of the electric field through the Earth's atmosphere, the antenna and the receiver system modifies the field. The propagation and instrumental effects can be described by a net 2x2 Jones matrix, $\mathbb{J}_m$ for antenna m, including the conversion from electric field to voltage

$$V_m = \mathbb{J}_m \, \mathcal{E}_m$$

The full-polarisation correlation of two such voltage signals V_m and V_n from antenna pair (m,n) can be expressed as a correlator output vector r_{mn}. The correlation of the electric field pairs can also be expressed as a vector, denoted S_{mn}. These two vectors take the form (Hamaker et al. 1996)

$$r_{mn} = \begin{pmatrix} < V_m^R V_n^{R*} > \\ < V_m^R V_n^{L*} > \\ < V_m^L V_n^{R*} > \\ < V_m^L V_n^{L*} > \end{pmatrix} \qquad S_{mn} = \begin{pmatrix} < \mathcal{E}_m^R \mathcal{E}_n^{R*} > \\ < \mathcal{E}_m^R \mathcal{E}_n^{L*} > \\ < \mathcal{E}_m^L \mathcal{E}_n^{R*} > \\ < \mathcal{E}_m^L \mathcal{E}_n^{L*} > \end{pmatrix}$$

The correlator output is related to the correlation vector by the outer product $\otimes$ of the Jones matrices describing the propagation and instrumental effects at each antenna on the baseline (m, n)

$$r_{mn} = (\mathbb{J}_m \otimes \mathbb{J}_n^*)\, S_{mn} \tag{4.2}$$

where the $*$ denotes complex conjugation (Hamaker et al. 1996). To form the outer product of two matrices $A \otimes B$, each element a_{ij} of matrix A is replaced by the product of that element and the full matrix B, to give $a_{ij}B$. An example of the outer product of two 2×2 matrices (Hamaker et al. 1996) is

$$\begin{pmatrix} a_{11} & a_{12} \\ a_{21} & a_{22} \end{pmatrix} \otimes \begin{pmatrix} b_{11} & b_{12} \\ b_{21} & b_{22} \end{pmatrix} = \begin{pmatrix} a_{11}B & a_{12}B \\ a_{21}B & a_{22}B \end{pmatrix} = \begin{pmatrix} a_{11}b_{11} & a_{11}b_{12} & a_{12}b_{11} & a_{12}b_{12} \\ a_{11}b_{21} & a_{11}b_{22} & a_{12}b_{21} & a_{12}b_{22} \\ a_{21}b_{11} & a_{21}b_{12} & a_{22}b_{11} & a_{22}b_{12} \\ a_{21}b_{21} & a_{21}b_{22} & a_{22}b_{21} & a_{22}b_{22} \end{pmatrix}$$

The net Jones matrix $\mathbb{J}$ includes many individual modifications to the electric vector, which are separable into individual Jones matrices. Due to the properties of the outer product, the action of multiple Jones matrices on the signal reduces to a series of matrix multiplications (Hamaker et al. 1996)

$$(\mathbb{J}_m^1 \mathbb{J}_m^2) \otimes (\mathbb{J}_m^{1*} \mathbb{J}_m^{2*}) = (\mathbb{J}_m^1 \otimes \mathbb{J}_n^{1*})\, (\mathbb{J}_m^2 \otimes \mathbb{J}_n^{2*})$$

The description of the signal passage in terms of individual Jones matrices is provided in more detail in the following section, Section 4.3.

The polarisation of an electromagnetic wave can be described by the Stokes parameters, as discussed in Section 3.4.2, and defined after Cohen (1958) in Equation 3.8 of the previous chapter

$$\begin{aligned} I &\equiv <(\mathcal{E}^R)^2> + <(\mathcal{E}^L)^2> \\ Q &\equiv <2\,\mathcal{E}^R\mathcal{E}^L> \cos\Delta\phi \\ U &\equiv <2\,\mathcal{E}^R\mathcal{E}^L> \sin\Delta\phi \\ V &\equiv <(\mathcal{E}^R)^2> - <(\mathcal{E}^L)^2> \end{aligned}$$

Each of the Stokes parameters I, Q, U, and V has a visibility counterpart $\mathcal{I}$, $\mathcal{Q}$, $\mathcal{U}$ and $\mathcal{V}$, given by the Fourier transform of the corresponding image-plane Stokes parameter in the narrow-field, quasi-monochromatic limit considered here. In matrix formalism, the visibility Stokes parameters described by Conway & Kronberg (1969) are related to the electric field coherence S_{mn} as follows

$$S_{mn} = \begin{pmatrix} <\mathcal{E}_m^R \mathcal{E}_n^{R*}> \\ <\mathcal{E}_m^R \mathcal{E}_n^{L*}> \\ <\mathcal{E}_m^L \mathcal{E}_n^{R*}> \\ <\mathcal{E}_m^L \mathcal{E}_n^{L*}> \end{pmatrix} = \begin{pmatrix} 1 & 0 & 0 & 1 \\ 0 & 1 & j & 0 \\ 0 & 1 & -j & 0 \\ 1 & 0 & 0 & -1 \end{pmatrix} \begin{pmatrix} \mathcal{I} \\ \mathcal{Q} \\ \mathcal{U} \\ \mathcal{V} \end{pmatrix} \tag{4.3}$$

The true Stokes visibility parameters can be derived from the measured correlator output by calibration, and inverted to solve for the source brightness distribution in full Stokes $\{I, Q, U, V\}$.

4.3 Propagation of a polarised signal

As noted above, electromagnetic waves emitted from a cosmic source are modified by a number of elements along the path of the wave, before their reception at the antenna and during their passage through the antenna and receiver system. This section provides a mathematical description of the changes to the original correlation vector at it propagates, following the matrix formalism described in the preceeding section. The wave path is considered from the electric vector's point of entry to the Earth's atmosphere through to the correlator. Each operation on the wave is described by a Jones matrix, and the matrices are sequentially combined to describe the overall effect on the wave. The Jones matrices are labelled following Hamaker et al. (1996) and Ott et al. (2010). The general format for the Jones matrices is given in Hamaker et al. (1996) and Thompson et al. (2001, pg. 110).

The radio wave detected at each individual antenna has passed through the neutral atmosphere and the ionosphere. For VLBI arrays the conditions in the atmosphere may vary considerably between antennas. At millimetre wavelengths, the dominant effect of the neutral atmosphere is in the troposphere, where water vapour and the other dry constituents can attenuate the signal and introduce phase fluctuations. At lower frequencies, the ionised plasma of the ionosphere can introduce a phase offset between the left circularly polarised (LCP) and right circularly polarised (RCP) components of the signal, causing ionospheric Faraday rotation of the electric field vector (Thompson et al. 2001, pg. 507-108, 554-555). The Jones matrices for phase transmission through the troposphere and ionosphere are denoted respectively as $\mathbb{T}$ and $\mathbb{F}$

$$\mathbb{T} = \begin{pmatrix} Te^{j\epsilon} & 0 \\ 0 & Te^{j\epsilon} \end{pmatrix} \qquad \mathbb{F} = \begin{pmatrix} e^{j\gamma^R} & 0 \\ 0 & e^{j\gamma^L} \end{pmatrix}$$

For antennas with altitude-azimuth mount geometries, such as the VLBA, the orientation of the antenna feed with respect to the source rotates during the course of the observations. This rotation can be described by the parallactic angle α, the angle between the great circle through the source position and zenith and the great circle between the source position and the north celestial pole (Thompson et al. 2001, pg. 88). The Jones matrix describing the parallactic angle rotation is given by $\mathbb{P}$

$$\mathbb{P} = \begin{pmatrix} e^{-j\alpha} & 0 \\ 0 & e^{j\alpha} \end{pmatrix}$$

At each radio antenna the electromagnetic wave from the source is detected with imperfectly-polarised receptors. The dual-polarisation receptors should receive nominally only one sense of polarisation from the incident field, but in practice each receptor receives some fraction of electromagnetic radiation from the orthogonal polarisation. This receptor characteristic is termed instrumental polarisation, because it will cause an unpolarised source to appear polarised (Morris et al. 1964). Instrumental polarisation is discussed by Morris et al. (1964) and Conway & Kronberg (1969).

Instrumental polarisation at each antenna can be modeled by two leakage terms, by convention called D-terms, which are complex numbers describing the response of each receptor to its orthogonal polarisation (Conway & Kronberg 1969). For narrow-band observations the D-terms can be assumed to be independent of time, frequency and direction in VLBI observations (Kemball et al. 1995). They are also assumed to be small ($||D|| \leq 0.1$). The D-terms are typically approximately 3% in magnitude

for VLBA antennas (Romney 2010). The instrumental response Jones matrix $\mathbb{D}$ can accordingly be written as

$$\mathbb{D} = \begin{pmatrix} 1 & D^R \\ D^L & 1 \end{pmatrix}$$

After detection at the receptor, the signal passes through the receiver system and is amplified and mixed with a local oscillator signal to shift it to an intermediate frequency. In connected-element interferometers each signal is then correlated with signals from the other antennas in real-time. For VLBI observations the signal is recorded on storage media for later off-line correlation at a central location, or correlated in near real-time over a WAN. During correlation, the differential geometric delays at each antenna are compensated for by adding offset delays and corresponding phase shifts to the signals (Thompson et al. 2004, pg. 169, 174).

The modifications to the signal within the receiver system and correlator can be represented by a time-variable net complex gain $G = ge^{j\phi}$ and a normalised frequency-dependent complex bandpass response $B = be^{j\beta}$. The Jones matrices for the gains and bandpasses are given by $\mathbb{B}$ and $\mathbb{G}$

$$\mathbb{B} = \begin{pmatrix} B^R & 0 \\ 0 & B^L \end{pmatrix} \qquad \mathbb{G} = \begin{pmatrix} G^R & 0 \\ 0 & G^L \end{pmatrix}$$

These various propagation effects can then be combined as a series of Jones matrices

$$\begin{aligned} V_m &= \mathbb{J}_m \, \mathcal{E}_m \\ V_m &= \mathbb{G}_m \, \mathbb{B}_m \, \mathbb{D}_m \, \mathbb{P}_m \, \mathbb{T}_m \, \mathbb{F}_m \, \mathcal{E}_m \end{aligned}$$

for antenna m. When two such voltage signals from antennas (m, n) are correlated, the correlator product is related to the correlation vector as follows (Hamaker et al. 1996)

$$r_{mn} = (\mathbb{G}_m \otimes \mathbb{G}_n^*) \, (\mathbb{B}_m \otimes \mathbb{B}_n^*) \, (\mathbb{D}_m \otimes \mathbb{D}_n^*) \, (\mathbb{P}_m \otimes \mathbb{P}_n^*) \, (\mathbb{T}_m \otimes \mathbb{T}_n^*) \, (\mathbb{F}_m \otimes \mathbb{F}_n^*) \, S_{mn} \tag{4.4}$$

When the D-terms are small, this system of equations can be linearised by neglecting terms of order $\mathrm{O}(D.\mathcal{RL})$, $\mathrm{O}(D.\mathcal{LR})$ and $\mathrm{O}(D^2)$ (Conway & Kronberg 1969).

In the correlator output data, the atmospheric effects described by $\mathbb{T}$ and $\mathbb{F}$ are mathematically degenerate with the gain in $\mathbb{G}$. During the calibration process the gain $\mathbb{G}$ is therefore considered to include the atmospheric effects. Only the Faraday rotation terms of the the form $e^{j(\gamma^R - \gamma^L)}$ cannot be absorbed into the gain. However, Faraday rotation scales as ν^{-2} (Thompson et al. 2001, pg. 555), so these terms can be disregarded at the high frequencies of the observations performed in this thesis.

4.4 Calibration

Calibration is the process of extracting the true electric vector spatial coherence from the correlator output. The techniques required to calibrate full-polarisation VLBI data were pioneered by Cotton et al. (1984) and Roberts et al. (1984). The extension of full-polarisation VLBI to spectral line observations was first reported by Garcia-Barreto et al. (1988), for main-line OH maser emission.

Another early experiment in VLBI spectral line polarimetry is described by Kemball (1992), for observations of OH masers towards IRC 10420. The techniques used to calibrate VLBI spectral line polarisation data are laid out in papers by Kemball et al. (1995) and Leppanen et al. (1995).

Following the formalism presented earlier, calibration entails solving for the antenna-based gains, bandpass responses and instrumental polarisation. The time-variable complex gain factor G_m^p can be decomposed into amplitude and phase components $G_m^p = g_m^p \, e^{j\phi_m^p}$, as can the frequency-dependent complex bandpass $B_m^p = b_m^p \, e^{j\beta_m^p}$. The calibration can be classified into four major steps, based on the term being solved for,

- The complex, frequency dependent, bandpass response B_m^p.
- The amplitude component of the complex gain g_m^p.
- The phase component of the complex gain ϕ_m^p.
- The complex instrumental polarisation D-terms.

Each of the calibration parameters must be solved for at each antenna and in each sense of nominal receptor polarisation $\{R, L\}$. The calibration techniques used to solve for the parameters are described in the following sections and summarised in Figure 4.2. Both the autocorrelation data of the individual antennas r_{mm} and the cross-correlation visibility data r_{mn} are utilised in the calibration process, as shown in Figure 4.2.

During calibration, phases solutions are determined for the phase components of both the complex gain G_m^p and the complex bandpass response B_m^p. The latter bandpass phase response is traditionally constrained to have zero-mean phase over frequency. Whenever the phase is solved for from cross-correlation data, the solutions are determined relative to a reference antenna at which the phase is set to zero. This is necessary because the antenna-based phase gains are derived from baseline-based data, which only contain phase differences between pairs of antennas (Cornwell & Wilkinson 1981).

A number of the calibration steps are performed using continuum calibrator data. For connected-element interferometers at centimetre wavelengths, the gains derived from a nearby unresolved calibrator can usually be applied directly to the source data. However, most of the calibrators used for connected element interferometry are resolved by VLBI arrays. There are also fewer calibrators at the higher frequencies observed in this thesis due to SNR limitations. The continuum calibrators observed along with the SiO maser source will therefore infrequently meet the criteria for direct phase referencing (Moran & Dhawan 1995). For this reason some steps in the calibration that are traditionally performed on continuum calibrators for connected-element arrays are instead performed in self-calibration mode on the target source for VLBI maser observations.

Every antenna in a VLBI array typically observes the source and calibrators with the same fixed topocentric frequency configuration. Because the antennas are located hundreds or thousands of kilometres apart, their instanteneous velocities along the line of sight to the source will differ due to the varying Doppler shift relative to the LSR at each location. The residual Doppler shifts are small but will cause the spectral line to move slightly in the observing band (Reid et al. 1980). The Doppler shift due to the rotation of the Earth is removed by the correlator at the VLBA, but further velocity shift corrections for the orbital motion of the Earth and its motion relative to the LSR must be performed in post-processing (Thompson et al. 2001, pg. 408).

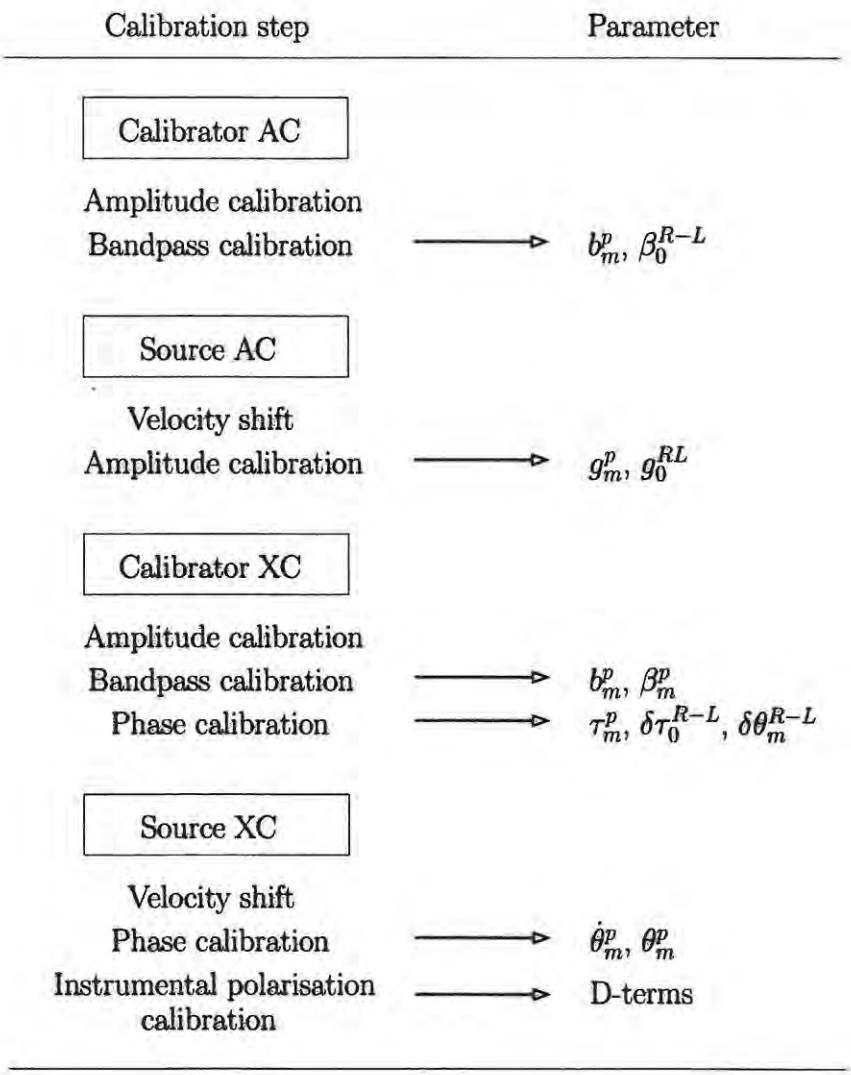

Figure 4.2: Chart of the calibration steps. The steps are laid out in order of calibration sequence from top to bottom in the left column, headed by the data set used to solve for the parameters (starting with the calibrator autocorrelation data). The right column gives the calibration parameter solved for in each step. The paramters not yet defined in the text are defined in Sections 4.4.1, 4.4.2, 4.4.3 and 4.4.4 on bandpass calibration, amplitude calibration, phase calibration and instrumental polarisation calibration respectively. The parameters are ultimately all applied collectively to the source correlator output vector to give the true correlation vector.

4.4.1 Bandpass calibration

The correlator output is a function of frequency, which includes the frequency-dependent response of the passband of the net antenna receiving systems. A complex bandpass response must therefore be determined and removed from the data, for each antenna and each sense of polarisation. The bandpass responses can be determined using observations of flat-spectrum continuum calibrators.

The full complex bandpass response B_m^p can be determined from the cross-correlation calibrator data, by performing a channel-by-channel χ^2 fit to the parallel-hand continuum calibrator data as follows

$$\chi^2 = \sum_{m=1}^{N_a} \sum_{n=m+1}^{N_a} \sum_{l=1}^{N_c} ||r_{mn}^{pp}(\nu_l) - B_m^p(\nu_l) B_n^{p*}(\nu_l)|| \tag{4.5}$$

where N_a is the number of antennas, N_c is the number of channels, and $r_{mn}^{pp}(\nu_l)$ is the calibrator correlator output function for antenna pair (m, n) and polarisation p, at channel frequency ν_l. The rates of change of the phase with frequency and with time must be determined and removed before this fit for the bandpass can be performed (Reid et al. 1980; Diamond et al. 1994; Kemball et al. 1995).

As mentioned above, the phase component of the bandpass solution is solved for relative to a reference antenna, for which the phase is set to zero. This leaves an unknown frequency dependent phase offset between the right and left circularly polarised systems, introduced by the unknown phase offset $\beta_0^{R-L}(\omega)$ between the right and left bandpass phase at the reference antenna. The offset can be solved using a similar χ^2 fit to Equation 4.5, instead using the cross-hand autocorrelation data r_{mn}^{pq}, and solving for the phase component only, as described in Kemball & Richter (2011).

In order to improve the SNR of the amplitude component of the complex bandpass solutions, the amplitude components b_m^p can be determined directly from the averaged calibrator autocorrelation data. In this case, the phase component β_m^p of the bandpass must be separately determined from the cross-correlation data, using a similar minimisation as Equation 4.5, but with the amplitude component fixed (Kemball & Diamond 1997). A polynomial or non-polynomial representation of B_m^p can be used in this method. Solving for the complex bandpass response in separate amplitude and phase components is preferable for high frequency observations, as the higher SNR autocorrelation data provide higher-SNR estimates of the bandpass amplitude.

In order to accurately reconstruct a band-limited signal, the signal must be sampled at the Nyquist rate $2\nu_n$, where ν_n is the cutoff frequency of the signal bandwith, centred on zero (Bracewell 1986, pg. 191-194). Although the VLBA observations in this thesis were sampled at the Nyquist rate, the bandpasses unavoidably have tails extending past ν_n (Walker 1995). In this situation aliasing will occur, with the roll-off at frequencies $> 2\nu_n$ folding back into the sampled spectra.

For cross-correlation data, the affect of aliasing will be reduced during correlator fringe rotation. Iguchi (2000) showed that noise due to aliasing is reduced to less than $\frac{1}{2\pi\nu_f T_c}$, where ν_f is the fringe frequency of the observation and T_c is the integration time. The smallest reduction will be for the shortest baseline, which will have the lowest fringe frequency. For the VLBA this is between the Pie Town antenna and a VLA antenna, if a VLA antenna is included in the observation, with a fringe frequency of $\nu_f \sim$ 400Hz for 43 GHz observations, and higher for 86 GHz. For an integration time of several seconds, this gives an amplitude reduction of more than -36 dB for the folded component. For longer baselines and higher frequencies the amplitude reduction is more pronounced.

The effect of aliasing is therefore not expected to be significant in the cross-correlation data,

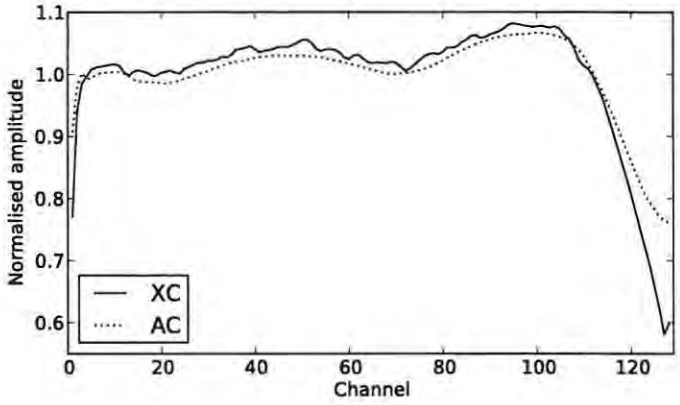

Figure 4.3: Autocorrelation (AC) and cross-correlation (XC) bandpass solutions for antenna Kitt Peak, at 43 GHz. The effect of aliasing can be seen in the autocorrelation bandpass, above channel ~ 118.

but it is seen in the autocorrelation data. Iguchi et al. (2000) confirmed this experimentally using modified filters with VSOP observations of 3C273. Figure 4.3 shows an example of cross-correlation and autocorrelation bandpasses, derived from data in this current thesis, where the effect of aliasing is seen at the high frequency end of the autocorrelation bandpass.

If the amplitude components of the bandpasses are solved for from the auto-correlation data, then the bandpasses must be corrected for aliasing. Although the folded spectrum only increases the amplitude of the upper $\sim$ 10 channels in a 128-channel VLBA spectrum, this increases the overall noise power in the spectrum and results in an overall amplitude offset across the whole spectrum when the spectra are normalised.

The amplitude components of the bandpasses can be corrected by using the bandpass amplitudes solved for separately from the cross-correlation and autocorrelation data, b^p_{XC} and b^p_{AC}, and then minimising

$$\chi^2 = \frac{1}{(N_c - N_0)} \sum_{l=N_0}^{N_c} \left[b^p_{XC}(l)^2 - f(l)^2\right]^2 + \left[b^p_{AC}(l)^2 - b^p_{XC}(l)^2 - f(2N_c - l)^2\right]^2 \tag{4.6}$$

where the sum is performed over a channel range $l \in (N_0, N_c)$ spanning the upper $\sim 20\%$ of the total channel range N_c, and the function $f(l)$ is an n-pole Butterworth function

$$f(l) = \frac{a}{\sqrt{1 + (l/l_b)^{2n}}} \tag{4.7}$$

where the cutoff frequency l_b, in units of channel number, and the scaling factor a, are free parameters in the minimisation (Kemball & Richter 2011).

The autocorrelation amplitude bandpass responses are then corrected with the folded Butterworth function and used in a fit for the phase component, minimising Equation 4.5. The final complex bandpass responses are normalised and used to correct the cross-correlation and autocorrelation correlator

output spectra of the source as follows (Reid et al. 1980; Kemball et al. 1995).

$$r^{pq'}_{mn}(\nu) = \frac{r^{pq}_{mn}(\nu)}{B^{p}_{m}(\nu)B^{q*}_{n}(\nu)}$$

$$r^{pp'}_{mm}(\nu) = \frac{r^{pp}_{mm}(\nu)}{b^{p}_{m}(\nu)^2}$$

4.4.2 Amplitude calibration

The task of amplitude calibration is to convert the uncalibrated normalised correlator output data into scaled units of correlated flux density (in Jy) by multiplying by the amplitude gain factors g^{p}_{m}.

This is accomplished by multiplying the correlator output data by the geometric mean of the system equivalent flux densities (SEFD) of the corresponding antenna pair involved. The amplitude gain applied to the correlator output data for antenna pair (m, n) and polarisations (p, q) is given by

$$g^{p}_{m}\, g^{q}_{n} = \eta_b \sqrt{\mathrm{SEFD}^{p}_{m}\ \mathrm{SEFD}^{q}_{n}}$$

where digitisation and sampling losses are included in the factor η_b (Reid 1995).

The SEFD for a particular antenna and receiving system is the product of the effective system temperature T_{sys} and the point source sensitivity PSS of the antenna, SEFD $= T_{sys} \times$ PSS (Reid 1995). The change in point source sensitivity with elevation angle is given by the gain curve of an antenna. The gain curve parameters are measured *a priori* for each antenna and receiver system, corrected for zero atmospheric opacity, and are used to calculate the point source sensitivity from the zenith angle over the course of the observation (Moran & Dhawan 1995). The system temperature T_{sys} is measured at the VLBA using a switched noise signal (Thompson 1995).

For observations of strong spectral line sources, the amplitude calibration can alternatively be performed using the autocorrelation data (Reid et al. 1980). The data model for the autocorrelation data follows Equation 4.4 above, for antenna m alone

$$r_{mm} = (\mathbb{G}_m \otimes \mathbb{G}^{*}_{m})\ (\mathbb{B}_m \otimes \mathbb{B}^{*}_{m})\ (\mathbb{D}_m \otimes \mathbb{D}^{*}_{m})\ (\mathbb{P}_m \otimes \mathbb{P}^{*}_{m})\ S_{mm} \tag{4.8}$$

where the tropospheric and ionospheric terms $\mathbb{T}$ and $\mathbb{F}$ have been subsumed into the gain $\mathbb{G}$, and the electric field correlation vector S_{mm} now includes a correlated self-noise term in the parallel-hand components

$$S_{mm} = \begin{pmatrix} < \mathcal{E}^{R}_{m}\mathcal{E}^{R*}_{m} > & + & \mathcal{N}^{R}_{m} \\ < \mathcal{E}^{R}_{m}\mathcal{E}^{L*}_{m} > & & \\ < \mathcal{E}^{L}_{m}\mathcal{E}^{R*}_{m} > & & \\ < \mathcal{E}^{L}_{m}\mathcal{E}^{L*}_{m} > & + & \mathcal{N}^{L}_{m} \end{pmatrix}$$

where the self-noise term is the product of the noise temperature and the point source sensitivity, $\mathcal{N}^{p}_{m} = T^{p}_{N}\ \mathrm{PSS}^{p}_{m}$, for $p \in \{R, L\}$ (Kemball & Richter 2011).

When the D-terms are small, second order terms in the linear polarisation and D-terms can be neglected (Conway & Kronberg 1969), as discussed above, and the bandpass corrected parallel-hand

components of Equation 4.8 reduce to

$$r_{mm}^{RR} = (g_m^R)^2 \, (< \mathcal{E}_m^R \mathcal{E}_m^{R*} > + \mathcal{N}_m^R) \tag{4.9}$$

$$r_{mm}^{LL} = (g_m^L)^2 \, (< \mathcal{E}_m^L \mathcal{E}_m^{L*} > + \mathcal{N}_m^L) \tag{4.10}$$

The time-dependent amplitude gain factors can then be determined by fitting each autocorrelation spectrum r_{mm} to a calibrated template spectrum selected from the data for its high SNR. The fit yields a single multiplicative quality factor (or amplitude gain) for each antenna and solution interval used for the fit, which scales each of the spectra to fit the template spectrum. This spectral line amplitude calibration method is termed template fitting, and was developed by Reid et al. (1980) for use with maser data. The quality factor is determined by minimising

$$\chi^2 = \frac{1}{N_c} \sum_{l=1}^{N_c} \left[\, r_{mm}^{pp}(\nu) - (g_m^p)^2 \, r^p(\nu) \; - b'(\nu) \, \right]^2$$

where $r_{mm}^{pp}(\nu)$ is the autocorrelation spectrum for antenna m and polarisation p, averaged over a specified time interval, $r^p(\nu)$ is the calibrated template spectrum, and a baseline term b' is included in the fit to account for the self-noise and residual errors in the bandpass removal (Kemball et al. 1995). The amplitude gains solved for with the template fitting method will include corrections for system temperature, atmospheric effects, and antenna gain variation, caused for example by pointing offsets (Reid 1995).

For full-polarisation observations, the template-fitting method fits all of the r^{RR} spectra to the RR component of the template spectrum $r^R(\nu)$, and the r^{LL} spectra to the LL component of the template spectrum $r^L(\nu)$. This results in an unknown R/L amplitude offset, g_0^{RL}, introduced by the unknown absolute calibration of the r^L template spectrum relative to the r^R template spectrum (Kemball et al. 1995). There are several ways to solve for g_0^{RL}, using either the source data itself or a continuum calibrator source assumed to have negligible circular polarisation. Possible methods include:

- **A differential polarisation R/L template-fit.** The r^R template spectrum is fitted to the r^L template spectrum, applying the same Reid et al. (1980) template fitting technique described above. The offset between the r^L and r^R template spectra gives the R/L amplitude offset g_0^{RL}. This method assumes that the Stokes V integrated over the source is small, which is a reasonable assumption for the VY CMa SiO maser data observed. Kemball & Diamond (1997) used this method to find g_0^{RL} for VLBA observations of SiO masers.

- **Amplitude self-calibration of a continuum calibrator source.** Self-calibration is a technique used to solve for the gain factor G_m^p and the source structure simultaneously by iterating between the visibility and image planes to improve the fit (Readhead et al. 1980). Self-calibration is discussed in detail in the following section on phase calibration. Amplitude self-calibration can be used to determine the residual RCP and LCP amplitude gains. The desired g_0^{RL} offset is then given by the ratio of the amplitude gain values (Kemball 1999).

- **A global continuum calibrator fit.** A global fit to all of the continuum calibrator cross-correlation data to solve for the R/L amplitude offset, assuming negligible circular polarisation for the calibrators (Kemball et al. 1995).

- **Calibrator imaging for a range of g^{RL} offsets.** Applying the source amplitude calibration solutions derived from the template-fitting method to the continuum calibrator data. The calibrator is then imaged for a range of g^{RL} offset values and a fit is performed to determine the offset which will minimise Stokes V for the continuum calibrator, g_0^{RL}.

Both the differential polarisation R/L template-fit method and the global continuum calibrator fit method were used to find the g_0^{RL} offsets for various data used in this thesis. A continuum calibrator source was also imaged for a range of g^{RL} offsets in order to assess the accuracy of the global continuum calibrator fit results. A description of the amplitude calibration method is provided in Section 5.3.3 of the following chapter. The motivation for the methods used to find the g_0^{RL} offset, and the accuracy of the methods, are discussed in Section 5.4.

4.4.3 Phase calibration

Phase errors in the correlator output arise from imperfect correlator models, incorrect baselines or source position coordinates, propagation effects through the atmosphere and ionosphere, and offsets between the station clocks at different antennas, among other reasons (Reid et al. 1980; Cotton 1995). These phase gains errors must be determined and removed from the correlator output.

For full-polarisation observations at altitude-azimuth antennas, the rotating parallactic angle must be corrected for, as a first step in the phase calibration process (Kemball et al. 1995). Thereafter, the phase gain is approximated by linear slopes in time and frequency over short time intervals. The rate of change of the phase with frequency is termed the residual group delay τ and the rate of change of the phase with time is termed the residual fringe rate $\dot{\theta}_m^p$ (Walker 1989). The phase gain at antenna m for polarisation p is approximated by a first order Taylor expansion in frequency and time in terms of the residual group delay and residual fringe rate as follows

$$\phi_m^p(\omega, t) = (\omega - \omega_0)(\tau_m^p - \tau_0^p) + (\dot{\theta}_m^p - \dot{\theta}_0^p)(t - t_0) + (\theta_m^p - \theta_0^p) \tag{4.11}$$

where θ_m^p is the residual phase and the subscript 0 denotes a reference antenna. The time t_0 is the reference time for the given solution interval, and ω_0 is the edge of the frequency band (Walker 1989; Kemball et al. 1995). The residual group delay, the residual fringe rate and the residual phase are set to zero at a chosen reference antenna.

Solving for the antenna-based phase gains from the cross-correlation data is possible because the problem is over-determined if there are three or more antennas. Over each solution interval, data from all of the baselines are used to solve for the antenna gains. An array with N antennas has $\frac{N(N-1)}{2}$ baselines. The total number of phase gains to be solved for will be 3N, for the residual group delay, the residual fringe rate and the residual phase at each of the N antennas. If these values are set to zero at a reference antenna, this leaves 3N-1 unknowns to be determined from $\frac{N(N-1)}{2}$ data points (Schwab & Cotton 1983).

Fringe fitting

Fringe fitting is the process of determining the residual delay and fringe rate values that maximise the amplitude of the averaged correlator output (Walker 1989).

Schwab & Cotton (1983) developed a global approach to fringe fitting, where each baseline-based delay or rate parameter is separated into two antenna-based components. The antenna-based phases are then solved for jointly over all of the antennas, using Equation 4.11 (Cotton 1995), after an initial baseline-based search. An additional innovation of the Schwab & Cotton (1983) algorithm was stacking the visibility data by summing over closure triangles before a preliminary baseline-based Fourier search for the delay and rate. The solutions provided by the preliminary search are used as initial parameter estimates for the global antenna-based fringe fit. This procedure offers several advantages over the earlier purely baseline-based methods of fringe fitting. Global fringe fitting forces closure of the fringe rates and delays, is more sensitive than baseline-based fringe fitting, and can incorporate baselines with low SNR into the global fit. This enables the fringe fit to be performed over shorter solution intervals, where the linearised approximation of Equation 4.11 is more appropriate (Schwab & Cotton 1983).

For spectral line sources the residual delay is best determined from a continuum calibrator source. The calibrator delays are then interpolated in time to be applied to the source data (Walker 1989).

However, the residual fringe rates for the source data cannot be determined from the calibrator (Walker 1989). For maser observations such as those performed in this thesis, the residual fringe rate values have to be determined directly from the source data. Because maser emission is extremely bright and originates in compact components, the residual rate can be determined from a single reference frequency channel (Reid et al. 1980). The reference channel is chosen by examining the maser spectra to find a channel with a strong spectral line at long and short baselines, which implies strong compact emission in that channel. Compact emission is ideal for the fit, but not a necessity as more complex structure can be corrected for in the subsequent self-calibration (Reid 1999). The fringe fit is then performed on the reference channel, which serves as a phase reference for the other channels, as described by Reid et al. (1980).

Self-calibration

The final residual phase $(\theta_m^p - \theta_0^p)$ is determined through the iterative process of self-calibration. A review of the technique can be found in Pearson & Readhead (1984).

For maser observations, the self-calibration can be performed on a single reference frequency channel, in the same way as the fringe rate solution was determined from a single channel. The phase gain solution determined from the single channel is then applied to all channels (Walker et al. 1978; Reid et al. 1980). All of the aforementioned calibration solutions must be applied to the visibility data before a self-calibration can be performed, so that the only unknown remaining term in Equation 4.11 is the frequency-independent residual phase.

The self-calibration algorithm simultaneously solves for the residual phase and the source structure, in two iterated steps. First, a least-squares fit is performed in the (u, v) plane, fitting the calibrated visibility data $r_{mn}(u, v)$ to the Fourier transform of a trial source model $\hat{r}_{mn}(u, v)$ over a series of solution intervals. The fit minimises the difference

$$\chi^2 = \sum_k \sum_{m=1}^{N_a} \sum_{n=m+1}^{N_a} w_{mn}(t_k) \left[r_{mn}(u_k, v_k, \nu_l) - g_m(t_k) g_n^*(t_k) \hat{r}_{mn}(u_k, v_k) \right]^2$$

where w_{mn} are weights, ν_l is the frequency of the reference channel and g_m and g_n are complex antenna-based residual gains to be determined from the fit. The sum is performed over all antennas m and n and over solution intervals k (Pearson & Readhead 1984; Kemball 1992). For phase self-calibration, as performed here, only $\arg(g_m)$ is solved for.

The residual gains solved with the trial model are then applied to the visibility data $r_{mn}(u,v)$. This corrected data set is imaged to produce a first iteration source map. The visibility data are deconvolved using the CLEAN algorithm, which is discussed in Section 4.5. The first iteration map is then used as the new trial source map in the second iteration (Pearson & Readhead 1984).

This procedure of iterating between the (u,v) plane and the image plane is repeated as many times as necessary. In each iteration the previous imaged map is used as a source model in solving for the residual gains in the (u,v) plane, then the resultant corrected visibility data are imaged to produce a new source map for the next iteration. As this process is repeated the solutions converge on the best estimates of the gains and source model (Pearson & Readhead 1984).

If the observed source has significant levels of circular polarisation, then the phases of the RCP and LCP data will be different. In this case independent self-calibration solutions for the phase gains of the RCP and LCP signals will lead to a positional offset between the RCP and LCP data sets (Kemball et al. 1995). In order to maintain the correct relative position information in the RCP and LCP signals, the phase solutions are determined in one sense of polarisation only, for example RCP. The phase offsets between LCP and RCP are then calculated and applied to the RCP solutions. In this way a single sense of polarisation at a single antenna is used as the overall phase reference for all of the visibility data (Kemball et al. 1995). The method used to do this is described in the following section.

Polarisation offsets

For full-polarisation observations, two orthogonally polarised signals are received by different receptors and propagate through independent receiver systems. These two receiver systems have different cable lengths, filters and receiving electronics. The two orthogonally-polarised signals will therefore be subject to different phase offsets as they pass through the two receiver systems. This will result in offsets between the residual delays and residual phases for the signals from the two polarisation systems (Kemball et al. 1995).

The polarisation fringe rate offset, on the other hand, is assumed to be negligible for stable electronic receiver systems (Cotton 1993). At each antenna the same local oscillator drives both RCP and LCP receiving systems, so residual fringe rates caused by clock errors will be the same for both systems. Fringe rate errors introduced by position errors will also be the same for both polarisations (Kemball et al. 1995). Faraday rotation is also not a consideration at the high frequencies observed in this thesis, as mentioned previously.

The residual delay and phase offsets at the reference antenna can be incorporated into the phase gain equation, Equation 4.11. If the reference polarisation is chosen to be RCP, then Equation 4.11

becomes (Kemball et al. 1995)

$$\begin{aligned}\phi_m^R &= (\tau_m^R - \tau_0^R)(\omega - \omega_0) + (\dot{\theta}_m^R - \dot{\theta}_0^R)(t - t_0) + (\theta_m^R - \theta_0^R) \\ \phi_m^L &= (\tau_m^L - \tau_0^L + \delta\tau_0^{L-R})(\omega - \omega_0) + (\dot{\theta}_m^R - \dot{\theta}_0^R + \delta\dot{\theta}_m^{L-R})(t - t_0) \\ &\quad + (\theta_m^R - \theta_0^R + \delta\theta_m^{L-R}) \end{aligned} \tag{4.12}$$

where the residual delay and the residual phase offset at the reference antenna are denoted $\delta\tau_0^{R-L} = \tau_0^R - \tau_0^L$ and $\delta\theta_0^{R-L} = \theta_0^R - \theta_0^L$ respectively, and the fringe rate offset $\delta\dot{\theta}_m^{R-L}$ is small enough to be disregarded.

The phase calibration method described in the preceding sections solves for the residual phase gain terms in each polarisation independently, setting the reference antenna values to zero. In order to complete the polarisation phase calibration, the polarisation offset terms $\delta\tau_0^{R-L}$ and $\delta\theta_m^{R-L}$ in Equation 4.12, must be solved for and removed.

Brown et al. (1989) advanced a method for solving for the delay offset, using a continuum calibrator. The delay offset at an antenna m can be found from the cross-hand and parallel-hand delay differences between antenna m and any other antenna n

$$\begin{aligned}\delta\tau_m^{R-L} &= \tau_{mn}^{RL} - \tau_{mn}^{LL} = \tau_{mn}^{RR} - \tau_{mn}^{LR} \\ \delta\tau_n^{R-L} &= \tau_{mn}^{RL} - \tau_{mn}^{RR} = \tau_{mn}^{LL} - \tau_{mn}^{LR}\end{aligned}$$

using shorthand for the delay differences $\tau_{mn}^{pq} = \tau_m^p - \tau_n^q + \epsilon_{mn}^{pq}$, where ϵ_{mn}^{pq} is a baseline-dependent term that is assumed to be negligible. When the parallel-hand delays have been removed, the delay offset can be determined directly from the cross-hand delay differences τ_{mn}^{RL}, through a fringe fit to the cross-hand polarisation calibrator data (Cotton 1993). Although this fit can be performed using a single baseline (Cotton 1993), Leppanen et al. (1995) have shown that a higher SNR solution can be obtained by averaging the visibilities over multiple baselines. Experiment has shown that delay offsets are stable over the course of a typical VLBI observation (Brown et al. 1989), so delay solutions found in this manner are averaged over the duration of an observation to give a single delay offset value for a VLBI observing run.

The residual polarisation phase offsets can be determined from the parallel-hand cross-correlation phases of a continuum calibrator with negligible circular polarisation. After applying the bandpass and delay solutions to the data, the r^{RR} data are divided by the r^{LL} data to give a new data set. This new data set will have amplitudes which are the ratio of the original r^{RR} to r^{LL} visibility amplitudes, and phases which are the difference between the original r^{RR} and r^{LL} visibility phases. These visibility phase differences $\Phi_{mn}^{RR} - \Phi_{mn}^{LL}$ are related to the residual phase polarisation offsets

$$\Phi_{mn}^{RR} - \Phi_{mn}^{LL} = \delta\theta_n^{R-L} - \delta\theta_m^{R-L}$$

where $\delta\theta_m^{R-L} = \theta_m^R - \theta_m^L$ for antenna m, and similarly for antenna n. This system of equations can be used to solve for the phase offset at each antenna relative to a reference antenna offset $\delta\theta_0^{R-L}$, which is unknown (Kemball et al. 1995).

The unknown absolute $R - L$ phase offset $\delta\theta_0^{R-L}$ translates into an unknown absolute electric vector position angle on the sky in the final images. A phase offset $\delta\theta_0^{R-L}$ will result in an EVPA

rotation of half of $\delta\theta_0^{R-L}$ (Cotton 1993). The electric vector position angle can be calculated from the Stokes Q and U values, and is given by

$$\text{EVPA} = \frac{1}{2}\tan^{-1}\frac{U}{Q} \tag{4.13}$$

(Conway & Kronberg 1969).

The final phase calibration step of finding $\delta\theta_0^{R-L}$ can be performed by observing a compact calibrator with a known absolute EVPA during the VLBI observation. These EVPA calibrator data are calibrated and imaged to determine the apparent EVPA of the calibrator on the sky. This angle is compared to the known absolute EVPA of the calibrator to determine the phase rotation $\delta\theta_0^{R-L}$ added by propagation through the receiver system (Cotton 1993).

The absolute EVPA of the EVPA calibrator can be determined relative to an absolute polarisation calibrator of known EVPA, such as 3C138, using auxilliary observations with a connected-element array such as the VLA, where the calibrators are unresolved (e.g. Cotton 1993; Leppanen et al. 1995).

4.4.4 Instrumental polarisation calibration

The final step in the calibration of VLBI spectral line polarisation data is the correction for instrumental polarisation. When the two polarised feeds on the antenna are sufficiently orthogonal then the feed models can be linearised and modeled as first-order D-terms, as discussed in Section 4.3.

Each cross-hand polarisation visibility in Equation 4.4 contains contributions from the cross-hand source model, and fractional contributions from the parallel-hand and opposite cross-hand source model modulated by the instrumenal polarisation. The cross-hand contribution rotates with parallactic angle for altitude-azimuth antennas such as the VLBA, while the fractional parallel-hand contributions are constant. These terms can then be separated, given adequate parallactic angle coverage of the source, and the D-terms solved for simultaneously with the source polarisation (Conway & Kronberg 1969).

The D-terms and fractional linear polarisation were solved for in this manner in early interferometric observations of quasars using unpolarised unresolved calibrator sources (e.g. Wardle & Kronberg 1974; Roberts et al. 1984; Wardle et al. 1986).

These fits require either extremely compact linearly polarised calibrators or completely unpolarised calibrators, both of which are rare at VLBI resolution (Kemball et al. 1995). Several adaptations of the technique were consequently developed to enable calibration with resolved sources. Cotton (1993) developed the similarity method, where a single scaled version of the total intensity distribution is used as an initial estimate of the linear polarisation. Leppanen et al. (1995) modified this method to divide the total intensity distribution into submodels and perform an independent similarity fit over each submodel region. Kemball et al. (1995) developed a spectral line adaptation of the similarity method, where each spectral channel in the source observation is treated as an independent calibrator with negligible linear polarisation. This technique was implemented by Kemball & Diamond (1997).

4.5 Imaging

The bandpass response, the amplitude gain, the phase gain and the instrumental polarisation calibration solutions are all applied to the correlator output r_{mn}, following Equation 4.4, to derive the source correlation vector S_{mn}. The final step in the data reduction process is imaging the visibilities in the correlation vector. Imaging is the process of performing a Fourier transform of the visibility data to give the brightness distribution of the source on the sky

$$I(l,m) = \int\int \mathcal{I}(u,v) e^{j2\pi(lu+mv)} du\, dv$$

(after Clark 1989) where I is the total intensity, and $\mathcal{I}(u,v)$ is the visibility counterpart of the total intensity, as given in Equation 4.3. This Fourier transform relationship is limited to the narrow-field regime, which is applicable to VLBI observations. For polarimetric imaging, the visibility counterparts of the four visibility Stokes parameters from Equation 4.3 can be inverted by Fourier transform to give images of the source in all four Stokes parameters I, Q, U and V (Clark 1989).

In VLBI observations the visibility data are very sparsely sampled in (u,v) space, as shown in Figure 4.1. The sparse visibility data can be considered to be a complete visibility function $\mathcal{I}(u,v)$, which fills the entire (u,v) plane, multiplied by a sampling function $S(u,v)$ which is zero where there is no (u,v) data. The Fourier transform of the measured visibility data yields what is known as the dirty image I^D

$$I^D(l,m) = \int\int S(u,v)\mathcal{I}(u,v) e^{j2\pi(lu+mv)} du\, dv \tag{4.14}$$

(Clark 1989). In terms of Fourier transform theory, the multiplication of the conceptual complete visibility and the sampling function in the (u,v) plane is equivalent to the convolution of the true image I with the Fourier transform of the sampling function in the image plane. The Fourier transform of the sampling function is termed the dirty beam P (Clark 1989). In the image plane the dirty image is therefore given by

$$I^D = P * I \tag{4.15}$$

The true image must then be extracted from the dirty image using a deconvolution algorithm (Clark 1989).

A deconvolution algorithm that is widely used in radio interferometry is the CLEAN algorithm developed by Högbom (1974). The CLEAN algorithm determines the dirty beam and dirty image from Fourier inversion of the sampling function and the sampled visibilities respectively, then successively removes scaled versions of the dirty beam from the maximum points in the dirty image. This process is continued until the residual dirty map values are below the expected noise level for the image. The removed delta-function components are returned to a final map convolved with a clean beam, which is conventionally an elliptical Gaussian fit to the main lobe of the dirty beam (Högbom 1974). The CLEAN algorithm is often implemented in software using the Clark version of the CLEAN algorithm, a computationally-efficient adaptation of the original Högbom CLEAN (Clark 1980).

The strengths of the CLEAN algorithm are its relatively straightforward implementation in software, and its proven capability. However, the CLEAN algorithm is non-linear, so the noise in CLEAN images is difficult to interpret. Broad smooth features in an image are also particularly problematic for CLEAN, and can result in spurious imaging artifacts (Thompson et al. 2001, pg. 431-434).

For full-polarisation observations, the four Stokes parameters are each imaged independently using the CLEAN algorithm. The final result of the calibration and imaging is four image cubes, one for each of the Stokes parameters. Each cube consists of a number of maps of the particular Stokes value, in right ascension and declination, one map for each of the spectral channels across the imaged bandwidth. The Stokes I cube gives a total intensity distribution of the source, for each spectral channel. The Stokes V cube is used to calculate the levels of circular polarisation, and the Stokes Q and U cubes are used to calculate the levels of linear polarisation.

A description of the the VLBI data sets observed in this thesis is given in the next chapter. The practical implementation of the data reduction process described in this chapter is also provided there.

Chapter 5

Observations and Data Reduction

The research in this thesis is based on VLBA observations conducted at two epochs: 2003 and 2007. Both projects sought interferometric detections of a number of vibrationally-excited rotational SiO maser transitions in ^{28}SiO and several other isotopologues, toward the supergiant VY CMa. At each epoch the target source observations were interleaved with observations of continuum calibrator sources. The VLBA is a dedicated VLBI array of ten 25m parabolic antennas distributed throughout the United States of America, with baselines ranging from less than a few hundred kilometres to over eight thousand kilometres. The locations of the antennas are given in Table 5.1.

Both epochs targeted rotational SiO maser transitions in the 43 GHz and 86 GHz frequency bands. The first set of observations made in 2003 was an extensive search for sixteen SiO transitions from the three isopotologues ^{28}SiO, ^{29}SiO and ^{30}SiO, as enumerated in Table 5.2. Because so many lines were included in the first observing run, each line was only observed for a relatively short period of time. Six of the sixteen lines were detected, as discussed in further detail below. The 2007 project was a follow-up to the 2003 project. The six lines detected in 2003 were re-observed, with a longer integration time for improved (u, v) coverage, greater sensitivity than the initial observations, and with the intent of imaging.

The two data sets are described below, followed by an outline of the data reduction procedure applied to the data, within the theoretical framework presented in the previous chapter.

5.1 Epoch 1: BK103

The first set of observations was undertaken between 20 and 23 December 2003, under VLBA project code BK103. The 43 GHz observations (BK103A) were scheduled on the first day and the 86 GHz observations (BK103B) on the second day. Unfortunately however, there were technical problems with the initial BK103 86 GHz observations, and they were rescheduled for the following night: 23 December 2003 (BK103C). The dates of the observations and details of the lines observed are listed in Table 5.2.

All spectral windows were centred at a Doppler-shifted frequency referenced to the mid-point of both the array and the observing interval, assuming a systemic LSR velocity of 18 km/s for the SiO maser emission towards VY CMa. The data were sampled using two-bit quantisation. Left-circularly polarised and right-circularly polarised signals were recorded at each antenna and the off-line correlation was performed in full polarisation at the VLBA correlator in Socorro (New Mexico).

Antenna	Abbreviation	N. Latitude [° ' "]	W. Longitude [° ' "]	Elevation [m]
St. Croix	SC	17 45 30.57	64 35 02.61	16
Hancock	HN	42 56 00.96	71 59 11.69	309
N. Liberty	NL	41 46 17.03	91 34 26.35	241
Fort Davis	FD	30 38 05.63	103 56 39.13	1615
Los Alamos	LA	35 46 30.33	106 14 42.01	1967
Pie Town	PT	34 18 03.61	108 07 07.24	2371
Kitt Peak	KP	31 57 22.39	111 36 42.26	1916
Owens Valley	OV	37 13 54.19	118 16 33.98	1207
Brewster	BR	48 07 52.80	119 40 55.34	255
Mauna Kea	MK	19 48 15.85	155 27 28.95	3720

Table 5.1: Geographic locations of the VLBA antennas (Napier 1994).

The subset of VLBA antennas used in each of the BK103A and BK103C observing runs is listed in Table 5.3. The astrometric position of VY CMa was taken as right ascension $07^h\ 22^m\ 58.3315^s$, declination $-25°\ 46'\ 03.174''$ (J2000), with annual parallax correction of 1.78 mas and proper motion correction of 9.84 mas/yr and 0.75 mas/yr (1991.25) in right ascension and declination (Perryman et al. 1997).

The BK103A project included the target source VY CMa and the continuum calibrators J0359+5057 and 3C273, while the BK103C project observed VY CMa with continuum calibrators J0423-0120 and 3C273. In each case, both calibrators were used for bandpass fitting and phase calibration, described in more detail in Section 5.3.

The calibrator J0359+5057 was also used to determine the absolute EVPA for the BK103A sources. The EVPA calibration method is described in the phase calibration section of the previous chapter, Section 4.4.3, and the practical implementation of this method is described in greater detail in Section 5.3.7 below. In this method, the VLA is used to observe one of the standard absolute EVPA polarisation calibrators with known polarisation position angle (Perley & Taylor 2003; Kemball 1999), along with secondary compact polarisation calibrators of unknown EVPA, which are also included in the VLBI schedule. The VLA observations of the primary polarisation calibrators are used to determine the absolute EVPA of the secondary polarisation calibrators, which can then be transferred to the VLBA data to calibrate their absolute EVPA (or equivalently, the residual unknown R-L phase difference at the reference antenna, assumed constant). Accordingly, the BK103A schedule included an auxilliary VLA observation on 20 December 2003. On this date the VLA was in B configuration. The VLA observed the primary polarisation calibrator J0521+166 (3C138)[1] and secondary polarisation calibrator J0359+5057 in Q-band.

It was not possible to perform absolute EVPA calibration for the 86 GHz data using this method however, as the VLA cannot reach the 86 GHz band.

One of the scientific goals of the first set of observations was to detect as many SiO maser lines as possible towards VY CMa in the 43 GHz and 86 GHz bands. For this reason the observations were strategically scheduled to interleave several frequency configurations (termed frequency IDs in later

[1] www.vla.nrao.edu/astro/calib/polar

Proj. Code	Date	Frequency			Line	Detected	Imaged
	12/2003	Band	FreqID	IF			
BK103A	20	43 GHz	1	1	v=1 J=1-0 ^{30}SiO		
BK103A	20	43 GHz	1	2	v=2 J=1-0 ^{29}SiO		
BK103A	20	43 GHz	1	3	v=0 J=1-0 ^{30}SiO	Y	
BK103A	20	43 GHz	2	1	v=2 J=1-0 ^{28}SiO	Y	Y
BK103A	20	43 GHz	2	2	v=0 J=1-0 ^{29}SiO		
BK103A	20	43 GHz	2	3	v=1 J=1-0 ^{28}SiO	Y	Y
BK103A	20	43 GHz	3	1	v=0 J=1-0 ^{28}SiO	Y	Y
BK103A	20	43 GHz	4	1	v=0 J=1-0 ^{30}SiO	Y	
BK103A	20	43 GHz	4	3	v=1 J=1-0 ^{29}SiO		
BK103C	23	86 GHz	1	1	v=1 J=2-1 ^{30}SiO		
BK103C	23	86 GHz	2	1	v=2 J=2-1 ^{29}SiO		
BK103C	23	86 GHz	3	1	v=0 J=2-1 ^{30}SiO		
BK103C	23	86 GHz	3	2	v=1 J=2-1 ^{29}SiO		
BK103C	23	86 GHz	4	1	v=2 J=2-1 ^{28}SiO		
BK103C	23	86 GHz	4	2	v=0 J=2-1 ^{29}SiO		
BK103C	23	86 GHz	5	1	v=1 J=2-1 ^{28}SiO	Y	Y
BK103C	23	86 GHz	6	1	v=0 J=2-1 ^{28}SiO		

Table 5.2: Epoch 1 observations, VLBA project code BK103. The columns from left to right are: the project code, calender date in December 2003 on which the observations took place, the frequency band of the observation, the frequency ID, the IF number within the frequency group in the observing schedule, the spectral line sought, whether or not the line was detected in the visibility spectra, and if it was successfully imaged.

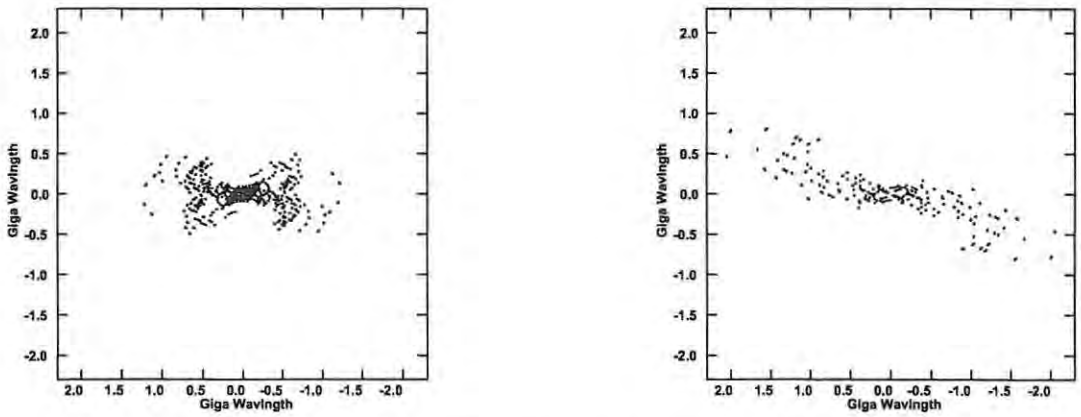

Figure 5.1: The (u,v) coverage for the BK103 observation of the 43 GHz v=1 J=1-0 ^{28}SiO line (left) and the 86 GHz v=1 J=2-1 ^{28}SiO line (right).

BK103A	BK103C	BR123A	BR123B	BR123C	BR123D
BR		BR	BR	BR	BR
FD	FD	FD			
HN	HN				HN
KP	KP	KP	KP	KP	KP
LA	LA	LA	LA	LA	LA
MK	MK	MK	MK	MK	MK
NL	NL	NL	NL	NL	NL
OV	OV	OV	OV	OV	OV
PT	PT	PT	PT	PT	PT
SC			SC	SC	SC
			VLA	VLA	VLA

Table 5.3: Antennas participating in the BK103 and BR123 projects. The VLBA antenna codes are given in Table 5.1. A single VLA antenna was included in three of the BR123 observing runs.

reduction) within the 43 GHz or 86 GHz receiver bands. Each frequency configuration was therefore optimised to include multiple SiO transitions. The scheduling is explained in more detail below, and the mapping between transition and frequency ID is summarised in Table 5.2.

The 43 GHz observations used four frequency IDs, each divided into four 4-MHz wide spectral windows (basebands) correlated with 128 spectral channels of nominal width 31.25 kHz. The 86 GHz observations used six frequency IDs, each comprising two 8-MHz wide basebands, correlated over 128 channels of nominal width 62.5 kHz. At this time, the VLBA correlator was restricted in cross-polarised spectral-line mode to a maximum 128 channels per spectral window. The schedule switched between individual 43 GHz or 86 GHz frequency configurations (Frequency IDs); although the number of recorded basebands differed between individual frequency configurations, their total bit rate did not, thus allowing direct interleaving in the schedule. Table 5.2 indicates that the first three listed spectral lines were all allocated to different basebands (IF numbers) in frequency ID 1, and were observed simultaneously. Similarly, the next three lines all fell into frequency ID 2 and were also observed simultaneously; and continuing in this manner through the table. The observing schedule switched between different frequency IDs approximately every five to six minutes. The target source VY CMa was observed for a total of approximately 23 minutes in each frequency ID in the course of the 86 GHz observations, and for 41 minutes in each frequency ID during the 43 GHz observations.

Representative (u,v) coverage for two single spectral lines from the BK103 observing run is shown in Figure 5.1. These figures show the projected baseline lengths in the plane orthogonal to the direction of the source, normalised by wavelength. The compact, dense (u,v) coverage for the 43 GHz observations is due to the shorter baseline lengths, in wavelength units, and the fact that almost twice as much observing time was spent on each of the 43 GHz lines as on each of the 86 GHz lines.

5.2 Epoch 2: BR123

The second set of observations were undertaken between 15 and 19 March 2007, under VLBA project code BR123. The project schedule was configured to re-observe the six SiO maser lines that were positively detected in the earlier BK103 project.

Proj. Code	Date 03/2007	Frequency Band	IF	Line	Imaged
BR123A	15-16	86 GHz	1	v=1 J=2-1 ^{28}SiO	Y
BR123B	16-17	43 GHz	1	v=0 J=1-0 ^{30}SiO	
BR123B	16-17	43 GHz	2	v=1 J=1-0 ^{29}SiO	
BR123C	17-18	43 GHz	1	v=0 J=1-0 ^{28}SiO	
BR123D	18-19	43 GHz	1	v=2 J=1-0 ^{28}SiO	Y
BR123D	18-19	43 GHz	2	v=1 J=1-0 ^{28}SiO	Y

Table 5.4: Epoch 2 observations, VLBA project code BR123. The columns from left to right are: the project code, calender date in March 2007 on which the observations took place, the frequency band of the observation, the baseband (IF number), the spectral line observed and whether or not the line was ultimately successfully imaged.

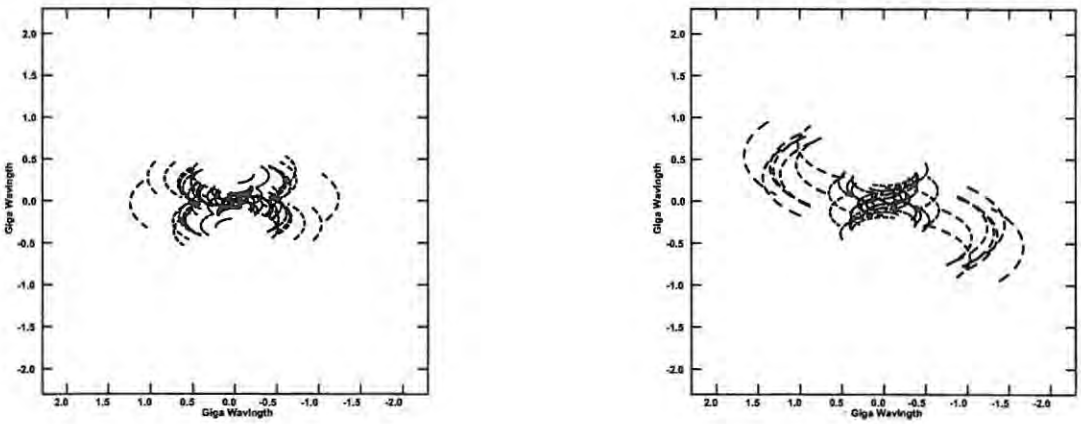

Figure 5.2: The (u,v) coverage for the BR123 observations of the 43 GHz v=1 J=1-0 ^{28}SiO line (left) and the 86 GHz v=1 J=2-1 ^{28}SiO line (right).

The BR123 project was allocated considerably more observing time than the BK103 project and also observed fewer lines than the original sixteen included in the BK103 schedule. Significantly more observing time could therefore be allocated to each line in the BR123 observations, and the reduced number of lines rendered the previous optimisation over frequency ID unneccessary. Instead, the six lines were observed over the four allocated days using a single frequency configuration with one baseband for the 86 GHz observations and two basebands for the 43 GHz observations. In this way either one or two lines were observed each day and the six lines could be sub-divided across four days of observation, as summarised in Table 5.4. The target source VY CMa was observed for approximately 150 minutes in total in each BR123 observing run. The subset of VLBA antennas used in each of the BR123 observing runs are listed in Table 5.3. A single VLA antenna was included in the 43 GHz observations.

Typical (u,v) coverage of a single spectral line in the BR123 observing run is shown in Figure 5.2. Comparison of the BR123 and BK103 (u,v) coverage (Figures 5.2 and 5.1) shows more complete (u,v) coverage in the BR123 observations, due to the greater net observing time. The BK103 86 GHz (u,v) coverage is more extended than the BR123 86 GHz coverage because of the use of the outlying Hancock VLBA antenna in the BK103 observations (see Table 5.3). The Hancock antenna did not have an 86 GHz receiver at the time of the BR123 observations.

As in the BK103 observations, both left- and right-circularly polarised signals were recorded at each antenna and the correlation was performed in full polarisation at the VLBA correlator. The BR123 observations were also centred on a systemic LSR velocity of 18 km/s adopted for VY CMa. Two-bit quantisation was used during sampling. The 43-GHz observations employed two 8-MHz basebands, each correlated over 128 spectral channels of nominal width 62.5 kHz. The 86-GHz observations contained a single baseband, correlated over 128 channels of nominal width 125 kHz. The baseband bandwidths and individual channel widths in the BR123 observations were double those used in the BK103 observations. This change was made because single dish observations of the v=1 and v=2 SiO maser lines towards VY CMa typically show emission spanning approximately 40 km/s towards this source (e.g. Spencer et al. 1981; Pardo et al. 2004; Kang et al. 2006). By contrast, the BK103 spectra only covered a velocity range of approximately 28 km/s. The astrometric position of VY CMa was taken as right ascension $07^h\ 22^m\ 58.3315^s$, declination $-25°\ 46'\ 03.174''$ (J2000) (Perryman et al. 1997), as for the BK103 observations. An annual parallax correction of 1.78 mas and proper motion correction of 9.84 mas/yr and 0.75 mas/yr (1991.25) in right ascension and declination (Perryman et al. 1997) was included for the BR123A observations, but not the BR123B, BR123C or BR123D observations.

In each BR123 observing run the source VY CMa was interleaved with observations of continuum calibrators 3C454.3, J0423-0120, J0609-1542, J0731-2341 and 3C273. All of the calibrators except for J0731-2341, which proved to have insufficient correlated spectral flux density, were used for bandpass and phase calibration. The purpose of the individual calibrators is described in more detail below and in Section 5.3.

The calibrator J0423-0120 was also used as a secondary polarisation calibrator for the absolute EVPA calibration method described in Section 5.3.7. The BR123 VLBA observations were accompanied by auxilliary VLA observations of 3C138, J0646+448, J0609-1542, J0423-013 and J0542+498 on 17 March 2007, when the VLA was in the D configuration. As in the BK103 observations, 3C138

served as the primary polarisation calibrator (Perley & Taylor 2003; Kemball 1999).

The source J0731-2341 was included in the observations as a potential phase reference calibrator, chosen for its proximity to VY CMa on the plane of the sky. The signal-to-noise ratio of the J0731-2341 data was found however to be too weak to be useful in calibrating the VY CMa data, and it was not included further in the data reduction procedure described below. The phase-referencing procedure is discussed in Section 5.5.

5.3 Data reduction procedure

The data reduction model used in this thesis follows the spectral line polarisation method described in Kemball et al. (1995) and Kemball & Richter (2011). The theoretical basis for the data reduction is given in Chapter 4. This section describes the practical data reduction steps which were applied to the BK103 and BR123 data sets. The data reduction was performed using the Astronomical Image Processing System (AIPS)[2], developed and maintained by the National Radio Astronomy Observatory (NRAO)[3] but modified here as needed.

Each baseband from the BK103 and BR123 observing runs containing a detected spectral line is considered a single data set in what follows. The data reduction described in this section was applied to each of the data sets. This amounted to six individual data sets from the BK103 project, and three data sets from the BR123 project. Two of the BK103 data sets were ultimately not imaged. Although the spectral line was detected in the cross-correlation spectra of these data sets, the signal-to-noise ratio of the visibility data was too low to allow reasonable calibration of the data and imaging was therefore not possible.

The calibration of the data can be broadly classified into four steps, following Chapter 4: bandpass calibration, amplitude calibration, phase calibration, and instrumental polarisation calibration. The data reduction sequence culminates by imaging the fully calibrated data.

The science goals of this thesis require high accuracy measurements of the circular polarisation of the SiO maser emission. During the course of this thesis several data reduction innovations were developed, with the aim of improving the quality of the circular polarisation measurements, as described in Kemball & Richter (2011). The innovations primarily involve improvements in the precision of the amplitude calibration of the data. The data reduction innovations involve the bandpass calibration and amplitude calibration steps, and are as follows:

- Solving for the bandpass phase offset $\beta_0^{R-L}(\omega)$ at the reference antenna.
- Applying an aliasing correction to the bandpass amplitudes determined from the autocorrelation data.
- The use of a composite spectrum for the template-fitting amplitude self-calibration.
- The use of autocorrelation polarisation self-calibration to solve for and remove the effects of instrumental polarisation during the amplitude calibration.
- The use of continuum calibrator data to determine the amplitude offset g_0^{RL} between the RCP and LCP systems.

[2] www.aips.nrao.edu
[3] www.nrao.edu

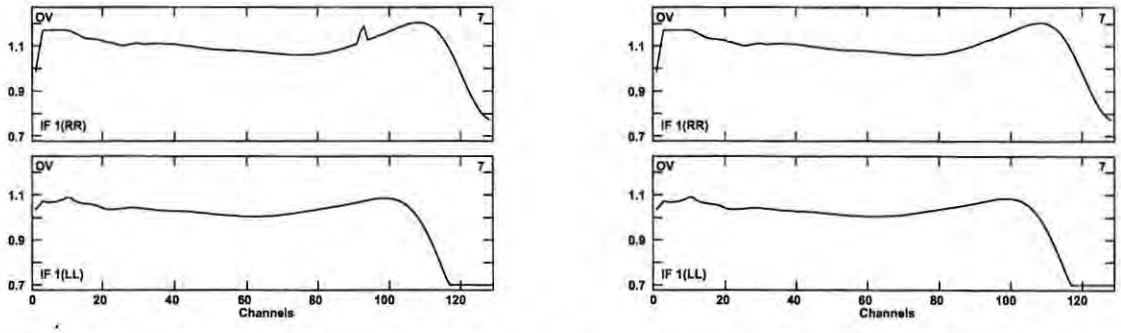

Figure 5.3: Plot of the r^{RR} and r^{LL} autocorrelation calibrator spectra observed by the Owens Valley VLBA antenna, from the 43 GHz BR123D IF1 data set. The spectra were averaged over the full observing run. A correlator "birdie" is visible in the r^{RR} spectrum on the left. The corrected spectrum after application of AIPS task BIRDI is shown on the right.

Each of these methods is described in more detail in the relevant sections below. These new data reduction methods were developed for use with the BR123 data sets. The BK103 reduction made use of earlier reduction methods described in Kemball et al. (1995) and Kemball & Diamond (1997). A discussion of the circular polarisation calibration is provided in Section 5.4, including the accuracy of the circular polarisation measurements.

Following the notation of Kemball et al. (1995), direction-independent calibration corrections are factorised per antenna and receptor polarisation. In the AIPS data reduction model, calibration solutions are determined incrementally and stored in solution tables accompanying the visibility data. The antenna-based gain solutions are ultimately applied in baseline-product pairs to the visibility data.

5.3.1 Data loading and preliminary calibration

Data from the VLBA is distributed in FITS (Flexible Image Transport System) format, specifically FITS-IDI (Greisen 2009), and read into AIPS using the task FITLD. Data with a correlation completeness weight of below 0.95 were excluded from import at this point. Initial inspection of the raw data revealed correlator "birdies" in the BR123 data sets, spectral spikes in the data created by the correlator. These were removed with a new AIPS task, BIRDI, developed for this purpose. This task removes spectral "birdies" by automatically locating local spectral spikes in a specified channel range and fitting an underlying baseline polynomial to remove the feature. An example is shown in Figure 5.3.

At this stage two *a priori* calibration steps were performed:

- The data were phase-corrected for the effect of parallactic angle rotation during the course of the observations, using the task CLCOR.
- The LSR velocity of the band centre was recorded in the data using the task SETJY. This velocity information is present in the observing schedule, but not in the output correlation data read by FITLD.

Bad visibility data were then flagged in three steps:

- The online observing software generates automatic flags for data known to be bad during the observations. This first round of flagging was included with the imported FITS data in a flag table.
- All data noted as problematic in the observing operator log file accompanying the data were flagged using the AIPS task UVFLG.
- Observations made at an elevation angle below 10° were also flagged using the AIPS task UVFLG. The total system temperature increases with increasing path length through the atmosphere, so low elevation data are removed to limit the effect of atmospheric noise.

After these initial flagging steps, the data were split into autocorrelation and cross-correlation products for both the source and calibrator data sets. Each of these four data sets were then processed separately.

5.3.2 Bandpass calibration

The complex bandpass response of each antenna was determined from the continuum calibrator data, as described in Section 4.4.1 of the previous chapter.

AIPS task CPASS was primarily used for bandpass calibration of the data in this thesis. CPASS fits Chebychev polynomials to the bandpass profiles using a least-squares minimisation algorithm. CPASS can take as an input an autocorrelation bandpass to use as the amplitude component of the full complex cross-correlation bandpass, solving only for the bandpass phase. This is preferable to solving for both the amplitude and phase bandpass from the cross-correlation data as the autocorrelation data have much higher SNR than the cross-correlation data. However, as discussed in Chapter 4.4.1, the autocorrelation bandpass response suffers from aliasing while the cross-correlation bandpass response does not. The aliasing must be removed from the autocorrelation bandpass amplitude response before it can be applied to the cross-correlation data.
The bandpass calibration was performed as a six-step process:

1. The amplitude component b^p_{AC} of the bandpass response was solved for using the calibrator autocorrelation data, for each antenna and for each sense of polarisation $p \in \{R, L\}$.

   The autocorrelation data were first interactively flagged using AIPS task IBLED. CPASS was then run on the edited autocorrelation data to determine the autocorrelation bandpass amplitude response b^p_{AC}.

2. The $R-L$ bandpass phase offset at the reference antenna β_0^{R-L} was solved for using the calibrator autocorrelation data.

   The polarisation labeling of the calibrator autocorrelation data was switched using AIPS task SWPOL, and $\beta_0^{R-L}(\omega)$ was determined from a phase-only bandpass fit to the r^{RL} and r^{LR} visibility data at the reference antenna using AIPS task CPASS.

3. The bandpass phase was solved for from the cross-correlation calibrator data, using the autocorrelation bandpass b^p_{AC} as the amplitude component of the full bandpass.

   The cross-correlation data phases have slopes in frequency and time, corresponding to residual group delays and fringe rates. As a result, fringe fitting and interactive flagging were performed

in an iterative process. The data were first averaged over eight-channel increments with the task AVSPC and a preliminary fringe fit performed on the averaged data with the task FRING. The fringe fit solutions were applied to the frequency-averaged data and the data were interactively flagged using IBLED. The IBLED flags were then applied to the original 128-channel data set and a second fringe fit was performed on the full data set at the original channel spacing. The bandpass phases $\beta_m^p(\omega) - \beta_0^p(\omega)$ were then solved for separately using the task CPASS, setting the amplitude component of the bandpass to b_{AC}^p, applying all cumulative flagging information and fringe fit solutions.

The amplitude component b_{AC}^p and the bandpass phase combine to form a full bandpass response B_{AC}^p.

4. A full bandpass response was solved for from the cross-correlation calibrator data.

   CPASS was used to solve for a full amplitude and phase bandpass response B_{XC}^p using the cross-correlation calibrator data and applying all cumulative prior flagging and fringe fit solutions.

5. The $R - L$ bandpass phase offset at the reference antenna $\beta_0^{R-L}(\omega)$ was applied to the full bandpass response B_{AC}^p with the task BPXRF.

6. The aliasing in the bandpass amplitude of B_{AC}^p was removed.

   The bandpass responses B_{AC}^p and B_{XC}^p were both provided as input to the task BPALC, which removes the aliasing by fitting a Butterworth function to the cross-correlation amplitude bandpass response. The fit was performed as described in Section 4.4.1 of the previous chapter, using the least-squares minimisation in Equation 4.5. A 12-pole Butterworth function was found empirically to provide a good fit for the bandpass aliasing in project BR123.

The tasks BPXRF and BPALC are new AIPS tasks developed for the high accuracy circular polarisation calibration required in this thesis.

As noted in Chapter 4.4.1, the aliasing in the autocorrelation amplitude response leads to an offset in the normalisation of the bandpass B_{AC}^p. This can introduce an amplitude offset of up to $\sim 1\%$ when the bandpasses are removed from the source data. An example of the aliasing correction at 43 GHz and 86 GHz is shown in Figure 5.4. The aliasing is more notable at 43 GHz than at 86 GHz, as shown by the figures. The amplitude offset, from before and after the aliasing correction is applied, is visible in the 43 GHz figures.

The motivation for using the autocorrelation data to determine the amplitude component of the bandpass is illustrated in the 86 GHz bandpass solution of Figure 5.4, where the bandpass amplitude b_{XC} determined from the cross-correlation data clearly has a much lower SNR than the corresponding bandpass amplitude b_{AC} determined from the autocorrelation data.

5.3.3 Amplitude calibration

The first step in the amplitude calibration process is a correction for sampler bias. All data reduced in this thesis were sampled with two-bit quantisation, which introduces amplitude errors in the data in the presence of sampler voltage threshold errors (Thompson et al. 2001, pg. 278-281). This bias was corrected using AIPS task ACCOR (Kogan 1995), which calculates the mean values of the autocorrelation spectra and spectra of perfectly sampled data.

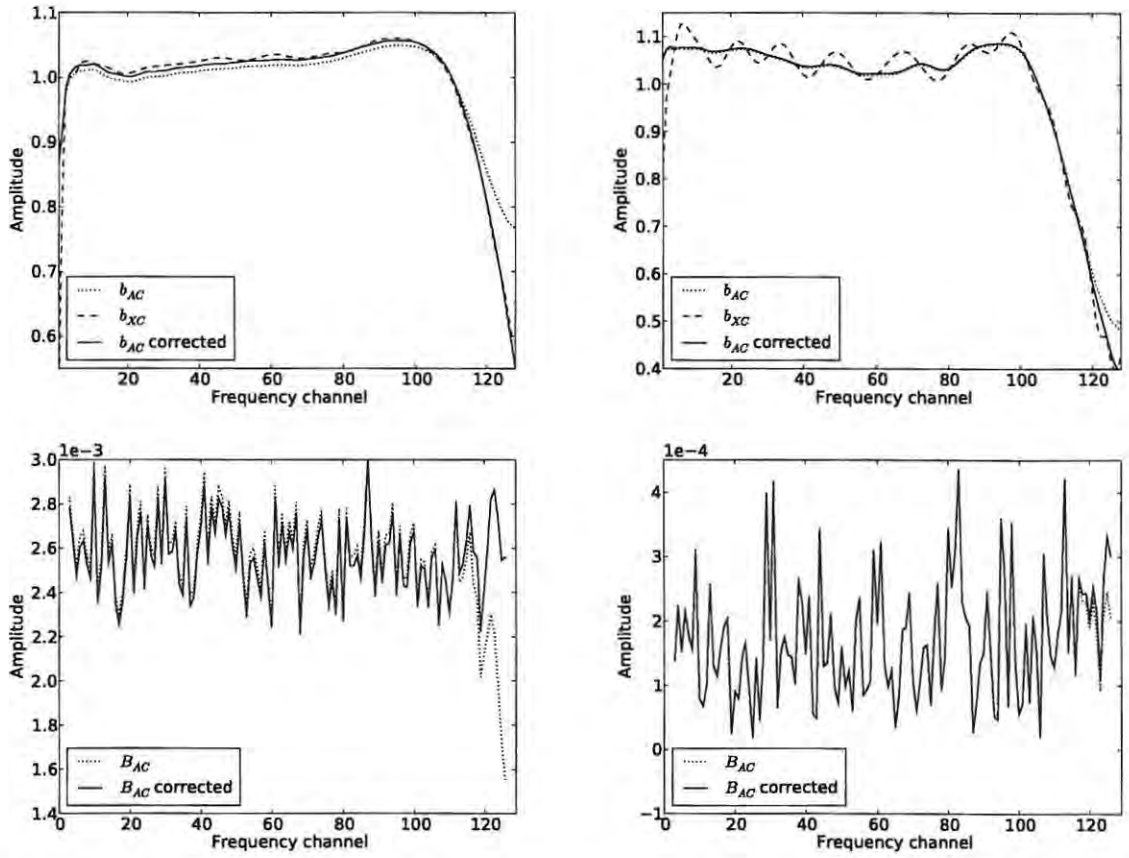

Figure 5.4: Top panel: Plot of the RCP amplitude components of the bandpass solutions at the Kitt Peak antenna, for the 43 GHz BR123D IF2 data set (left) and the BR123A IF1 86 GHz data set (right).
Bottom panel: Plot of the Kitt Peak - Mauna Kea cross-correlation data for a single seven-minute scan of calibrator J0423-0120, applying the full complex bandpass with and without the aliasing correction, for the 43 GHz BR123D IF2 data set (left) and the BR123A IF1 86 GHz data set (right).

The amplitude calibration of the continuum calibrators was performed using the default method of multiplying each uncalibrated cross-power spectrum by the geometric mean of each antenna's system equivalent flux density (SEFD) for that baseline, following Chapter 4.4.2. The accuracy of this method is limited by the inherent uncertainty in the *a priori* SEFD measurements. The accuracy is estimated to be $\sim 10\%$ at 43 GHz and $\sim 15\%$ at 86 GHz (Kemball & Richter 2011).

For spectral line observations, the template-fitting amplitude calibration method, described in Chapter 4.4.2, provides a means to improve upon this accuracy in amplitude calibration. As discussed in Chapter 4.4.2, the template-fitting method leaves an unknown amplitude gain offset g_0^{RL} between the RCP and LCP data.

The amplitude calibration of the calibrator and source data are described in more detail below.

Calibrator amplitude calibration

The ACCOR sampler bias corrections derived from the calibrator autocorrelation data were applied to the calibrator cross-correlation data. The calibrator cross-correlation data were then further calibrated

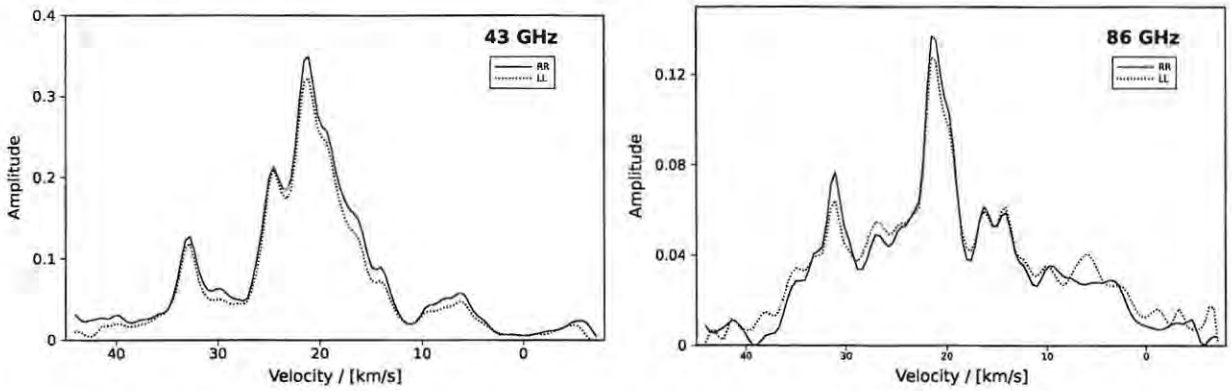

Figure 5.5: Single-scan spectra from the Los Alamos antenna from the data set BR123D IF2 at 43 GHz (left) and from BR123A at 86 GHz (right). The vertical axis of the plot is uncalibrated amplitude. Linear residual baselines have been removed from the spectra. These spectra were chosen for their high SNR relative to the other scans in the observing runs, and illustrate the difference in SNR of the spectra between the two frequencies.

in amplitude using the AIPS task APCAL. This task uses measurements of the system temperature T_{sys} made during the observations, combined with point-source sensitivity (PSS) measurements in auxilliary VLBA service observations, to derive the overall amplitude calibration. The T_{sys} and PSS information is provided in tables accompanying the visibility data. No correction was made for opacity during the calibrator amplitude calibration. These calibrators are used to solve for phase-related quantities (e.g. the differential polarisation delay offset at the reference antenna), and high accuracy amplitude calibration is unnecessary for this purpose.

Source amplitude calibration

Before amplitude calibration, the VY CMa data were interactively flagged using task IBLED, then corrected for the varying residual Doppler shift during the observing run. The auto- and cross-correlation source data were both corrected for this effect using task CVEL, by shifting the spectra to the LSR velocity reference frame. The bandpasses determined from the calibrator data were also applied during the CVEL step. Before solving for the VY CMa amplitude gains, the ACCOR sampler bias corrections were also applied to the autocorrelation data.

The VY CMa amplitude calibration was then further refined, using a new autocorrelation polarisation self-calibration technique that extends the template spectrum method of Reid et al. (1980). Template spectrum fitting is usually well-suited to maser observations due to the high SNR of maser autocorrelation data. Traditionally the template spectrum is chosen to be a single scan at high elevation with high SNR (Reid et al. 1980). However, our 86 GHz spectra have considerably lower SNR than the 43 GHz spectra, as illustrated in Figure 5.5. Therefore, instead of using a single scan as the template spectrum, a composite template spectrum was created by averaging high elevation spectral line autocorrelation data from a number of antennas.

The composite template spectra were created with a new AIPS task RLAVG, which averages autocorrelation spectra over multiple antennas, optionally: i) removing a piece-wise spectral baseline; ii) enforcing the constraint that integrated Stokes V is zero; and, iii) rotating the cross-polarised autocorrelation spectra to have zero phase before averaging. A subset of antennas with high SNR

spectra at high elevation were used to form the composite spectra. This subset of autocorrelation data was amplitude calibrated with APCAL prior to averaging with RLAVG, using the *a priori* T_{sys} and *PSS* information as for the contiunuum calibrator data.

The template fitting task ACFIT was then used to fit the source autocorrelation scans against the composite template spectrum over two minute solution intervals, using least-squares minimisation. The fitting produces amplitude gain factors for the data with respect to the template spectrum. Residual quadratic baselines were removed from the spectra for each ACFIT solution interval during the fit. The amplitude gain solutions solved for by ACFIT were clipped to remove outliers before being applied to the data.

The unknown amplitude offset g_0^{RL} between the r^R and r^L components of the template spectrum was solved for using a global fit to the continuum calibrator cross-correlation data. The ACFIT gain solutions were applied to the calibrators J0423-0120 and J0609-1542 and an overall amplitude offset between the r^{RR} and r^{LL} data solved for with a new AIPS task UVRAT. This task solves for the g_0^{RL} offset that minimises the objective function

$$\chi^2 = \sum_{t_k} \sum_{m,n>m} \sum_{\omega_k} \left[\frac{g_0^{RL}\, r_{mn}^{LL}(t_k,\omega_k) - r_{mn}^{RR}(t_k,\omega_k)}{g_0^{RL}\, r_{mn}^{LL}(t_k,\omega_k) + r_{mn}^{RR}(t_k,\omega_k)} \right]^2 \tag{5.1}$$

where the fit is performed over solution interval t_k and frequency units ω_k (Kemball & Richter 2011).

The global calibrator fit requires calibrators with negligible circular polarisation, which is the case for both J0423-0120 and J0609-1542.

No circular polarisation has been detected towards J0423-1020. Reported upper limits from VLBA observations of J0423-1020 circular polarisation are 0.11% at 5 GHz (Homan et al. 2001), 0.16% at 15 GHz (Homan & Lister 2006; Vitrishchak et al. 2008), 0.3% at 22 GHz (Vitrishchak et al. 2008), and 0.5% at 43 GHz (Vitrishchak et al. 2008). Observations with the IRAM 30 m telescope give an upper limit of 0.35% at 86 GHz (Agudo et al. 2010).

Circular polarisation has been detected towards J0609-1542 with the VLBA at a level of -0.65% at 8 GHz and -0.23% at 15 GHz (Homan & Wardle 2003). Homan et al. (2001) and Aller et al. (2003) also report circular polarisation detections at ~ 5 GHz and 8 GHz, at levels of $\sim -0.2\%$, using the VLBA and the University of Michigan 26 m telescope respectively. However, in subsequent 15 GHz VLBA observations in 2003, Homan & Lister (2006) did not detect circular polarisation towards J0609-1542, reporting an upper limit of 0.21%. Circular polarisation was also not detected in higher frequency 86 GHz observations with the IRAM 30 m telescope, which reported an upper limit of 0.53% (Agudo et al. 2010). In the 43 GHz BR123D observations, the J0609-1542 images had a maximum intensity of 0.74 Jy/beam, and in the 86 GHz BR123A observations, the J0609-1542 data had insufficient SNR to be sucessfully calibrated and imaged. Circular polarisation at a level of $\gtrsim 0.5\%$ will therefore not be significant relative to the noise for the 43 GHz and 86 GHz J0609-1542 VLBA observations considered in this thesis, making J0609-1542 a suitable UVRAT calibrator.

The calibrators 3C454.3 and 3C273 were not included in the UVRAT fit as they are located further from VY CMa than J0423-0120 and J0609-1542. At the low elevation of the VY CMa observations, path length differences through the atmosphere can be significant for modest angular separations. This leads to large interpolation errors when applying the ACFIT solutions to the the calibrators, so the more distant calibrators were not used in the UVRAT fit. These errors are also present, though

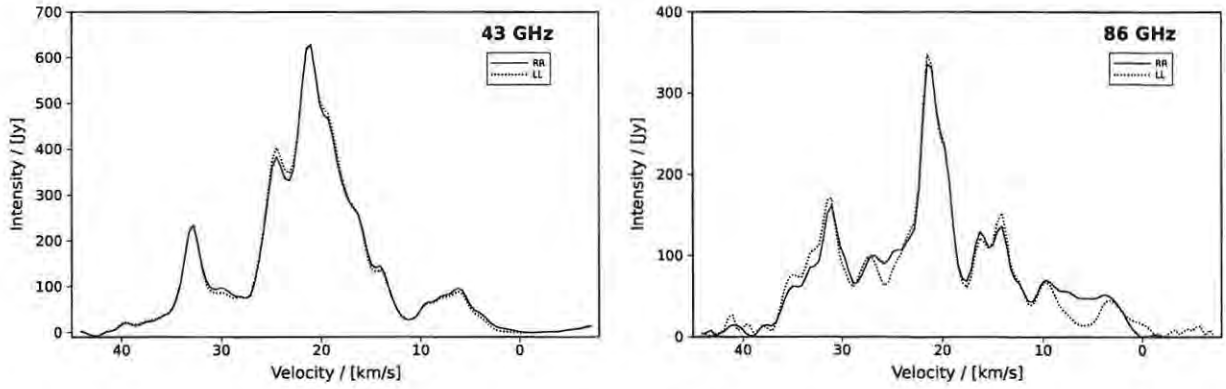

Figure 5.6: The final composite template spectra for the BR123D IF2 data set at 43 GHz (left) and the BR123A data set at 86 GHz (right). The vertical axis of the plot is calibrated flux density.

to a lesser degree, for the calibrators J0423-0120 and J0609-1542. Accordingly, the J0423-0120 and J0609-1542 data were flagged below an elevation cutoff of 25° before the global fit was performed, in order to minimise interpolation errors.

An autocorrelation polarisation self-calibration was then performed, to fit the VY CMa autocorrelation data to the data model described in Chapter 4.4.2. The ACFIT amplitude gains and the UVRAT g_0^{RL} offset were first applied to the autocorrellation VY CMa data, then the data were fit to the model using the new AIPS task ACPOL. For each antenna a χ^2 minimisation was performed of the objective function

$$\chi^2 = r_{mm} - (\mathbb{G}_m \otimes \mathbb{G}_m^*)\,(\mathbb{D}_m \otimes \mathbb{D}_m^*)\,(\mathbb{P}_m \otimes \mathbb{P}_m^*)\,S_{mm} \tag{5.2}$$

where amplitude gain solutions have been applied, so that the term $\mathbb{G}_m \otimes \mathbb{G}_m^*$ reduces to

$$\mathbb{G}_m \otimes \mathbb{G}_m^* = \begin{pmatrix} 1 & 0 & 0 & 0 \\ 0 & e^{j(\theta^{R-L}+\omega\,\tau^{R-L})} & 0 & 0 \\ 0 & 0 & e^{-j(\theta^{R-L}+\omega\,\tau^{R-L})} & 0 \\ 0 & 0 & 0 & 1 \end{pmatrix}$$

The free parameters in the fit at each antenna are the complex D-terms D^R and D^L, the $R-L$ phase offset θ^{R-L} and delay offset τ^{R-L}, and the parallel-hand self-noise, which was modelled as a constant baseline. ACPOL can model the noise baselines in polynomial form, but linear baselines were found to be most appropriate to the BR123 data sets.

The model fit was performed iteratively. The initial estimate of the source model spectrum, $< \mathcal{E}_m^p \mathcal{E}_m^{q*} >$ for $p, q \in \{R, L\}$, was provided by the composite template spectrum used in ACFIT.

The above parameter values solved for in the model fit were then applied to the VY CMa autocorrelation data, and a subset of the corrected data was averaged with RLAVG as described above, to provide a new composite template spectrum. The autocorrelation data were then fitted to the data model again, using the new composite spectrum for the source model spectrum $< \mathcal{E}_m^p \mathcal{E}_m^{q*} >$.

The process of fitting the autocorrelation model and constructing a new composite template spectrum from the corrected data was iterated, until the the composite spectra and parameter estimates

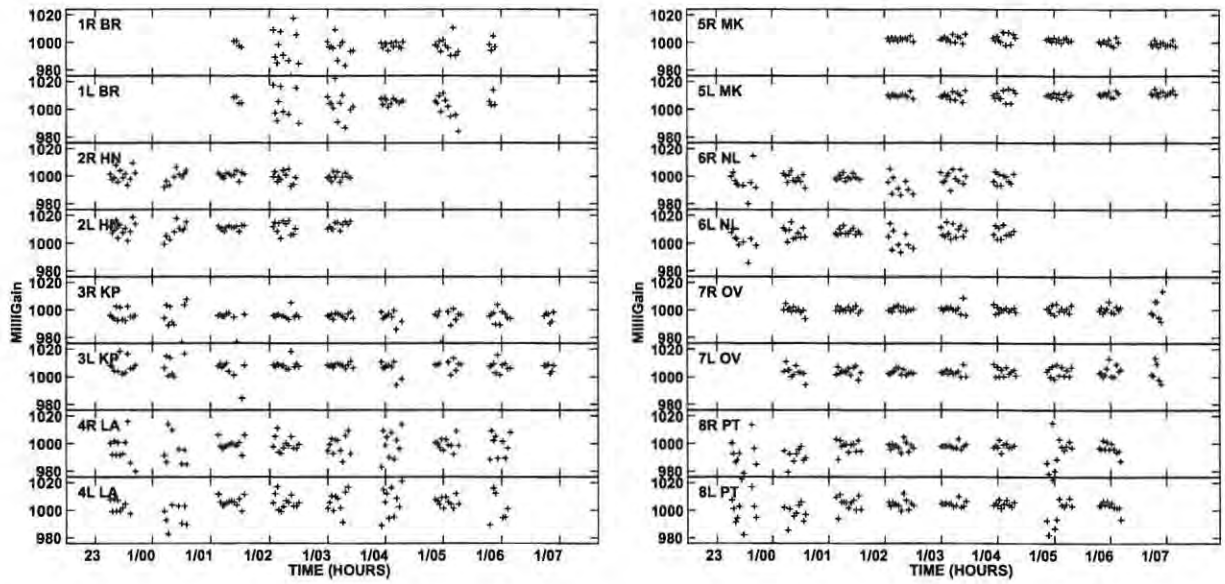

Figure 5.7: Secondary ACFIT solutions for the BR123D IF2 data set, for a subset of the antennas. The polarisation and antenna codes are located on the top left of each panel.

converged. For the 43 GHz BR123D IF2 data set, three iterations were sufficient for convergence to be achieved. The parallel-hand components of the final composite template spectrum are shown in the left panel of Figure 5.6. For the 86 GHz BR123A data set the model fit did not converge sufficiently to be helpful, and the autocorrelation polarisation self-calibration step was not included in the data reduction. The BR123A template spectrum shown in the right panel of Figure 5.6 is the initial RLAVG composite spectrum, with no corrections from the autocorrelation data model.

After the autocorrelation polarisation self-calibration, the final corrected autocorrelation data set was fit to the final composite template spectrum in a secondary ACFIT step. The g_0^{RL} offset of the final template spectrum was determined with UVRAT from the continuum calibrator cross-correlation data, as described above, completing the amplitude calibration. Examples of the final ACFIT solutions for the BR123D IF2 data set are plotted in Figure 5.7.

The final ACFIT step accounts for any changes in the parallel-hand data amplitude after the spectra have been corrected by the autocorrelation data model. The effect of instrumental polarisation on the parallel-hand autocorrelation data would be presented as an amplitude variation with parallactic angle, which is not visible in the secondary ACFIT solutions. We can therefore conclude that at the instrumental polarisation levels and SNR levels of these observations, the effect of instrumental polarisation on the parallel-hand amplitudes is not large.

Two examples of autocorrelation model fits are given in Figure 5.8, from the 43 GHz BR123D IF2 data set. The rotation of Stokes Q spectrum with parallactic angle is visible in the figures.

As mentioned above, the autocorrelation polarisation self-calibration was not sucessful for the 86 GHz BR123A data set. This failure was due to the the low SNR of the autocorrelation spectra, particularly for the cross-polarised data, and due to difficulties in isolating the spectral baseline. There is no emission-free region on the low channel end of the BR123A spectrum in our frequency configuration, which resulted in imperfect baseline fitting. However, when the autocorrelation polarisation

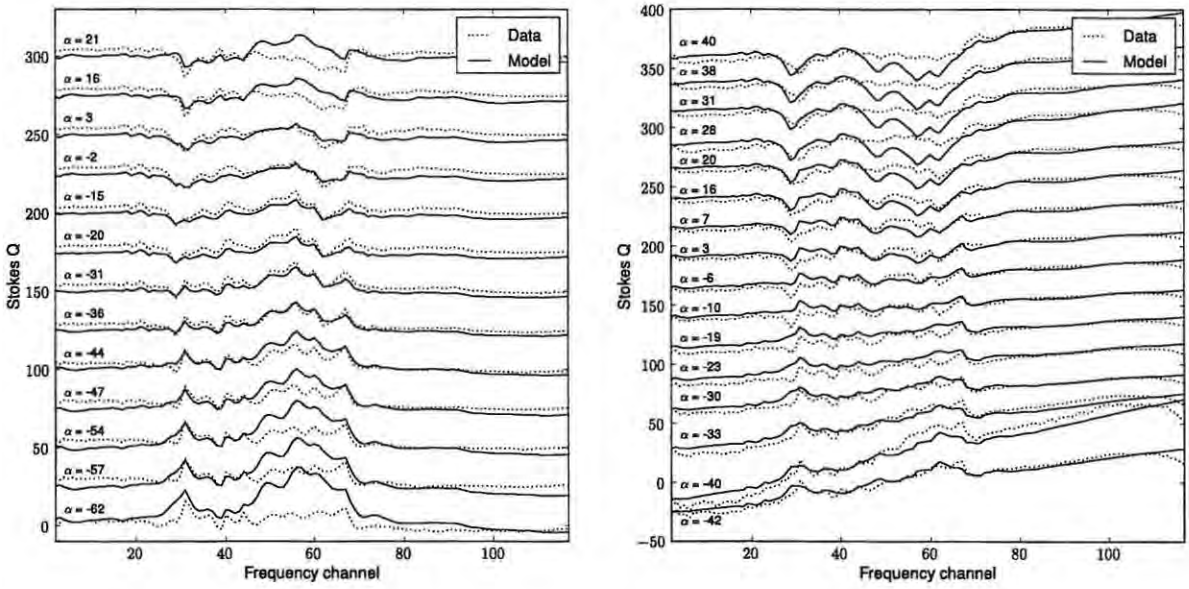

Figure 5.8: Stokes Q autocorrelation spectra for each VY CMa ACPOL solution interval of 14.25 minutes, for the 43 GHz BR123D IF2 data set, for Mauna Kea (left) and Pie Town (right). The data are overlaid with the autocorrelation model fits from the final iteration of the amplitude polarisation self-calibration. The average parallactic angle α for each scan is displayed on the left. The data and model baselines are offset by equal constant amplitudes, in order to view individual spectra.

self-calibration was first attempted for the 86 GHz BR123A data set, it was noted that even for poor fits to the data and higher than expected estimates of the D-terms, there was no systematic variation in the secondary ACFIT solutions with parallactic angle, at a level of statistical significance above the noise level of the solutions. The self-calibration step could therefore be safely omitted.

The autocorrelation model fits in Figure 5.8 can be compared to Figure 10 of Kemball & Richter (2011). Kemball & Richter (2011) performed the autocorrelation self-calibration described above for 43 GHz VLBA observations of the Mira variable TX Cam. Their results give a better fit to the autocorrelation data model than the 43 GHz BR123 VY CMa fit presented in Figure 5.8 of this chapter. The poor quality of the BR123 fit can be attributed to poor baseline subtraction, and relatively weak BR123 cross-hand autocorrelation spectra. The latter factor is due to the weak integrated linear polarisation of supergiant stars relative to Mira variables (e.g. Glenn et al. 2003).

The accuracy of the amplitude calibration is discussed in Section 5.4.

5.3.4 Phase calibration

The phases of VLBI data have slopes in both frequency and time, due to the path of the signal through the atmosphere and receivers, as discussed in Chapter 4.4.3. The phase calibration process consists of determining the slope in frequency (the residual group delay), the slope in time (the residual fringe rate) and the residual phase over specified solution intervals, and correcting them. The theoretical basis of these methods is described in Chapter 4.4.3.

For each data set a reference antenna was chosen and the phase solutions were determined relative to the reference antenna, for which the phase solution was set to zero (Walker 1989). The reference antenna was chosen to be an antenna that was present for a majority of the observing period, had adequate SNR, and was preferentially located towards the centre of the array. The reference antennas used for each data set are listed in Tables 5.5 and 5.6.

Residual group delay

The residual group delay was determined through a fringe fit to the calibrator cross-correlation data (Walker 1989; Diamond 1989). The final cross-correlation bandpasses, the calibrator ACCOR gains and the calibrator amplitude gains were applied to the cross-correlation calibrator data before a final fringe fit was performed using AIPS task FRING. The residual group delay, rate and phase solutions determined by this fringe fit were clipped and smoothed using the task SNSMO.

FRING determines the RCP and LCP residual group delays independently, using the RR and LL parallel-hand data. The RCP and LCP group delay solutions are both set to zero at the reference antenna. The RCP group delay solutions are then measured relative to the RCP group delay at the reference antenna, and the LCP solutions relative to the LCP group delay at the same antenna. This leaves an unknown offset between the RCP and LCP residual group delays (Brown et al. 1989).

The $R-L$ delay offset at the reference antenna was determined following Leppanen et al. (1995). All of the cross-correlation calibrator data containing baselines to the reference antenna were copied to a new data file. The phase solutions calculated in the above fringe fit were applied to this data file. The task SWPOL was then used to switch the polarisation labelling of the file, so that FRING could be run on the r^{RL} and r^{LR} data, re-labelling these data as r^{RR} and r^{LL}. The fringe fit of this cross-polarisation data gave the group delay polarisation offset, which was averaged and stored as a solution table, using task POLSN. These solutions were averaged over the entire observing run, as the $R-L$ delay offset is expected to be constant during the observation (Brown et al. 1989). The absolute magnitudes of the offsets determined from the BK103 and BR23 observations varied from a few nanoseconds up to almost 25 nanoseconds.

Applying the solutions

Before the final phase calibration could be determined for the source data, the solutions found in prior data reduction steps were applied to the VY CMa cross-correlation data, comprising:

- The sampler bias corrections from the autocorrelation VY CMa data.
- The amplitude calibration solutions from template-fitting of the autocorrelation VY CMa data, which included amplitude polarisation self-calibration for the 43 GHz BR123 data sets.
- The g_0^{RL} amplitude offsets from the continuum calibrator cross-correlation data.
- The delay solutions from the final continuum calibrator cross-correlation fringe fit.
- The $R-L$ delay offset from the continuum calibrator cross-correlation data.

At this stage the amplitude calibration process was complete. The two remaining phase calibration steps were finding the residual fringe rate and phase for the VY CMa cross-correlation data.

Residual fringe rate

Given the prior correction for group delay, the fringe rate was determined for a single frequency channel and then applied across the full 128 channels (Reid et al. 1980; Diamond 1989). The channel used to determine the rate should ideally have compact spatial structure, with sufficient SNR on both long and short baselines. The data were first examined and an appropriate channel chosen, subject to those criteria. A rate-only fringe fit was then performed on this channel with all prior calibration applied. The rate solution was then applied to the data and the corrected data were interactively flagged using IBLED in a second pass. These flags were applied to the data and a second fringe fit was performed to give the final residual fringe rate solutions. The solutions were clipped to remove outliers using task SNSMO.

The two fringe fits performed during this rate solution process were attempted with solution intervals ranging from 30 seconds to 3 minutes. In each data set the solution interval that maximised the percentage of good solutions was used; this varied between 1.5 minutes and 3 minutes.

The RCP residual fringe rate solutions were applied to both the RCP and LCP data sets, and the LCP residual fringe rates solved for above were discarded. There should be no significant offset between the RCP and LCP residual instrumental fringe rates (Leppanen et al. 1995; Kemball et al. 1995). However, in the presence of significant circular polarisation, the source visibilities may have differing fringe rates in the two polarisation systems. The same fringe rate solution is therefore applied to both the RCP and LCP systems in order to maintain positional coincidence between the two systems (Kemball et al. 1995).

Residual phase

The residual phase was found using self-calibration, an iterative process, alternating between the image plane and visibility plane (Pearson & Readhead 1984). This is implemented in AIPS with the two tasks CALIB and IMAGR. CALIB compares the observed visibility data with visibilities derived from a source model and returns the complex antenna-based gain solutions required to make the real visibility data fit the model visibilities. In the self-calibration procedure used here, CALIB was used to find phase gain solutions only, not amplitude gains, in order to preserve Stokes V. The task IMAGR applies the Clark CLEAN algorithm decribed in Chapter 4.5 to image and deconvolve the visibility data.

The self-calibration was performed on a single reference channel on the r^{RR} data only. The same channel was used in the self-calibration as in the fringe rate calibration. In practice, the self-calibration method first used CALIB to compare the single channel visibility data to a unit flux density point source model. The resultant solutions were applied to the visibility data and the calibrated data were imaged with IMAGR. The IMAGR CLEAN continued down to the first negative component, then the deconvolution was terminated. The resulting CLEAN components were then used as the source model input to CALIB, in the next iteration of the self-calibration procedure. The first three iterations of self-calibration used a solution interval of 3 minutes in CALIB and stopped CLEAN deconvolution in IMAGR at the first negative component. Thereafter the solution interval in CALIB was decreased linearly at a rate that would reach 20 seconds in the final tenth iteration. The CLEAN deconvolution limit used between the third and tenth iterations was decreased linearly from the off-source root mean squared (RMS) noise in the third self-calibrated image to the target RMS thermal noise in the tenth

Project Code	Line	Frequency Band	Integration Time	Number of Antennas	Reference Antenna†	Clean Beam [μarcsec]
BK103A	v=2 J=1-0	43 GHz	2.097152	10	PT	790 × 170
BK103A	v=1 J=1-0	43 GHz	2.097152	10	LA	820 × 170
BK103A	v=0 J=1-0	43 GHz	2.097152	10	PT	860 × 200
BK103C	v=1 J=2-1	86 GHz	2.097152	8	LA	1220 × 360

Table 5.5: BK103 data reduction parameters for the imaged ^{28}SiO maser lines. The columns from left to right are: project code, the spectral line observed, the frequency band of the observation, the correlator integration time, the number of antennas used in the observations, the reference antenna used in the data reduction and the size of the clean beam used to restore the final VY CMa image.
† Abbreviations found in Table 5.1.

iteration. During this iterative process, alternating sets of visibility plane and image plane constraints are enforced. This technique is broadly equivalent to regularisation.

The RMS thermal noise ΔS in an interferometric image in natural weighting is given by

$$\Delta S = \frac{\text{SEFD}}{\eta_s \sqrt{N_{vis} \Delta t_{corr} \Delta \nu}}$$

where N_{vis} is the total number of visibility data being imaged, Δt_{corr} is the correlator integration time, $\Delta \nu$ is the bandwidth, η_s is the net quantisation and correlator efficiency (Thompson et al. 2001, pg 191). The SEFD provided by the VLBA Observational Status Summary is 1436 Jy for 7mm observations and 4000 Jy for 3mm observations (Ulvestad 2008). The integration times for each data set are given in Tables 5.5 and 5.6 and the channel widths in Sections 5.1 and 5.2.

VY CMa is a particularly bright maser source, so the imaging is limited predominantly by deconvolution and calibration errors rather than by thermal noise. The images are consequently dynamic-range limited, although not profoundly so. The self-calibration could therefore only clean down to a flux of several times the thermal noise before the imaging would diverge.

For each of the BK103 and BR123 observations the self-calibration was repeated to find optimal values of the solution interval and final CLEAN flux threshold. The parameters that produced the best final RR image were used in the final self-calibration. The images were judged according to the following criteria:

- The lowest limiting CLEAN flux density before divergence.
- The achieved RMS noise in an off-source region of the map.
- The deepest negative component in the image.

Deep negatives in the images are indicative of deconvolution or calibration errors, so the deepest negative in an image provides a means to assess the quality of the map. The next chapter describes how these values can be used to derive an intensity threshold value for real maser emission, below which the emission is considered noise or deconvolution error. The RMS noise in the images was measured with AIPS verb IMSTAT. It was calculated in an emission free corner region of the maps, in a box of size approximately (10 x 10) % of the overall map dimensions.

Project Code	Line	Frequency Band	Integration Time	Number of Antennas	Reference Antenna†	Clean Beam [μarcsec]
BR123A	v=1 J=2-1	86 GHz	1.966080	8	OV	420 × 90
BR123D	v=2 J=1-0	43 GHz	2.097152	9	KP	430 × 140
BR123D	v=1 J=1-0	43 GHz	2.097152	10*	KP	460 × 150

Table 5.6: BR123 data reduction parameters for the imaged ^{28}SiO maser lines. The columns from left to right are: project code, the spectral line observed, the frequency band of the observation, the correlator integration time, the number of antennas used in the observations, the reference antenna used in the data reduction, and the size of the clean beam used to restore the final VY CMa image.

† Abbreviations found in Table 5.1.

* This observation included one VLA antenna.

This self-calibration was used to solve for the residual phase of the RCP data only. The offset between the RCP and LCP residual was then determined and applied to the RCP residual phase solutions to find the residual LCP phase. The residual phase calibration is performed in this manner in order to retain positional coincidence between the RCP and LCP data, which is lost if the self-calibration is performed independently for RCP and LCP (Kemball et al. 1995; Homan & Wardle 1999).

The residual $R - L$ phase offsets at each antenna were determined from the calibrator cross-correlation data. The calibrated continuum calibrator cross-correlation data were averaged over all spectral channels. The r^{RR} visibility data was then divided by the r^{LL} visibility data using AIPS task DIFRL. This division gives a visibility data set with phases that are the difference between the phases of the original data sets, in this case, the difference between the r^{RR} and r^{LL} phases. The task CALIB was then used to compare the new data set to a point source model at the phase centre, which has zero phase. The phase solutions calculated by CALIB are therefore the negative of the differences between the r^{RR} and r^{LL} phases, calculated over each solution interval.

The RCP residual phase solutions solved for during the self-calibration were applied to the RCP and LCP data sets. The residual phase offset determined above was then negated and applied to the LCP data to account for the offset between the RCP and LCP phases. The AIPS tasks SNCOR and SNDUP were used to apply the phase offset.

5.3.5 Instrumental polarisation calibration

The final calibration step was solving for the instrumental polarisation. The D-terms were determined using the AIPS task SPCAL, from the VY CMa cross-correlation data (Kemball et al. 1995). Before the SPCAL task was run, all of the calibration solutions calculated during the preceding data reduction process were applied to the VY CMa cross-correlation data.

5.3.6 Imaging

After all of the calibration solutions were obtained and applied to the VY CMa cross-correlation data, the data were imaged and deconvolved using CLEAN (Cornwell & Braun 1989), as implemented in the AIPS task IMAGR. IMAGR was run four times for each data set, to image each of the four Stokes

Calibrator	Purpose
BK103	
J0521+166 (3C138)	Primary flux calibrator; Primary polarisation calibrator
J0359+5057	Secondary polarisation calibrator
BR123	
J0521+166 (3C138)	Primary flux calibrator; Primary polarisation calibrator
J0609-1542	Secondary polarisation calibrator
J0423-0120	Secondary polarisation calibrator

Table 5.7: Calibrators observed with the VLA as part of the BK103 and BR123 projects.

parameters.

Each image was created with 4096 by 4096 pixels in sine projections of right ascension and declination (Greisen 1994), using cell sizes of 30 μarcsec. The sizes of the clean beams used in restoring each of the image cubes are given in Table 5.5 and Table 5.6. The BK103 data sets were imaged with pure natural weighting. When the BR123D IF2 data set was imaged it was found to have a significant amount of relatively low intensity extended emission. When imaged with natural weighting this led to deep negatives and spurious features in the images. The BR123 data sets were therefore imaged with pure uniform weighting, which minimised these problems.

Channels 10 through 118 of the full 128 frequency channels were imaged. The edge channels were not imaged to avoid possible corruption by bad bandpasses at the edges of the bands. This gave four image cubes with 109 channels each.

5.3.7 EVPA calibration

The method used to determine the phase gain and the $R - L$ phase offsets leaves an unknown RCP and LCP phase difference at the reference antenna, as explained in Chapter 4.4.3. Equivalently, the true EVPA in the image plane is unknown and must be determined with respect to a polarisation calibrator.

The EVPA calibration was a two-step process because most absolute polarisation calibrators are resolved by the VLBA, as discussed in the description of the observations in Section 5.1. The first step was to observe unresolved polarisation calibrators of unknown EVPA during the VLBA observations (hereafter termed secondary polarisation calibrators). The secondary polarisation calibrators were then observed with the VLA along with a primary polarisation calibrator, for which the absolute EVPA is known (Kemball 1999). This allowed the absolute EVPA of the secondary calibrators to be determined relative to the primary. The VLBA images of the secondary calibrators were then used to transfer absolute EVPA calibration to the target source VY CMa. This method of EVPA calibration was only possible for the 43 GHz observations as the VLA does not have 86 GHz receivers.

The VLBA data for the secondary polarisation calibrators from each of the BK103 and BR123 data sets were reduced in AIPS. The calibration method followed the reduction path outlined for continuum data in the AIPS Cookbook (Greisen 2004), applying the same calibration solutions as those applied to the VY CMa data. The calibrated continuum calibrator data were then averaged across all channels and self-calibrated to find the residual phase. The continuum calibrators were then

Project	Line	Source	Absolute EVPA [Deg]	Measured VLBA EVPA [Deg]	Rotation [Deg]
		3C138	-14		
BK103A	v=0 J=1-0 ^{28}SiO	J0359+5057	62.25±0.29	-64.92±0.74	127.17±0.80
BK103A	v=1 J=1-0 ^{28}SiO	J0359+5057	62.25±0.29	-57.95±0.75	120.20±0.80
BK103A	v=2 J=1-0 ^{28}SiO	J0359+5057	62.25±0.29	-83.85±0.72	146.10±0.78
BR123D	v=1 J=1-0 ^{28}SiO	J0423-0120	-62.40±0.19	-55.61±0.62	-6.79±0.65
BR123D	v=2 J=1-0 ^{28}SiO	J0423-0120	-62.40±0.19	27.64±0.60	-90.04±0.63

Table 5.8: Electric vector position angles calculated during the BK103 and BR123 calibration processes. The columns from left to right are: project code, observed spectral line, polarisation calibrator, absolute EVPA, EVPA from the VLBA observations, rotation required to align the VLBA EVPA to the absolute EVPA. The absolute EVPA of the primary polarisation calibrator 3C138 was set to -14° and the absolute EVPAs of the secondary calibrators were determined from VLA observations.

imaged with IMAGR, using a cell size of 30 μarcsec and image dimensions of 256 by 256 or 512 by 512 cells. The calibrators were imaged in Stokes I, Q and U.

The calibrator J0609-1542 in the BR123 data set was discarded at this stage. It was intended for use as a secondary polarisation calibrator. However, the final polarisation images of J0609-1542 showed that this calibrator is partially resolved at 43 GHz in Stokes Q and U, with different polarisation position angles for two separate components. This was verified by comparison with 15 GHz linear polarisation images of J0609-1542 from the MOJAVE database (Lister et al. 2009). The 2007 15 GHz MOJAVE polarisation image also shows different polarisation position angles across the J0609-1542 image. The calibrator J0609-1542 could therefore not be used robustly as an EVPA calibrator.

The VLA data for the primary and secondary polarisation calibrators were reduced in AIPS following the VLA Calibrator Manual (Perley & Taylor 2003) and the AIPS Cookbook (Greisen 2004). The sources observed during the VLA observations accompanying the BK103 and BR123 VLBA observations are listed in Table 5.7. The VLA data were loaded into AIPS using task FILLM. Baseline corrections were performed at some antennas using task CLCOR, to adjust antenna positions to reflect more accurate antenna positions determined in later VLA service observations. The fluxes of the absolute flux density calibrators (listed in Table 5.7) were set with SETJY. The first integration time of each scan was flagged with the task QUACK to remove bad data at the beginning of scans. This was followed by interactive flagging with IBLED and UVFLG where necessary. In the BR123 VLA data, antennas 17, 20 and 24 were flagged completely. A Q-band model of 3C138 was created with task CALRD, for use in the phase and amplitude calibration. An initial phase calibration was performed with CALIB. The phase solutions were applied to the data and an amplitude and residual phase calibration was then performed with CALIB. In both cases the CALIB solutions on the 3C138 data used the CALRD source model. The flux densities of the secondary calibrators were determined using the task GETJY. The instrumental polarisation was then solved for with PCAL. The fully calibrated VLA data for each calibrator was finally imaged with IMAGR, down to the RMS thermal noise

limit given by

$$\Delta S = \frac{42.4K}{\sqrt{N_{vis}\Delta t_{corr}\Delta\nu}}\text{mJy} \tag{5.3}$$

where N_{vis} is the total number of visibility data being imaged, Δt_{corr} is the correlator integration time in seconds, $\Delta\nu$ is the bandwidth of the observations in MHz and K is a system constant which is equal to 35 for Q-band VLA observations (Ulvestad et al. 2009). The data were imaged in I, Q and U for each of the two IF bands separately in the VLA data, by design, for reasons discussed below.

The linear polarisation position angle was determined for each calibrator image, from the VLBA and VLA data sets. The position angle was calculated as EVPA $= \frac{1}{2}\tan^{-1}\frac{U}{Q}$. The Q and U values were extracted from the images with AIPS task IMSTAT, taking the mean value in a small box in the centre of the the calibrator emission. The uncertainties in the VLBA EVPAs were calculated from the Stokes Q and U RMS values, which were determined with IMSTAT in a corner box with sides 10% of the image width.

The VLA Calibrator Manual (Perley & Taylor 2003) reports an absolute $R-L$ phase difference of -28° at 43 GHz for 3C138 in 1999. This equates to an absolute linear polarisation position angle of -14°. The 3C138 polarisation position angles from each VLA data set were therefore set to -14° by rotating the position angle by an appropriate number of degrees. The same rotation was applied to each of the secondary calibrators in the VLA data to establish the absolute EVPAs of the secondary calibrators. The absolute EVPAs were determined separately from the images of each calibrator in both of the IF bands used in the VLA observations, giving two EVPA values for each VLA calibrator. The two values were averaged to give the final absolute EVPAs, listed in Table 5.8. The uncertainties in the absolute EVPA were taken to be the difference between the EVPA calculated from each IF band, divided by the $\sqrt{2}$.

The VLBA images of the secondary calibrators were then compared to their EVPA-calibrated VLA images. The linear polarisation position angles measured from the VLBA images were rotated to align with the absolute EVPAs calculated from the VLA images. The rotation angles are recorded in Table 5.8. The rotation angle errors were determined through propogation of the VLA and VLBA EVPA errors. This rotation accounts for half the residual phase offset between RCP and LCP at the reference antenna.

The position angle rotation calculated from the calibrators was ultimately applied to the source data to establish the absolute VY CMa EVPA.

5.4 Circular polarisation calibration

One of the primary goals of this thesis requires measurement and comparison of the levels of circular polarisation in the 43 GHz and 86 GHz SiO maser emission. The circular polarisation of the VY CMa SiO maser emission is expected to be low, at a level of only a few percent (e.g. McIntosh et al. 1994; Herpin et al. 2006). Very accurate calibration is therefore required for the circular polarisation measurements.

The accuracy of the circular polarisation measurements is dependent on the accuracy of the relative amplitude calibration of the RCP and LCP data. An error in the g_0^{RL} offset discussed above will systematically offset all of the RCL and LCP data, leading to spurious Stokes V in the final maps.

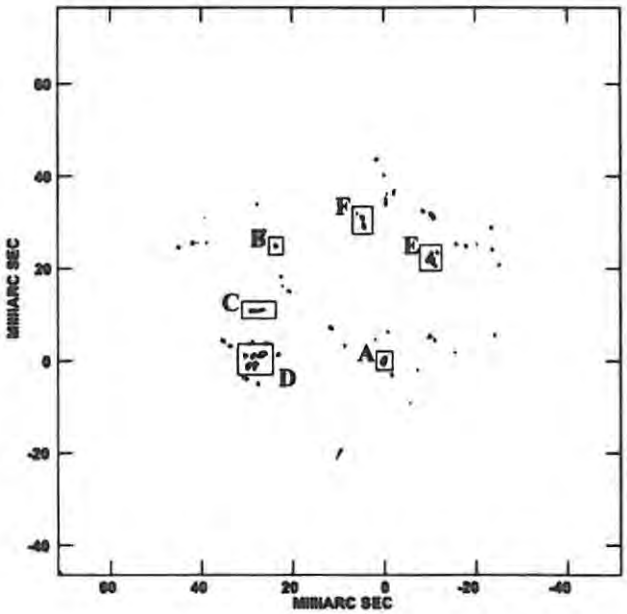

Figure 5.9: A contour plot of the Stokes I emission for the line v=1 J=2-1 ^{28}SiO, from observation BR123A. The six groups of spots used to illustrate the effect of applying varying ϵ_{gRL} offsets are shown on the plot. The change in m_c with ϵ_{gRL} for the maser spots in each of these regions is plotted in Figure 5.10.

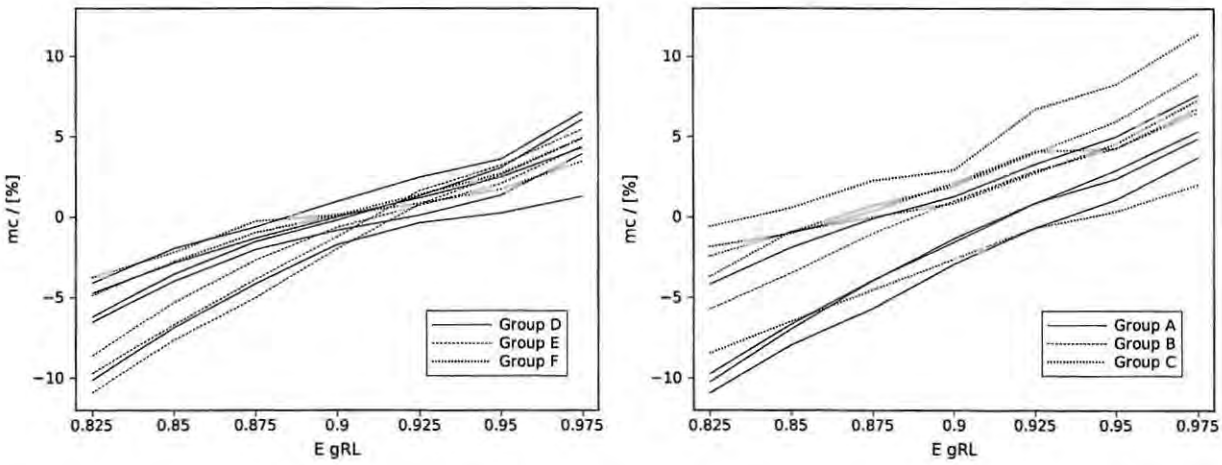

Figure 5.10: The change in m_c with ϵ_{gRL} for twenty spots in the v=1 J=2-1 ^{28}SiO map, from observation BR123A. Each line represents a different spot, where the line styles denote groups of spots. The spots are grouped in six regions, as shown in Figure 5.9.

This can be illustrated by applying a range of artificial multiplicative g^{RL} offsets ϵ_{gRL} in the amplitude calibration stage of the VY CMa data reduction sequence, and measuring the resultant circular polarisation of the final images. This was done for the 86 GHz BR123A data set, using seven ϵ_{gRL} values of 0.825, 0.85, 0.875, 0.9, 0.925, 0.95, 0.975. The data were reduced and imaged in Stokes I and V for each of the ϵ_{gRL} value data sets. Twenty spots were identified in the Stokes I maps to be used in testing the final circular polarisation levels. The spots are grouped in six regions, labelled A through F in Figure 5.9. For each of the seven I cubes the twenty spots were fitted with Gaussian functions using the AIPS talk JMFIT. The values of I and V were then extracted from the map at the pixel position of the Gaussian peak. The I and V values were used to calculate the m_c value of each spot, where $m_c = V/I$.

The change in percentage m_c with the applied ϵ_{gRL} is plotted in Figure 5.10, for each of the twenty spots. The percentage m_c increases systematically with increasing ϵ_{gRL} value. However, when the Stokes V value of a spot becomes close to zero, then the deconvolution taking place during the imaging process does not find any emission at the location of the Stokes I spot. When this is the case, the measured Stokes V is the residual noise floor. This effect is particularly visible for spot groups D, E and F.

Figure 5.10 illusrates the fact that an incorrect value of g_0^{RL} will offset all of the m_c measurements for a particular data set. This is particularly problematic in terms of the science goals of this thesis, which include comparisons of the circular polarisations of the different SiO maser transitions.

For the Epoch 1 BK103 data sets, the g_0^{RL} offset was determined through a differential polarisation template-fit, by fitting the r^R component of the single-scan template spectrum to the r^L component of the same template spectrum using ACFIT. In the first attempt at reducing the Epoch 2 BR123 data the g_0^{RL} offset was also determined in this manner. However, as illustrated in Figure 5.3.3 in Section 5.5, the SNR of the 86 GHz spectra is considerably poorer than that of the 43 GHz spectra. This led to poorer differential polarisation template-fits for the 86 GHz data. For the 43 GHz BR123 data the differential polarisation template-fit g_0^{RL} offsets had uncertainties of about 0.5%, while the 86 GHz BR123 g_0^{RL} offset uncertainties were significantly higher, usually a few percent.

Because of the importance of accurate m_c measurements, alternative means of amplitude calibration were attempted and new methods developed, as described in the previous section. The final amplitude calibration method applied to the BR123 data set has been described in Section 5.3.3. The use of a composite RLAVG template spectrum in ACFIT, and the use of the UVRAT global continuum calibrator fit method of finding the g_0^{RL} offset were chosen over the differential polarisation template-fit method using a single-scan template spectrum, because of the poor performance of the latter method at 86 GHz.

The errors in the global continuum calibrator fit g_0^{RL} results were determined through jackknife estimation. The data with baselines to a particular antenna were left out of UVRAT when solving for g_0^{RL}. This was repeated for all antennas to provide a sample of g_0^{RL} estimates. The resulting RMS uncertainties are listed in Table 5.9.

The accuracy of the UVRAT g_0^{RL} results was also assessed through imaging a calibrator for a range of multiplicative g^{RL} offsets, a method also described in Section 4.4.2 of the previous chapter. This entails applying the source amplitude calibration solutions to a continuum calibrator data set, then imaging the calibrator for a range of user-specified ϵ_{gRL} offsets. Calibrator J0423-1020 was chosen for

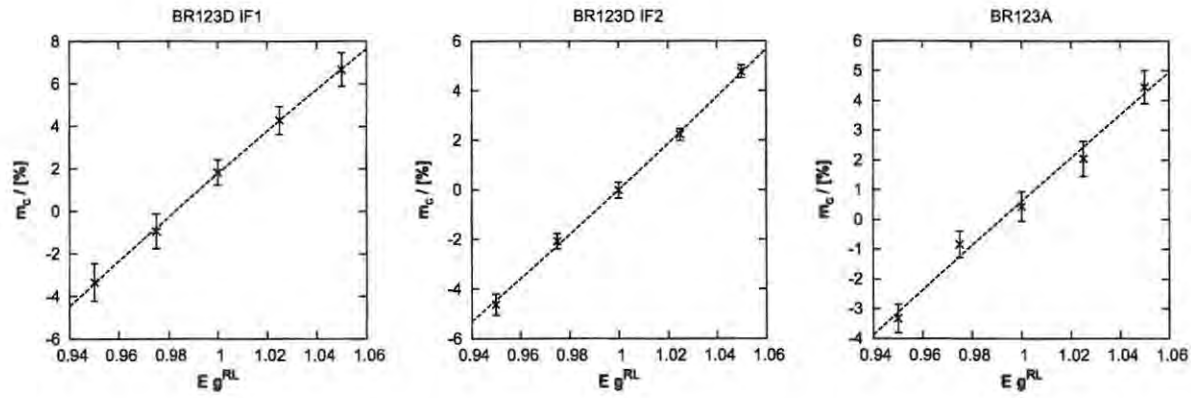

Figure 5.11: Plots of circular polarisation m_c versus ϵ_{gRL} offset for calibrator J0423-0120, for the 43 GHz data sets BR123D IF1 (left) and BR123D IF2 (middle), and the 86 GHz BR123A data set (right). For each data set a second order polynomial was fitted to the data, which is plotted on the figures.

this test because it is the brightest calibrator in the BR123 observations that is observed throughout the observing run, and no circular polarisation has been detected towards J0423-1020 (Homan et al. 2001; Homan & Lister 2006; Vitrishchak et al. 2008; Agudo et al. 2010).

The J0423-1020 data were extracted from the full calibrator cross-correlation data set, applying the phase gains already calculated for the continuum calibrator data, the ACCOR quantisation correction, and the ACFIT and UVRAT amplitude calibration gains determined during the VY CMa amplitude calibration described in the amplitude calibration section, Section 5.3.3. An additional user-specified ϵ_{gRL} offset was applied to the data at this stage.

The J0423-1020 data were then interactively flagged. Ten iterations of self-calibration were performed to find the residual phase, imaging down to a final flux density of a few times the thermal noise. The data were imaged with a cell size of 30 μarcsec image dimensions of 256 by 256 cells. The instrumental polarisation D-tems were then determined with SPCAL. The fully calibrated J0423-1020 data were imaged in Stokes I and V. The BR123D IF1 and BR123D IF2 data were imaged with pure uniform weighting. For the BR123A data set, pure uniform weighting led to severe corrugations across the Stokes V image, with a peak-to-peak amplitude of $\sim$ 2% of the peak Stokes I value. A robustness parameter of zero was found to remove the corrugations, and was therefore used in imaging the BR123A data set. The calibration and imaging of J0423-1020 was performed using ϵ_{gRL} offsets of 0.95, 0.975, 1.0, 1.025 and 1.05.

J0423-0120 was only observed for nine scans of approximately seven minutes each over the course of the BR123 observations, so the J0423-0120 data set does not contain a large number of visibilities. When the ACFIT amplitude corrections were interpolated from the VY CMa scans to the J0423-0120 scans, visibility data from times when there was no interpolated amplitude solution were lost. This further decreased the number of visibility points that were ultimately imaged, so that the final data sets only had between 6000 and 15000 visibilities. Deconvolution errors can be introduced when imaging with such a small number of visibilities. It was a concern that deconvolution errors may bias the circular polarisation values calculated from the Stokes I and V images. A range of interpolation methods and flagging limits were therefore used to find the optimal means to interpolate the VY CMa amplitude solutions to the calibrator data, retaining enough data to image while removing data where

Project Code	Line	Frequency Band	g_0^{RL} Error	m_c Error
BR123A	v=1 J=2-1	86 GHz	0.0085	0.6081%
BR123D IF1	v=2 J=1-0	43 GHz	0.0075	1.7662%
BR123D IF2	v=1 J=1-0	43 GHz	0.0074	0.0006%

Table 5.9: The circular polarisation accuracy parameters for the BR123 data sets. The columns from left to right are: project code, the spectral line observed, the frequency band of the observation, the amplitude calibration g_0^{RL} jackknife error estimate, the circular polarisation offset at $\epsilon_{gRL} = 1$.

interpolation errors are most extreme. The method finally chosen to apply in the reduction was to use a three point median window filter to interpolate the data, and an interpolation limit of 14.25 minutes, half the length of a VY CMa scan.

The level of circular polarisation of the calibrator was determined from the final Stokes I and Stokes V images, for each ϵ_{gRL} offset. The Stokes I and V values were taken to be the average values over a box covering the centre of the Stokes I emission. The resulting circular polarisation values are plotted in Figure 5.11. The errors in the measurements were determined by measuring the off source RMS noise in a small box in the corner of the Stokes I and V maps. These error bars are shown in the figure.

The calibrator imaging method of determining g_0^{RL} uses the same data set as the final UVRAT step in the VY CMa amplitude calibration method. Applying the source amplitude calibration solutions to the calibrator, including the UVRAT value, should therefore give a $m_c = 0$ intercept for $\epsilon_{gRL} = 1$. The deviation of m_c from zero provides an upper bound on the error in the R/L amplitude calibration, given interpolation errors. In order to find the m_c offset at $\epsilon_{gRL} = 1$, a second order polynomial was fitted to the data points in the figures. The m_c values calculated at the $\epsilon_{gRL} = 1$ intercept of the fitted curved are listed in Table 5.9.

Even for the best choice of interpolation and imaging parameters, the images J0423-1020 were of poor quality, displaying off-source negative and positive artifacts. Whether the cross-correlation calibrator data are used to solve for the g_0^{RL} offset directly with UVRAT, or through the additional step of imaging the calibrator, both methods suffer from interpolation errors. The calibrator imaging test suffers from additional imaging errors due to the limited number of visibilities, and is more sensitive to outliers. The calibrator imaging estimates of g_0^{RL} are consequently less reliable than the UVRAT estimates.

In the case of the BR123D IF1 data set the calibrator imaging gives a particularly poor result, giving a fitted circular polarisation of 1.7662% at $\epsilon_{gRL} = 1$ (Table 5.9). Of the three data sets, the imaging artifacts were most extreme for the Stokes V BR123D IF1 images, with deep off-source negatives around the source region. When the Stokes V values for this data set are averaged over a larger box incorporating the negative regions around the Stokes I source position, the fitted $\epsilon_{gRL} = 1$ intercept occurs at $\|m_c\| \leq 0.5\%$.

Outside of this discrepant BR123D IF1 calibrator imaging estimate of g_0^{RL}, the results in Table 5.9 show that the errors in the g_0^{RL} estimates are $\leq 1\%$. The circular polarisation calibration method described in this chapter and applied to the BR123 data set can therefore be assumed to be correct

to within $\sim 1\%$.

The method described in this chapter is presented in Kemball & Richter (2011), where the accuracy is estimated to be $\leq 0.5 - 1\%$ at 43 GHz and $\leq 1\%$ at 86 GHz from VLBA observations of SiO maser emission towards TX Cam. The poorer performance reported for the BR123 data set in this thesis is due in part to the greater distance between the source VY CMa and calibrators J0423-1020 and J0609-1542, compared to the distance between the source and calibrators used in Kemball & Richter (2011). The BR123 data set also contained less data for each calibrator than in the data set used in Kemball & Richter (2011). The greater distance coupled with the low elevation of the VY CMa observations led to more severe interpolation errors for the observations presented in this thesis.

5.5 Phase referencing

In the data reduction method described in this chapter, the final residual phase is determined through the process of self-calibration, as described in Section 5.3.4. The self-calibration was performed on data from a single reference channel with strong compact emission, and the solutions applied to all channels. When all of the channels are finally imaged to make a data cube, the positions of spots in all channels are then relative to the phase centre of the reference channel, which was set by the self-calibration solutions. In this process absolute position information is lost.

One of the goals of this thesis is to compare maser emission from different SiO maser lines. In this context it is important to know the absolute alignment of the maps of different SiO lines. The spatial offset between the maser emission from different SiO lines provides an observational test of which pumping mechanism is sustaining the maser, as discussed in Section 3.3. It is also necessary to align the maps of different maser lines in order to analyse characteristics of the emission in different lines at the same physical location. For example, observing the levels of circular polarisation of co-located v=1 J=1-0 and J=2-1 SiO masers provides a test of maser polarisation models, as discussed in Chapter 3.4.9.

The lack of absolute alignment is therefore problematic. This issue has arisen in numerous comparisons of different SiO maser transition maps, from the earliest v=1 and v=2 J=1-0 SiO comparison made by Miyoshi et al. (1994). A number of methods have been used to overcome this problem and are discussed in Chapter 6.4.

For the purposes of this thesis, an attempt was made to register the maps in the BR123 data set using a phase referencing technique. The observations of VY CMa were interleaved with observations of calibrator J0731-2341 with a duty cycle of 40 seconds, with the intention of using J0731-2341 as a phase referencing calibrator. VY CMa was correlated at a position of right ascension $07^h\ 22^m\ 58.3315^s$, declination $-25°\ 46'\ 03.174''$ (J2000) (Perryman et al. 1997). J0731-2341 is the second closest source to VY CMa on the VLBA calibrator list[4], with a separation of 2.78°. It was chosen over the closer calibrator J0725-2640 because of it's greater flux density at 8.6 GHz, which is the higest frequency of observations reported for these calibrators in the VLBA calibrator list.

The phase referencing technique entails applying the same phase calibration to the J0731-2341 and the VY CMa data. Phase calibrated maps of the source and calibrator J0731-2341 would then be produced for all of the BR123 data sets. The VY CMa images of different transitions would be

[4] www.vlba.nrao.edu/astro/calib

aligned by aligning each accompanying J0731-2341 map.

Unfortunately, the phase-referencing with this choice of phase calibrator proved unsuccessful, and a different technique was used to align images in separate transitions, as discussed in the following chapter.

Chapter 6

Results

This chapter presents the results of the two epochs of VLBA observations (projects BK103 and BR123, as enumerated in Tables 5.2 and 5.4 of Chapter 5).

The results from the Epoch 1 BK103 observations are presented in Section 6.1 below, followed by the Epoch 2 BR123 results in Section 6.2. The results are presented in this chapter in the form of images in both Stokes $\{I, V\}$ and linear polarisation. For the J=1-0 data sets, the orientation of the EVPAs were calibrated following Section 5.3.7 of the previous chapter, and trace the true absolute EVPA in the plane of the sky. Absolute EVPA calibration was not however possible for the J=2-1 data sets, as the VLA does not operate at 86 GHz.

The Epoch 2 BR123 observations were much more sensitive than the Epoch 1 BK103 observations, and could be more accurately calibrated in amplitude, as discussed in Chapter 5. The Epoch 2 observations were therefore used to perform the polarisation tests proposed in Chapter 3. In order to perform these tests, the Stokes parameters were measured at component-level. The method of identifying maser features and extracting their Stokes parameter values is described in Section 6.3. For each spot the Stokes parameter values were then used to derive the fractional circular and linear polarisation, as described further in Section 6.5 below. The parameters of the fitted maser features of the Epoch 2 data that were imaged are enumerated in tables at the end of the chapter.

Absolute astrometric information is lost during the data reduction process. Methods of aligning maser maps of different transitions are discussed in Section 6.4, and the aligned maps are presented in Section 6.4.1. The maps presented in previous sections are not aligned across different transitions.

6.1 Epoch 1 results

The imaged Epoch 1 observations are summarised in Table 6.1 and displayed in Figures 6.1 to 6.4. For each spectral line the associated figure includes the following sub-plots: i) a contour plot of the total intensity emission (Stokes I); ii) an image of the linear polarisation distribution; iii) a contour plot of the Stokes V emission; and, iv) the single dish autocorrelation spectrum superimposed on a summed interferometric spectrum of the Stokes I emission over the inner 90% of each channel of the interferometric image cube. The images presented in sub-plots (i) to (iii) are colour-coded to indicate frequency panel of the image cube. Channel-by-channel contour plots of the Stokes I, linear polarisation, and Stokes V images for each spectral line are provided in Appendix A to D of the electronic version of this thesis.

Spectral line	Proj. code	FreqID	IF	Figure
^{28}SiO v=1 J=1-0	BK103A	2	3	6.1
^{28}SiO v=2 J=1-0	BK103A	2	1	6.2
^{28}SiO v=0 J=1-0	BK103A	3	1	6.3
^{28}SiO v=1 J=2-1	BK103C	5	1	6.4
^{28}SiO v=1 J=1-0	BR123D		2	6.6
^{28}SiO v=2 J=1-0	BR123D		1	6.7
^{28}SiO v=1 J=2-1	BR123A		1	6.8

Table 6.1: List of the Epoch 1 images, displayed in Figures 6.1 to 6.4 (top), and the Epoch 2 images, displayed in Figures 6.6 to 6.8 (bottom). The columns from left to right are: spectral line, project code, Frequency ID, IF number, and the figure where the images of the line are displayed. Further details of this observing epoch are given in Table 5.4.

In Figure 6.5 the total-power spectra for the four spectral lines imaged in the Epoch 1 observations are plotted together, alongside the corresonding Epoch 2 total-power spectra.

6.2 Epoch 2 results

From the Epoch 2 observations, the imaged spectral lines are summarised in Table 6.1 and displayed in Figures 6.6 to 6.8. For each spectral line the associated figure includes the same four sub-plots described above for the Epoch 1 observations. Channel-by-channel contour plots of the Stokes I, linear polarisation, and Stokes V images for each spectral line are provided in Appendix E to G of the electronic version of this thesis.

The motivation for observing the SiO maser emission with VLBI was to avoid spatial blending, so that the emission from different transitions can be compared on a component-level for coincident maser features. This requires that the maser emission images obtained from the various SiO transitions be compared at the same angular resolution. However, the (u,v) coverage is not identical for the three imaged BR123 observations, because of differences in observing frequency and the participation of different subsets of antennas. The VLA antenna was included in the BR123D project observing the ^{28}SiO v=1 J=1-0 spectral line only, and only contributed to the BR123D IF2 data set.

The resolution of the final image is given by the size of the restoring beam, which is listed in Table 5.6 in the previous chapter, and in the caption of each of the figures below. In order to enforce the condition that all three maps be compared at the same angular resolution, the images were restored from their CLEAN components again, but using the same restoring beam for all of the maps. The 43 GHz BR123D IF2 (v=1 J=1-0) image had the largest beam size of the three, 0.46 × 0.15 mas, so the BR123D IF2 beam was used to establish the resolution scale.

The image restoration with the larger clean beam was performed with the AIPS task RSTOR. For each data set, all four Stokes cubes were restored with the larger beam size (0.46 × 0.15 mas) and all subsequent image analysis was performed on these image cubes.

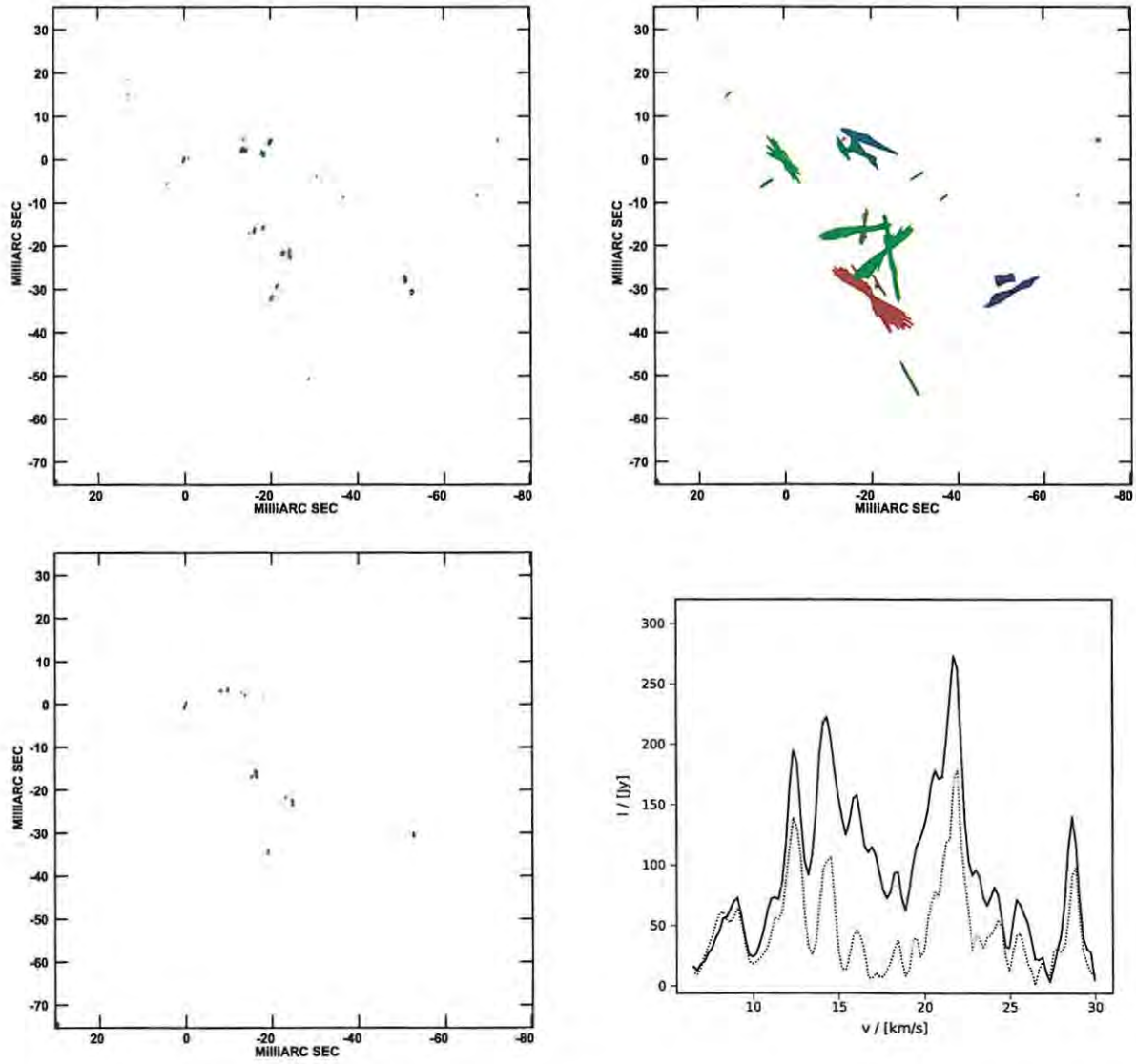

Figure 6.1: Epoch 1 ^{28}SiO v=1 J=1-0 maser images (BK103A).

Top left: Contour plot of the total intensity (Stokes I) maser emission. The contour levels are -20, 20, 40, 60 and 80% of the peak brightness in the Stokes I cube, 19.18 Jy/beam.

Top Right: The linear polarisation distribution of the maser emission, calculated from the underlying Stokes Q and U cubes. The length and orientation of the vectors represent the linearly-polarised intensity and position angle of the linear polarisation, with a vector length of 1 mas = 8.33×10^{-2} Jy/beam.

Bottom Left: Contour plot of the Stokes V maser emission. The contour levels are -30, 30% of the absolute value peak brightness in the Stokes V cube, 0.66 Jy/beam. Negative contours are represented by dashed lines.

Bottom Right: Single-dish total intensity autocorrelation spectrum at Los Alamos (solid) and the summed interferometric total intensity spectrum (dotted).

The synthesised beam is shown in the bottom left of each contour plot, and is 0.82 × 0.17 mas in half-power with a position angle of -11.01°. The radial velocity of the emission is colour-coded, with the most redshifted features being red and the most blueshifted features, blue.

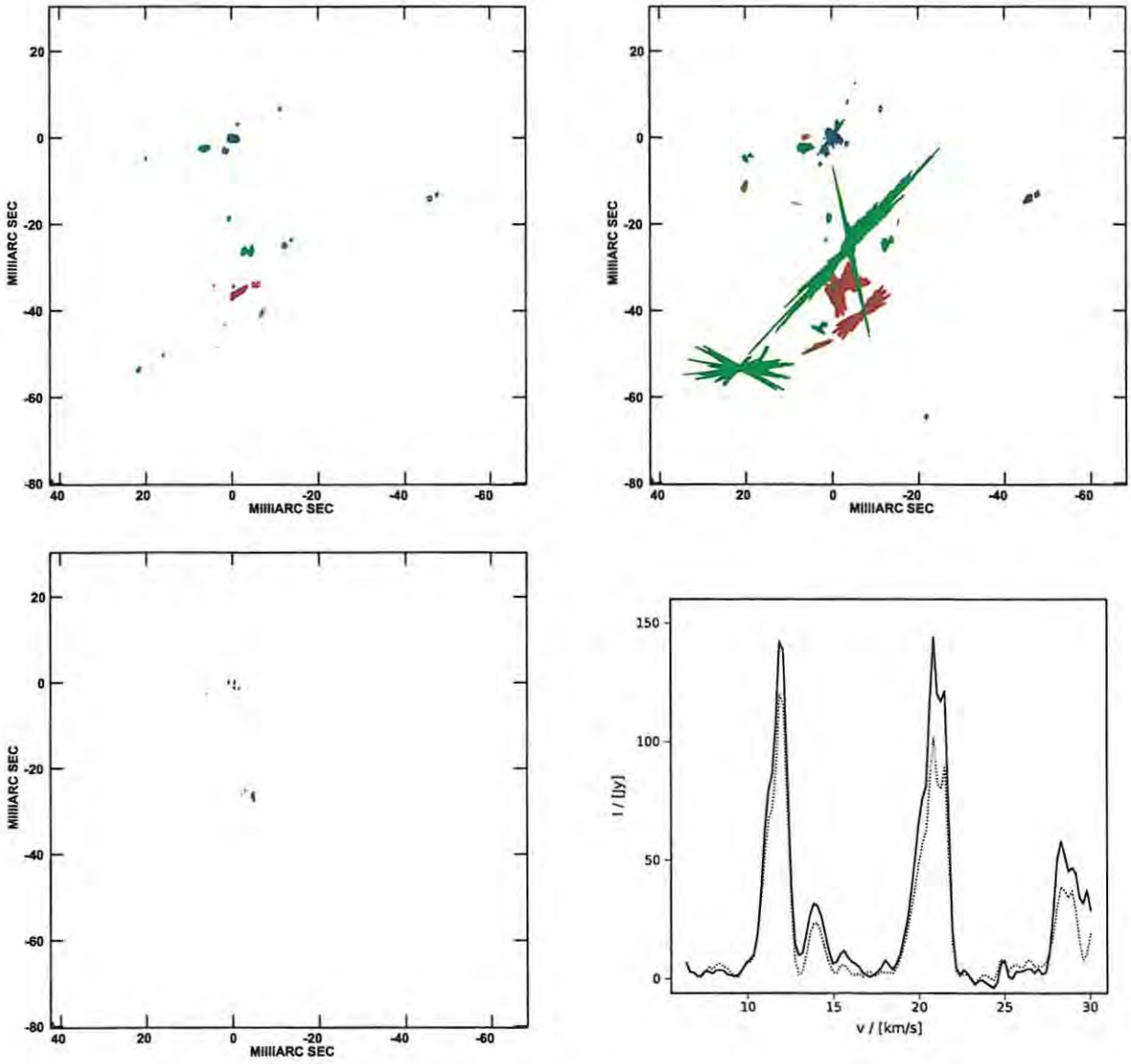

Figure 6.2: Epoch 1 ^{28}SiO v=2 J=1-0 maser images (BK103A).

Top left: Contour plot of the total intensity (Stokes I) maser emission. The contour levels are -2, 2, 5, 10, 20, 40, 60 and 80% of the peak brightness in the Stokes I cube, 45.75 Jy/beam.

Top Right: The linear polarisation distribution of the maser emission, calculated from the underlying Stokes Q and U cubes. The length and orientation of the vectors represent the linearly-polarised intensity and position angle of the linear polarisation, with a vector length of 1 mas = 8.33×10^{-2} Jy/beam.

Bottom Left: Contour plot of the Stokes V maser emission. The contour levels are -30, 30% of the absolute value peak brightness in the Stokes V cube, 0.76 Jy/beam. Negative contours are represented by dashed lines.

Bottom Right: Single-dish total intensity autocorrelation spectrum at Pie Town (solid) and the summed interferometric total intensity spectrum (dotted).

The synthesised beam is shown in the bottom left of each contour plot, and is 0.79 × 0.17 mas in half-power with a position angle of $-10.34°$. The radial velocity of the emission is colour-coded, with the most redshifted features being red and the most blueshifted features, blue.

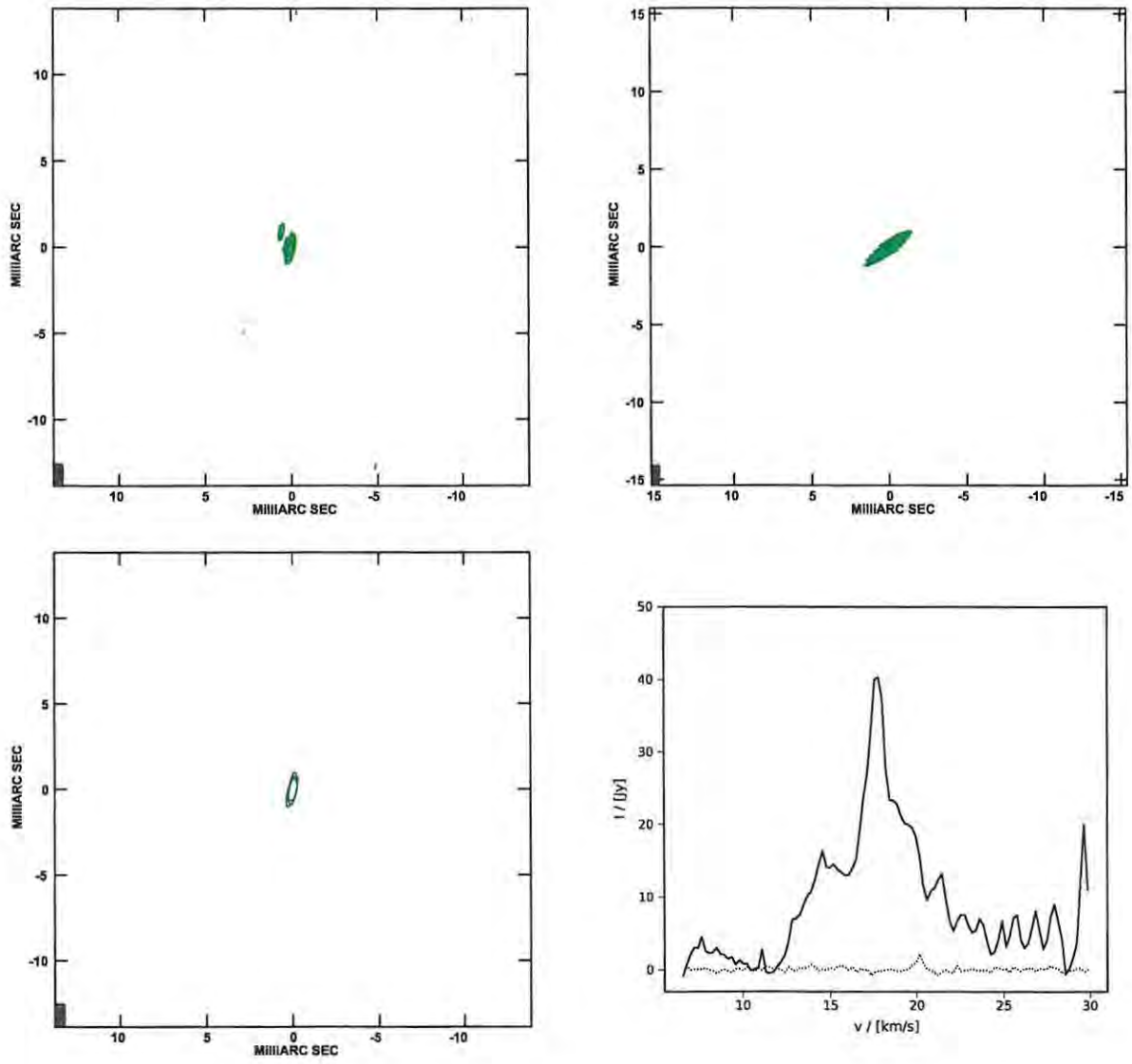

Figure 6.3: Epoch 1 ^{28}SiO v=0 J=1-0 maser images (BK103A).

Top left: Contour plot of the total intensity (Stokes I) maser emission. The contour levels are -10, 10, 20, 40, 60 and 80% of the peak brightness in the Stokes I cube, 1.04 Jy/beam.

Top Right: The linear polarisation distribution of the maser emission, calculated from the underlying Stokes Q and U cubes. The length and orientation of the vectors represent the linearly-polarised intensity and position angle of the linear polarisation, with a vector length of 1 mas $= 8.33 \times 10^{-2}$ Jy/beam.

Bottom Left: Contour plot of the Stokes V maser emission. The contour levels are -10, 10% of the absolute value peak brightness in the Stokes V cube, 1.04 Jy/beam. Negative contours are represented by dashed lines.

Bottom Right: Single-dish total intensity autocorrelation spectrum at Pie Town (solid) and the summed interferometric total intensity spectrum (dotted).

The synthesised beam is shown in the bottom left of each contour plot, and is 0.86 × 0.20 mas in half-power with a position angle of $-9.25°$. The radial velocity of the emission is colour-coded, with the most redshifted features being red and the most blueshifted features, blue.

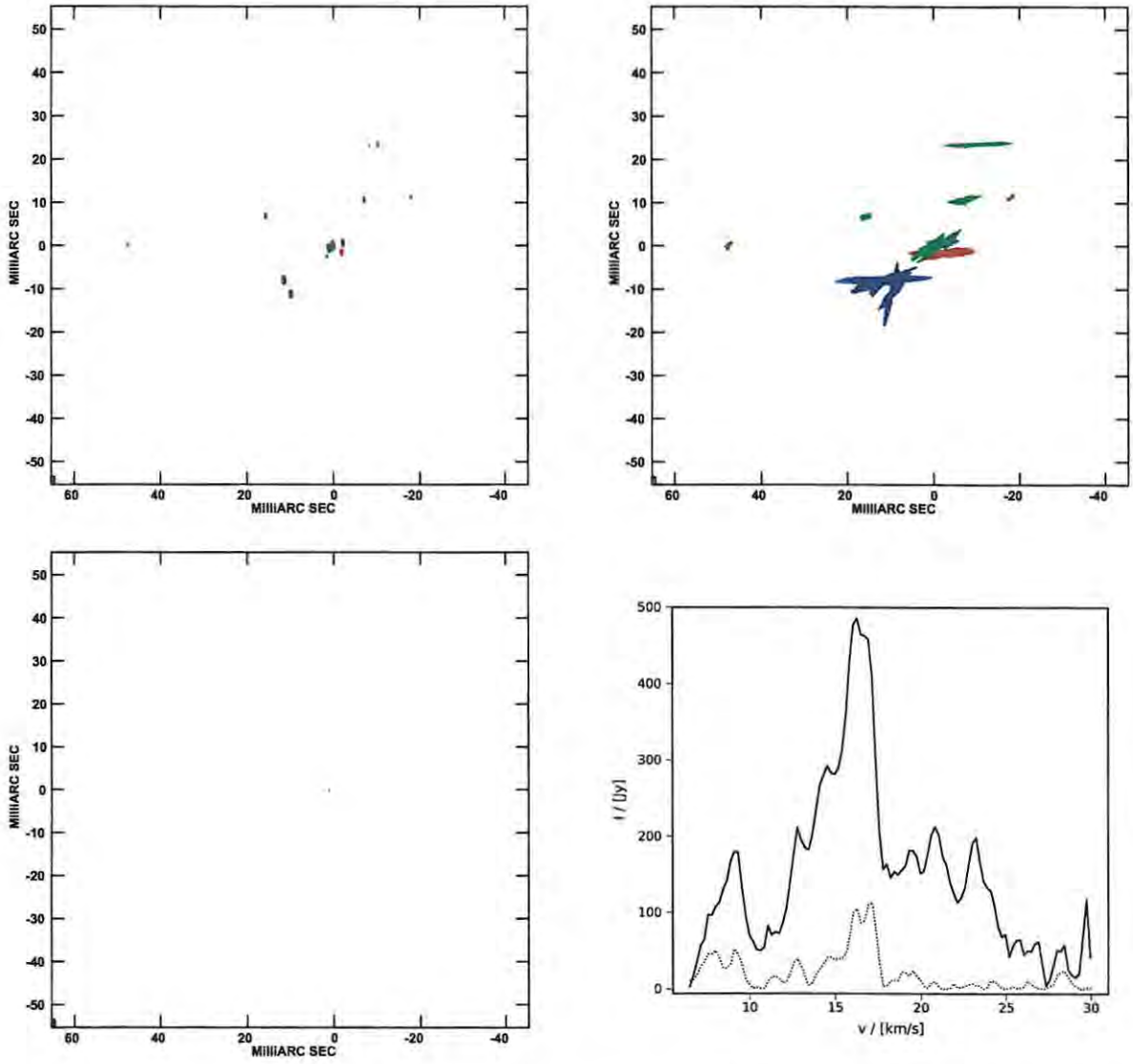

Figure 6.4: Epoch 1 ^{28}SiO v=1 J=2-1 maser images (BK103C).

Top left: Contour plot of the total intensity (Stokes I) maser emission. The contour levels are -10, 10, 20, 40, 60 and 80% of the peak brightness in the Stokes I cube, 59.93 Jy/beam.

Top Right: The linear polarisation distribution of the maser emission, calculated from the underlying Stokes Q and U cubes. The length and orientation of the vectors represent the linearly-polarised intensity and position angle of the linear polarisation, with a vector length of 1 mas = 8.33×10^{-2} Jy/beam.

Bottom Left: Contour plot of the Stokes V maser emission. The contour levels are -80, 80% of the absolute value peak brightness in the Stokes V cube, 1.82 Jy/beam. Negative contours are represented by dashed lines.

Bottom Right: Single-dish total intensity autocorrelation spectrum at Los Alamos (solid) and the summed interferometric total intensity spectrum (dotted).

The synthesised beam is shown in the bottom left of each contour plot, and is 1.22×0.36 mas in half-power with a position angle of 5.81°. The radial velocity of the emission is colour-coded, with the most redshifted features being red and the most blueshifted features, blue.

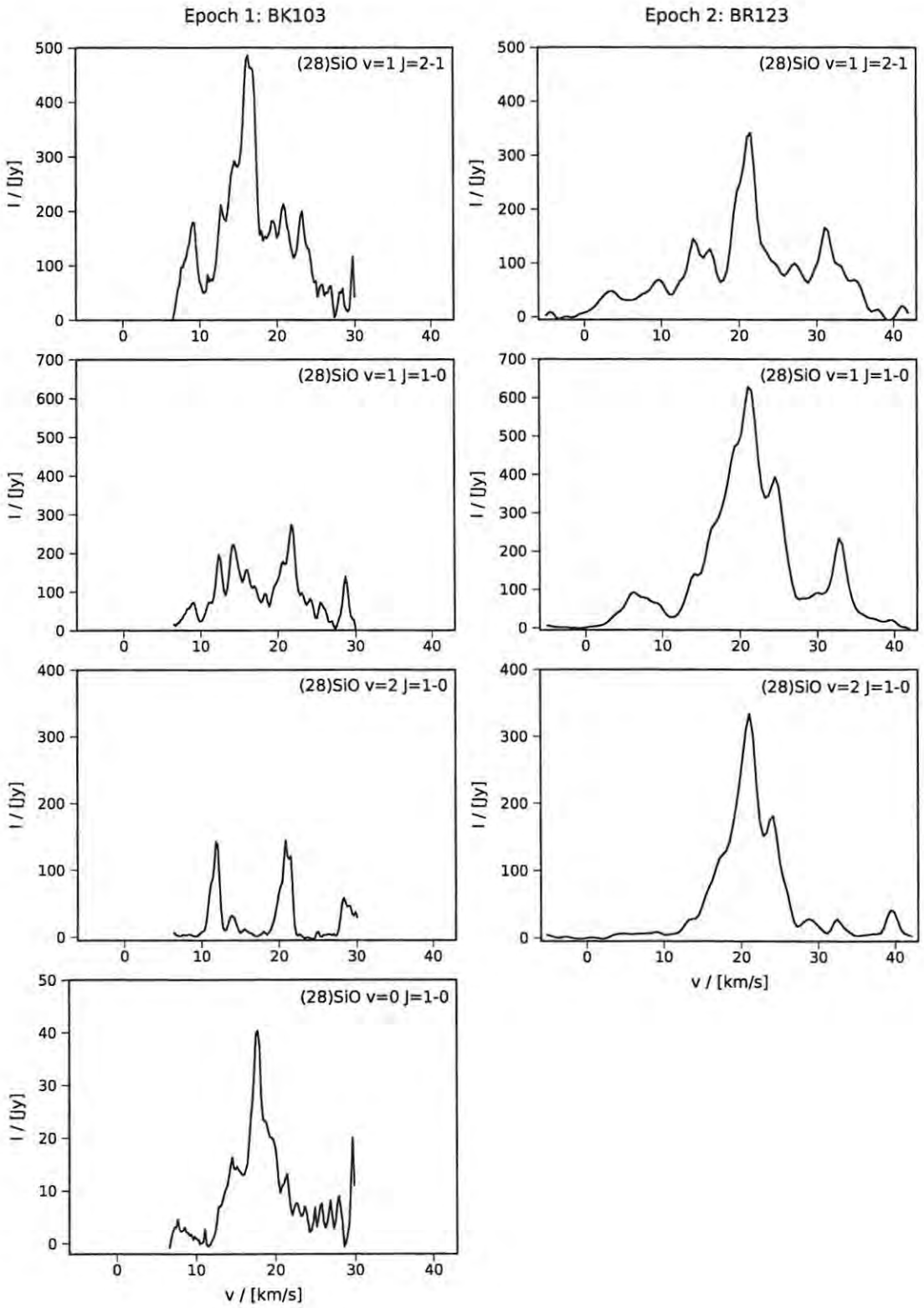

Figure 6.5: Single-dish autocorrelation spectra of the SiO maser lines imaged in the Epoch 1 (Left) and Epoch 2 (Right) observations.

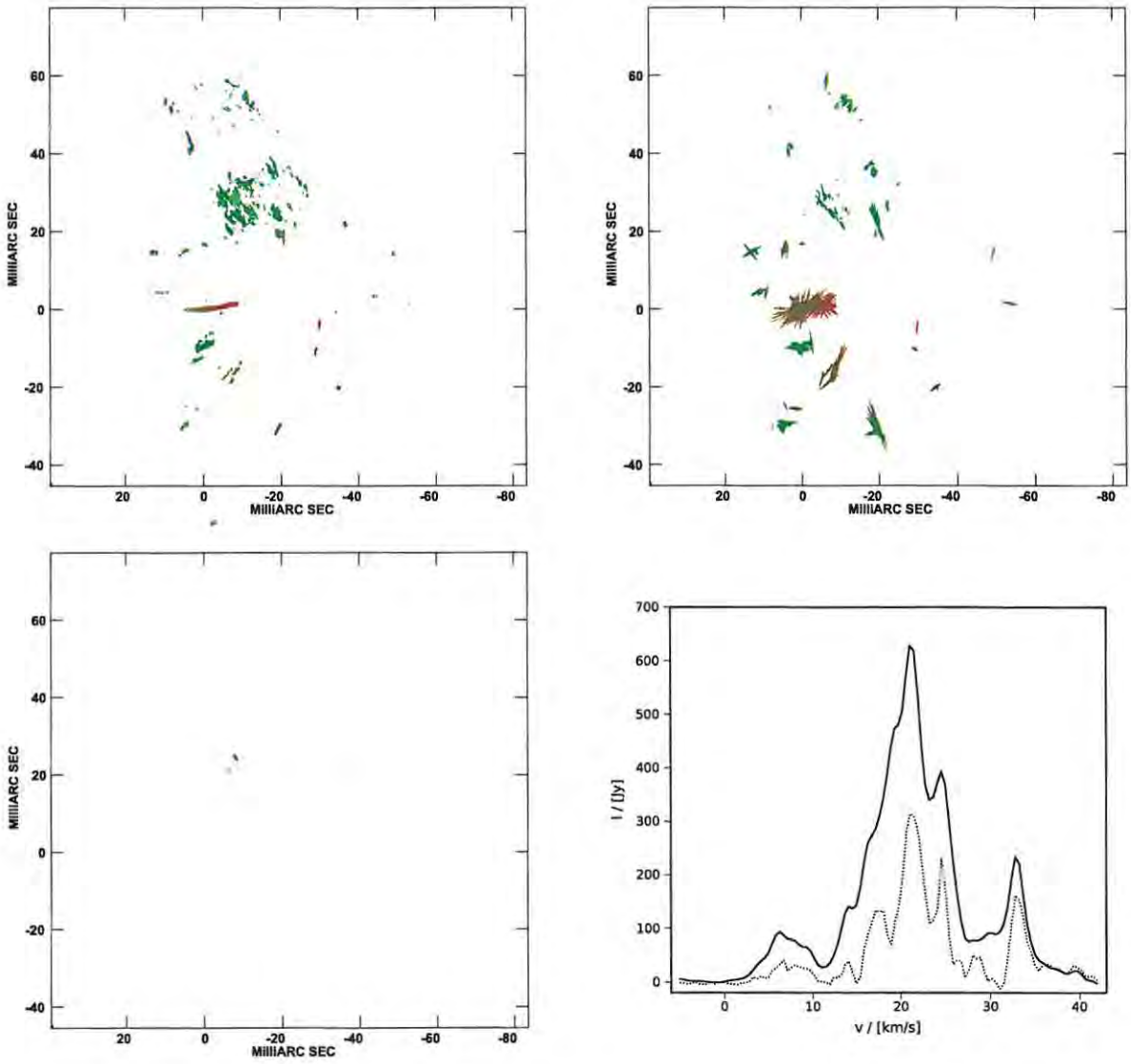

Figure 6.6: Epoch 2 ^{28}SiO v=1 J=1-0 maser images (BR123D).

Top left: Contour plot of the total intensity (Stokes I) maser emission. The contour levels are -2, 2, 10, 20, 40, 60 and 80% of the peak brightness in the Stokes I cube, 22.15 Jy/beam.

Top Right: The linear polarisation distribution of the maser emission, calculated from the underlying Stokes Q and U cubes. The length and orientation of the vectors represent the linearly-polarised intensity and position angle of the linear polarisation, with a vector length of 1 mas = 8.33×10^{-2} Jy/beam.

Bottom Left: Contour plot of the Stokes V maser emission. The contour levels are -20, 20% of the absolute value peak brightness in the Stokes V cube, 0.745 Jy/beam. Negative contours are represented by dashed lines.

Bottom Right: Single-dish total intensity composite autocorrelation spectrum (solid) and the summed interferometric total intensity spectrum (dotted).

The synthesised beam is shown in the bottom left of each contour plot, and is 0.46 × 0.15 mas in half-power with a position angle of $-1.80°$. The radial velocity of the emission is colour-coded, with the most redshifted features being red and the most blueshifted features, blue.

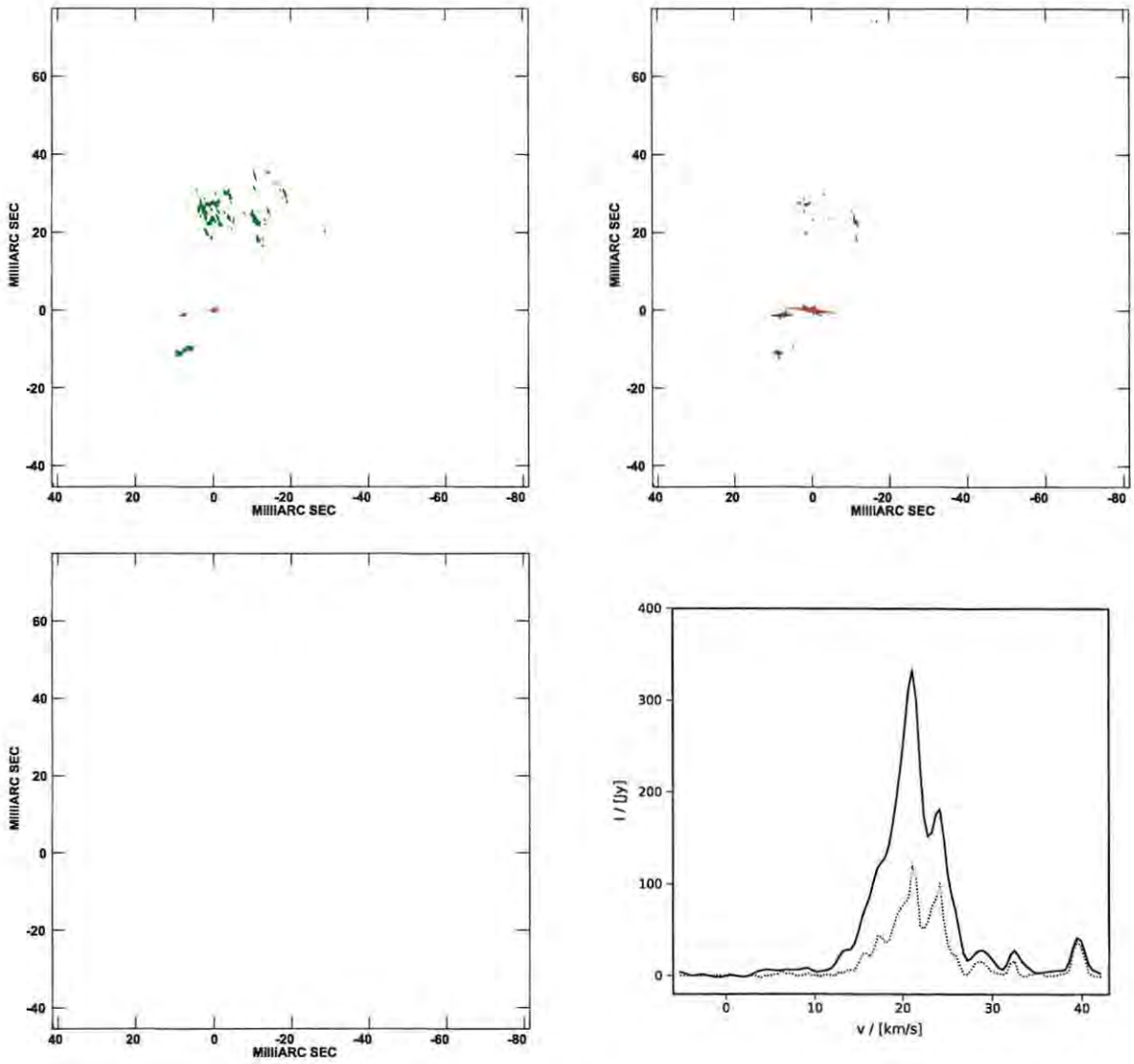

Figure 6.7: Epoch 2 ^{28}SiO v=2 J=1-0 maser images (BR123D).

Top left: Contour plot of the total intensity (Stokes I) maser emission. The contour levels are -5, 5, 10, 20, 40, 60 and 80% of the peak brightness in the Stokes I cube, 12.16 Jy/beam.

Top Right: The linear polarisation distribution of the maser emission, calculated from the underlying Stokes Q and U cubes. The length and orientation of the vectors represent the linearly-polarised intensity and position angle of the linear polarisation, with a vector length of 1 mas = 8.33×10^{-2} Jy/beam.

Bottom Left: Contour plot of the Stokes V maser emission. The contour levels are -40, 40% of the absolute value peak brightness in the Stokes V cube, 0.446 Jy/beam. Negative contours are represented by dashed lines.

Bottom Right: Single-dish total intensity composite autocorrelation spectrum (solid) and the summed interferometric total intensity spectrum (dotted).

The synthesised beam is shown in the bottom left of each contour plot, and is 0.43 x 0.14 mas in half-power with a position angle of $-0.94°$. The radial velocity of the emission is colour-coded, with the most redshifted features being red and the most blueshifted features, blue.

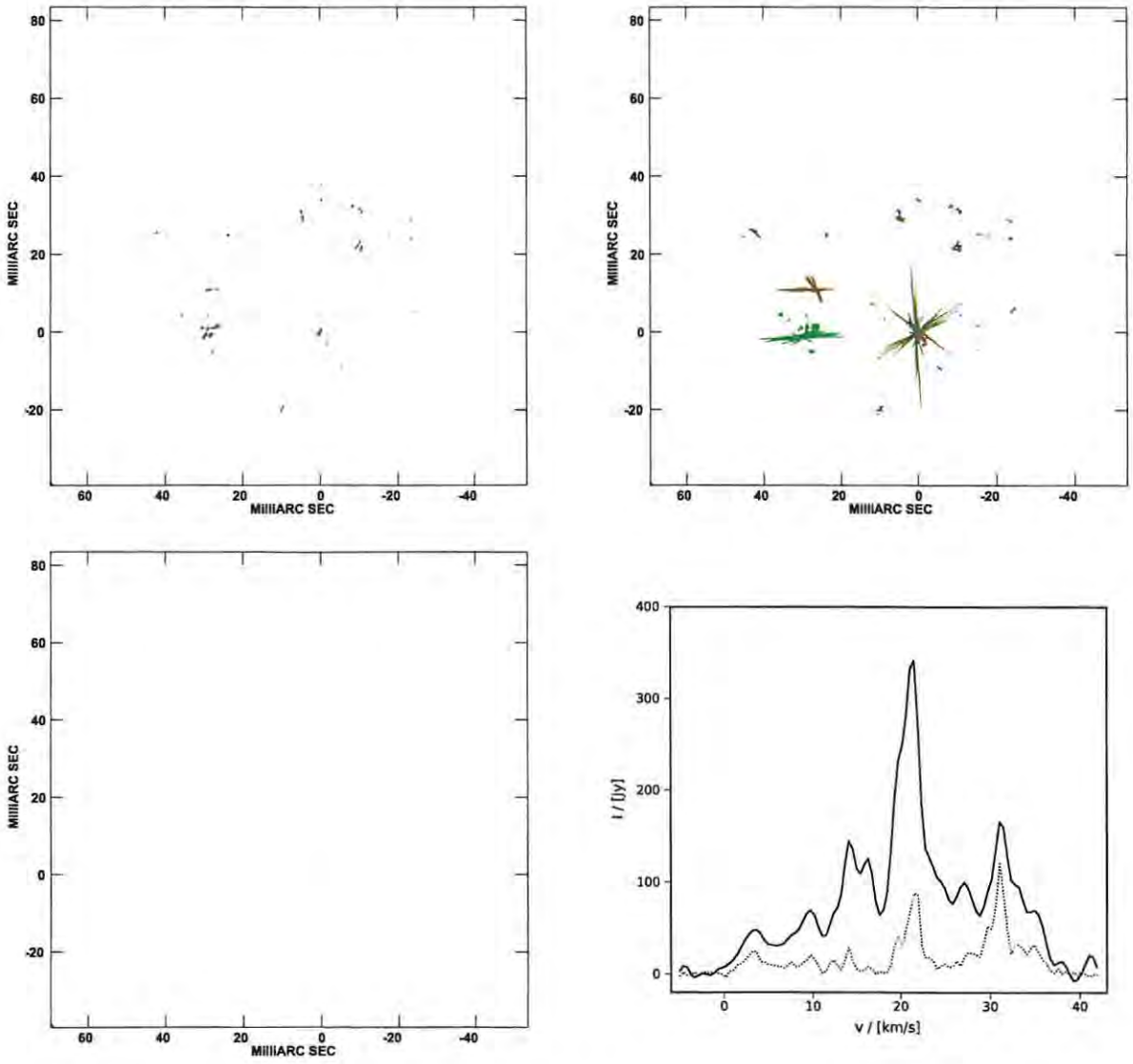

Figure 6.8: Epoch 2 ^{28}SiO v=1 J=2-1 maser images (BR123A).

Top left: Contour plot of the total intensity (Stokes I) maser emission. The contour levels are -2,2, 10, 20, 40, 60 and 80% of the peak brightness in the Stokes I cube, 46.96 Jy/beam.

Top Right: The linear polarisation distribution of the maser emission, calculated from the underlying Stokes Q and U cubes. The length and orientation of the vectors represent the linearly-polarised intensity and position angle of the linear polarisation, with a vector length of 1 mas = 8.33×10^{-2} Jy/beam.

Bottom Left: Contour plot of the Stokes V maser emission. The contour levels are -40, 40% of the absolute value peak brightness in the Stokes V cube, 1.173 Jy/beam. Negative contours are represented by dashed lines.

Bottom Right: Single-dish total intensity composite autocorrelation spectrum (solid) and the summed interferometric total intensity spectrum (dotted).

The synthesised beam is shown in the bottom left of each contour plot, and is 0.42 x 0.09 mas in half-power with a position angle of $-16.35°$. The radial velocity of the emission is colour-coded, with the most redshifted features being red and the most blueshifted features, blue.

6.3 Maser feature identification

Component-level parameters of the individual maser features were extracted using the three-dimensional source detection software Duchamp[1]. The source detection was only performed for the Epoch 2 BR123 data sets, because only these data sets were of sufficient quality to allow the polarisation tests discussed in Chapter 3.

Duchamp is a source finder designed for use on three-dimensional image cubes, and is particularly suited to maps of many isolated sources on large backgrounds. This makes it appropriate for use with SiO maser images. Duchamp detects source components based on their proximity on the sky and their presence in multiple spectral channels. As output, Duchamp provides a a list of the detected features and their characteristics, including the peak intensity of a feature, the spatial and velocity position of the peak of the maser feature, and the velocity full-width at half-maximum.

Duchamp was run on the Stokes I maps from the BR123A data set and the BR123D IF1 and BR123D IF2 data sets. The cubes were too large to be processed by Duchamp in a single run, so Duchamp was run over nine overlapping panels covering the inner 90% of the maps. The overlap ensured that regions of emission did not fall on panel edge. Maser features that fell in the overlapping region were examined to ensure that the full extent of the feature was detected in one or more of the panels, and included only once in the list of detections. An illustrative example of a Duchamp output detection map for these data is shown in Figure 6.9.

The detection threshold in Duchamp was set according to the noise in the Stokes I image. For each channel in the four Stokes image cubes the RMS noise σ_I^0, σ_Q^0, σ_U^0 and σ_V^0 was measured in an off-source box in the corner of the maps, using the AIPS task IMSTAT. These values are underestimates of the true noise in the maps however, as deconvolution and calibration net errors are more pronounced close to emission peaks. The off-source noise estimate can be broadened empirically to take into account the non-Gaussian tail of the noise distribution caused by the imaging errors (Kemball 1992). The broadening was performed following the empirical recipe in Kemball (1992). If a map of size 4096 by 4096 pixels has a Gaussian noise distribution centred on zero with unity standard deviation, one pixel is expected to have a value of less than or equal to -5.295. If $\sigma = 1$ would result in a maximum negative of -5.295, then a measured minimum of I_{neg} implies a broadened standard deviation of $\sigma = |\mathrm{I}_{neg}|/5.295$.

The Stokes I standard deviation of each channel was set to this broadened RMS noise value of $\sigma_I = |\mathrm{I}_{neg}|/5.295$. The ratio β of the broadened standard deviation to the measured standard deviation of the Stokes I image, $\beta = \sigma_I^0/\sigma_I$, is used to broaden the measured noise estimates of the Stokes Q, U and V maps: $\sigma_Q = \beta\sigma_Q^0$, $\sigma_U = \beta\sigma_U^0$, $\sigma_V = \beta\sigma_V^0$ (Kemball 1992).

The noise in each map channel is then approximated as normally distributed, $N(\mu, \sigma)$ with $\mu = 0$, where the standard deviation is given by the broadened standard deviation σ_I, σ_Q, σ_U or σ_V.

The Duchamp detection threshold was set to five times the broadened noise, σ_I, in the channel with the highest RMS. The noise thresholds used were 0.691, 0.445 and 1.000 Jy/beam for the BR123D IF1, BR123D IF2 and BR123A images respectively. The minimum channel width for feature detection was set to two channels. The narrowest line widths of SiO maser features are observed to be ~ 0.5 km/s (e.g. Glenn et al. 2003). The channel width used in the Epoch 2 observations was 0.44 km/s, so maser features should span more than one channel.

[1] www.atnf.csiro.au/people/Matthew.Whiting/Duchamp

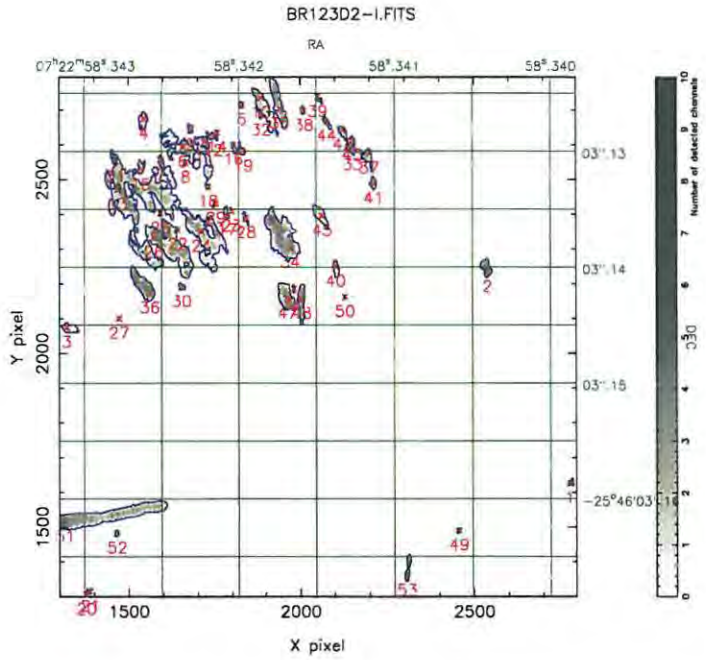

Figure 6.9: Source detection map produced by Duchamp for a single panel of the Epoch 2 BR123D IF2 Stokes I map. Each detected source feature in numbered. The gray-scale image shows the number of channels spanned by the features (see right colour wedge).

The maser features detected with Duchamp in Stokes I are listed in Tables 6.4, 6.3 and 6.5 for the three BR123 data cubes. The Stokes Q, U and V values reported in the tables were taken to be the associated value of the emission at the pixel position of the feature reported by Duchamp, which is the position of the maximum Stokes I in the feature.

The positions in the tables are given as offsets on the projected plane of the sky, measured in milliarcseconds and increasing in the direction of increasing right ascension and declination. The offset is measured from the centre of the map after relative alignment of the various BR123 observations using methods described in Section 6.4.1. The aligned maps are shown in Figure 6.11.

6.4 Map alignment

As discussed in Section 5.5 of Chapter 5, the absolute position information of VLBI maps is lost during the data reduction process. Accurate relative alignment is critical however, when investigating maser excitation mechanisms or when comparing levels of polarisation of the same maser feature in different transitions.

As the absolute position information is lost, the alignment of the maser maps must be performed subsequent to imaging the data. One method of determining the absolute position of VLBI maps is through phase referencing, described in Section 5.5. The double beam of the VERA array is an ideal instrument for absolute positioning, as it can be used to monitor a phase reference calibrator in the second beam (Rioja et al. 2008). This technique was attempted by Rioja et al. (2008) for SiO maser observations of R Leo Minoris, but the phase reference calibrator was too weak to be

imaged. They were able to use the observations of a primary calibrator, which were interleaved with the source observations, as a phase reference and determine the positional offset between two epochs of observations. Choi et al. (2008a) used the dual beam capabilities of VERA for phase referencing observations of VY CMa, sucessfully obtaining absolute positions of the v=1 and v=2 J=1-0 SiO maser maps as well as the 22 GHz H_2O maser map. Kamohara et al. (2010) also used the VERA dual beam for phase referencing observations of the v=1 and v=2 J=1-0 SiO maser maps towards R Aqurii, spanning eight epochs.

Phase referencing was attempted on the BR123 data set, using the calibrator J0731-2341, as described in Section 5.5. The phase referencing was ultimately unsuccessful due to the low SNR of the phase reference calibrator. As the phase referencing failed, alternative means had to be used to align the BR123 maps. A discussion of various alternative methods is given below.

The simplest method of map alignment is aligning the maps "by eye": finding spots that seem to be the same in both maps in frequency and position, then shifting the maps to align these spots. Desmurs et al. (2000) aligned two v=1 and v=2 J=1-0 SiO maser maps by eye. They found two spots in the same velocity channel that appeared to be coincident and the maps were then manually aligned by setting these spots to be the phase centres of each map. The same method was used by Desmurs et al. (2002) to align v=1 J=1-0 and J=2-1 maps of several AGB stars. Cotton et al. (2006) also resorted to the simple method of aligning features that appeared to match over the two transition frequencies. Chen & Shen (2008) and Zhang et al. (2012) used reference features to align multiple v=1 J=1-0 SiO maser maps of AH Sco and VY CMa respectively. The weakness of this manual alignment is that it relies on the assumption that the two spots chosen to align are coincident, which may not be the case. It is also not strictly reproducible, in the sense that individual observers might choose to align spots slightly differently.

Cotton et al. (2004) used a form of phase referencing to register v=1 and v=2 J=1-0 SiO maps of several Mira variables. The two lines were observed simultaneously in adjacent IF bands. The phase calibration was then performed on one of the two lines, using a channel with a simple emission structure and high intensity. This solution was transferred to the other line, so that the phase solutions applied to the two lines were the same. The two maps therefore have the same phase centres and are aligned with each other, although the absolute positions of the two maps are still unknown.

Yi et al. (2000), Yi et al. (2002) and Yi et al. (2005) pioneered a technique of registering similtaneous v=1 and v=2 J=1-0 observations by measuring the group delay offset between the observing bands in which the two transitions are located. They did this by scheduling the observations over 8 IF bands, with the two spectral lines in the outer two fequency bands. The inner 6 bands covered the intervening 300 MHz between the v=1 43.122027 GHz and v=2 42.820542 GHz lines. The inner bands were used to determine the group delay across the full bandwidth, which was then applied to the the outer bands containing the lines. The data were fringe fit across the full 8 bands and a self-calibration performed on the v=1 band and applied to both the v=1 and v=2 bands. Because the same phase calibration is applied to both transitions the final images maps are aligned with a common phase centre, as in Cotton et al. (2004). This technique can only be used for spectral lines close enough in frequency to fit in a single observing intermediate receiver band. This is possible for the v=1 and v=2 J=1-0 lines, which both fall in the 43 GHz band. It is not possible to use this technique to register the v=1 J=1-0 and J=2-1 lines because the J=1-0 line falls in the 43 GHz band and the J=2-1 line falls in

the 86 GHz band. In two of the epochs observed by Yi et al. (2005), there were problems with the position of TX Cam used in the data correlation. In these cases they resorted to "by eye" alignment, by locating a common reference feature in both the v=1 and v=2 maps and aligning these features by shifting the images.

Soria-Ruiz et al. (2004) compared v=1 and v=2 J=1-0 and J=2-1 maps of SiO maser emission toward χ Cyg and IRC +10011. They aligned the maps by aligning the centroids of the maser eimssion. Where there was uncertainty in the centroid position, the alignment was guided by the velocity of the maser spots. Soria-Ruiz et al. (2005) aligned ^{28}SiO and ^{29}SiO maser maps of IRC +10011 by fitting a ring to the maser emission and comparing the distance of each ring from the fitted centre, also effectively aligning them at the fitted centre. Soria-Ruiz et al. (2007) used a similar method of aligning the maps by emission centroid.

Another means to align maps is by cross-correlating them and finding the maximum of the correlation function. This maximum gives the offset between the two maps. Miyoshi (2003) performed an alignment of two v=1 and v=2 J=1-0 VY CMa SiO maser maps by cross-correlating corresponding velocity channel images and finding the position shift that maximised the correlation function. Phillips et al. (2003) also used the correlation method to align v=1 J=1-0 and J=2-1 SiO maps of R Cas. The cross-correlation method was employed to align the maps imaged in this thesis. The total intensity images of different transitions were correlated and the peak of the correlation functions was taken to be the offset between the two maps.

Underlying assumptions of the correlation method are that there is overlapping emission in the two maps being aligned, and that there are no systematic global linear offsets between the emission in the correlated maps. A global linear offset is not scientifically expected for the maps presented in this chapter, as there is no large scale linear effect across the circumstellar envelope which could lead to an overall offset between emission from the different transitions. For the geometry of the maser emission, located around a central star, any possible offsets are more likely caused by radial effects. These might include maser pumping dependencies either on density, which decreases radially, or radial stellar radiation. In the absence of a global linear offset, the maximum of the spatial correlation between the two maps will give the true alignment. However, if there is no overlapping emission then this method will not work.

6.4.1 Map correlation

The correlation between SiO maser images in different transitions was performed on two-dimensional peak intensity maps of the Stokes I emission. These maps were created from the original three-dimensional image cubes by taking the maximum intensity at each pixel along the frequency axis, using the AIPS task SQASH. These squashed maps were then cross-correlated in pairs to give a cross-correlation product, also a two-dimensional FITS image. The peak of the cross-correlation product gives the offset required to maximise the spatial correlation of the two maps.

When performing the correlations, it was found that extremely high intensity maser spots could bias the spatial correlation; in this case the peak in the correlation product aligns the two highest spots in the two input images even if they are clearly not aligned with a simple visual check. In order to prevent this, the squashed input maps were transformed to have unity intensity where the original intensity was greater than a specified cutoff level, and zero below this cutoff. The cutoff values were

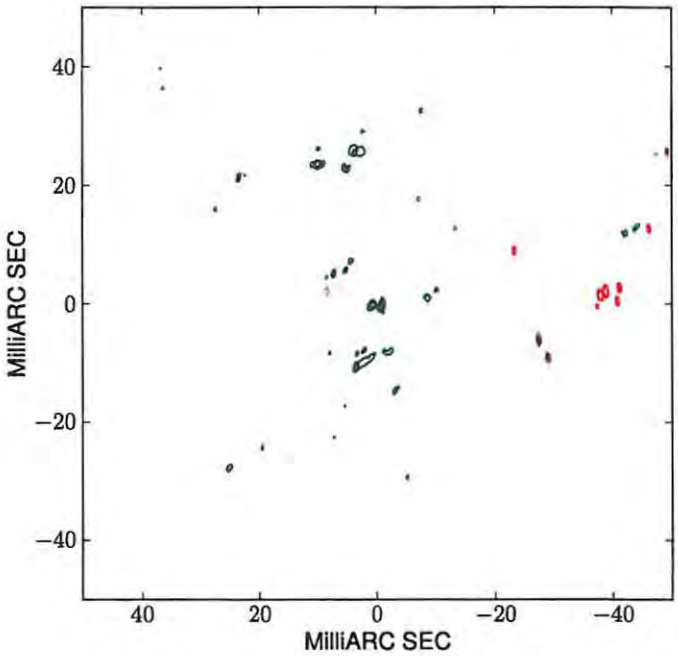

Figure 6.10: Overlaid contour plots of the Epoch 1 BK103 Stokes I images of the transitions v=1 J=1-0 (blue), v=2 J=1-0 (green), and v=1 J=2-1 (red). The contour levels are 20%, 2% and 10% of the image maxima for the three lines respectively, as cited in the captions to Figures 6.1, 6.2 and 6.4.

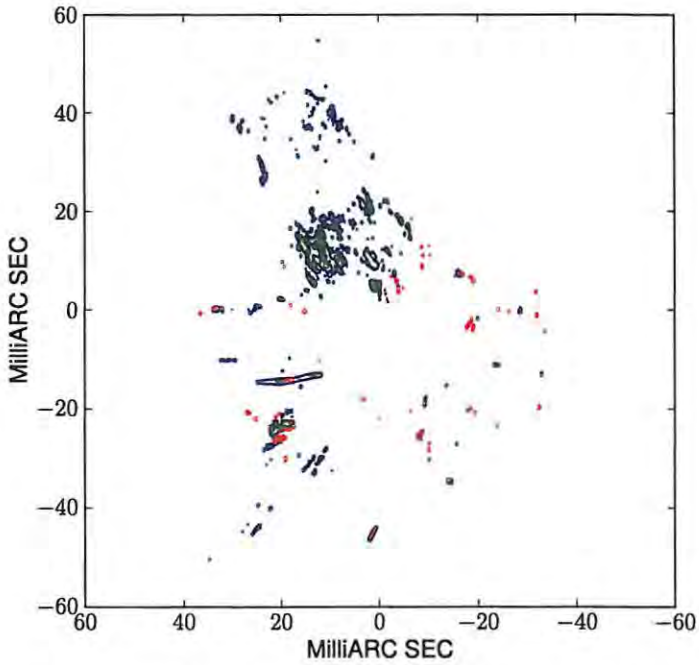

Figure 6.11: Overlaid contour plots of the Epoch 2 BR123 Stokes I images of the transitions v=1 J=1-0 (blue), v=2 J=1-0 (green), and v=1 J=2-1 (red). The contour levels are 2%, 5% and 2% of the image maxima for the three lines respectively, as cited in the captions to Figures 6.6, 6.7 and 6.8.

Project code		v=2 J=1-0	v=1 J=2-1
BK103	v=1 J=1-0	1.4 mas	0.08 mas
BR123	v=1 J=1-0	2.3 mas	1.6 mas

Table 6.2: Geometric average FWHM from Gaussian fits to the peak in the the spatial cross-correlation images, as described in the text.

set at five times the maximum broadened noise variance σ_I of the Stokes I cubes for the BR123 data sets, and ten times the maximum σ_I for the BK103 data sets. This image manipulation was performed with the AIPS task COMB.

The offset and its uncertainty were determined from a Gaussian fit to the peak in the cross-correlation map, using the AIPS task JMFIT. The uncertainty in the fit was derived from the geometric mean of the major and minor axes of the full width at half maximum (FWHM) size of the fitted Gaussian. The geometric mean FWHM values are reported in Table 6.2. The uncertainty in the fit is estimated by dividing these FWHM values by the SNR of the images, following Phillips et al. (2003). The SNR values were calculated for each channel of the cubes. The minimum SNR was $\lesssim 4$, while the maximum was > 100 for all channels, and all cubes. For the Epoch 2 cubes the maximum SNR values were $\gtrsim 400$. The uncertainty in the map alignment is therefore estimated to be < 0.05 mas. The aligned maps are shown in Figure 6.10.

In the case of the Epoch 1 v=1 J=1-0 and v=1 J=2-1 SiO maser emission, the cross-correlation map had a number of peaks of the same order. In this case where there are a limited number of apparently overlapping features, the correlation alignment method performs poorly and requires manual refinement. The highest peaks in the the cross-correlation map were tested manually to determine which peak provides the most appropriate offset between these images, considering the frequency distrubution of the emission as well as the maximum intensity Stokes I image. The best fit is shown in Figure 6.10.

6.5 Fractional polarisation measurement

The fractional circular polarisation m_c, the fractional linear polarisation m_l and the linear polarisation position angle χ were calculated for each of the maser features listed in Tables 6.3, 6.4 and 6.5. The polarisation values were derived from the Stokes I, Q, U and V measurements as follows

$$m_c = \frac{V}{I}$$

$$m_l = \frac{P}{I}$$

$$\chi = \frac{1}{2}\arctan\left(\frac{U}{Q}\right)$$

where $P = \sqrt{Q^2 + U^2}$.

While the Stokes parameters measured from the images are approximately normally distributed, the fractional polarisations m_c and m_l are not normally distributed. This must be taken into account

when assessing the statistical significance of the calculated m_c and m_l values, and to account for possible bias in the polarisation values.

Measurements of the linear polarisation are intrinsically biased due to the Rice probability distribution of the non-negative P (Wardle & Kronberg 1974). This bias is taken into account by correcting the linear polarisation as $P' = \sqrt{P^2 - \sigma_{QU}^2}$ (Wardle & Kronberg 1974). The noise levels in the Stokes Q and U maps are similar, so the assumption is made that $\sigma_Q \sim \sigma_U$ in the noise analysis, and σ_{QU} is set to be $\sqrt{\sigma_Q \sigma_U}$.

Like Stokes I, the Stokes Q and U values can be assumed to be drawn from Normal probability distributions. In order to find a rejection threshold for the fractional linear polarisation, Kemball (1992) derived the probability density function for zero-mean Normal variables Q and U with standard deviations σ_Q and σ_U

$$\phi(\mathrm{m}_l) = \frac{1}{\sqrt{2\pi}\sigma_{QU}^2 \sigma_I \mathrm{m}_l^2} \left[\frac{b}{a^2} e^{-\frac{I^2}{2\sigma_I^2}} + \frac{(2b^2 + a)}{2} \sqrt{\frac{\pi}{a^5}} e^{\frac{b^2}{a} - \frac{I^2}{2\sigma_I^2}} \mathrm{erf}\left(\frac{b}{\sqrt{a}} \right) \right] \tag{6.1}$$

where

$$a = \frac{1}{2\sigma_{QU}^2} + \frac{1}{2\sigma_I^2 \mathrm{m}_l^2}$$
$$b = \frac{1}{2\sigma_I^2 \mathrm{m}_l}$$

The detection threshold for the linear polarisation m_l is determined by evaluating the null hypothesis that m_l is equal to zero. By convention, the null hypothesis is determined to be false if the calculated m_l falls outside of the 95% probability interval for $\mathrm{m}_l = 0$. The 95% detection limit u_l for the linear polarisation can be found through numerical integration of the probability distribution given in Equation 6.1, $\int_0^{u_l} \phi(\mathrm{m}_l)\, \mathrm{dm}_l = 0.95$. The detection limit u_l determined in this matter can be approximated by a range estimator

$$u_l = \frac{1.65}{\sqrt{2}} \left[\frac{P' + \sigma_{P'}}{I - \sigma_I} - \frac{P' - \sigma_{P'}}{I + \sigma_I} \right]$$

where $\sigma_{P'} = \frac{\sqrt{Q^2\sigma_Q^2 + U^2\sigma_U^2}}{P'}$ (Kemball 1992). The range estimator approximation was used to determine the detection limits in this thesis. Kemball (1992) found that the range estimator approximation of u_l is an underestimation by up to 10% for m_l values up to 5%, but when the fractional linear polarisation is large the range estimator can overestimate u_l by 35% when m_l is large.

If a calculated value of m_l is lower than the threshold u_l then the m_l value falls in the 95% confidence interval for $\mathrm{m}_l = 0$ and is not significantly different to zero. In these cases the m_l value is left out of the tables. However, when the calculated value of m_l is greater than the detection limit u_l, then m_l is listed in the tables, as well as the linear polarisation position angle χ. There is no bias correction needed for the position angle (Wardle & Kronberg 1974). The uncertainties in m_l and χ are also included in the tables, calculated by propagation of the Stokes parameter RMS errors.

For the circular polarisation, the probability density functions of the measured Stokes I and V values are again approximately Normal. The probability density function of the circular polarisation $m_c = V/I$ can then be determined from the Normal Stokes I and V probability densities. The

probability density of the ratio of two Gaussian probability densities is given by

$$\phi(\mathrm{m}_c) = \frac{1}{2\pi\sigma_I\sigma_V}\left[\frac{1}{p}e^{-\frac{c}{2}} + \frac{q}{p}\sqrt{\frac{\pi}{p}}e^{\frac{q^2}{p}-\frac{c}{2}}\mathrm{erf}\left(\frac{q}{\sqrt{p}}\right)\right] \tag{6.2}$$

where the means and standard deviations of I and V are given by μ_I, σ_I and μ_V, σ_V respectively, and

$$q = \frac{\mu_V m_c}{2\sigma_V^2} + \frac{\mu_I}{2\sigma_I^2}$$
$$p = \frac{m_c^2}{2\sigma_V^2} + \frac{1}{2\sigma_I^2}$$
$$c = \frac{\mu_V^2}{\sigma_V^2} + \frac{\mu_I^2}{\sigma_I^2}$$

This version of the ratio probability density function was derived by Fieller (1932) and Hinkley (1969) for the ratio of two correlated normal random variables, where in this case the variables I and V are uncorrelated. This probability density function was derived by Kemball (1992) for the case of $\mu_V = 0$. A simplified form of this function was also derived by McKinnon (2002) for use in modeling circularly polarised pulsar emission. In his derivation he assumed that the standard deviation of the Stokes I and V noise distributions were the same.

The detection threshold for the circular polarisation m_c was determined by evaluating the null hypothesis that m_c is equal to zero. When $\mathrm{m}_c = 0$, then $\mu_V = 0$ in Equation 6.2. The circular polarisation rejection threshold can be determined by integrating over the probability density function given in Equation 6.2. Alternatively, the 95% probability interval can be calculated using the Geary-Hinkley transformation, as described by Hayya et al. (1975), to give upper and lower limits of

$$\mathrm{u}_c = \pm 1.96\frac{\sigma_V}{\sqrt{\mu_I^2 - 1.96^2\sigma_I^2}}$$

This approximation is good at a 5% level when $\sigma_I < 0.39\mu_I$ and $\sigma_V > 0.005\mu_V$ (Hayya et al. 1975). Both conditions are met for the values of these parameters in Tables 6.3 to 6.5. The Geary-Hinkley transformation method was therefore used to find the circular polarisation theshold for the features listed in these tables.

If a calculated value of m_c is higher than the threshold u_c then the m_c value is included in the table, as well as the uncertainty in the fractional circular polarisation σ_c, calculated from propagation of the Stokes parameter RMS errors.

Table 6.3: List of maser features detected in the Epoch 2 BR123D IF2 ^{28}SiO v=1 J=1-0 observations.

v [km/s]	Δv [km/s]	$\Delta\alpha$ [mas]	$\Delta\delta$ [mas]	I [Jy/bm]	σ_I [Jy/bm]	Q [Jy/bm]	σ_Q [Jy/bm]	U [Jy/bm]	σ_U [Jy/bm]	V [Jy/bm]	σ_V [Jy/bm]	m_c [%]	σ_c [%]	m_l [%]	σ_l [%]	χ [deg]	σ_χ [deg]
3.22	1.74	-14.52	-34.77	2.280	0.020	0.093	0.021	-0.005	0.019	-0.010	0.020			4.01	0.94	-8.36	6.21
4.09	0.87	-13.95	-34.68	2.792	0.021	0.008	0.020	-0.259	0.020	-0.057	0.020	-2.03	0.72	9.25	0.73	-50.86	2.26
5.40	0.44	26.76	36.30	1.023	0.018	0.008	0.018	-0.005	0.018	0.015	0.017						
5.40	0.44	20.79	43.23	0.740	0.018	-0.008	0.018	0.012	0.018	0.011	0.017						
5.83	0.44	27.96	38.37	0.922	0.031	-0.003	0.029	0.006	0.028	-0.011	0.027						
6.27	1.74	28.68	37.20	3.211	0.036	-0.011	0.034	0.012	0.033	0.017	0.034						
6.27	0.44	-23.28	-11.22	0.698	0.036	-0.002	0.034	0.008	0.033	1.8e-4	0.034						
6.70	1.74	29.91	39.33	1.622	0.032	-0.028	0.030	0.013	0.030	0.013	0.030						
6.70	2.61	-16.14	7.02	5.258	0.032	-0.009	0.030	-0.008	0.030	0.145	0.030	2.75	0.57				
8.44	2.17	23.73	29.19	1.755	0.021	-0.004	0.020	0.037	0.020	-0.011	0.019						
9.74	1.30	23.10	27.39	2.040	0.018	-0.096	0.018	0.064	0.018	-0.014	0.018			5.57	0.88	66.40	4.52
9.74	1.30	20.40	2.25	2.042	0.018	-0.094	0.018	-0.030	0.018	0.014	0.018			4.73	0.87	-87.92	5.37
12.35	1.30	25.47	0.15	1.402	0.018	0.004	0.018	0.122	0.018	0.002	0.018			8.63	1.32	37.27	4.31
12.79	0.44	26.37	-0.63	0.719	0.016	-0.013	0.015	0.010	0.015	0.001	0.015						
13.65	1.30	13.68	20.28	1.058	0.020	0.013	0.019	0.013	0.021	-0.002	0.019						
14.09	0.87	33.42	0.18	7.551	0.024	-0.108	0.024	-0.500	0.024	0.139	0.023	1.84	0.31	6.77	0.31	-57.91	1.33
14.52	0.44	5.10	21.45	0.852	0.021	0.002	0.022	-0.019	0.024	0.004	0.023						
14.96	0.44	11.34	37.74	0.759	0.025	0.101	0.026	-0.145	0.024	0.008	0.026			23.12	3.39	-34.34	4.17
15.39	3.48	10.32	17.82	1.763	0.027	-0.005	0.026	-0.015	0.027	0.061	0.027	3.48	1.51				
15.83	0.87	24.48	-43.68	1.011	0.034	-0.350	0.035	0.008	0.035	-0.007	0.034			34.47	3.66	82.52	2.89
15.83	2.17	12.24	16.71	1.523	0.034	0.007	0.035	-0.003	0.035	0.025	0.034						
15.83	0.44	10.05	16.50	0.655	0.034	0.014	0.035	0.011	0.035	0.030	0.034						
16.26	1.30	9.63	19.29	0.616	0.052	-0.014	0.052	0.014	0.053	0.026	0.053						
16.26	0.87	-28.62	-0.18	5.903	0.052	0.314	0.052	-0.061	0.053	-0.145	0.053	-2.45	0.89	5.35	0.90	-12.28	4.85
17.13	0.87	14.01	44.04	2.161	0.034	0.402	0.035	-0.006	0.036	0.013	0.036			18.55	1.66	-7.23	2.60
17.13	2.17	3.42	22.08	1.832	0.034	-0.003	0.035	-0.065	0.036	0.001	0.036						
17.57	1.30	24.03	26.58	1.223	0.037	0.150	0.037	0.011	0.036	0.017	0.035			11.91	3.13	-4.78	7.25
17.57	0.44	13.44	39.96	0.624	0.037	0.006	0.037	-0.024	0.036	-0.003	0.035						
17.57	0.87	12.84	43.11	0.753	0.037	0.020	0.037	0.007	0.036	-0.002	0.035						

Continued on the next page

v [km/s]	Δv [km/s]	$\Delta\alpha$ [mas]	$\Delta\delta$ [mas]	I [Jy/bm]	σ_I [Jy/bm]	Q [Jy/bm]	σ_Q [Jy/bm]	U [Jy/bm]	σ_U [Jy/bm]	V [Jy/bm]	σ_V [Jy/bm]	m_c [%]	σ_c [%]	m_l [%]	σ_l [%]	χ [deg]	σ_χ [deg]
18.00	0.44	14.91	36.84	0.651	0.034	0.013	0.037	-0.008	0.034	-0.009	0.036						
18.00	0.44	14.04	36.81	0.860	0.034	0.022	0.037	4.1e-4	0.034	-0.007	0.036						
18.00	0.44	11.40	42.72	0.690	0.034	0.006	0.037	-0.007	0.034	0.008	0.036						
18.00	4.35	8.43	18.30	1.324	0.034	0.004	0.037	6.4e-5	0.034	0.006	0.036						
18.43	0.44	7.68	18.78	0.776	0.045	0.020	0.046	0.005	0.048	0.019	0.046						
18.87	0.44	19.86	-21.51	0.979	0.048	0.008	0.051	0.017	0.049	0.009	0.048						
18.87	0.87	7.71	37.98	2.262	0.048	0.226	0.051	-0.072	0.049	-0.002	0.048			10.26	2.29	-15.56	6.15
18.87	0.44	7.38	37.02	0.753	0.048	0.140	0.051	-0.018	0.049	0.010	0.048						
19.30	0.44	21.54	-22.65	0.933	0.077	-0.001	0.070	0.003	0.069	-0.024	0.071						
19.30	0.44	20.91	-22.68	0.667	0.077	-0.001	0.070	0.019	0.069	-0.009	0.071						
19.30	6.52	15.99	14.16	5.225	0.077	-0.023	0.070	0.015	0.069	-0.194	0.071	-3.72	1.36				
19.30	1.30	9.48	40.98	2.219	0.077	0.017	0.070	-0.023	0.069	-0.004	0.071						
19.30	0.87	8.43	38.01	0.916	0.077	0.008	0.070	-0.039	0.069	-0.022	0.071						
19.30	0.44	7.32	19.08	0.658	0.077	0.005	0.070	0.002	0.069	0.015	0.071						
19.30	0.44	1.35	30.93	0.744	0.077	0.011	0.070	-0.004	0.069	0.012	0.071						
19.74	1.30	13.95	15.87	0.823	0.066	0.004	0.061	0.003	0.058	0.014	0.063						
20.17	0.44	5.88	18.00	0.739	0.041	-0.007	0.043	-0.008	0.042	-0.004	0.045						
20.61	0.44	22.92	-27.78	0.660	0.075	0.002	0.071	-0.014	0.068	-3.1e-4	0.066						
20.61	0.44	21.51	-27.24	0.554	0.075	-0.003	0.071	-0.008	0.068	0.017	0.066						
20.61	0.87	20.97	-26.88	0.819	0.075	-0.002	0.071	-0.016	0.068	0.006	0.066						
20.61	0.44	8.10	14.40	0.813	0.075	0.006	0.071	0.003	0.068	0.008	0.066						
20.61	0.44	6.48	36.75	1.462	0.075	0.042	0.071	-0.119	0.068	0.012	0.066						
20.61	0.44	6.45	11.94	0.981	0.075	0.005	0.071	0.005	0.068	0.008	0.066						
20.61	0.44	6.00	35.67	0.696	0.075	0.022	0.071	-0.013	0.068	0.006	0.066						
20.61	0.44	4.98	17.46	0.994	0.075	-0.009	0.071	-0.013	0.068	-0.005	0.066						
21.04	0.87	22.41	-27.48	1.082	0.087	-0.009	0.074	-0.003	0.069	0.024	0.072						
21.04	0.87	18.72	-20.85	0.905	0.087	-0.005	0.074	0.001	0.069	0.023	0.072						
21.04	0.44	18.36	-20.58	0.652	0.087	-0.002	0.074	0.005	0.069	0.013	0.072						
21.04	0.44	10.77	10.71	0.679	0.087	-0.010	0.074	0.005	0.069	0.005	0.072						
21.04	0.44	6.03	12.27	0.509	0.087	-0.009	0.074	-0.008	0.069	0.001	0.072						
21.04	0.44	4.98	34.11	0.629	0.087	-0.001	0.074	-0.080	0.069	-0.012	0.072						

Continued on the next page

v [km/s]	Δv [km/s]	$\Delta\alpha$ [mas]	$\Delta\delta$ [mas]	I [Jy/bm]	σ_I [Jy/bm]	Q [Jy/bm]	σ_Q [Jy/bm]	U [Jy/bm]	σ_U [Jy/bm]	V [Jy/bm]	σ_V [Jy/bm]	m_c [%]	σ_c [%]	m_l [%]	σ_l [%]	χ [deg]	σ_χ [deg]
21.48	3.48	21.48	-24.66	16.871	0.089	-0.029	0.066	0.275	0.062	0.026	0.065			1.60	0.38	41.26	7.22
21.48	0.44	12.24	12.12	0.828	0.089	0.003	0.066	-0.003	0.062	0.003	0.065						
21.48	4.35	8.70	10.53	3.235	0.089	0.001	0.066	0.027	0.062	0.026	0.065						
21.91	0.44	15.84	3.03	0.526	0.059	0.006	0.048	0.051	0.049	0.027	0.047						
21.91	3.91	12.84	10.02	7.306	0.059	0.017	0.048	0.242	0.049	0.410	0.047	5.62	0.65	3.25	0.69	36.15	5.94
21.91	0.44	7.44	12.96	0.687	0.059	-0.001	0.048	0.014	0.049	0.022	0.047						
21.91	0.44	4.74	11.70	0.778	0.059	-0.002	0.048	-0.010	0.049	-0.008	0.047						
22.35	0.87	10.41	5.76	0.932	0.037	0.009	0.035	0.022	0.034	0.026	0.034						
22.78	0.44	16.38	31.05	0.610	0.034	-0.019	0.033	0.024	0.031	0.014	0.032						
23.65	0.44	16.14	16.56	0.653	0.044	-0.011	0.036	-0.009	0.040	-0.007	0.041						
23.65	0.44	3.42	20.55	1.020	0.044	0.012	0.036	-0.001	0.040	-0.007	0.041						
24.08	0.44	2.91	23.94	1.295	0.068	0.003	0.063	-0.018	0.065	-0.031	0.065						
24.08	0.87	-4.56	17.55	1.372	0.068	-0.011	0.063	-0.023	0.065	-0.003	0.065						
24.52	1.30	1.80	21.12	5.650	0.062	0.029	0.049	-0.134	0.052	-0.044	0.050						
24.52	3.91	0.90	9.12	11.387	0.062	0.415	0.049	0.361	0.052	-0.239	0.050	-2.10	0.44	4.81	0.44	13.70	2.66
25.39	4.35	13.17	5.22	9.455	0.063	-0.013	0.055	-0.011	0.056	0.030	0.056						
25.39	0.44	-0.30	20.94	0.945	0.063	-0.007	0.055	-0.001	0.056	-0.010	0.056						
25.39	0.44	-1.53	22.14	0.959	0.063	0.006	0.055	0.005	0.056	-0.006	0.056						
25.39	0.87	-5.97	17.28	1.379	0.063	-0.009	0.055	-0.010	0.056	0.010	0.056						
25.82	1.30	-3.06	7.50	2.621	0.033	0.054	0.030	0.001	0.029	0.012	0.031						
25.82	0.87	-6.36	14.64	2.127	0.033	0.015	0.030	-0.008	0.029	0.005	0.031						
26.26	0.44	-2.31	20.04	0.735	0.027	0.019	0.025	-0.011	0.025	-0.003	0.026						
26.26	1.30	-3.69	19.29	1.203	0.027	0.025	0.025	0.020	0.025	0.003	0.026						
26.26	0.44	-4.50	18.39	0.871	0.027	-5.2e-5	0.025	-0.008	0.025	0.004	0.026						
26.69	0.87	-1.89	11.88	2.741	0.025	0.274	0.025	0.024	0.025	-0.050	0.024	-1.82	0.88	9.99	0.94	-4.25	2.62
28.00	1.74	1.35	-45.03	4.416	0.028	-0.099	0.026	0.590	0.027	-0.011	0.027			13.54	0.61	42.99	1.25
28.86	0.87	0.54	5.58	0.858	0.020	-0.011	0.020	0.005	0.020	-0.004	0.019						
29.30	4.35	1.14	4.74	3.700	0.022	0.020	0.021	0.014	0.022	0.012	0.022						
30.60	0.44	24.33	0.63	1.289	0.023	0.384	0.022	0.054	0.023	-0.001	0.023			30.00	1.78	-2.81	1.68
30.60	4.78	-0.12	4.74	4.387	0.023	0.099	0.022	0.230	0.023	0.069	0.023	1.58	0.54	5.68	0.52	26.51	2.53
31.04	0.44	13.47	-33.12	1.932	0.022	0.024	0.020	-0.466	0.021	-0.051	0.021	-2.65	1.10	24.15	1.11	-50.33	1.26

Continued on the next page

v [km/s]	Δv [km/s]	$\Delta\alpha$ [mas]	$\Delta\delta$ [mas]	I [Jy/bm]	σ_I [Jy/bm]	Q [Jy/bm]	σ_Q [Jy/bm]	U [Jy/bm]	σ_U [Jy/bm]	V [Jy/bm]	σ_V [Jy/bm]	m_c [%]	σ_c [%]	m_l [%]	σ_l [%]	χ [deg]	σ_χ [deg]
31.47	0.44	-8.64	-24.81	1.925	0.024	-0.113	0.023	0.108	0.023	0.113	0.023	5.88	1.21	8.06	1.23	61.37	4.36
31.91	0.44	14.49	-31.41	0.787	0.022	-0.002	0.021	-0.100	0.022	0.020	0.022			12.37	2.94	-52.32	6.37
31.91	0.44	14.07	-30.78	0.620	0.022	0.089	0.021	-0.028	0.022	0.016	0.022			14.66	3.56	-15.35	7.24
32.34	0.44	-3.87	4.89	0.568	0.031	0.005	0.029	-2.8e-4	0.029	0.021	0.028						
32.34	0.44	-13.68	-15.30	0.752	0.031	0.027	0.029	0.013	0.029	4.8e-4	0.028						
32.78	10.43	20.58	-14.55	22.149	0.061	-1.233	0.050	-0.333	0.048	-0.723	0.050	-3.26	0.23	5.76	0.23	-89.24	1.08
32.78	0.87	11.55	-29.73	1.476	0.061	0.651	0.050	-0.225	0.048	-0.008	0.050			46.52	3.91	-16.32	2.02
33.64	0.44	11.07	-28.35	1.835	0.034	0.742	0.032	-0.154	0.032	0.007	0.033			41.25	1.89	-12.65	1.20
33.64	2.17	-8.28	-26.04	1.088	0.034	0.020	0.032	0.005	0.032	0.004	0.033						
35.38	0.44	16.02	-15.54	0.722	0.021	-0.009	0.019	0.005	0.019	0.012	0.019						
38.42	0.44	-15.60	-27.18	0.614	0.020	0.012	0.020	0.003	0.020	0.007	0.019						
39.29	3.04	-9.18	-19.23	5.232	0.033	0.328	0.030	0.019	0.031	-0.008	0.029			6.24	0.58	-5.15	2.76

The columns from left to right are:
Velocity v, full velocity extent Δv of the feature, position offsets $\Delta\alpha$ and $\Delta\delta$ relative to the aligned image centre, Stokes I, error in Stokes I σ_I, Stokes V, error in Stokes V σ_V, Stokes Q, error in Stokes Q σ_Q, Stokes U, error in Stokes U σ_U, fractional circular polarisation m_c, error in fractional circular polarisation σ_c, fractional linear polarisation m_l, error in fractional linear polarisation σ_l, polarisation position angle χ, error in polarisation position angle σ_χ.
The velocity and Stokes parameters of each feature are measured at the position of the peak Stokes I.

Table 6.4: List of maser features detected in the Epoch 2 BR123D IF1 ^{28}SiO v=2 J=1-0 observations.

v [km/s]	Δv [km/s]	$\Delta\alpha$ [mas]	$\Delta\delta$ [mas]	I [Jy/bm]	σ_I [Jy/bm]	Q [Jy/bm]	σ_Q [Jy/bm]	U [Jy/bm]	σ_U [Jy/bm]	V [Jy/bm]	σ_V [Jy/bm]	m_c [%]	σ_c [%]	m_l [%]	σ_l [%]	χ [deg]	σ_χ [deg]
6.18	0.44	-16.27	7.02	3.187	0.018	-0.002	0.018	-0.010	0.018	0.139	0.018	4.36	0.56				
15.37	0.44	9.74	17.40	0.998	0.027	0.003	0.026	-0.005	0.025	8.9e-5	0.025						
15.37	0.44	9.47	16.74	1.054	0.027	0.010	0.026	-0.019	0.025	0.002	0.025						
15.81	0.88	16.85	17.34	1.475	0.030	-0.029	0.030	4.0e-4	0.030	0.011	0.029						
16.25	0.44	8.72	16.68	1.229	0.036	-0.002	0.036	0.002	0.037	-0.010	0.036						
16.69	0.44	11.27	14.97	2.028	0.035	0.028	0.032	-0.015	0.033	0.015	0.034						
17.12	0.88	7.97	15.72	1.690	0.069	0.016	0.067	0.001	0.060	0.018	0.065						
17.56	0.44	7.91	14.40	0.898	0.070	-0.012	0.069	-0.010	0.069	-0.006	0.072						
18.00	2.63	14.03	14.01	3.338	0.039	0.068	0.039	-0.013	0.040	-0.012	0.038						
18.88	0.44	14.75	14.19	0.957	0.070	0.007	0.064	-0.018	0.065	0.007	0.065						
18.88	0.44	13.01	12.66	1.424	0.070	0.008	0.064	0.008	0.065	0.019	0.065						
19.31	3.94	15.08	12.60	5.120	0.066	-0.005	0.059	-0.005	0.061	0.021	0.059						
19.31	0.44	11.09	11.85	1.302	0.066	0.006	0.059	-0.026	0.061	-0.007	0.059						
19.31	1.31	9.62	11.82	0.958	0.066	-0.006	0.059	0.005	0.061	0.005	0.059						
19.75	0.44	17.48	-22.77	1.377	0.082	-0.036	0.071	0.018	0.070	-0.015	0.073						
20.63	2.19	19.43	-23.01	6.353	0.138	0.007	0.127	-0.006	0.123	0.104	0.125						
20.63	2.19	11.48	10.62	4.847	0.138	-0.013	0.127	-0.013	0.123	0.017	0.125						
21.06	1.75	21.35	-24.66	12.669	0.079	-0.207	0.076	-0.139	0.070	-0.004	0.073			1.88	0.61	-163.15	9.08
21.06	1.75	12.68	10.17	6.566	0.079	0.006	0.076	-0.030	0.070	0.293	0.073	4.46	1.12				
21.06	0.88	8.36	10.50	3.047	0.079	-0.084	0.076	0.003	0.070	0.059	0.073						
21.06	0.44	4.64	11.94	1.250	0.079	0.004	0.076	-0.031	0.070	-0.006	0.073						
21.50	0.88	21.92	-23.91	6.219	0.102	0.101	0.090	0.028	0.091	0.009	0.093						
21.50	0.88	13.25	9.30	6.429	0.102	-0.013	0.090	-0.016	0.091	0.003	0.093						
21.94	0.44	15.89	10.92	2.467	0.057	0.006	0.054	-0.006	0.052	0.017	0.052						
22.38	0.44	14.03	8.97	2.420	0.041	-0.004	0.040	-0.005	0.039	-0.011	0.040						
22.81	0.44	7.73	7.62	0.877	0.039	-0.020	0.036	-0.002	0.035	0.005	0.037						
23.25	1.75	14.45	7.08	8.069	0.054	-0.019	0.048	-0.048	0.047	0.246	0.048	3.05	0.59				
23.69	3.50	1.46	9.33	6.535	0.046	-0.014	0.037	-0.004	0.035	-0.144	0.039	-2.20	0.60				
24.13	0.44	1.67	21.12	3.879	0.044	-0.013	0.040	0.042	0.038	-0.065	0.039						

Continued on the next page

v [km/s]	Δv [km/s]	$\Delta\alpha$ [mas]	$\Delta\delta$ [mas]	I [Jy/bm]	σ_I [Jy/bm]	Q [Jy/bm]	σ_Q [Jy/bm]	U [Jy/bm]	σ_U [Jy/bm]	V [Jy/bm]	σ_V [Jy/bm]	m_c [%]	σ_c [%]	m_l [%]	σ_l [%]	χ [deg]	σ_χ [deg]
24.13	0.44	-4.78	17.70	1.410	0.044	0.013	0.040	0.022	0.038	0.028	0.039						
24.56	0.88	12.95	5.31	2.278	0.034	0.006	0.033	-0.020	0.032	-0.017	0.031						
24.56	0.44	1.76	17.94	1.525	0.034	0.015	0.033	-0.036	0.032	-0.016	0.031						
24.56	0.44	-0.97	8.94	1.338	0.034	0.003	0.033	-0.015	0.032	-0.095	0.031	-7.13	2.36				
25.00	0.44	-1.66	22.17	1.752	0.029	-0.007	0.029	-0.012	0.029	0.004	0.030						
25.00	0.88	-5.95	16.92	2.346	0.029	-0.005	0.029	0.017	0.029	-0.004	0.030						
25.44	0.88	-3.85	19.38	1.448	0.030	-0.017	0.028	-0.005	0.027	0.014	0.027						
25.44	0.44	-6.52	14.70	2.593	0.030	-0.027	0.028	-0.004	0.027	-0.004	0.027						
25.88	0.88	-2.08	11.67	1.951	0.032	-0.024	0.030	-0.001	0.031	-0.005	0.031						
28.50	1.75	1.10	4.95	3.739	0.022	-0.026	0.021	0.039	0.021	-0.003	0.021						
29.82	0.88	-0.13	5.10	1.147	0.018	0.012	0.018	0.011	0.018	0.020	0.018						
32.00	0.44	-0.28	3.33	1.053	0.017	-0.014	0.017	-0.003	0.017	-0.023	0.017						
32.44	0.88	20.42	-14.49	3.294	0.019	0.471	0.019	-0.003	0.019	-0.189	0.020	-5.75	0.60	14.28	0.60	-90.20	1.18
34.63	0.44	-1.69	2.16	0.976	0.016	0.003	0.015	-0.009	0.015	-0.004	0.015						
39.01	2.19	12.62	-13.26	12.563	0.028	0.873	0.028	-0.166	0.028	0.334	0.027	2.66	0.22	7.07	0.22	-95.43	0.90

The columns from left to right are:
Velocity v, full velocity extent Δv of the feature, position offsets $\Delta\alpha$ and $\Delta\delta$ relative to the aligned image centre, Stokes I, error in Stokes I σ_I, Stokes V, error in Stokes V σ_V, Stokes Q, error in Stokes Q σ_Q, Stokes U, error in Stokes U σ_U, fractional circular polarisation m_c, error in fractional circular polarisation σ_c, fractional linear polarisation m_l, error in fractional linear polarisation σ_l, polarisation position angle χ, error in polarisation position angle σ_χ.
The velocity and Stokes parameters of each feature are measured at the position of the peak Stokes I.

Table 6.5: List of maser features detected in the Epoch 2 BR123A ^{28}SiO v=1 J=2-1 observations.

v [km/s]	Δv [km/s]	$\Delta\alpha$ [mas]	$\Delta\delta$ [mas]	I [Jy/bm]	σ_I [Jy/bm]	Q [Jy/bm]	σ_Q [Jy/bm]	U [Jy/bm]	σ_U [Jy/bm]	V [Jy/bm]	σ_V [Jy/bm]	m_c [%]	σ_c [%]	m_l [%]	σ_l [%]	χ [deg]	σ_χ [deg]
-1.99	0.44	-6.33	-20.64	1.311	0.055	0.014	0.052	0.062	0.051	-0.027	0.053						
3.23	3.48	-18.93	-3.93	11.113	0.063	0.071	0.058	0.023	0.061	-0.131	0.059	-1.18	0.53				
3.23	2.61	-19.20	5.73	3.308	0.063	-0.040	0.058	0.048	0.061	-0.046	0.059						
4.53	0.44	-13.95	-34.44	1.935	0.051	0.005	0.051	0.083	0.050	-0.020	0.049						
5.40	1.74	15.30	-0.30	4.117	0.050	-0.026	0.050	0.003	0.049	-0.050	0.051						
7.14	1.30	-18.39	-19.92	2.171	0.048	0.042	0.049	0.004	0.048	-0.102	0.050	-4.71	2.29				
7.14	0.87	-24.12	0.00	1.897	0.048	-0.101	0.049	0.035	0.048	0.015	0.050						
7.57	2.61	-18.69	6.45	2.554	0.047	-0.004	0.050	0.010	0.047	0.014	0.050						
8.87	0.87	-19.35	-20.88	1.875	0.056	0.007	0.053	0.026	0.052	-0.043	0.053						
8.87	0.87	-26.25	-0.36	1.808	0.056	0.016	0.053	-0.002	0.052	0.042	0.053						
9.74	1.30	-16.95	7.11	5.497	0.051	-0.035	0.050	-0.021	0.051	-0.049	0.048						
9.74	0.87	-18.63	-2.55	1.900	0.051	-0.021	0.050	0.062	0.051	0.017	0.048						
10.18	0.87	-17.76	-3.54	5.643	0.045	-0.014	0.048	0.047	0.049	-0.019	0.046						
12.35	1.30	-18.24	-2.94	8.091	0.045	0.059	0.046	-0.061	0.046	-0.142	0.043	-1.76	0.53				
13.65	0.87	-18.78	-1.95	2.703	0.055	0.008	0.054	-0.026	0.053	-0.052	0.053						
14.09	0.44	33.45	0.36	2.903	0.078	0.031	0.075	0.065	0.074	-0.057	0.073						
14.09	0.44	-31.86	3.63	2.255	0.078	-0.064	0.075	0.050	0.074	-0.034	0.073						
14.09	0.44	-32.01	-1.11	3.829	0.078	-0.046	0.075	-0.072	0.074	-0.021	0.073						
19.30	0.87	20.46	-21.06	1.537	0.061	0.072	0.058	0.065	0.060	0.004	0.060						
19.30	0.44	16.65	-23.58	1.046	0.061	-0.069	0.058	0.007	0.060	-0.028	0.060						
19.74	0.44	19.14	-24.12	2.575	0.102	0.034	0.101	-0.011	0.102	-0.015	0.101						
20.61	1.30	20.43	-24.42	5.166	0.107	0.268	0.101	-0.045	0.104	-0.061	0.102						
20.61	2.17	18.33	-23.79	5.595	0.107	-0.026	0.101	0.238	0.104	-0.037	0.102						
20.61	0.44	0.24	-22.02	1.568	0.107	-0.033	0.101	-0.008	0.104	0.018	0.102						
21.04	1.30	19.86	-25.98	12.601	0.185	-0.626	0.176	-0.099	0.182	-0.193	0.187			4.83	1.14	-85.50	8.94
21.48	0.44	22.08	-24.30	3.641	0.200	-0.018	0.194	-0.117	0.192	-0.092	0.187						
21.91	0.87	21.51	-26.58	16.183	0.156	-2.407	0.163	-0.422	0.169	-0.268	0.157			15.07	1.58	-85.03	1.99
22.78	0.44	19.23	-30.21	8.730	0.057	-0.101	0.055	0.045	0.054	-0.128	0.053	-1.46	0.61				
23.22	0.44	25.20	-22.17	1.731	0.063	0.002	0.063	-0.067	0.063	-0.046	0.060						

Continued on the next page

v [km/s]	Δv [km/s]	$\Delta\alpha$ [mas]	$\Delta\delta$ [mas]	I [Jy/bm]	σ_I [Jy/bm]	Q [Jy/bm]	σ_Q [Jy/bm]	U [Jy/bm]	σ_U [Jy/bm]	V [Jy/bm]	σ_V [Jy/bm]	m_c [%]	σ_c [%]	m_l [%]	σ_l [%]	χ [deg]	σ_χ [deg]
24.95	0.44	27.15	-20.76	4.136	0.046	-0.058	0.045	-0.056	0.046	0.007	0.046						
26.69	0.44	-8.70	12.69	1.797	0.050	0.023	0.048	0.011	0.049	0.014	0.046						
27.13	0.44	-2.46	6.69	1.192	0.071	-0.019	0.070	0.048	0.069	0.014	0.064						
27.13	0.44	-8.67	9.96	1.072	0.071	-0.050	0.070	0.018	0.069	-0.054	0.064						
27.13	0.44	-23.79	-23.43	3.003	0.071	-0.056	0.070	-0.018	0.069	-0.065	0.064						
27.56	0.87	-8.73	8.76	5.864	0.056	-0.009	0.056	0.088	0.056	0.034	0.058						
28.43	0.44	1.11	-44.55	1.999	0.059	-0.005	0.060	0.009	0.058	-0.055	0.057						
29.30	0.44	12.18	-10.17	1.175	0.060	-0.033	0.059	-0.009	0.059	-0.006	0.062						
29.73	1.74	-3.69	5.64	6.151	0.067	0.104	0.065	0.054	0.067	-0.016	0.069						
30.17	0.44	-32.49	-19.62	3.033	0.058	0.058	0.057	-0.213	0.055	-0.034	0.055			7.05	0.88	-37.42	7.89
31.04	2.61	-3.93	3.96	7.506	0.142	-0.149	0.145	0.019	0.138	-0.021	0.142						
31.04	8.26	-8.37	-25.26	53.815	0.142	-1.694	0.145	-3.012	0.138	-1.187	0.142	-2.21	0.26	6.42	0.48	-59.68	1.19
32.78	1.30	20.64	-14.40	6.326	0.063	-1.866	0.061	-0.081	0.065	0.004	0.062			29.51	1.35	-88.75	1.01
33.64	0.44	-4.92	4.47	1.294	0.056	-0.067	0.059	0.036	0.060	0.015	0.058						
34.51	0.44	18.45	-14.22	2.751	0.055	0.380	0.056	0.793	0.055	-0.119	0.057	-4.31	2.06	31.88	1.98	32.20	1.83
34.95	0.44	3.51	-18.03	1.624	0.051	-0.076	0.046	0.041	0.046	0.033	0.049						
36.25	0.87	-9.99	-28.35	2.632	0.051	-0.017	0.051	-0.107	0.052	0.084	0.051						
37.99	0.44	-10.08	-27.09	1.890	0.042	-0.060	0.041	-0.185	0.040	-0.031	0.041			10.05	0.97	-53.98	6.26
40.16	0.44	-9.12	-18.99	1.796	0.048	-0.032	0.049	-0.032	0.049	-0.037	0.050						

The columns from left to right are:
Velocity v, full velocity extent Δv of the feature, position offsets $\Delta\alpha$ and $\Delta\delta$ relative to the aligned image centre, Stokes I, error in Stokes I σ_I, Stokes V, error in Stokes V σ_V, Stokes Q, error in Stokes Q σ_Q, Stokes U, error in Stokes U σ_U, fractional circular polarisation m_c, error in fractional circular polarisation σ_c, fractional linear polarisation m_l, error in fractional linear polarisation σ_l, polarisation position angle χ, error in polarisation position angle σ_χ.
The velocity and Stokes parameters of each feature are measured at the position of the peak Stokes I.

Chapter 7

Discussion

High resolution images of SiO maser emission in the near-circumstellar envelope of VY CMa obtained from the current work were presented in the previous chapter. The maser emission can be used as a probe of the circumstellar environment, providing information about the gas kinematics, and providing magnetic field estimates, subject to a SiO maser polarisation model.

The simultaneous maps of multiple SiO maser transitions also allows these observations to be used to test models of maser excitation and polarised maser transport, as discussed in Chapter 3. We discuss these results in the current chapter.

The spectra and morphology of the total intensity images are discussed in Section 7.1. In Section 7.2 spectra and enlarged contour plots are provided for a number of individual maser features, which will be used in subsequent observational tests. Comparisons are made between the Epoch 1 and 2 images and to previous VY CMa SiO maser observations, in Sections 7.3 and 7.4 respectively. The maser maps are then discussed in terms of the SiO maser excitation models in Section 7.5, and in terms of SiO maser polarisation models in Section 7.6. In Section 7.7 the magnetic field in the SiO maser region is discussed, and in Section 7.8 the results are discussed in terms of the larger scale geometry of the VY CMa circumstellar envelope.

7.1 Total intensity morphology

For all transitions observed in the Epoch 1 and Epoch 2 total intensity maser maps, the emission falls within a region $\sim 100 \times 100$ mas in angular extent. Adopting a stellar diameter of 18.7 mas and dust formation radius of $\sim 40 - 50$ mas (Section 2.1), most of the observed emission is therefore located within a few stellar radii from the star, and within the dust formation radius.

Only a fraction of the total intensity SiO maser emission is detected in the VLBA maps, as discussed in further detail below. The missing flux can be attributed either to diffuse emission, on a scale too large to be resolved by the VLBA, or to numerous low intensity maser spots which fall below the noise levels of the images, an alternative suggested by Gray et al. (2009).

7.1.1 Epoch 1

In the Epoch 1 maps, no clear ring structure is visible in the distribution of maser spots from the individual transitions (Figure 6.10). However, when the maser emission from transitions v=1 J=1-0,

v=2 J=1-0 and v=1 J=2-1 are overlaid as in Figure 6.10, the emission appears to encircle a possible stellar position centred approximately at (-20,15) mas relative to the field centre, with a gap in emission in the north-northwest.

In Figures 6.1 to 6.4, the autocorrelation spectra are compared with the summed interferometric Stokes I emission in the final image cubes. For the v=1 J=1-0 and v=2 J=1-0 lines respectively, $\sim$ 50% and $\sim$ 75% of of integrated intensity from the autocorrelation spectra is recovered in the VLBA Stokes I images. However, for the v=1 J=2-1 line the fraction recovered is much lower, $\sim$ 14%, and for the v=0 J=1-0 map $<$ 1% of the total intensity is recovered.

7.1.2 Epoch 2

In the Epoch 2 total intensity maps, the SiO maser emission appears to be located in a sparse wide ring. The radial extent of the maser ring ranges from $\sim$ 20 mas to a maximum of $\sim$ 40 mas for the v=1 J=1-0 emission in the northeast. Both the v=1 and v=2 J=1-0 maps display concentrated emission regions in the east and northeast. One of the most sriking features in the images is an $\sim$ 14 mas elongated feature to the east, which is also visible in J=1-0 SiO maser maps presented by Choi et al. (2008a) and Zhang et al. (2012). These individual regions of emission are discussed in more detail in subsequent sections.

An estimate of the stellar position is required for a number of the observational tests performed later in this chapter; we adopt the zeroth-order assumption that the central star is most likely located toward the centroid of the inner shell of SiO maser features. An estimate of the position was made through a grid search of the inner 30 mas of the image, to find the the position which maximises the minimum projected distance to the closest maser feature. The feature positions in Tables 6.3, 6.4 and 6.5 were used in this minimisation. This method locates the star in a plausible position near the centre of the emission. A circle representing the star is shown on Figure 7.1, centred on the estimated stellar position, with a diameter of 18.7 mas (Monnier et al. 2004).

Zhang et al. (2012) recently presented images of the SiO maser emission towards VY CMa, referenced to the stellar position through VLA observations of the radio photosphere. The stellar position estimated by the method described above lies $\lesssim 5 \times 5$ mas to the southwest of the stellar position given in Zhang et al. (2012). This offset is within the 10 mas uncertainty they quote for the stellar position relative to the VLBA SiO maser maps.

Approximately 35 – 40% of the total emission from the J=1-0 lines was recovered in the VLBA images, as shown in the spectra in Figures 6.6 and 6.7. For the v=1 J=2-1 line, approximately 22% of the total emission shown in the autocorrelation spectrum displayed in Figure 6.8 was recovered interferometrically.

7.2 Maser feature analysis

Seven maser features were chosen from the higher quality Epoch 2 images for more detailed analysis. The features were chosen due to their spatial coincidence, or near spatial coincidence, in more than one SiO maser transition. The positions of the feaures are shown in Figure 7.1, where they are labelled F1 through F7. Two extended regions of emission are also indicated on the figure, as R1 and R2. These regions contain multiple maser features which overlap in more than one transition. They are

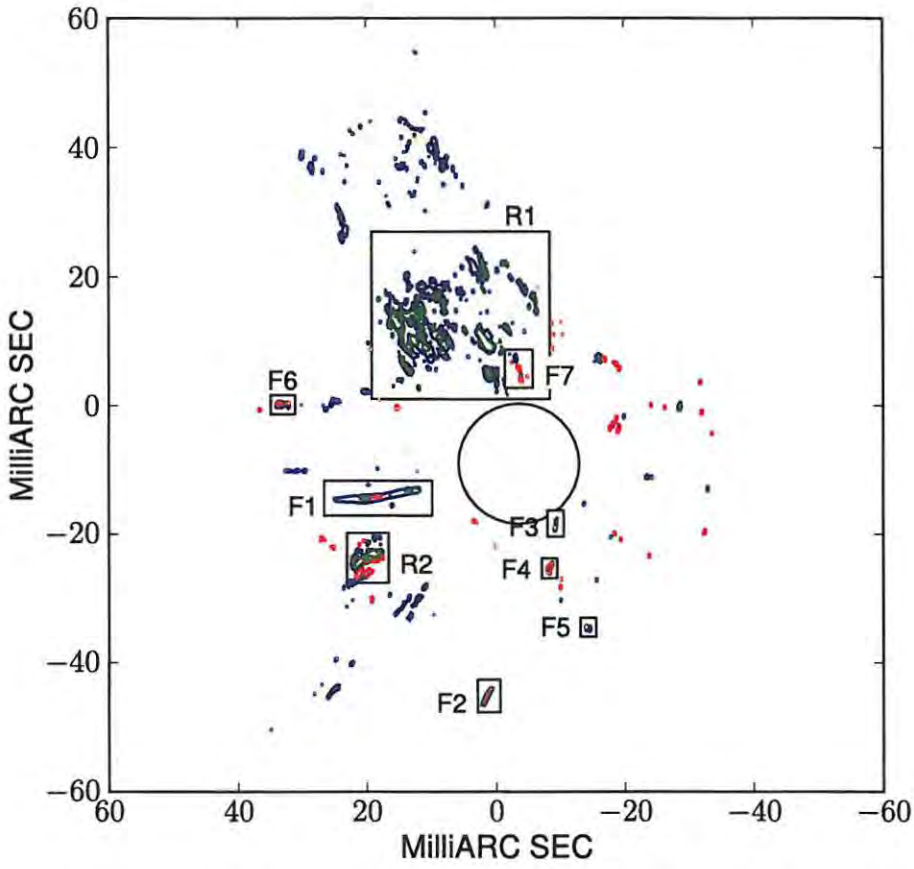

Figure 7.1: Overlaid contour plots of the Epoch 2 BR123 Stokes I images of the transitions v=1 J=1-0 (blue), v=2 J=1-0 (green), and v=1 J=2-1 (red), reproduced from Figure 6.11. The features F1 to F7 and regions R1 and R2 are discussed in the text and plotted in Figures 7.2 through 7.10. A circle of diameter 18.7 mas is plotted at the adopted stellar position, as described in Section 7.1.2.

	NIST		SLAIM		CDMS
	Predicted	Measured	Predicted	Measured	Predicted
v=1 J=1-0		43122.09 ± 0.02	43122.07 ± 0.002	43122.09 ± 0.002	43122.03 ± 0.05
v=2 J=1-0		42820.57 ± 0.02	42820.58 ± 0.002	42820.57 ± 0.002	42820.48 ± 0.05
v=1 J=2-1	86243.43 ± 0.04		86243.43 ± 0.004	86243.37 ± 0.1	86243.37 ± 0.05

Table 7.1: Rest frequencies of the observed SiO maser lines, in units of GHz, from the NIST (Lovas 1992), SLIAM (Remijan et al. 2007) and CDMS (Müller et al. 2005) catalogues.

plotted separately in Figures 7.9 and 7.10. Spectra are not presented for R1 and R2 in these figures, due to their complexity.

For each of the seven features F1 to F7, the peak Stokes I value was extracted for each frequency channel across the feature. The Stokes Q, U and V values were then extracted at the pixel position of the Stokes I maximum, and the circular and linear polarisation calculated from these values, following the method described in Section 6.5 of the previous chapter.

The features and their spectra are plotted in Figures 7.2 through 7.8. In a few cases the features consist of multiple distinct spots, separated in position or frequency. In these cases the spots are labelled separately in the figures, and separate spectra are plotted for each spot.

For each feature, a contour plot of overlapping v=1 J=1-0 (blue), v=2 J=1-0 (green) and v=1 J=2-1 (red) emission is shown. The contour levels are drawn at three and five times the maximum broadened noise for each cube, as described in the figure captions. If the contours for a particular transition are absent, this indicates that the emission is less than the lowest contour. Separate contour and EVPA plots are provided for the transitions with statistically significant measurements of linear polarisation.

In the plotted Stokes I spectra, only intensity values greater than three times the broadened noise specific to each channel were included in the plot. Where significant linear or circular polarisation was measured, the percentage polarisation values are shown in separate spectra.

The BR123 v=2 J=1-0 image cube appears to have a constant frequency offset of ~ 2 channels from the v=1 J=1-0 and v=1 J=2-1 BR123 cubes. The offset was noted from the positional alignment of maser components two channels removed in frequency, with the ~ 2 channel offset alignment persisting over the velocity range of individual maser features. The velocity increment over each spectral channel differs slightly between the v=1 and v=2 lines, due to their different rest frequencies. However, the observed offset is to large to be explained by the velocity increment differences. Instead, the offset may be due to an error in the assumed rest frequency of this line.

Table 7.1 lists the v=1 J=1-0, v=2 J=1-0 and v=1 J=2-1 rest frequencies reported in the catalogues "The Cologne Database for Molecular Spectroscopy" (CDMS) (Müller et al. 2005), the "NIST Recommended Rest Frequencies for Observed Interstellar Molecular Microwave Transitions" (NIST) (Lovas 1992) and the "Spectral Line Atlas of Interstellar Molecules" (SLIAM) (Remijan et al. 2007). The CDMS rest frequencies were used in the VLBA schedule for the BK103 and BR123 observations.

The v=2 J=1-0 rest frequency given by the CDMS differs from the NIST and SLAIM rest frequencies by 0.09-0.1 MHz, which is larger than the quoted errors and corresponds to ~ 1.5 channels for the BR123 43 GHz channel width of 0.0625 MHz. A simple χ^2 quadratic fit for x-axis position versus velocity was performed to the v=1 J=1-0 and v=2 J=1-0 spots comprising feature F1 (Figure

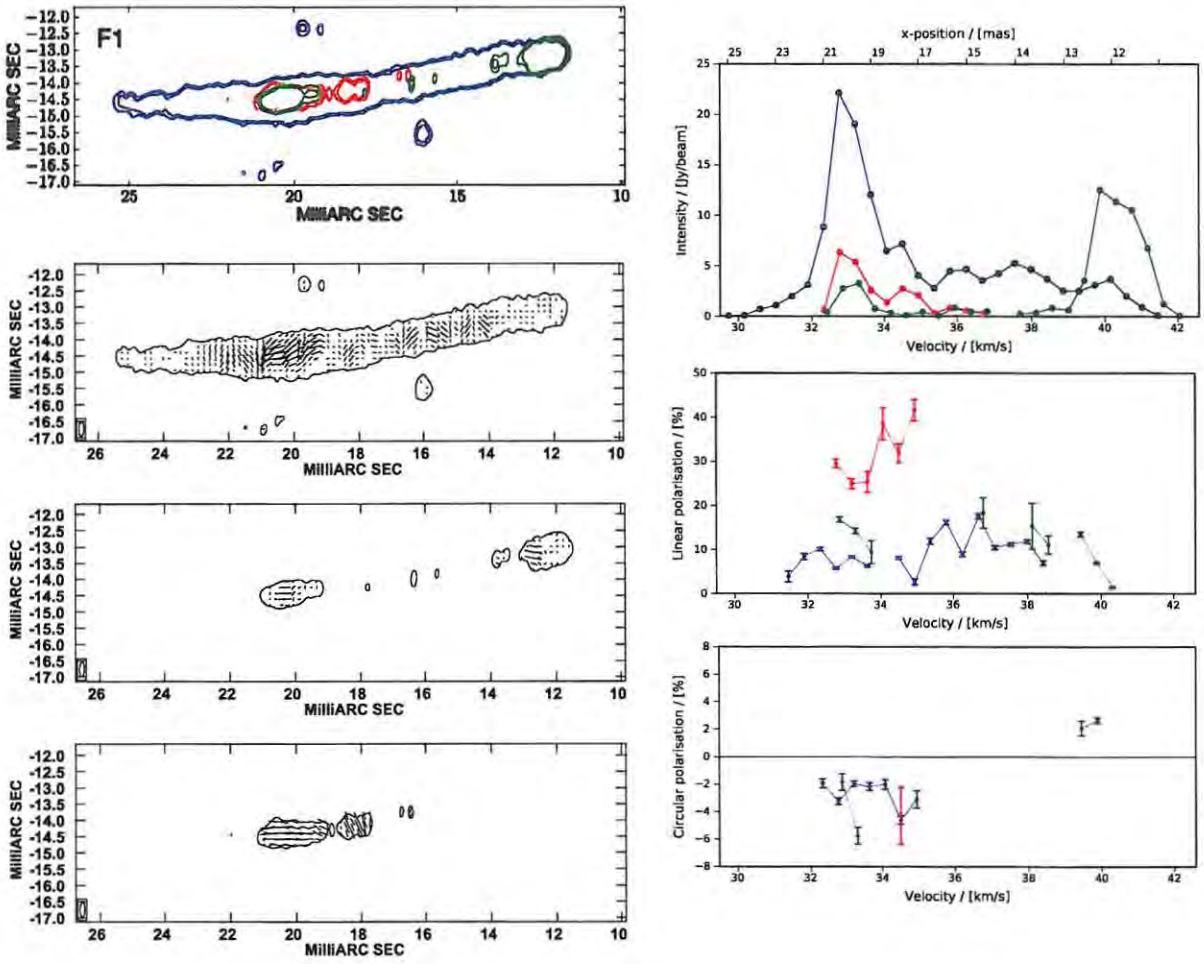

Figure 7.2: Plots of feature F1, as indicated on Figure 7.1.
Left column, top to bottom: overlaid contour plot of the v=1 J=1-0 (blue), v=2 J=1-0 (green) and v=1 J=2-1 (red) maser emission drawn at contour levels of three and five times the maximum Stokes I broadened noise for each cube (89, 138 and 200 mJy/beam respectively); contour plots of the v=1 J=1-0, v=2 J=1-0 and v=1 J=2-1 emission overlaid with linear polarisation EVPA vectors, where a vector length of 1 mas = 27.78×10^{-3} Jy/beam in linearly-polarised intensity. The vector orientation is in the direction of absolute EVPA for the J=1-0 lines. The synthesised beam is shown in the bottom left of the polarisation images, and is 0.46×0.15 mas in half-power with a position angle of $-1.80°$.
Right column, top to bottom: Stokes I (top), percentage linear polarisation (middle) and percentage circular polarisation (bottom) spectra of the feature, plotted against line of sight velocity (in km/s) in the Local Standard of Rest (LSR) frame. The upper axis of the Stokes I spectrum shows the x-position where the v=1 J=1-0 Stokes parameters were measured, at each velocity channel across the feature.

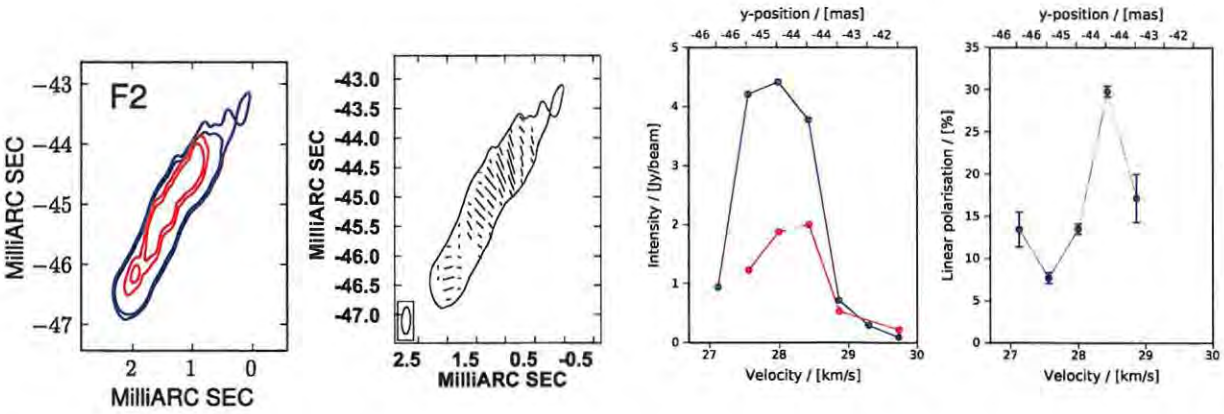

Figure 7.3: Plots of feature F2, as indicated on Figure 7.1.
Left: overlaid contour plot of the v=1 J=1-0 (blue) and v=1 J=2-1 (red) maser emission drawn at contour levels of three and five times the maximum Stokes I broadened noise for each cube (89 and 200 mJy/beam respectively). Centre left: contour plot of the v=1 J=1-0 emission overlaid with linear polarisation EVPA vectors, where a vector length of 1 mas = 27.78×10^{-3} Jy/beam in linearly-polarised intensity. The vector orientation is in the direction of absolute EVPA; The synthesised beam is shown in the bottom left of the polarisation image, and is 0.46×0.15 mas in half-power with a position angle of $-1.80°$. Centre right: Stokes I spectrum of the feature, plotted against line of sight velocity (in km/s) in the Local Standard of Rest (LSR) frame. Right: Percentage linear polarisation spectrum of the feature. The upper axes of the spectra show the y-position where the v=1 J=1-0 Stokes parameters were measured, at each velocity channel across the feature.

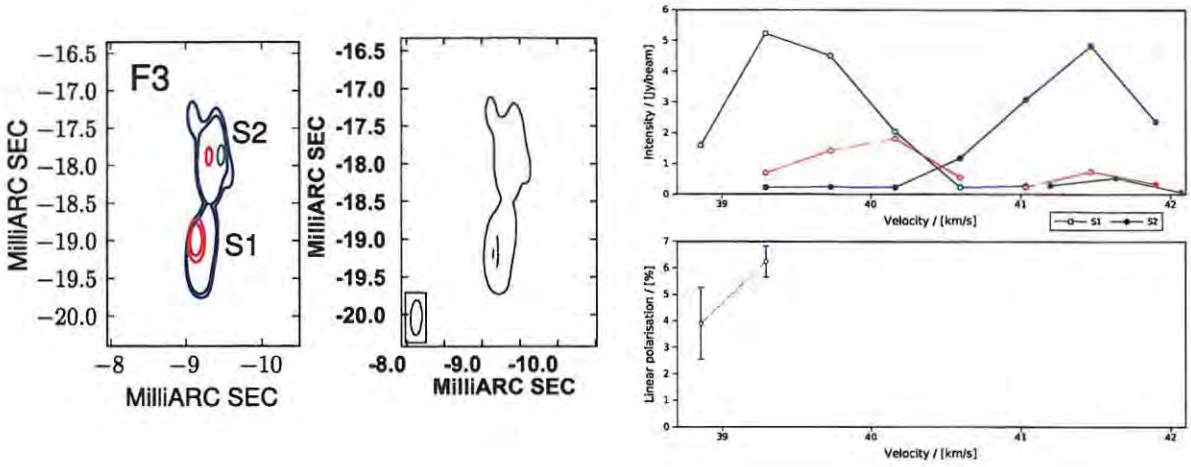

Figure 7.4: Plots of feature F3, as indicated on Figure 7.1.
Left: overlaid contour plot of the v=1 J=1-0 (blue), v=2 J=1-0 (green) and v=1 J=2-1 (red) maser emission drawn at contour levels of three and five times the maximum Stokes I broadened noise for each cube (89, 138 and 200 mJy/beam respectively). Middle: contour plot of the v=1 J=1-0 emission overlaid with linear polarisation EVPA vectors, where a vector length of 1 mas = 27.78×10^{-3} Jy/beam in linearly-polarised intensity. The vector orientation is in the direction of absolute EVPA. The synthesised beam is shown in the bottom left of the polarisation image, and is 0.46×0.15 mas in half-power with a position angle of $-1.80°$. Right: Stokes I and percentage linear polarisation spectra of each of the spots in the feature, plotted against line of sight velocity (in km/s) in the Local Standard of Rest (LSR) frame.

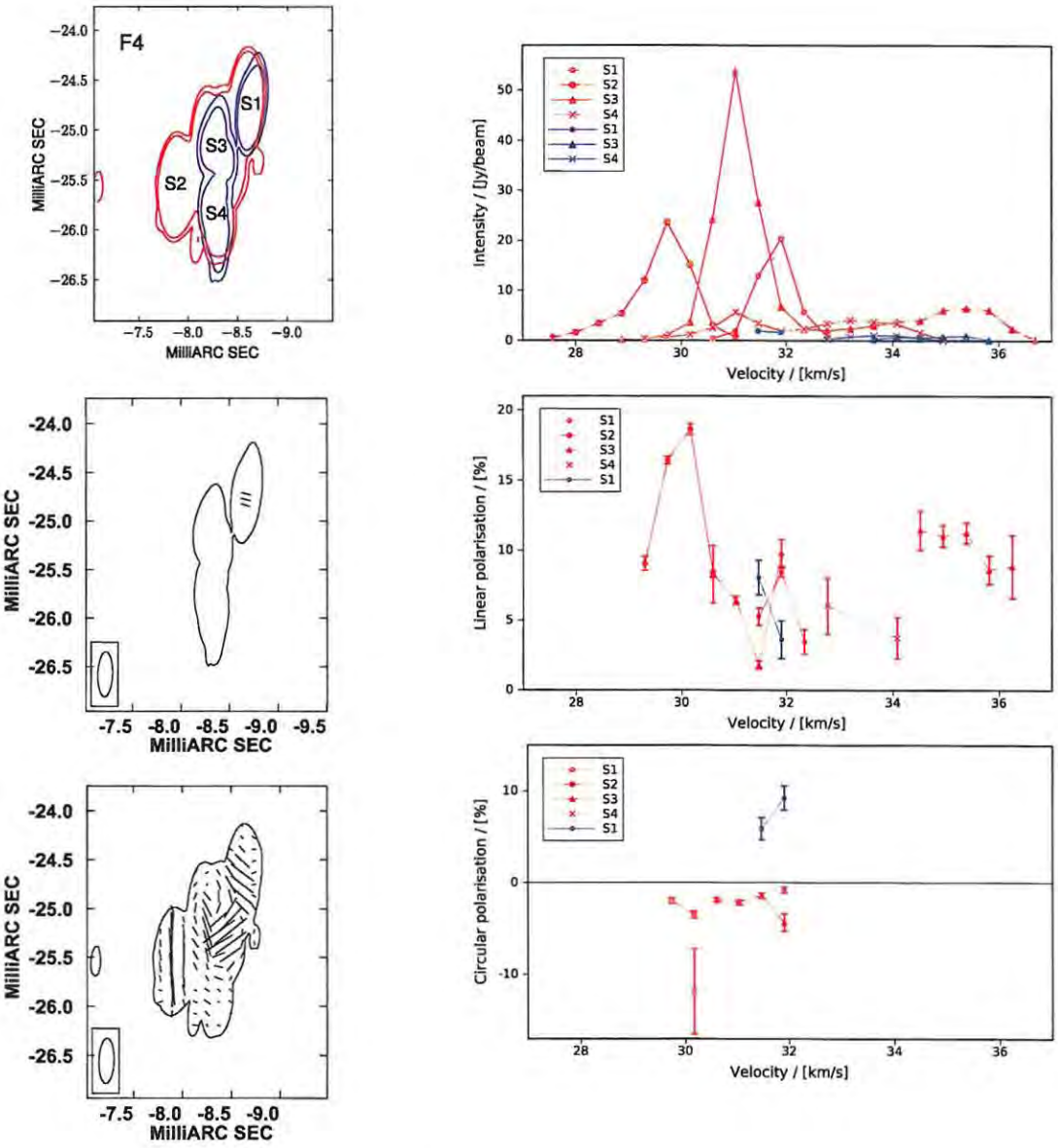

Figure 7.5: Plots of feature F4, as indicated on Figure 7.1.

Left column, top to bottom: overlaid contour plot of the v=1 J=1-0 (blue) and v=1 J=2-1 (red) maser emission drawn at contour levels of three and five times the maximum Stokes I broadened noise for each cube (89, 138 and 200 mJy/beam respectively); contour plot of the v=1 J=1-0 and v=1 J=2-1 emission overlaid with linear polarisation EVPA vectors, where a vector length of 1 mas = 27.78×10^{-3} Jy/beam (v=1 J=1-0) and 1 mas = 83.33×10^{-3} Jy/beam (v=1 J=2-1) respectively in linearly-polarised intensity. The vector orientation is in the direction of absolute EVPA for the J=1-0 line. The synthesised beam is shown in the bottom left of the polarisation images, and is 0.46 × 0.15 mas in half-power with a position angle of $-1.80°$.

Right column, top to bottom: Stokes I, percentage linear polarisation and percentage circular polarisation spectra for each of the spots in the feature, plotted against line of sight velocity (in km/s) in the Local Standard of Rest (LSR) frame.

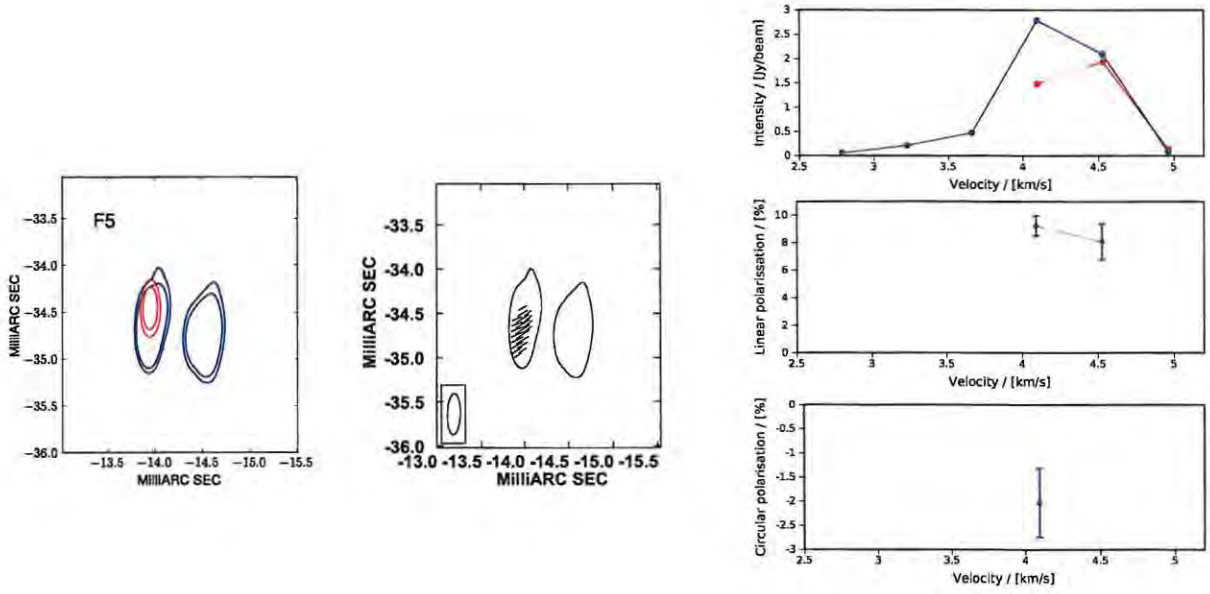

Figure 7.6: Plots of feature F5, as indicated on Figure 7.1.
Left: overlaid contour plot of the v=1 J=1-0 (blue) and v=1 J=2-1 (red) maser emission drawn at contour levels of three and five times the maximum Stokes I broadened noise for each cube (89 and 200 mJy/beam respectively). Middle: contour plot of the v=1 J=1-0 emission overlaid with linear polarisation EVPA vectors, where a vector length of 1 mas = 27.78×10^{-3} Jy/beam in linearly-polarised intensity. The vector orientation is in the direction of absolute EVPA. The synthesised beam is shown in the bottom left of the polarisation image, and is 0.46×0.15 mas in half-power with a position angle of $-1.80°$. Right: Stokes I, percentage linear polarisation and percentage circular polarisation spectra of the overlapping eastern spot, plotted against line of sight velocity (in km/s) in the Local Standard of Rest (LSR) frame.

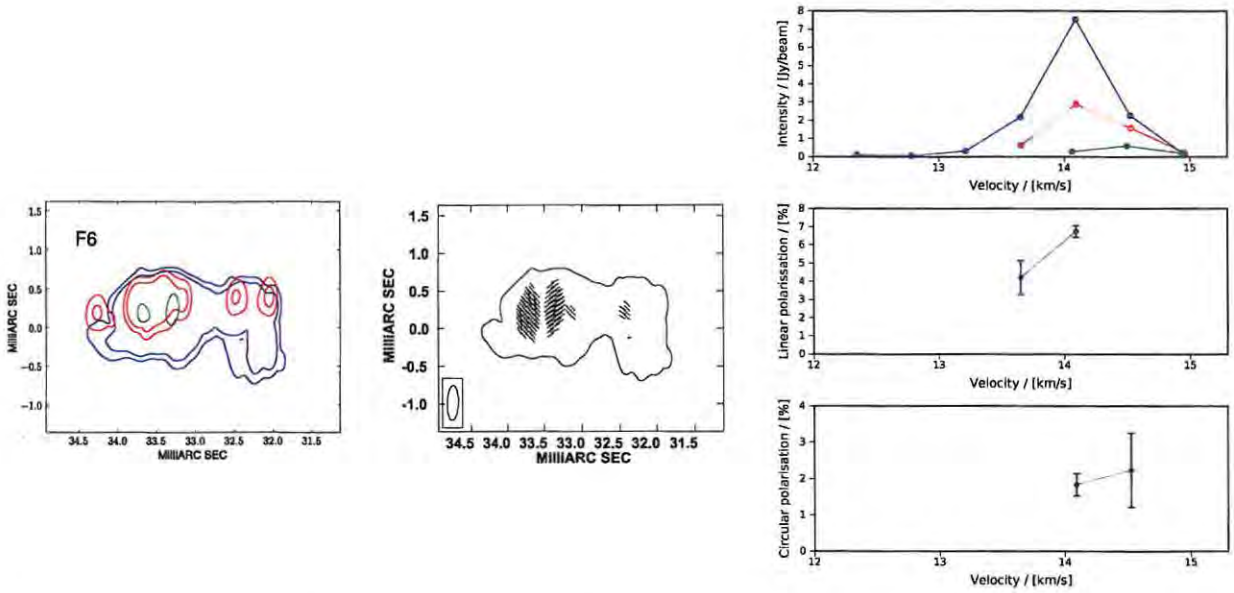

Figure 7.7: Plots of feature F6, as indicated on Figure 7.1.
Left: overlaid contour plot of the v=1 J=1-0 (blue), v=2 J=1-0 (green) and v=1 J=2-1 (red) maser emission drawn at contour levels of three and five times the maximum Stokes I broadened noise for each cube (89, 138 and 200 mJy/beam respectively). Middle: contour plot of the v=1 J=1-0 emission overlaid with linear polarisation EVPA vectors, where a vector length of 1 mas = 27.78×10^{-3} Jy/beam in linearly-polarised intensity. The vector orientation is in the direction of absolute EVPA. The synthesised beam is shown in the bottom left of the polarisation image, and is 0.46×0.15 mas in half-power with a position angle of $-1.80°$. Right: Stokes I, percentage linear polarisation and percentage circular polarisation spectra of the feature, plotted against line of sight velocity (in km/s) in the Local Standard of Rest (LSR) frame.

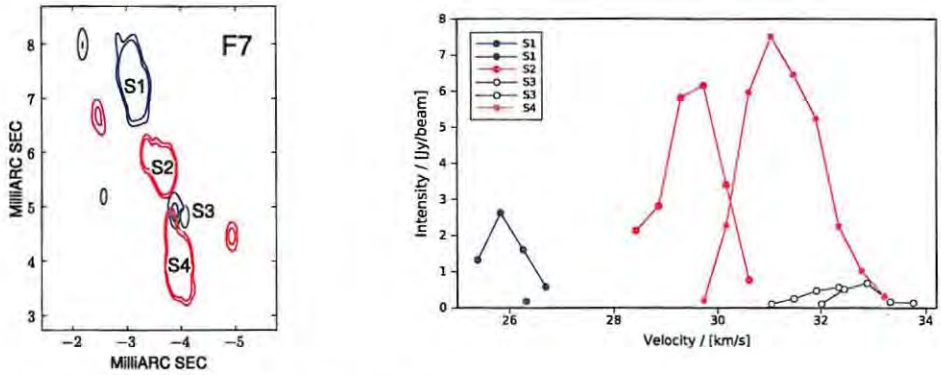

Figure 7.8: Plots of feature F7, as indicated on Figure 7.1.
Left: Overlaid contour plot of the v=1 J=1-0 (blue), v=2 J=1-0 (green) and v=1 J=2-1 (red) maser emission drawn at contour levels of three and five times the maximum Stokes I broadened noise for each cube (89, 138 and 200 mJy/beam respectively). Right: Stokes I component spectra for each of the individual spots, plotted against line of sight velocity (in km/s) in the Local Standard of Rest (LSR) frame.

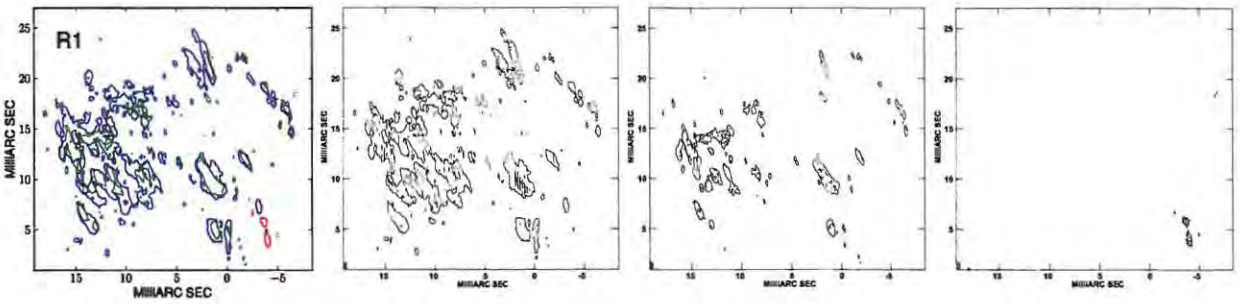

Figure 7.9: Plots of region R1, as indicated on Figure 7.1.
Left to right: overlaid contour plot of the v=1 J=1-0 (blue), v=2 J=1-0 (green) and v=1 J=2-1 (red) maser emission drawn at contour levels of five times the maximum Stokes I broadened noise for each cube (89, 138 and 200 mJy/beam respectively); contour plots of the v=1 J=1-0, v=2 J=1-0 and v=1 J=2-1 emission overlaid with linear polarisation EVPA vectors. The EVPA vector length is 1 mas = 9.26×10^{-3} Jy/beam in linearly-polarised intensity, a scale three times larger than most of the vectors shown in Figures 7.2 to 7.8 above. The vector orientation is in the direction of absolute EVPA for the J=1-0 lines. The synthesised beam is shown in the bottom left of each polarisation image, and is 0.46 × 0.15 mas in half-power with a position angle of $-1.80°$.

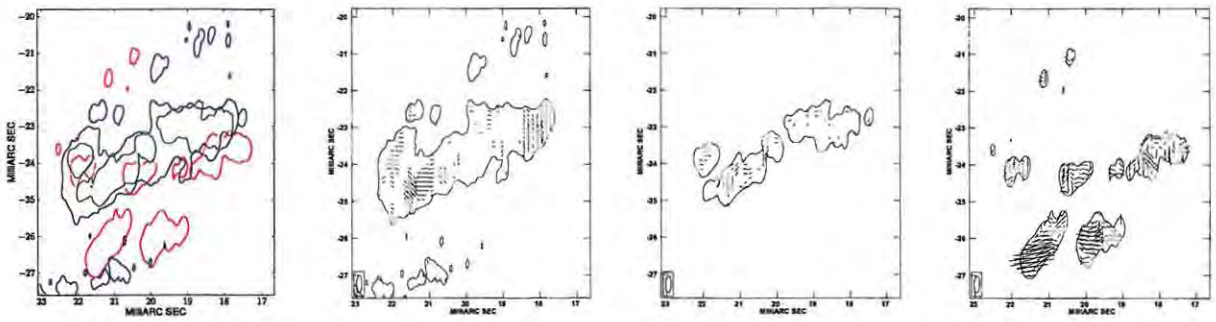

Figure 7.10: Plots of region R2, as indicated on Figure 7.1.
Left to right: overlaid contour plot of the v=1 J=1-0 (blue), v=2 J=1-0 (green) and v=1 J=2-1 (red) maser emission drawn at contour levels of five times the maximum Stokes I broadened noise for each cube (89, 138 and 200 mJy/beam respectively); contour plots of the v=1 J=1-0, v=2 J=1-0 and v=1 J=2-1 emission overlaid with linear polarisation EVPA vectors. The EVPA vector length is 1 mas = 27.78×10^{-3} Jy/beam in linearly-polarised intensity. The vector orientation is in the direction of absolute EVPA for the J=1-0 lines. The synthesised beam is shown in the bottom left of each polarisation image, and is 0.46 × 0.15 mas in half-power with a position angle of $-1.80°$.

7.2), including a velocity offset between the two lines. The fitted velocity offset was 0.667 km/s, corresponding to $\sim$ 1.5 channels, consistent with the v=2 J=1-0 rest frequency differences between the catalogues.

The observed velocity offset implies a relative error between the assumed rest frequencies of the v=1 J=1-0 and v=2 J=1-0 transitions. The correct absolute rest frequencies of these lines cannot be determined from the observed relative offset. However, the frequency spacing between the three lines is more consistent with the SLAIM rest frequencies, and we recommend the SLAIM catalogue for future observations.

The v=2 J=1-0 spectra in Figures 7.2 to 7.8 were shifted by two channels to account for the offset. High precision velocity information is not required by the observational tests that follow, so precise corrections for the offset were not attempted.

7.3 Comparison: Epoch 1 and Epoch 2

The changes in the total power spectra of the SiO maser emission between Epoch 1 and Epoch 2 are shown in Figure 6.5.

The overall flux density of the v=1 J=2-1 line in Epoch 1 was more than double that of Epoch 2, over the matching velocity range. The peak in the v=1 J=2-1 spectrum also moved from an LSR velocity of $\sim$ 16 km/s in Epoch 1 to a velocity of $\sim$ 21.5 km/s in Epoch 2.

Conversely, for the v=1, 2 J=1-0 spectral lines the flux density is much higher in Epoch 2. For both lines the flux density more than doubled from Epoch 1 to Epoch 2, and the form of the spectra changed considerably. The Epoch 1 spectra are dominated by strong, spectrally-isolated features, particularly in the case of the v=2 J=1-0 line, with v=1 and v=2 J=1-0 peaks located at LSR velocities of $\sim$ 22 and $\sim$ 21km/s respectively. The Epoch 2 v=1, 2 J=1-0 spectra are dominated by a broad region of emission spanning $\sim$ 10 km/s around the adopted stellar velocity of $\sim$ 21 km/s (Table 2.3).

The broad, central region of emission has a similar spectral form in both the v=1 and v=2 J=1-0 transitions and is peaked at a velocity of $\sim$ 21 km/s. It corresponds predominantly to emission from the extended regions R1 and R2 in the images.

The fact that only 35 − 40% of the single-dish flux density from the Epoch 2 J=1-0 lines is recovered in the interferometric images may imply considerable undetected larger scale emission. Inspection of the spectra in Figures 6.6 and 6.7 show that the greatest shortfall in total power single-dish flux density recovered interferometrically lies in the region of the spectrum near the stellar velocity. The missing flux density may include diffuse emission surrounding R1 and other strong features in the maps. In support of this hypothesis, regions around R1 and F1 in the v=1 and v=2 J=1-0 maps displayed imaging artifacts indicative of larger scale emission around these features. The visibilities were ultimately imaged with uniform weighting to mitigate these artifaces.

The changes in the J=1-0 spectra between the Epoch 1 observations in 2003 and the Epoch 2 observations in 2007 are consistent with single-dish long-term monitoring observations of the v=1 and v=2 J=1-0 SiO masers published by Pardo et al. (2004). The spectra presented by Pardo et al. (2004) show variability in both the peak flux density and velocity extent of the central spectral region. A strong spike at a velocity of $\sim$ 22.5 $\pm$ 0.5 km/s persists throughout the 11 year period of their observations. A peak at a velocity of $\sim$ 21 − 22 km/s is present in all of the spectral lines observed

in this thesis, across Epoch 1 and Epoch 2. These peaks are close to the adopted stellar velocity of $\sim$ 21 km/s; they likely persist for long periods because of the tangential nature of the SiO maser amplification, which leads to preferential maser amplification near the stellar velocity.

In the images, the number of maser features detected is considerably greater in the Epoch 2 observations, as shown in Figures 6.10 and 6.11, primarily due to the greater sensitivity and velocity extent of the Epoch 2 observations.

The full velocity extent of the SiO maser emission towards VY CMa in the v=1 J=2-1, v=2 J=1-0 and v=1 J=2-1 lines is approximately 40 km/s (e.g. Spencer et al. 1981; Pardo et al. 2004; Kang et al. 2006). An observation of weak 2σ line wings extends the velocity range to $\sim$ 49 km/s (Cernicharo et al. 1997). Due to instrumental trade-offs, the Epoch 1 maps only cover 28 km/s, while the Epoch 2 maps extend over about 46 km/s, both centered on the scheduled central velocity of 18 km/s. The Epoch 1 maps therefore only show emission from an inner subset of the total velocity range of the maser emission.

The maser features cannot be confidently tracked between Epoch 1 and Epoch 2 images, due to the $\sim$ 3.5 year interval between the observations, and the differences in sensitivity and velocity range of the observations. Nonetheless, a possible alignment of the Epoch 1 and Epoch 2 maps is shown in Figure 7.11. For this alignment, the two main features that overlap are the features labeled F1 and R2 in the Epoch 2 map in Figure 7.1.

The v=1 J=1-0 Epoch 1 feature that appears to overlap with F1 spans a velocity range of 20.0 to 21.7 km/s. This is considerably different to the 29.7 to 41.5 km/s spanned by feature F1 in the Epoch 2 v=1 J=1-0 map (Figure 7.3). However, the upper velocity limit in the v=1 J=1-0 Epoch 1 observations was 29.9 km/s, so if the observed $\sim$ 21 km/s Epoch 1 feature is associated with a longer feature at velocities higher than 30 km/s, the high frequency component would not have been detected in Epoch 1.

The v=1 J=1-0 Epoch 1 feature that appears to overlap with R2 spans a velocity range of 24.8 to 25.9 km/s. In Epoch 2, feature R2 spans a velocity range of $\sim$ 18.9 to 22.8 km/s. These features are sufficiently similar in shape and close in velocity over the two epochs that it is plausible that they they are the the same maser feature.

Both features F1 and R2 are present in all four Zhang et al. (2012) v=1 J=1-0 maser images, discussed in the next section. This adds support to the hypothesis they may have counterparts in the Epoch 1 map, which preceds the first Zhang et al. (2012) image by two years.

One area of morphological commonality between the two epochs is the J=1-0 maser emission is concentrated to the east of the assumed stellar position in both epochs. This trend is also seen in previous v=1 and v=2 J=1-0 images, as discussed in the next section.

7.4 Comparison: Previous SiO maser images

While the SiO maser emission towards VY CMa shown in Figures 6.10 and 6.11 does appear to encircle the central supergiant star, the ring of maser emission is radially thicker and less well defined than the rings often observed around AGB stars (e.g. Diamond et al. 1994; Yi et al. 2005; Cotton et al. 2008; Gonidakis et al. 2010). This morphology of a sparse extended ring of emission has been observed previously towards VY CMa in a number of published v=1 and v=2, J=1-0 and J=2-1 interferometric

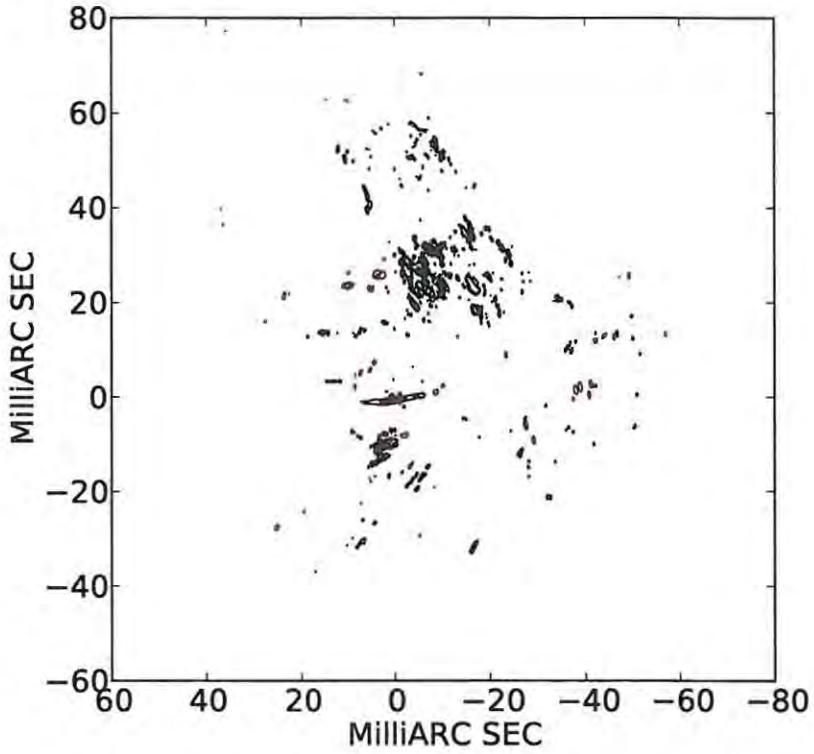

Figure 7.11: Overlaid contour plots of Epoch 1 BK103 Stokes I (magenta) and Epoch 2 BR123 Stokes I (black), showing the possible alignment between the two images. In each case, contours are plotted for tansitions v=1 J=1-0, v=2 J=1-0 and v=1 J=2-1, at the level of the lowest contour used in each of Figures 6.1, 6.2 and 6.4 (Epoch 1), and Figures 6.6, 6.7 and 6.8 (Epoch 2).

images, discussed earlier in Section 2.3.7.

Miyoshi et al. (1994) imaged the v=1 and v=2 J=1-0 lines with KNIFE and found that the distribution of maser features was similar for the two transitions, concentrated in two regions spaced approximately 30 mas apart along a north north-east south south-west direction. A ring structure is not visible in these maps, and the location of the maser emission relative to the star is unknown. The masers were observed over a limited velocity range of $15.05 - 28.96$ km/s, approximately a quarter of the full velocity range of the SiO maser emission. Subsequent VLBA imaging of the same two lines by Miyoshi (2003) shows emission concentrated in radially-extended, partial ring sections predominantly to the east of the star. The v=1 and v=2 J=1-0 maps presented by Miyoshi (2003) are very similar, with many components coincident in the two images.

VLBA maps of the v=1 and v=2 J=1-0 emission toward VY CMa for two epochs separated by nine years were presented by Richter et al. (2007). These images also show emission concentrated to the east of the assumed stellar position, in radially-extended partial ring fragments. We note that the second epoch presented in Richter et al. (2007) are the Epoch 1 images presented in this thesis.

Choi et al. (2008a) published phase-referenced maps of SiO maser emission in the v=1 and v=2 J=1-0 transitions observed using VERA, and reproduced in Figure 2.6 in Chapter 2. These observations show a very similar maser distribution to the Epoch 2 images presented in this thesis. The Choi et al. (2008a) observations were undertaken in 2006, while the Epoch 2 observations presented in this thesis took place in March 2007. Many of the features observed in this thesis are also visibile in the Choi et al. (2008a) images, including the extended region R1 to the northeast of the star, the elongated feature F1 to the east of the star, and the region of emission R2 immediately south of F1.

Zhang et al. (2012) recently published four epochs of VLBA images of the v=1 J=1-0 SiO maser emission towards VY CMa, observed during October 2005, April 2006, September 2006 and April 2007. The final set of observations took place 14 April 2007, only twenty-seven days after the Epoch 2 v=1 J=1-0 images presented in this thesis. The distribution of SiO masers in the Epoch 2 v=1 J=1-0 image is very similar to the Zhang et al. (2012) images, in particular the April 2007 image, as expected from the proximity of the observations. All four of the Zhang et al. (2012) images display a similar overall morphology to the Epoch 2 image, with a concentration of maser features in the northeast, an elongated feature in the east and relatively sparse emission in the west and southwest. Many individual maser features can be visually associated between the Zhang et al. (2012) images and the Epoch 2 image, including the features labelled F1, F2, F3, F4, F6, F7 and R2 in Figure 7.1. Zhang et al. (2012) found nine maser features that persisted throughout the $\sim$ 18 month period of their observations, so the correspondence of the March 2007 Epoch 2 image with the Zhang et al. (2012) images is consistent with their observed lifetime of both the individual maser features and the overall maser distribution.

VY CMa has also been imaged in the v=1 J=2-1 line, using a single VLBI baseline between the 14 m TRAO telescope and the 45 m NRO telescope (Shibata et al. 2004). The observations took place in 2002 and 2003. The 2002 map is reproduced in Figure 2.6 in Chapter 2. The maser emission appears to be located primarily to the south and west of the assumed stellar position. The distribution of maser emission in the 2003 map of Shibata et al. (2004) (their Figures 3b and 4b) is similar to the Epoch 1 v=1 J=2-1 map observed in 2003 and presented in Figure 6.4. The overall distribution of emission is similar, and several spots can be tentatively cross-identified between the two maps. The Shibata et al. (2004) 2003 map is shown alongside the Epoch 1 v=1 J=1-0 map (Figure 6.4) in Figure 7.12.

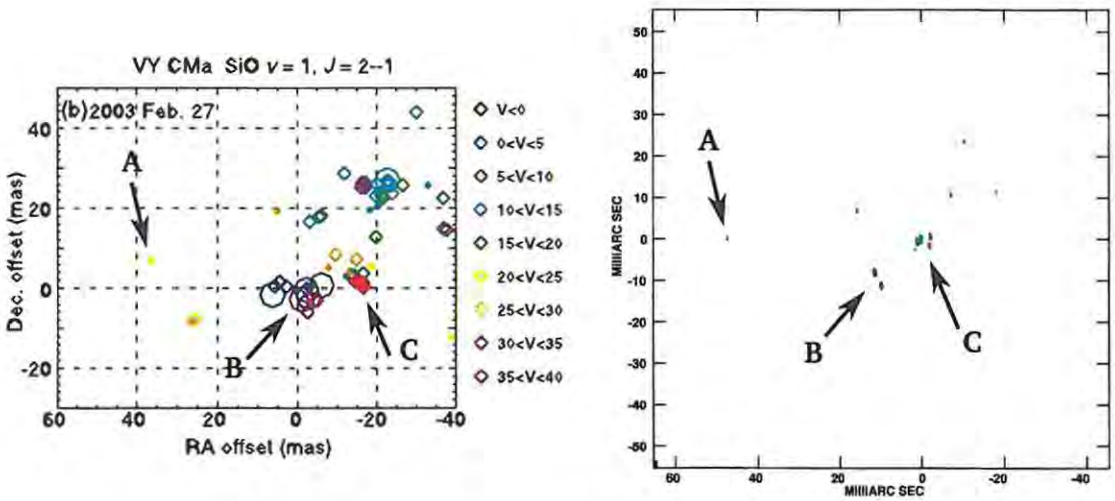

Figure 7.12: The 2003 Shibata et al. (2004) (left) and Epoch 1 (right) v=1 J=2-1 SiO maser maps. The maser features labelled A, B and C can be identified across the two maps.

Maser features that can be identified across the two maps are indicated in the figure. The existence of coincident maser features in these two images provides supporting evidence for the alignment between the Epoch 1 J=1-0 maps and J=2-1 map adopted here and shown in Figure 6.10, which places the J=2-1 emission predominantly to the south and west of the central star.

The relationship between the large-scale morphology of the VY CMa nebula and the SiO maser maps is discussed in Section 7.8.

7.5 Circumstellar SiO maser models

Models for SiO maser excitation around evolved stars were reviewed in Section 3.3 of Chapter 3. The models rely either on radiative pumping, collisional pumping, or a combination of the two. Which pumping mechanism is at work can be evaluated through several observational tests, which are discussed in this section. The maser pumping models have also been combined with hydrodynamical models of circumstellar envelopes (e.g. Gray et al. 2009, and further discussion below). These composite models provide predictions which can be compared to observed SiO maser distributions.

Several key predictions of these models concern the relative characteristics of the v=1 J=1-0, v=2 J=1-0 and v=1 J=2-1 SiO maser emission. The main predictions of the models that can be tested against the images presented in this thesis are summarised in Section 7.5.1. This is followed in Section 7.5.2 by a discussion of the observational evidence for or against the models. A number of the model predictions discussed below involve identifying coincident regions of emission from different transitions. The maser maps presented in this thesis are not astrometrically registered, so the maps were aligned using cross-correlation, as described in Section 6.4 of the previous chapter. As previously discussed, the uncertainties in the map alignment were derived from a Gaussian fit to the peaks in the cross correlation function, and are estimated to be less than 0.05 mas.

7.5.1 SiO maser model predictions

In both radiative and collisional pumping models, the v=1 and v=2 J=1-0 masers are inverted under different conditions (e.g. Lockett & Elitzur 1992; Bujarrabal 1994).

However, while radiative pumping predicts almost no overlap between v=1 and v=2 transitions, they can show a significant amount of overlap for collisional pumping (Lockett & Elitzur 1992). Extensive overlap between the v=1 and v=2 J=1-0 emission therefore argues for a collisional pumping mechanism maintaining the maser emission. In the collisional pumping model of Lockett & Elitzur (1992), the range of conditions under which the v=1 J=1-0 masing occurs is wider than that of the v=2 J=1-0 transition, with the v=2 line requiring higher density conditions.

Alternatively, extensive overlap between the v=1 and v=2 J=1-0 emission may be caused by a line overlap between the v_2=0 $12_{75} \rightarrow$ v_2=1 11_{66} H_2O transition at 1219.10 cm^{-1} and the v=1 J=0 $\rightarrow$ v=2 J=1 SiO transition at 1219.15 cm^{-1}. This H_2O line overlap mechanism was originally invoked to explain the anomolously low v=2 J=2-1 SiO maser emission (Olofsson et al. 1981; Bujarrabal et al. 1996). Soria-Ruiz et al. (2004) investigated the effect of the line overlap using the primarily radiative SiO maser excitation model of Bujarrabal et al. (1996). The main result of their work is that when the line overlap is included, the conditions for v=1 and v=2 J=1-0 masers to occur overlap considerably, but the conditions where the v=1 J=1-0 and and J=2-1 masers both occur are more limited.

The SiO maser excitation models that have been coupled to hydrodynamical models of the circumstellar environment have been used to create simulated images of SiO maser emission in circumstellar envelopes (Humphreys et al. 1996; Gray & Humphreys 2000; Humphreys et al. 2002; Gray et al. 2009). The models have had various sucesses, including predicting the existence of SiO maser emission from high angular momentum states above J=6 (Gray et al. 1995a,b), and predicting the ring geometry of the maser emission (Humphreys et al. 1996). Although these models do include a radiative pumping component, the pumping mechanism is found to be predomnantly collisional (Humphreys et al. 1996).

The hydrodynamical SiO maser models make a number of specific predictions about the relative location of SiO maser emission from the v=1 J=1-0, v=2 J=1-0 and v=1 J=2-1 transitons. The predictions are outlined in Humphreys et al. (1996), Humphreys et al. (2002) and Gray et al. (2009), and include:

- The v=1 J=1-0 maser ring is thicker than that of the other two transitions, and maser emission occurs over a wider range of physical conditions (Gray & Humphreys 2000).
- The v=2 masers lie closer to the star than the v=1 masers (Gray & Humphreys 2000; Gray et al. 2009).
- The v=1 J=1-0 and J=2-1 lines often arise in shared components, in rings of similar radii, and the radial motions of the rings from these two lines are coupled (Gray & Humphreys 2000; Humphreys et al. 2002).
- There will be a greater number of v=1 J=1-0 maser features than v=1 J=2-1 features in the envelope (Humphreys et al. 2002).
- Where v=1 J=2-1 and v=1 J=1-0 features overlap, the v=1 J=2-1 emission will be brighter (Humphreys et al. 2002).

7.5.2 Total intensity observational tests

v=1 J=1-0 and v=2 J=1-0

Simultaneous observations of the v=1 and v=2 J=1-0 masers have been performed towards numerous late-type evolved stars. The earliest maps, presented by Miyoshi et al. (1994), show overlap between maser features in these two lines. Subsequent higher-resolution observations by Desmurs et al. (2000), on the other hand, show a systematic offset between emission from the two transitions. Desmurs et al. (2000) regard this offset as supportive of radiative pumping models, which predict that if emission is present from both lines in the same maser clump, the v=2 line will mase in the region closest to the star, as is found in their observations.

A number of later observations at similar angular resolution to the Desmurs et al. (2000) observations show significant overlap between the v=1 and v=2 masers (e.g. Miyoshi 2003; Yi et al. 2005; Cotton et al. 2006, 2008). In the overlapping v=1 and v=2 features present in the Yi et al. (2005) maps, the v=2 emission tends to arise closer to the star, and the v=1 emission at greater distance from the star, with an intermediate region of overlap.

More recent astrometrically-aligned maps of the v=1 and v=2 J=1-0 emission towards R Aquarii produced by the VERA array show that the number of coincident maser spots in these two lines is actually small, but that v=1 and v=2 spots are clustered together and may appear coincident at lower resolution, or if absolute position information about the images is not available (Kamohara et al. 2010). This supports the Desmurs et al. (2000) result. Kamohara et al. (2010) find a number of spot clusters that have offsets of 1-2 mas between the v=1 and v=2 J=1-0 emission.

In both epochs of images presented in this thesis, there is a significant amount of overlap between the v=1 and v=2 J=1-0 emission. In the Epoch 1 observations, the v=2 emission is more radially extended in some cases than the v=1 emission, and there are several v=2 features with no coincident, or even nearby, matching v=1 features. However, in Epoch 1 the v=1 J=1-0 images had lower SNR than the v=2 J=1-0 images, so the more limited v=1 emission in Epoch 1 may simply be an SNR artifact.

In the Epoch 2 observations however, the v=2 emission is located almost exclusively in a subset of v=1 emission regions. This is consistent with the Gray & Humphreys (2000) hydrodynamical model, which predicts a thicker maser ring for the v=1 J=1-0 line, and the v=2 masers arising in a subset of the v=1 conditions.

Of the Epoch 2 maser features analysed in more detail in Section 7.2, features F1, F3 and F6 show overlapping emission from the v=1 and v=2 J=1-0 transitions, and feature F7 shows adjacent emission. In the elongated feature F1 the v=2 J=1-0 emission is located in two main regions within the v=1 J=1-0 emission region: near the region of peak intensity, and at the inner end of the feature, closest to the star. Where the v=1 and v=2 J=1-0 emission overlaps, it is expected that the v=2 emission will occur closest to the star, under a radiative pumping scheme (Desmurs et al. 2000), or in higher density conditions (also presumably closer to the star), under a collisional pumping scheme (Doel et al. 1995; Gray & Humphreys 2000). So the v=2 emission at the inner end of the long feature can be explained by either pumping mechanism. The overlapping region in the peak intensity centre of the F1 may be due to competitive gain, where transitions in different vibrationally-excited states become coupled as the maser emission saturates (Doel et al. 1995). Alternatively, the coherent path

length of the maser emission may be longest in this region, allowing significant amplification for all three maser species.

The more extended regions of emission R1 and R2 also display overlapping v=1 and v=2 J=1-0 maser emission. Most of the v=2 emission appears to follow the v=1 emission closely in these regions, occupying the same, or smaller, regions as those exhibiting v=1 emission. The large overlap argues either for a predominantly collisional pumping mechanism at work in these regions, or for the H_2O line overlap mechanism dscussed by Soria-Ruiz et al. (2004) coupling the v=1 and v=2 J=1-0 lines under a predominantly radiative model. The linear polarisation is weak in region R1 however, as shown in Figure 7.9, where the scale of the linear polarisation EVPA vectors is larger than that of the other figures. Linear polarisation is a defining characteristic of radiative pumping from the central star (Bujarrabal & Nguyen-Q-Rieu 1981), so the lack of linear polarisation in this feature argues against radiative pumping in this region. Radiative pumping would also lead to decreasing maser pumping with distance from the star, as stellar radiation is diluted over a greater volume. So the radial extent of the maser emission in region R1 also argues against radiative pumping in this region. However, the close coupling of the v=1 and v=2 J=1-0 maser emission in region R1 may still be evidence of a H_2O line overlap, but possibly combined with a collisional pumping mechanism.

In summary, our results discussed in this section favor predominant collisional pumping, particularly in the context described by Gray & Humphreys (2000).

v=1 J=1-0 and v=1 J=2-1

For technical reasons, simultaneous observations of the v=1 J=1-0 and v=1 J=2-1 SiO masers are less common than those of v=1 and v=2 J=1-0 SiO masers. In most of the published simultaneous observations, the distributions of spots have been different, usually with no observed overlapping maser emission (Desmurs et al. 2002; Soria-Ruiz et al. 2004, 2005, 2006, 2007). An exception is R Cassiopeiae, which displays definitively overlapping v=1 J=1-0 and v=1 J=2-1 SiO maser features in a map published by Phillips et al. (2003).

Unlike most previous observations, the maps in this thesis show a significant number of overlapping v=1 J=1-0 and v=1 J=2-1 SiO maser features. Both observing epochs display overlapping features, but only for a small subset of the total number of maser features in the two transitions. Most of the v=1 J=2-1 features have no counterpart in v=1 J=1-0, and *vice versa*. The J=2-1 emission is also notably absent from the large-scale northeastern region of J=1-0 maser emission in the Epoch 2 maps.

In terms of the number of detected maser spots listed in Tables 6.3 and 6.5 of the previous chapter, the v=1 J=1-0 maser emission is present in about double as many spots as the v=1 J=2-1 emission. The Epoch 1 maps also display a larger number of maser features in the v=1 J=1-0 map than in the v=1 J=2-1 map. This is consistent with the predictions of the Humphreys et al. (2002) hydrodynamical model. However, the instrumental sensitivity of the VLBA is much lower at 86 GHz so fewer components are expected to be detected for the J=2-1 emission.

All of the maser features described in Section 7.2 show coincident emission in the v=1 J=1-0 and J=2-1 transitions, except for feature F7. This feature was selected as an example of v=1 J=1-0 and J=2-1 emission that seemingly require spatially separated excitation conditions. Feature F7 displays a velocity gradient with distance from the star, with the v=1 J=2-1 spot S3 being located in what appears to be a gap, or intensity minimum, in the v=1 J=2-1 emission between spots S2 and S4.

As described in the preceding section, the coincidence of v=1 J=1-0 and J=2-1 SiO maser emission is consistent with both radiative and collisional pumping schemes, as maser emission should occur naturally along rotational ladders within a given vibrational state (Alcolea 2004). No existing SiO maser maps have shown this level of coincidence between v=1 J=1-0 and J=2-1 lines, however, so these maps in this thesis provide new observational evidence constraining current maser excitation models.

In features F1, F2, F3 and F5 the v=1 J=2-1 emission falls inside the v=1 J=1-0 emission region, and in feature F6 this is also the case for most of the v=1 J=2-1 emission. The spectra of these features show similar shape in the J=1-0 and J=2-1 lines, with the J=2-1 emission weaker in all cases. The similar spectral shapes provide evidence that the coincident maser emission from these two transitions arises from the same physical regions of gas. This relative weakness of the J=2-1 masers conflicts with the Humphreys et al. (2002) model prediction of greater intensity in the J=2-1 line, for overlapping components.

Under the predominantly collisional pumping SiO maser model of Doel et al. (1995), the v=1 J=2-1 maser amplification is greater than that of v=1 J=1-0 masers for intermediate densities around 5×10^9 H_2 cm^{-1}. The v=1 J=1-0 amplification becomes greater for both higher or lower density conditions. The amplification can be stronger for the v=1 J=1-0 line than the v=1 J=2-1 line for high densities $\gtrsim 6 \times 10^9$ H_2 cm^{-1}, but the amplication factors are very low relative to the amplification of both of these lines under lower density conditions. The weaker J=2-1 features may therefore imply lower densities of $\lesssim 4 \times 10^9$ H_2 cm^{-1} in the overlapping features. Phillips & Boboltz (2000) also found that the v=1 J=2-1 emission was weaker than the coincident v=1 J=1-0 emission in their maps, and make the same suggestion about low gas density.

The Doel et al. (1995) model prediction of greater amplification for the v=1 J=2-1 maser emission in the intermediate density regime discussed above may provide an explanation for the fact that most of the v=1 J=2-1 features do not have a v=1 J=1-0 counterpart. This trend is particularly visible in the west of Figure 7.1. If the masing gas in these regions falls in the intermediate intensity regime, then the amplification of v=1 J=2-1 maser emission may be much larger than that of the v=1 J=1-0 maser emission, so that v=1 J=1-0 maser emission is not significant in v=1 J=2-1 maser regions. This is not expected from the Gray & Humphreys (2000) model, which predicts that the v=1 J=2-1 masers occur in a subset of the conditions where the v=1 J=1-0 masers occur.

Alternatively, the existence of v=1 J=2-1 masers without v=1 J=1-0 counterparts may be indicative of radiative pumping of these masers. Under the predominantly radiative pumping model of Bujarrabal (1994), v=1 J=2-1 emission is stronger than the v=1 J=1-0 emission over most of the range of envelope conditions they investigated, with a greater difference at lower densities. Bujarrabal (1994) found a second regime of collisionally pumped maser emission for higher density conditions, where the v=1 J=1-0 emission can be stronger than the v=1 J=2-1 emission.

On the other hand, region R1 displays a notable lack of v=1 J=2-1 maser emission. This region contains many maser features from the v=1 J=1-0 and v=1 J=2-1 transitions, as discussed in the previous section. Under the collisional pumping model of Doel et al. (1995), the absence of v=1 J=2-1 emission in this region may imply lower density conditions in this region, which leads to low amplification of the v=1 J=2-1 maser. However, if the close correspondence between the v=1 J=1-0 and v=1 J=2-1 emission in this region is due to the effects of an H_2O line overlap, as discussed

above, then the notable lack of v=1 J=2-1 emission may imply higher density conditions in this region (Soria-Ruiz et al. 2004).

Finally, feature F4 is the only feature which is stronger and more extensive in the J=2-1 line than the J=1-0 line. Feature 4 extends over almost 10 km/s in velocity in the J=2-1 line, with an intense peak over the velocity range 29-32 km/s and an extended weaker tail up to $\sim$ 36 km/s. The J=1-0 emission is located in the weaker tail of the J=2-1 emission. This feature is also strongly linearly polarised. The marked difference between the characteristics of this feature and the other overlapping features may imply different physical conditions in the gas, or a different excitation route, for this feature.

In summary, the v=1 J=1-0 and J=2-1 maser maps presented in this thesis display a greater level of coincident features than has previously been observed. However, in contradiction to the Humphreys et al. (2002) model predictions, the J=2-1 emission is weaker than the J=1-0 emission in most cases for the coincident features. This behaviour is consistent with the Doel et al. (1995) model, where the relative weakness of the v=1 J=2-1 emission implies a low density constraint.

7.6 Polarisation tests

The polarisation tests proposed in Section 3.4.9 of Chapter 3 were performed using the Epoch 2 observations, due to the higher sensitivity of this observational epoch and the more accurate circular polarisation calibration. The tests were performed using the maser feature lists in Tables 6.3, 6.4 and 6.5 in the previous chapter, and, for the multi-transition tests, the coincident features identified in Figures 7.2 to 7.7.

The polarisation errors quoted in this section are formal errors calculated from propogation of errors in the Stokes parameters, as described in Section 6.5. As discussed in Section 5.4, the circular calibration method is believed to be accurate to $\leq 0.5 - 1\%$ for the J=1-0 masers, and $\leq 1\%$ for the J=2-1 masers.

The stellar diameter of VY CMa is assumed to be 18.7 mas and the distance to VY CMa is assumed to be 1.14 kpc throughout this section (see Table 2.3). As discussed in Section 3.2, the SiO masers are probably saturated, but the exact level of saturation cannot be known due to the unknown beaming angle.

7.6.1 Linear polarisation in v=1 J=1-0 and v=1 J=2-1

The Epoch 2 features in Tables 6.3, 6.4 and 6.5 which display statistically significant linear polarisation are shown in Figures 7.13, 7.14 and 7.15. The SiO maser models make predictions about the relative linear polarisation in the different transitions, as discussed in Section 3.4.9. For these tests, the linear polarisation must be compared at component-level in maser features with coincident emission in the v=1 J=2-1 and v=1 J=2-1 transitions. In particular, it is necessary that the maser emission be compared for regions where the angle between the magnetic field and the line of sight are the same.

Of the overlapping v=1 J=1-0 and v=1 J=2-1 features, the only two meeting these conditions that showed statistically significant linear polarisation in both lines are feature F1 (Figure 7.2) and feature F4 (Figure 7.5).

In feature F1 the linear polarisation is considerably greater in the v=1 J=2-1 line, with an average

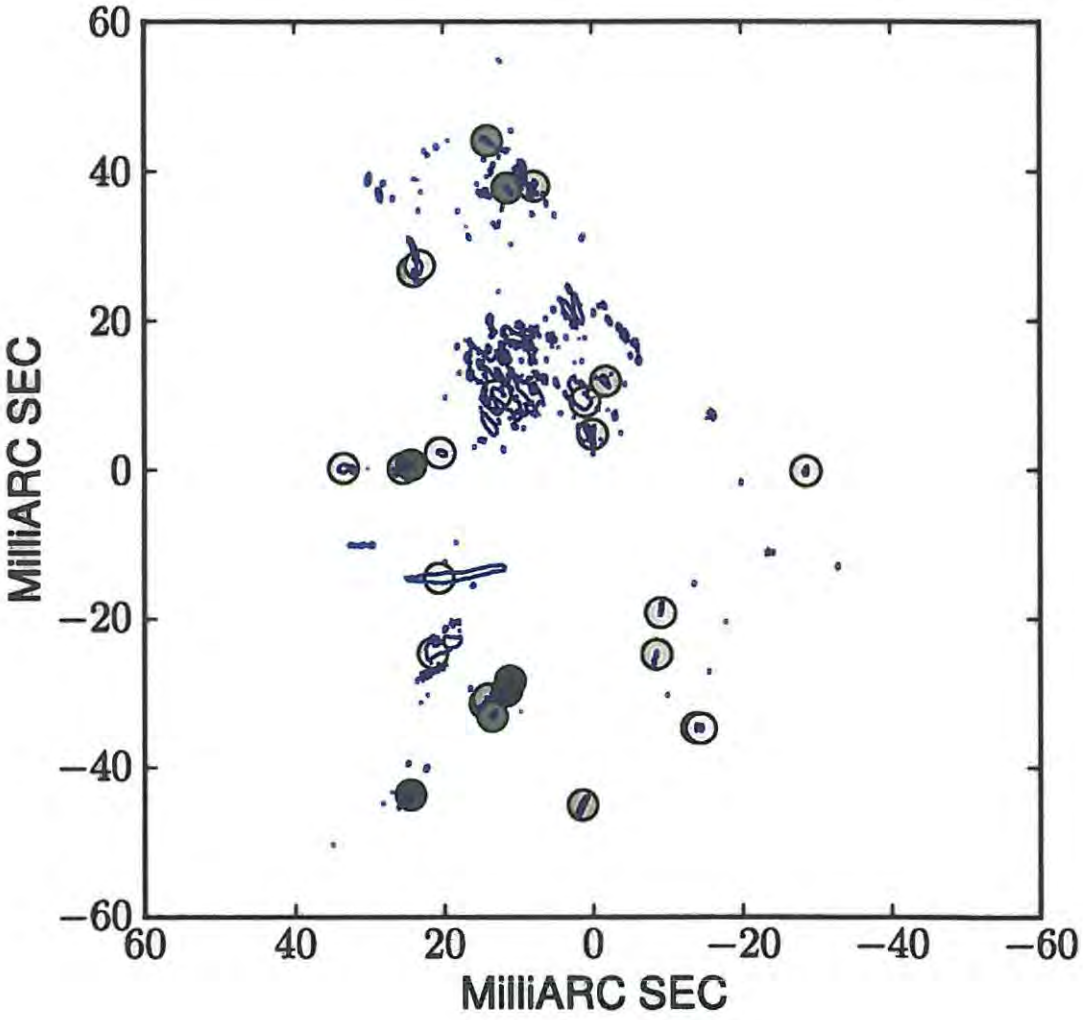

Figure 7.13: Epoch 2 v=1 J=1-0 linearly polarised features, from Table 6.3. Each linearly polarised feature is represented by a circle around the centre of the feature, with the gray scale level of the circle representing the level of the linear polarisation. The overall minimum linear polarisation in all three transitions is 1.6%, and the overall maximum is 46.5%, and the same grey polarisation scale is used in Figures 7.14, 7.13 and 7.15.

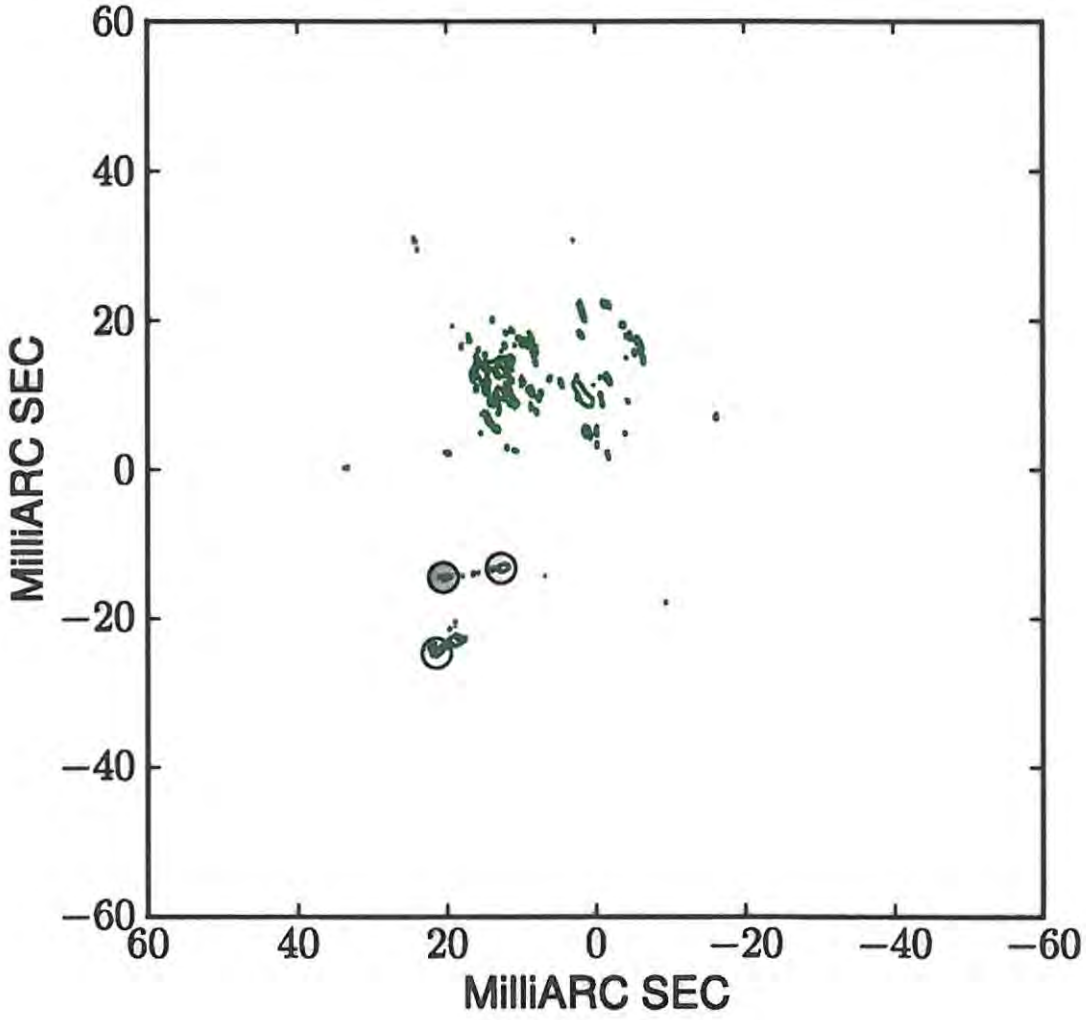

Figure 7.14: Epoch 2 v=2 J=1-0 linearly polarised features, from Table 6.4. Each linearly polarised feature is represented by a circle around the centre of the feature, with the gray scale level of the circle representing the level of the linear polarisation. The overall minimum linear polarisation in all three transitions is 1.6%, and the overall maximum is 46.5%, and the same grey polarisation scale is used in Figures 7.14, 7.13 and 7.15.

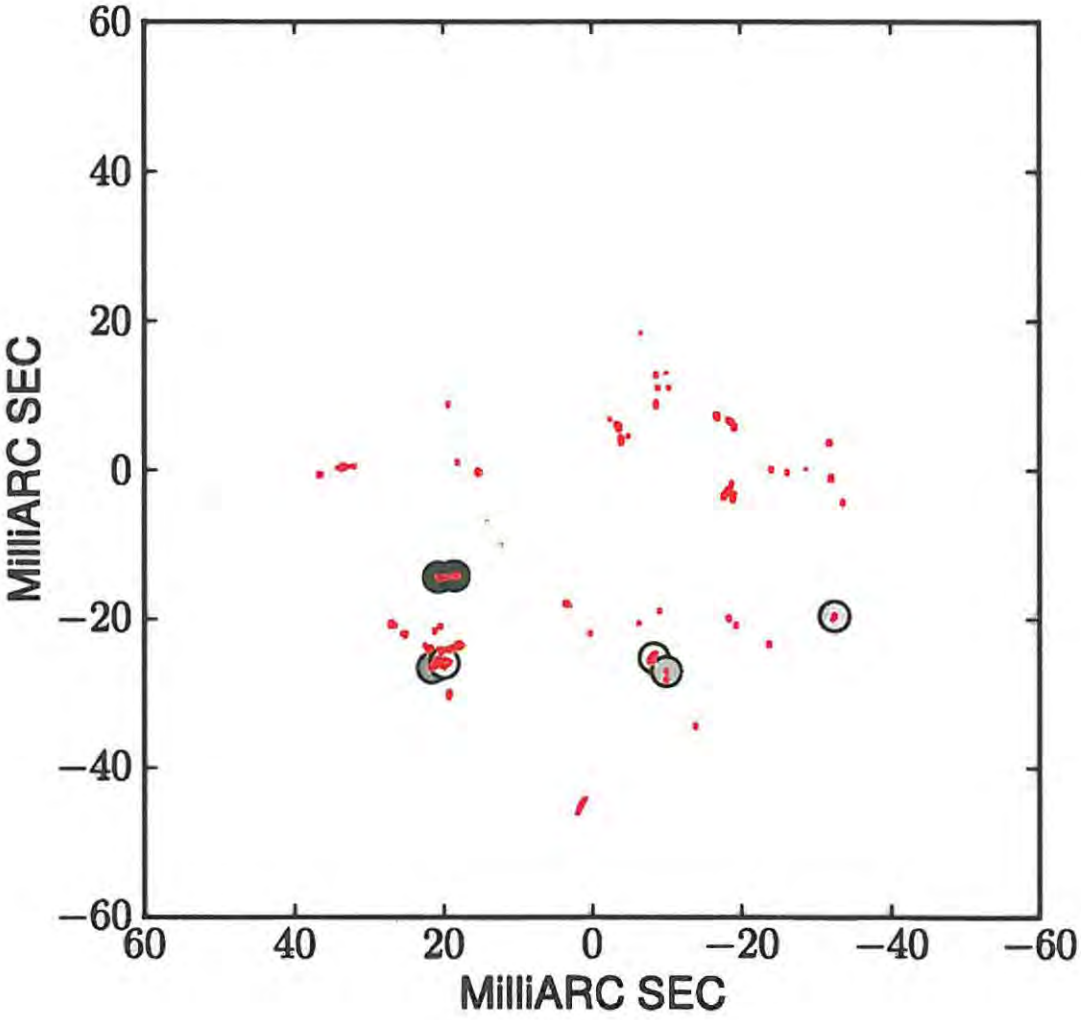

Figure 7.15: Epoch 2 v=1 J=2-1 linearly polarised features, from Table 6.5. Each linearly polarised feature is represented by a circle around the centre of the feature, with the gray scale level of the circle representing the level of the linear polarisation. The overall minimum linear polarisation in all three transitions is 1.6%, and the overall maximum is 46.5%, and the same grey polarisation scale is used in Figures 7.14, 7.13 and 7.15.

Feature	Spot	Ordinal relation in m_l	$\bar{m}_l$ J=1-0	$\bar{m}_l$ J=2-1	Note
F1		J=2-1 > J=1-0	6.3%	32.0%	
F2		J=1-0 > J=2-1	16.4%		*
F3			5.1%		
F4	S1	J=1-0 ~ J=2-1	5.8%	6.8%	
F4	S3	J=2-1 > J=1-0		8.4%	*
F4	S4			4.9%	
F5		J=1-0 > J=2-1	8.7%		*
F6			5.5%		

Table 7.2: Linear polarisation comparison between the v=1 J=1-0 line and v=1 J=2-1 line.
* Linear polarisation only detected for the more linearly polarised line. Equal or greater fractional linear polarisation for the missing line would have been detected at the sensitivity of the observations for these components.

percentage linear polarisation of 32% over the feature. The corresponding average in the v=1 J=1-0 line is 6%.

In feature F4, only spot S1 shows significant linear polarisation in the v=1 J=1-0 line. In this spot, the linear polarisation level is similar for both transitions. Significant linear polarisation is only measured at two frequency channels across the J=1-0 feature, and three across the J=2-1 line. In both cases the peak linear polarisation is 8%, measured at the brightest S1 pixel in the peak Stokes I channel.

In features F2, F3, F6 and the other F4 spots, linear polarisation is detected in the v=1 J=1-0 line, but not in the v=1 J=2-1 line. The SNR of the v=1 J=2-1 maps is lower than the v=1 J=1-0 maps, so it is possible that the lack of linear polarisation detections in J=2-1 is due either to higher noise levels in these maps or to relatively weaker J=2-1 emission. This was investigated by assuming that the v=1 J=2-1 masers are linearly polarised at the level of the v=1 J=1-0 masers, and checking if the J=2-1 linear polarisation would be detectable by the test of significance described in Section 6.5. In the case of F2 and F5, linear polarisation would be detectable in the J=2-1 line. We can therefore conclude that for these two features, the v=1 J=2-1 maser emission is objectively less linearly polarised than the v=1 J=1-0 emission.

In feature F3 however, linear polarisation at the level of the v=1 J=1-0 line would not be detectable in the J=2-1 line and we can make no statements about the relative strength of the linear polarisation in these two lines for this component.

For the other two overlapping F4 spots, S3 and S4, linear polarisation is detected only in the v=1 J=2-1 line, which is much stronger than the v=1 J=1-0 line in total intensity for this feature. Spots S3 and S4 were tested as above to check whether linear polarisation at the level measured in the v=1 J=2-1 line would be detected in the v=1 J=1-0 line. For S3, linear polarisation at the v=1 J=2-1 level would be detected in the v=1 J=1-0 line, and we conclude that the J=2-1 linear polarisation is greater than the J=1-0 polarisation. For S4, linear polarisation at the level of the v=1 J=2-1 line would not be detectable in the J=1-0 line, so we can make conclusions about the relative linear polarisation levels for this spot.

A summary of the statistically-significant coincident linear polarisation results is given in Table 7.2.

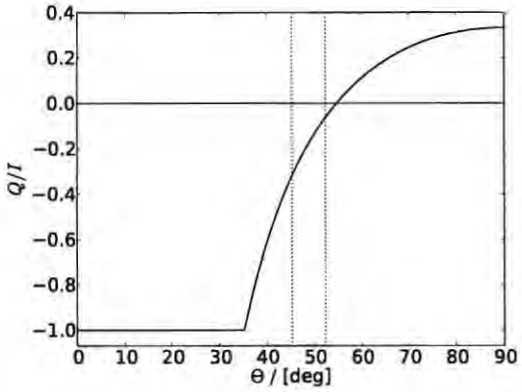

Figure 7.16: Plot of the GKK fractional linear polarisation solution, Equation 3.16. Vertical dotted lines are plotted through $Q/I = -0.32$ and -0.063.

For F1 and F4 S1, the average linear polarisation $\bar{m}_l$ values listed in the table are the averages over the channel range where linear polarisation is detected in both lines. All other averages are computed over all detected linear polarisation values in the line, without any requirement for multi-transition detection.

As discussed in Chapter 3, Section 3.4.9, the Elitzur model predicts broadly similar fractional linear polarisation in J=1-0 and J=2-1, while the Watson model predicts lower fractional linear polarisation for J=2-1 than J=1-0, if the two lines have comparable saturation. Overall, Table 7.2 shows no clear preference for either of these cases. For the two components in which both transitions are detected, the J=2-1 transition has similar (F4 S1) or significantly higher (F1) fractional linear polarisation than J=1-0.

The component-level comparison described above allows a more precise test of the dependence of fractional linear polarisation on rotational transition than is possible in single-dish studies, such as those discussed in Section 3.4.10. However, even at VLBI resolution uncontrolled factors enter into the multi-transition comparison. These factors include Faraday rotation, the degree of anisotropic pumping, unknown levels of saturation, and possible differences in the angle Θ between the magnetic field and the line of sight between the two transitions. These are discussed briefly below and in later sections.

Significant Faraday rotation will lead to greater fractional linear polarisation for the J=2-1 SiO masers, relative to J=1-0. However, this would be accompanied by a large EVPA rotation between the two transitions. The relatively close agreement in EPVA between the v=1 J=1-0 and v=1 J=2-1 masers across feature F1 ($\Delta\chi \leq 20-30°$, see Section 7.6.4 below) argues against a substantial Faraday rotation contribution for this component.

In the case of anisotropic pumping, higher fractional linear polarisation is expected for the J=1-0 line than the J=2-1 line, if the transitions are at similar levels of saturation, as discussed in Section 3.4.9. Such a trend is not observed.

For optically thin Δv=1 vibrational transitions, the radiative decay rate is J-independant for the lower J-levels. In this case the radiative decay rate is $\Gamma \sim 5$ s^{-1} for the v=1 level and $\Gamma \sim 10$ s^{-1} for the v=2 level. For optically thick vibrational transitions the radiative decay rate decreases below these

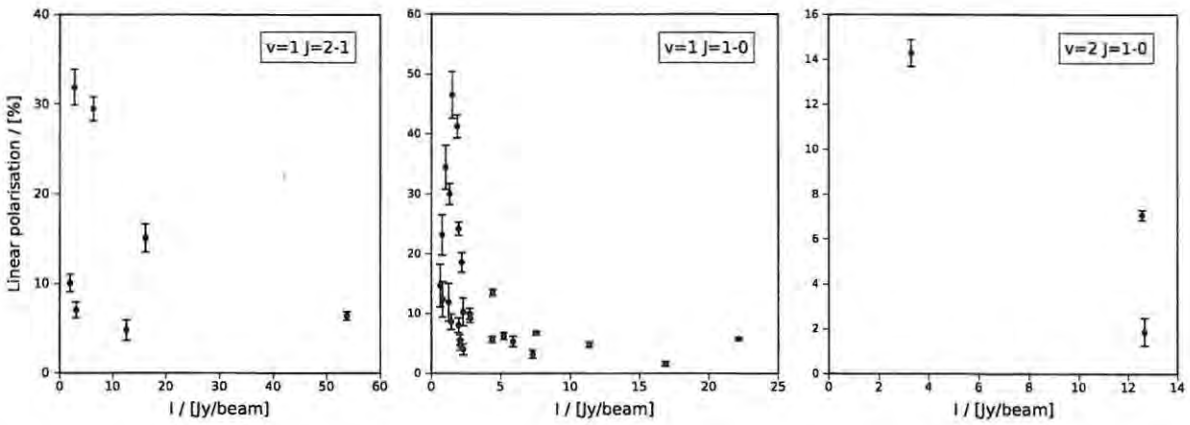

Figure 7.17: Plot of linear polarisation versus total intensity, for the v=1 J=2-1 (left), v=1 J=1-0 (centre), and v=2 J=1-0 (right) maser features from Epoch 2.

levels (Elitzur 1992, pg. 281-282). The stimulated emission rate R is marginally greater for the v=1 J=2-1 transition than the J=1-0 transitions, for the same intensity and beaming angle (Goldreich & Keeley 1972; Plambeck et al. 2003). Therefore, when all other factors are equal, the levels of saturation are expected to be similar for the v=1 J=2-1 and the v=1 J=1-0 transitions.

If we make the assumption that the two transitions are at similar levels of saturation, then the results in Table 7.2 are more consistent with models predicting similar fractional linear polarisation for both transitions. In this context, the larger J=2-1 fractional linear polarisation in feature F1 can be explained through a slight positional offset between the maser emission from the J=1-0 and J=2-1 transitions, which will lead to differing angle Θ between the magnetic field and the line of sight, consistent with $\Delta\chi$ given above. Within the GKK model this would lead to a different fractional linear polarisation between the two transitions. The GKK linear polarisation solution from Equation 3.16 is plotted in Figure 7.16. The offset in F1 m_l between the v=1 J=1-0 emission (6.3% on average) and the v=1 J=2-1 emission (32.0% on average) can readily be explained due to the gradient in the $Q/I \simeq -0.05$ to -0.3 region of the figure, where a Θ offset of $< 10°$ can account for the change in m_l. This feature is discussed in more detail in Section 7.6.4.

7.6.2 Linear polarisation versus saturation

The Watson and Elitzur models make different predictions about the relationship between the level of maser saturation and the fractional linear polarisation. The Elitzur model predicts that the limiting GKK linear polarisation values are achieved long before saturation, while in the Watson model the linear polarisation levels will increase slowly with saturation, only asymptotically approaching the GKK solution. As noted above however, the saturation level of an individual maser component cannot be determined from a measurement of component brightness without knowledge of the beaming angle, a parameter that cannot readily be determined.

With this caveat, the level of linear polarisation is plotted against the intensity of each of the maser features with significant linear polarisation in Figure 7.17. The plots show a trend of higher linear polarisation for the weaker maser emission, particularly for the v=1 J=1-0 emission, for which the largest number of maser features were detected. Trends of higher linear polarisation for the weaker

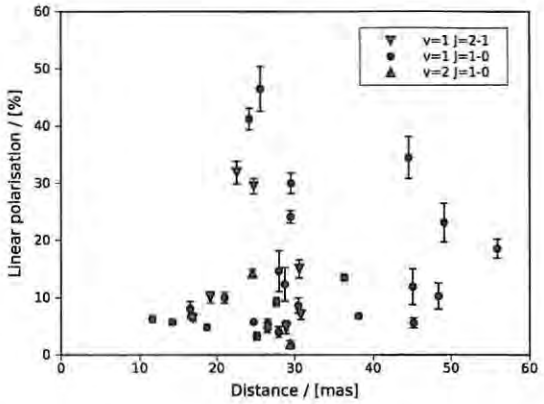

Figure 7.18: Linear polarisation versus projected radial distance from the assumed stellar position, for the Epoch 2 v=1 J=1-0, v=2 J=1-0 and v=1 J=2-1 maser features.

SiO masers have also been observed in other late-type evolved stars, as discussed in Section 3.4.10. We note that the lowest intensity maser features ($\leq$ 1.5 Jy/beam) in the v=1 J=1-0 and v=1 J=2-1 plots have relatively low linear polarisation percentages.

The saturation is governed by the ratio of the stimulated emission rate R to the decay rate Γ (Goldreich et al. 1973). The stimulated emission rate is dependent on the intensity as well as the beaming angle. The beaming angle decreases for increasing maser path length. For a path length l, the beaming angle varies as $\sim\ l^{-1}$ for most unstaturated masers, and l^{-2} for saturated masers (Elitzur 1992, pg. 117). The intensity is also related to the path length of the maser, increasing with increasing path length.

The net effect is that the stimulated emission rate may even have a I^{-1} relationship to intensity. In the latter case, some high intensity maser features may actually be less saturated than weaker masers, and if the linear polarisation increases with increasing saturation, it will decrease with increasing intensity.

Because of the complex relationship between the intensity and level of saturation, neither the Elitzur or Watson models can be ruled out by the results presented in Figure 7.17.

The trend of higher linear polarisation for the weaker masers can also be attributed to anisotropic pumping (e.g. Nedoluha & Watson 1990a), as discussed in Section 3.4.10. Under anisotropic pumping models, the linear polarisation percentage decreases as the maser saturates, with the drop-off occurring at higher levels of saturation for the v=1 J=2-1 maser than the v=1 J=1-0 maser. There is marginal (but inconclusive) evidence for this hypothesis in the data.

Faraday rotation has also been invoked to explain the trend of stronger linear polarisation for weaker masers, with McIntosh et al. (1989) arguing that stronger maser emission arises out of longer maser path lengths, which will also suffer the greatest levels of Faraday depolarisation.

7.6.3 Linear polarisation versus distance

If the maser emission is anisotropically pumped from radiation from the central star, then we can expect higher levels of linear polarisation closer to the star, where the excitation anisotropy is most extreme. Linear polarisation is plotted against projected distance from the assumed stellar position

in Figure 7.18, for the Epoch 2 v=1 J=1-0, v=2 J=1-0 and v=1 J=2-1 maser features. The figure shows no trend of stronger linear polarisation closer to the star. Anisotropic pumping is therefore not supported by this test.

However, we note that in the extended region of emission R1, the level of linear polarisation is larger closer to the star, as can be seen in Figures 7.9 and 7.13. We note that VY CMa, as a supergiant, has a complex circumstellar environment with likely asymmetric mass loss.

7.6.4 Linear polarisation position angle

As discussed in Section 3.4.10, 90° flips in the polarisation position angle over a maser feature can arise as the angle Θ between the magnetic field and the line of sight moves through the critical angle of 55° (Elitzur 2002). If circumstellar SiO maser emission falls in the $\Delta\omega \gg g\Omega \gg R$ Case 2a regime investigated by Goldreich et al. (1973), then the relationship between Θ and the linear polarisation is given in Equation 3.16, plotted in Figure 7.16. When $\Theta > 55°$ the observed linear polarisation vectors are perpendicular to the projected magnetic field direction. When $\Theta < 55°$ the observed linear polarisation vectors are parallel to the projected magnetic field direction (Goldreich et al. 1973).

The following sub-sections describe candidate features showing $\sim 90°$ EVPA rotations.

Feature F2

Epoch 2 feature F2 is the first candidate considered for a 90° flip due to magnetic field rotation through the critical angle. The rotation is apparent in Figure 7.3, and is accompanied by the expected decrease in linear polarisation at the point that the 90° transition takes place.

Using a similar method to Kemball et al. (2011), a fit was performed for the fractional linear polarisation across the feature, modeling the angle Θ as a second order polynomial in projected angular distance along the feature,

$$\Theta = p\,(d - d_{55})^2 + q\,(d - d_{55}) + 55 \tag{7.1}$$

where Θ is expressed in degrees, and d_{55} is the projected angular position of the minimum in the polarised emission, between the 90° EVPA rotation. The projected angular distances were measured radially from the assumed stellar position. The measured fractional linear polarisation values were fitted to Equations 3.16 and 7.1, using a χ^2-fit for parameters p and q.

The quality of the fit is marginal, as shown Figure 7.19. The functional form of Θ with projected angular distance d is unknown, so higher order polynomial fits could be performed to provide a better fit to the data. However, the number of data points across this feature is very small, so higher order polynomial fits were not attempted in this case. Although the fit is poor, it is not inconsistent with the GKK linear polarisation solution. A similar fit reported by Kemball et al. (2011) to a TX Cam SiO maser feature gives good agreement with the GKK model.

The GKK linear polarisations are reproduced in the Elitzur model (Elitzur 1991), where they are shown to be attained well before maser saturation (Elitzur 1996). In the Watson model the linear polarisation solutions approach the GKK solution at high levels of saturation (Western & Watson 1984; Watson & Wyld 2001). In the $g\Omega \gg R$ regime, for high saturation, the form of the linear polarisation as a function of Θ is similar to the GKK solution, without the sharp cutoff at the 35°

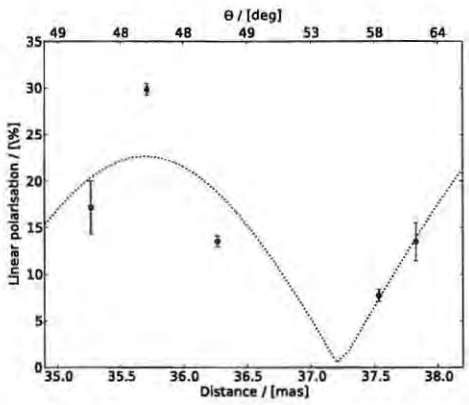

Figure 7.19: Fractional linear polarisation fit for feature F2 against the GKK model. The plot shows percentage linear polarisation versus projected angular distance from the assumed stellar position (bottom) and fitted angle Θ between the magnetic field and the line of sight (top).

break angle (Watson & Wyld 2001; Goldreich et al. 1973, pg. 183-184). The linear polarisation flip of feature F2 may therefore also be produced by a transition through the critical angle under the Watson polarisation model, in the $g\Omega \gg R$ regime, or by the Elitzur model over far less restrictive saturation constraints.

Rotation of the polarisation position angle is also characteristic of the $g\Omega \simeq R$ regime, in the Watson model (Nedoluha & Watson 1994). In this regime the linear polarisation position angle rotates with saturation level. However, the rotation is at most $\sim 45°$ over an order of magnitude in saturation level, except for very large magnetic field levels (100G) directed almost perpendicular to the line of sight (75°). It is unlikely that the abrupt $\sim 90°$ change in polarisation position angle observed in this feature is caused by this mechanism.

The characteristics of this feature are also not consistent with linear polarisation caused by anisotropic pumping. Polarisation position angle rotations of $\lesssim 45°$ can be caused by anisotropic pumping in the presence of a magnetic field (Asensio Ramos et al. 2005), but the rotation observed in this feature is too large to be explained in this way. Alternatively, in the absence of magnetic fields, a 90° flip in polarisation position angle of anisotropically pumped maser emission could be caused by a change in anisotropy direction, between radial and tangential (Asensio Ramos et al. 2005). This could occur, for example, as the maser pump changes from stellar radiative pumping close to the star, to tangential collisional pumping from the circumstellar material further from the star (Western & Watson 1983b; Asensio Ramos et al. 2005). In the absence of a magnetic field, radial anisotropic pumping will lead to tangential linear polarisation, and the opposite for tangential anisotropic pumping (Western & Watson 1983b). This is the opposite of what is observed in feature F2, where the EVPA is radially directed closest to the star. Feature F2 is also not close to the star, where radiative anisotropic pumping from the star would be expected to be most extreme, so a change from radial to tangential anisotropy direction over the length of this feature is unlikely.

Feature F1

A second candidate feature for a 90° EVPA rotation in the Epoch 2 data set the elongated feature F1, shown in Figure 7.2. The change in linear polarisation is most apparent in the v=1 J=2-1 emission, shown in the lower left panel of Figure 7.2 and enlarged in Figure 7.20. However, closer inspection of the plot shows that the rotation of the position angle is not as abrupt as for feature F2, and the linear polarisation plot on the right of Figure 7.2 does not show clearly the characteristic minimum in fractional linear polarisation at the position of EVPA rotation (near 34 km/s).

The linear electric vector polarisation position angles across the feature are shown in Figure 7.21. The two channel shift discussed in Section 7.2 has been applied to the v=2 J=1-0 data in the figure. The position angles have a 180° ambiguity, so they were all rotated by integral multiples of 180° to fall within $[0°, 180°]$. Error bars are omitted from the v=1 J=2-1 data points to indicate that these polarisation position angles could not be calibrated relative to a known EVPA calibrator, so the absolute values of these angles are not known. In this case an arbitrary EVPA rotation can be applied to the v=1 J=2-1 masers if it can be physically justified through, for example, alignment with the EVPAs of SiO maser emission from other transitions. For the Epoch 2 data, no attempt was made to align the v=1 J=2-1 with those of the other two transitions. The EVPA alignment given by direct calculation of χ from the v=1 J=2-1 Stokes parameters was deemed sufficiently close to the absolute EVPAs of the v=1 J=1-0 and v=2 J=1-0 EVPAs that further EVPA rotation was not justified. This can be seen by comparing the v=2 J=1-0 and v=1 J=2-1 EVPAs of F1 (Figure 7.2 and Figure 7.20) and comparing the v=1 J=1-0 and v=1 J=2-1 EVPAs of F4 (Figure 7.5). In the overlapping region of F1 the EVPAs of all three transitions agree relatively closely, within $\leq 20 - 30°$ (Figure 7.21). All of which suggests that the Epoch 2 v=1 J=2-1 EVPAs are close to their absolute values, within $\sim 20 - 30°$.

The v=1 J=1-0 and v=2 J=1-0 error bars in Figure 7.21 were determined through propagation of the error in the EVPA rotation angle (listed in Table 5.8 and described in Section 5.3.7) and the Stokes parameter RMS errors of each maser component measured with IMSTAT. These are formal statistical errors, which do not factor in systematic errors due to the different angular scales sampled by the VLBA and VLA during the absolute EVPA rotation calibration, or the time delay between the VLA and VLBA observations. The systematic errors are estimated to be $\leq 5\%$.

The v=1 J=1-0 emission from F1 displays what appear to be multiple $\sim 90°$ EVPA rotations across the length of the feature. This is visible in the EVPA-contour plot in Figure 7.20, and in Figure 7.21. It is possible that these flips are caused by multiple transitions across the 55° critical angle. The v=1 J=1-0 fractional linear polarisation of this feature is $\lesssim 20\%$. According to the GKK Equation 3.16 (plotted in Figure 7.16), linear polarisation of less than 20% arises over a range of angles Θ between the line of sight and magnetic field in the range: $\Theta = 48°$ to 66°. The position of the feature in the circumstellar envelope is unknown, but for tangential amplification in an accelerating shell we would expect maser emission arising further from the stellar velocity to arise in regions of gas moving closer to the line of sight. The line of sight velocity of this feature is redshifted by $\sim 11 - 21$km/s relative to the stellar velocity, so it is possible that this feature is elongated along an axis oriented near 55° to the line of sight, possibly along a local magnetic field direction.

Radially elongated features are often observed in circumstellar maser images, with polarisation position angles parallel to, or perpendicular to, the radial direction. This implies that the features

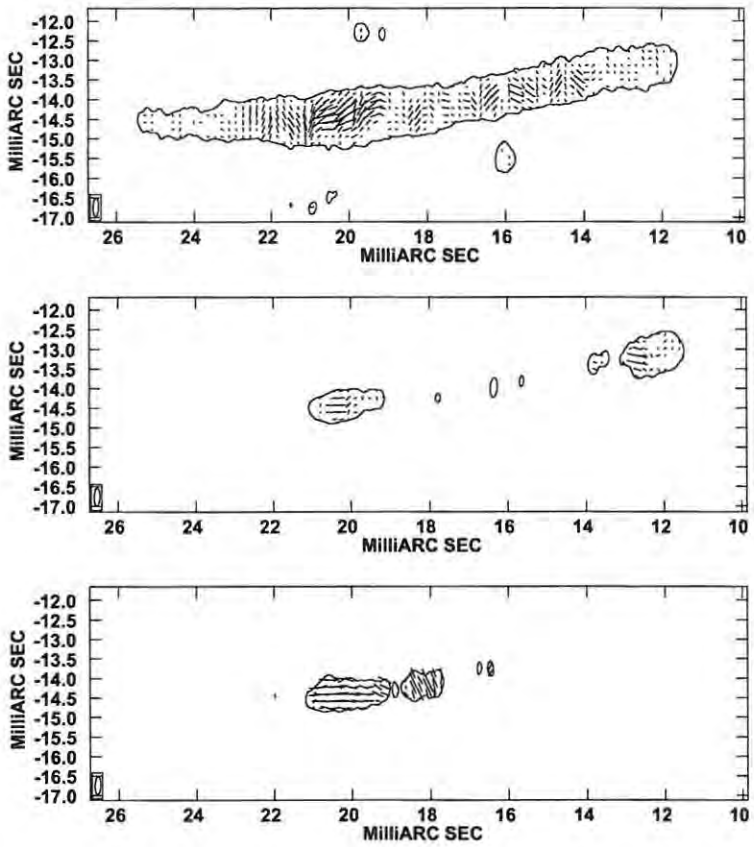

Figure 7.20: Contour plots of the v=1 J=1-0 (top), v=2 J=1-0 (middle) and v=1 J=2-1 (bottom) emission overlaid with linear polarisation EVPA vectors, where a vector length of 1 mas = 27.78×10^{-3} Jy/beam in linearly-polarised intensity. The vector orientation is in the direction of absolute EVPA for the J=1-0 lines. The synthesised beam is shown in the bottom left of the polarisation images, and is 0.46×0.15 mas in half-power with a position angle of $-1.80°$. These plots are reproduced from Figure 7.2 for comparison with Figure 7.21 above.

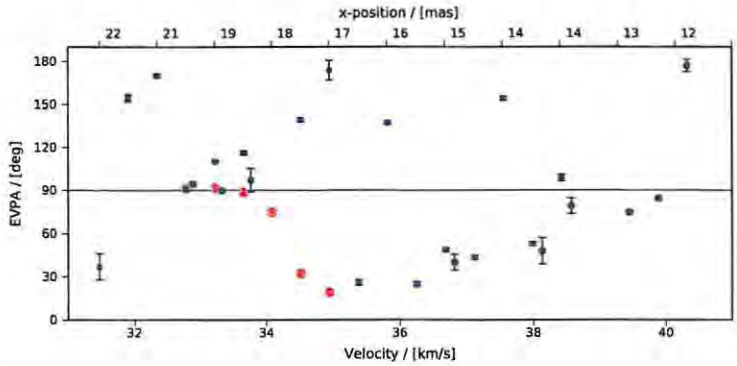

Figure 7.21: Linear polarisation EVPAs for feature F1, for the v=1 J=1-0 (blue), v=2 J=1-0 (green) and v=1 J=2-1 (red) SiO maser emission. The lower x-axis shows the velocity channels, and the upper x-axis shows the x-position where the v=1 J=1-0 Stokes parameters were measured, at each velocity channel across the feature. The formal statistical errors are shown for the v=1 J=1-0 and v=2 J=1-0 emission, and the error bars are smaller than the data points in some cases. Additional systematic errors are estimated to be $\leq 5\%$, as discussed in the text.

are aligned with magnetic field lines (Cotton et al. 2006). Depending on the strength of the magnetic field, elongated regions of emission could be caused by ionised gas dragging the magnetic field along the direction of outflow, or a stronger magnetic field may constrain the ionised gas to move along the field lines (Vlemmings et al. 2005; Cotton et al. 2006).

We note that the measured EVPA values across the feature in the images are integrated along the three-dimensional coherent path length of the maser emission, and the maser excitation conditions and SiO density likely vary locally across this region. In addition, the measured EVPAs are also spatially filtered by the different surface brightness sensitivity of the 43 GHz and 86 GHz bands. The combined effect of these conditions will introduce some level of variance in the emission from different transitions across the feature, even for physically coincident maser components. The similarity of the total intensity spectral shape in the v=1, J=1-0 and v=1, J=2-1 transitions across F1 shown in Figure 7.2 is strongly suggestive that these transitions arise from the same physical conditions, but within the envelope of variance noted above. Possible differences could include, for example, modest changes in the angle Θ between the magnetic field and line of sight for each transition. Figure 7.21 shows relative agreement in EVPA χ between the transitions. This is especially true for v=1 J=1-0 and v=2 J=1-0, which also match relatively closely in m_l across the feature (Figure 7.2), unlike the v=1 J=1-0 and v=1 J=2-1 transitions. As discussed in Section 7.6.1, the v=1 J=1-0 and v=1 J=2-1 difference could be explained in terms of the proposed modest differences in Θ between these two transitions.

The multiple $\sim 90°$ rotations visible in the v=1 J=1-0 emission can be interpreted, as noted earlier, as a change of magnetic field direction about the critical value of 55°. Alternatively, the v=1 J=1-0 polarisation position angle flips could be caused by a helical magnetic field threading the elongated maser feature. In this geometry the polarisation position angle would rotate around 180° through the coils of the helix, and there is no need to invoke a transition through the 55° critical angle to explain 90° flips.

The difference between the v=1 J=1-0 and v=1 J=2-1 linear polarisation could also be attributed to the maser emission falling in the $g\Omega \simeq R$ regime, or to the effects of Faraday rotation. In the $g\Omega \simeq R$ regime the linear polarisation position angle is dependent on the intensity of the maser emission, as discussed above for feature F2. However, it is not clear how this could explain the multiple 90° EVPA rotations across the v=1 J=1-0 emission. The $g\Omega \simeq R$ regime rotation is also expected to decrease as the maser saturates (Nedoluha & Watson 1994), so if the v=1 J=1-0 maser emission falls in this regime then we would expect less variation in the polarisation position angle across the most intense regions. This is not evident in the current data. The hypothesis of the maser emission falling in the $g\Omega \simeq R$ regime does not provide a good explanation for the EVPA characteristics of this feature.

Faraday depolarisation becomes significant when the dimension of the region of plasma traversed by the radiation becomes close to the length scale $2 \times 10^{16} (\lambda^2\ n\ B_{||})^{-1}$, where λ is the wavelength of the radiation, n is the electron density of the plasma and $B_{||}$ is line of sight magnetic field (Elitzur 1992, pg. 188-190). The electron density in the SiO maser region of VY CMa is unknown. The electron density of the semiregular variable W Hydrae has been estimated to be ~ 2 cm^{-3}, from main line OH maser EVPA rotation (Szymczak et al. 1998), but Wallin & Watson (1997) suggest that electron densities of up to 1000 cm^{-3} may be possible theoretically in the SiO maser region. The excess 8.4 GHz emission measured around VY CMa may be evidence of a partially ionized chromosphere around the

star (Knapp et al. 1995), and VLA continuum observations of VY CMa at 15, 22 and 43 GHz have been modelled as a radio photosphere extending out to 1.5-2 $R_\star$ (Lipscy et al. 2005).

For a line of sight magnetic field of 0.5 G, a similar level to that observed in the H_2O maser region around AGB stars (Vlemmings 2007) and an electron density of 100 cm^{-3}, the Faraday depolarisation length scale is 3.6 $R_\star$ at 43 GHz and 8.3 $R_\star$ at 86 GHz. For these parameters, Faraday depolarisation would not be a significant effect for this feature, even for the 43 GHz J=1-0 masers. However, for an electron density of 1000 cm^{-3} and the same magnetic field level, the depolarisation length scale drops to 0.4 $R_\star$ at 43 GHz and 0.8 $R_\star$ at 86 GHz. The same length scales arise from the original electron density of 100 cm^{-3}, but with a magnetic field of 5 G.

So if the electron density or the magnetic field is very large, Faraday depolarisation will be a factor. However, on balance, current data for feature F1 do not support a dominant contribution from Faraday rotation. Faraday rotation does not explain the multiple v=1 J=1-0 EVPA flips across the feature, and and is inconsistent with the general agreement in χ shown in Figure 7.21.

If Faraday rotation is a significant factor, we would also expect to see lower levels of linear polarisation in the J=1-0 lines compared to the J=2-1 line throughout Figures 7.2 to 7.7, which is not the case, as discussed in Section 7.6.1. The average linear polarisation across all linearly-polarised features is 13.7% and 7.7% for the 43 GHz v=1 J=1-0 and v=2 J=1-0 emission, and 15.0% for the 86 GHz v=1 J=2-1 emission.

7.6.5 Circular polarisation in v=1 J=1-0 and v=1 J=2-1

The Epoch 2 features in Tables 6.3, 6.4 and 6.5 with statistically significant circular polarisation are displayed in Figures 7.22, 7.23 and 7.24. The different SiO maser models make important predictions about the relative circular polarisation in these two rotational transitions, as discussed in Section 3.4.9. As in the tests above, the circular polarisation must be compared at component-level in maser features with coincident emission in the two transitions.

Only two of the overlapping Epoch 2 features show significant circular polarisation in both the v=1 J=1-0 and v=1 J=2-1 transitions. These are features F1 (Figure 7.2) and F4 (Figure 7.5).

In feature F1, only one channel displays statistically significant circular polarisation in both transitions: $-4.61 \pm 0.30\%$ for v=1 J=1-0, and $-4.31 \pm 2.06\%$ for v=1 J=2-1. The standard Zeeman circular polarisation model predicts approximately double the circular polarisation for the v=1 J=1-0 line as for the v=1 J=2-1 line. However, the large uncertainty of the v=1 J=2-1 circular polarisation measurement means that standard Zeeman splitting cannot be ruled out for this feature.

Under the Watson model, saturation effects can increase the standard Zeeman circular polarisation by factors of a few (Watson & Wyld 2001). The similar circular polarisation of the v=1 J=1-0 and v=1 J=2-1 line in the single overlapping circular polarisation point could be due to more highly saturated v=1 J=2-1 emission. This is possible, but unlikely, due to the lower intensity of the v=1 J=2-1 line, as discussed in previous sections.

The other feature displaying circular polarisation in both transitions is F4, which is a group of spots spanning almost 10 km/s. Spot S1 is the only region of the feature displaying significant circular polarisation in both the v=1 J=1-0 and v=1 J=2-1 lines. The measured S1 fractional circular polarisation is completely different for the two lines, with a maximum of $9.22 \pm 1.31\%$ in the v=1 J=1-0 line, and $-0.84 \pm 0.32\%$ in the v=1 J=2-1 line. Closer inspection of the feature shows that the

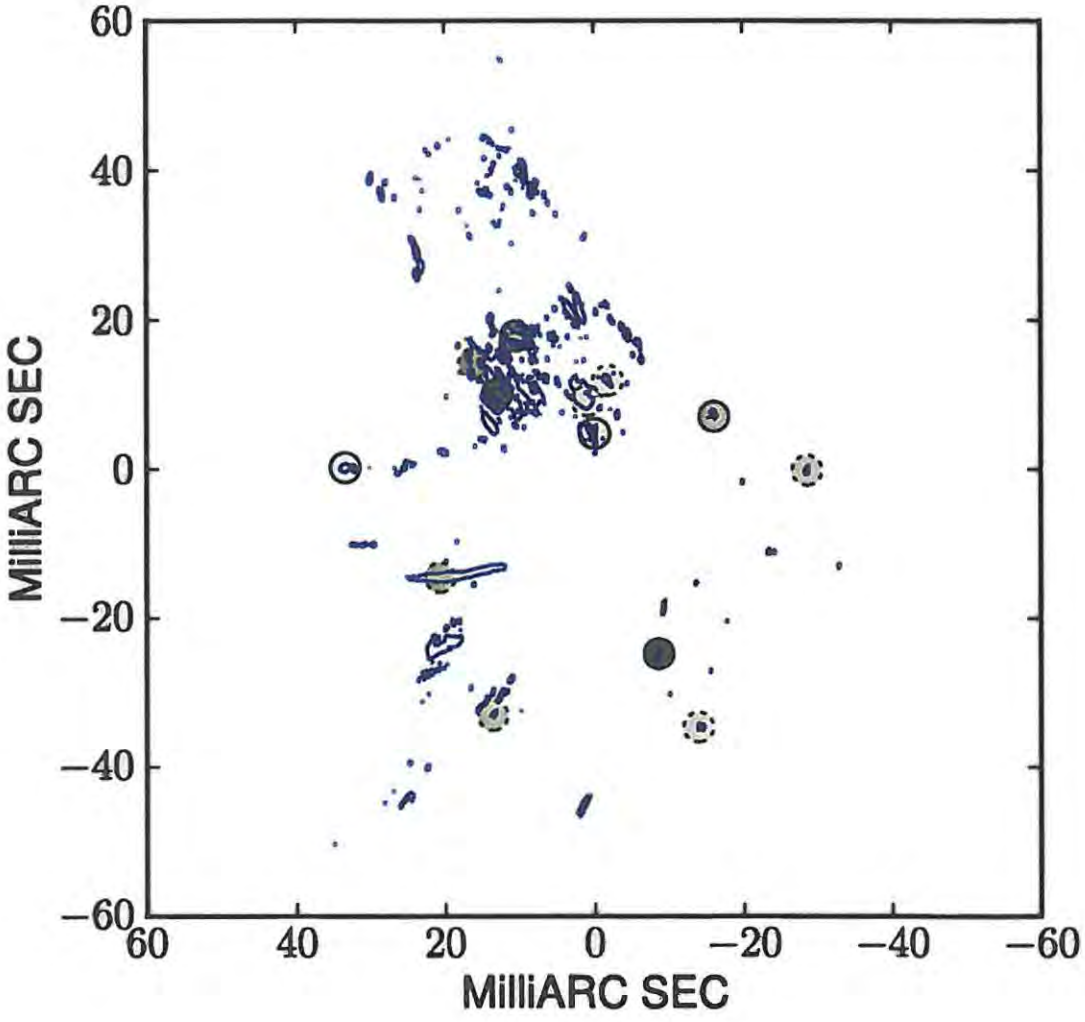

Figure 7.22: Epoch 2 v=1 J=1-0 circularly polarised features, from Table 6.3. Each circularly polarised feature is represented by a circle around the centre of the feature. The gray scale level of the circle represents the absolute circular polarisation level, and the black border of the circle shows whether it is positive (solid) or negative (dashed). The overall minimum absolute circular polarisation in all three transitions is 1.2%, and the overall maximum is 7.1%, and the same grey polarisation scale is used in each Figures 7.23, 7.22 and 7.24.

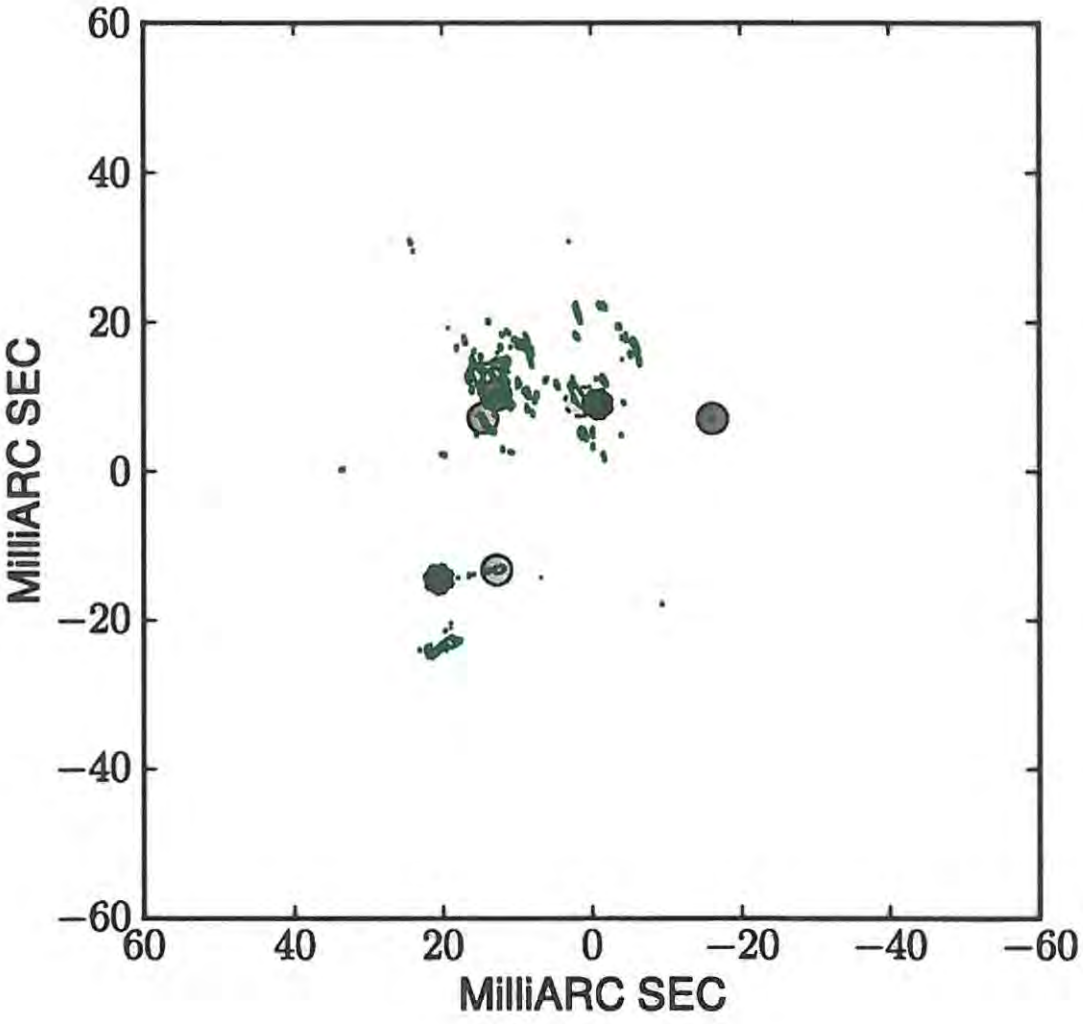

Figure 7.23: Epoch 2 v=2 J=1-0 circularly polarised features, from Table 6.4. Each circularly polarised feature is represented by a circle around the centre of the feature. The gray scale level of the circle represents the absolute circular polarisation level, and the black border of the circle shows whether it is positive (solid) or negative (dashed). The overall minimum absolute circular polarisation in all three transitions is 1.2%, and the overall maximum is 7.1%, and the same grey polarisation scale is used in each Figures 7.23, 7.22 and 7.24.

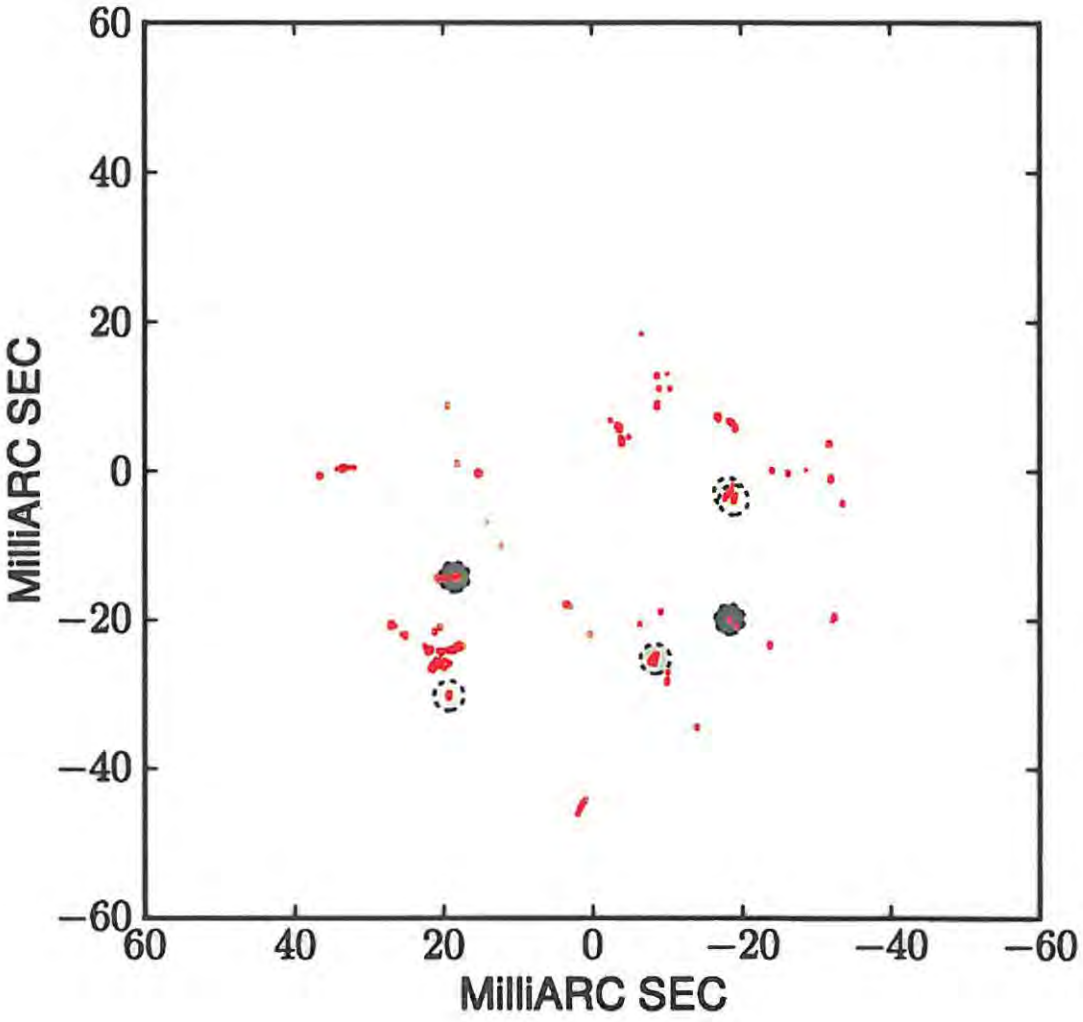

Figure 7.24: Epoch 2 v=1 J=2-1 circularly polarised features, from Table 6.5. Each circularly polarised feature is represented by a circle around the centre of the feature. The gray scale level of the circle represents the absolute circular polarisation level, and the black border of the circle shows whether it is positive (solid) or negative (dashed). The overall minimum absolute circular polarisation in all three transitions is 1.2%, and the overall maximum is 7.1%, and the same grey polarisation scale is used in each Figures 7.23, 7.22 and 7.24.

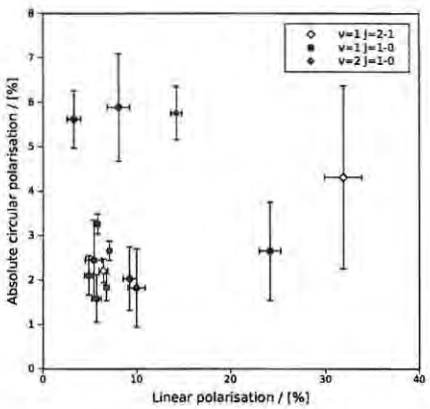

Figure 7.25: Plot of fractional circular polarisation magnitude versus fractional linear polarisation magnitude, for the v=1 J=1-0, v=2 J=1-0 and v=1 J=2-1 maser features from Epoch 2.

circular polarisation of spot S1 is offset between the two lines. The circular polarisation measurements are therefore unlikely to be probing the same region of gas, and we do not include this component in the current test.

The average fractional circular polarisation magnitude across all of the circularly polarised features shown in Figures 7.22, 7.23 and 7.24 is 3.0% for the v=1 J=1-0 line, 4.2% for the v=2 J=1-0 line, and 2.6% for the v=1 J=2-1 line. We note however that this is not a comparison between individual coincident components.

7.6.6 Linear polarisation versus circular polarisation

The circular polarisation percentages are plotted versus linear polarisation percentages in Figure 7.25, for maser features with statistically significant linear and circular polarisation. There is no correlation between the circular and linear polarisation values. A correlation would have supported the Watson model, either for non-Zeeman circular polarisation (generation by Faraday rotation or in the $g\Omega \simeq R$ regime), or for saturation-dependent Zeeman circular polarisation in the $g\Omega \gg R$ regime (Watson 2009).

In total, there are 37 maser features that display statistically significant linear polarisation in the v=1 J=1-0, v=2 J=1-0 and v=1 J=2-1 feature lists in Tables 6.4, 6.3 and 6.5. Of those 37 features, 14 display statistically significant circular polarisation. Another 12 features display circular polarisation without significant linear polarisation. All of the 14 circularly-polarised features are circularly polarised at a level $> m_l^2/4$.

This is strongly suggestive that the circular polarisation does not fall in the Watson non-Zeeman category (Wiebe & Watson 1998), either due to Faraday rotation changing the relative alignment of the linear polarisation and the projected magnetic field or due to a changing magnetic field direction along the maser path, in the $g\Omega \gg R$ regime, or due to intensity dependent linear polarisation angle rotation in the $g\Omega \simeq R$ regime.

Cotton et al. (2011) report a similar result from polarised VLBA observations of the AGB star IK Taurii in v=1 J=1-0 and v=2 J=1-0 SiO maser emission.

7.7 Magnetic field

The component-level tests presented in the previous section provide important constraints on theories of polarised maser transport that are important for inferring magnetic fields from measured maser circular polarisation data. In general the tests do not support non-Zeeman mechanisms for circular polarisation.

The most definitive test that a standard Zeeman interpretation applies is the comparison between m_c in the J=1-0 and J=2-1 transitions. Unfortunately, the current data set contains only one component measurement that can be used for this test, which is not sufficient for a conclusive result.

If we assume that the fractional circular polarisation is generated by the standard Zeeman mechanism, then magnetic field estimates can be derived from the circular polarisation levels. In Epoch 2, the average magnitude of the fractional circular polarisation is 3.0% for the v=1 J=1-0 line, 4.2% for the v=2 J=1-0 line, and 2.6% for the v=1 J=2-1 line. The maximum fractional circular polarisation values are 5.88±1.21% in the v=1 J=1-0 line, 7.13±2.36% in the v=2 J=1-0 line and 4.71±2.29% in the v=1 J=2-1 line.

From Elitzur (1996), the magnetic field can be calculated from standard Zeeman circular polarisation, as $B = 2m_c\Delta v_5$ G for J=1-0 SiO maser transitions, where Δv_5 is the Doppler width of the line in units of km/s, m_c is taken as a percentage, and adopting $\Theta = 45°$. The magnetic field relation will be approximately double for the higher frequency J=2-1 transition, $B = 2 \times 2m_c\Delta v_5$ G (Elitzur 1996).

The Elitzur (1996) SiO maser polarisation model therefore predicts magnetic field levels of up to $\sim$ 10 G in the SiO maser features, assuming a Doppler velocity line-width of 0.6 km/s. Similar magnetic field estimates have been reported by Kemball & Diamond (1997) for the circumstellar TX Cam SiO masers, and by Barvainis et al. (1987) for SiO maser emission towards a number of late-type evolved stars. The VY CMa magnetic field estimate reported by Barvainis et al. (1987) is larger than the magnetic field reported here, due to a different scale factor in the Zeeman relation than the Elitzur (1996) expression used here.

Under the Watson model for Zeeman circular polarisation, the magnetic field estimates differ from the Elitzur (1996) estimates discussed above by only a factor of $\sim 2 - 3$ due to saturation effects (Watson & Wyld 2001; Watson 2009).

Magnetic field values of a few Gauss are consistent with a power law relationship between magnetic field and distance from the star, as discussed in Section 2.4. Published magnetic field estimates from satellite-line OH maser emission (Cohen et al. 1987), main line OH maser emission (Benson & Mutel 1982), H_2O maser emission (Vlemmings et al. 2002) are plotted on Figure 7.26, along with a magnetic field value of 5 G in the SiO maser region. A solar-type $B \propto r^{-2}$ law is plotted on the figure for comparison.

If the magnetic field is as large as a few Gauss at the position of the SiO maser emission, the question arises as to whether these field estimates are evidence of a strong global magnetic field in the circumstellar envelope, or localised fields, which are strong only in certain regions of the envelope. Inspection of Figures 7.22, 7.23 and 7.24 shows that maser features displaying circular polarisation are dispersed throughout the circumstellar envelope. There is no apparent trend of circular polarisation by feature morphology (the more extended emssion in the northeast, the elongated feature, the isolated features in the west). If the circular polarisation is evidence of stronger localised magnetic fields, then

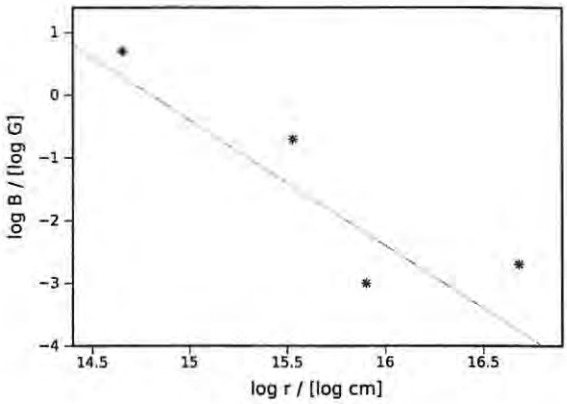

Figure 7.26: Magnetic field versus radial distance from the star. The data points represent B-field estimates from SiO maser emission, H_2O maser emission, OH main line maser emission and OH satellite maser emission, with increasing distance from the star. The line is a solar-type $B \propto r^{-2}$ law.

the stronger fields appear to be randomly distributed throughout the maser region. It is possible that stronger magnetic fields leads to more coherent flow of the circumstellar material, in which case the maser emission may occur preferentially in regions of enhanced magnetic field.

Considering the elongated feature F1, the v=1 J=1-0 emission displays circular polarisation at a level of ~ -2 to -4% across a region of ~ 4 mas in angular extent containing the highest total intensity emission. Following Elitzur (1996), this equates to a magnetic field of ~ 2 to 5 G. With a magnetic field of this level, the magnetic energy density exceeds the thermal and kinetic energy densities in the masing gas, and we would expect the magnetic field to shape this feature, as suggested by Vlemmings et al. (2005) and Cotton et al. (2006). If the magnetic field values along this feature are as high as the Zeeman interpretation suggest, then this feature may be caused by highly magnetised outflow above a magnetic cool spot or convective cell.

7.8 Circumstellar envelope morphology

As discussed in Section 7.4, the SiO maser maps presented in this thesis are consistent in morphology with previous SiO maser maps of VY CMa. Overall, the v=1 and v=2 J=1-0 maps of VY CMa display maser emission concentrated predominantly to the east of the star, while the v=1 J=2-1 maps show sparser maser emission which is more uniformly spread around the star, with a distinct lack of emission in the northeast of the star where more extended J=1-0 emission is observed. Gaps in SiO maser rings can arise out of random maser spot configurations (Gray et al. 2009), so the morphology of single epoch SiO maser maps must be interpreted cautiously. However, these trends are observed in several maser maps and appear to be persistent characteristics.

In Section 2.4, observational evidence for an axisymmetric circumstellar envelope around VY CMa was discussed. The possible disk geometry discussed in that section, and plotted in Figure 2.7, is overlaid on the Epoch 2 SiO maser emission in Figure 7.27. The disk shown in the figure is tilted towards us in the east, with a projected polar axis directed northeast-southwest.

The maser emission in the west and southwest of the Epoch 2 maps is generally more compact and further from the stellar velocity, compared to the eastern and northeastern emission, which is

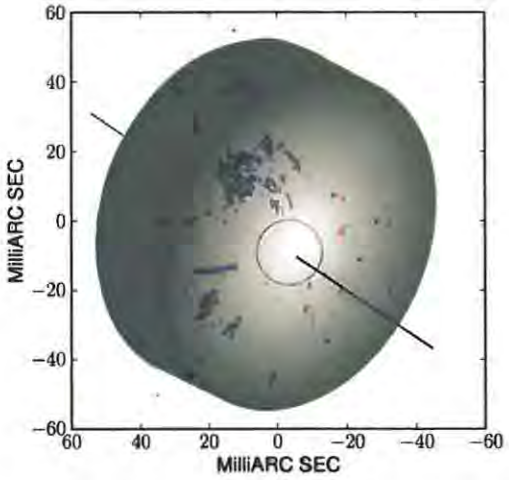

Figure 7.27: Maser emission overlaid with disk geometry. The disk geometry from Figure 2.7 overlaid on the Epoch 2 maser emission from Figure 7.1.

more extended and has more concentration near the stellar velocity. This is consistent with the disk geometry shown in the figure if the western and southwestern emission emanates from the polar region, where the flow of circumstellar material is faster and the gas is possibly less dense. This may limit the velocity coherence, leading to the more compact maser features observed in this region. The relatively large number of v=1 J=2-1 maser features in the polar region, relative to the J=1-0 masers, may be due to favourable envelope conditions for v=1 J=2-1 maser. This may imply lower densities in the polar region, as discussed in Section 7.5.2, which is consistent with higher velocity outflows in this region.

In this picture, the more extended regions of J=1-0 emission closer to the stellar velocity may fall in the equatorial plane, and may be probing a disk around the star. The extended emission in region R1 and the emission further from the star in the northeast, display a velocity gradient away from the stellar velocity with distance from the star, consistent with a location in the forward lobe of the disk in Figure 7.27. The extent of the emission in R1 in particular is indicative of favourable conditions for the J=1-0 masers in this region. This may imply greater velocity coherence in this region, or temperature and density conditions favourable to these masers.

Possible origins of a circumstellar disk were discussed in Section 2.4.2. It is possible that a pre-main sequence disk has survived over the stellar evolution of VY CMa, and that part of the western emission is located in the disk, where density conditions and dust levels differ from the polar regions. A disk could also be formed through excess dust formation and mass loss over magnetic cool spots in the equatorial plane. If this were the case we might expect to see larger circular polarisation levels in the equatorial plane, which is not observed. However, as discussed earlier, stronger magnetic fields may lead to more coherent outflows, so the persistant trend of larger scale J=1-0 maser emission to the east of the star may be evidence that these masers are located in the equatorial plane in the presence of larger magnetic fields.

However, the morphology of the SiO maser emission can be explained in a variety of ways outside of the bipolar model. Zhang et al. (2012) recently published a proper motion study of four epochs of v=1

J=1-0 SiO maser emission towards VY CMa. The SiO masers display slow, quasi-spherical outflow, with no strong evidence for a bipolar outflow. They model six observed spoke-like SiO maser features using a ballistic-orbit model, which provides a good fit for most of the features. However, they note that the ballistic model assumed that the maser features are radially aligned, which is at odds with the expansion model they fit to the proper motion of the features. They suggest that more realistic modeling of the complex near-circumstellar envelope may require acceleration driven by pulsation or giant convective cells (Schwarzschild 1975) and the use of a hydrostatic inner envelope (Zhang et al. 2012).

A number of recent observations of VY CMa have shown that the circumstellar envelope is highly inhomogeneous and mass-loss from the star may occur in localised events (Smith et al. 2001; Humphreys et al. 2005; Smith et al. 2009), as discussed in Section 2.5. The variable characteristics of the VY CMa SiO maser emission across the circumstellar envelope may be evidence of localised enhanced mass-loss from the star. In this context, the sparser region of more compact masers in the southwest may be a region of enhanced mass loss, where the circumstellar material is more turbulent.

Chapter 8

Conclusion

This thesis describes simultaneous VLBA imaging of 43 GHz and 86 GHz SiO maser emission towards the supergiant star VY CMa, with a particular focus on component-level observational tests of SiO maser polarisation models, which lie in the weak-splitting regime.

Two epochs of VLBA observations were performed. The first epoch was a broad search for sixteen J=1-0 and J=2-1 rotational transitions in vibrational bands v=0, 1 and 2 from the three isopotologues ^{28}SiO, ^{29}SiO and ^{30}SiO. The second epoch was a follow-up observation, with longer observing time allocated to the lines successfully detected in the first epoch.

The first epoch of observations was reduced using spectral-line polarimetric VLBI data reduction techniques described in Kemball et al. (1995) and extended to higher frequencies (43 GHz) by Kemball & Diamond (1997). These data reduction methods were found to be inadequate for the level of circular polarisation accuracy required by the science goals of this thesis, particularly for the 86 GHz observations of the v=1 J=2-1 SiO maser transition. In order to improve the accuracy of the circular polarisation calibration at millimetre wavelengths, several alternative data reduction techniques were developed, which are discussed in Section 8.1.

The resultant SiO maser images are discussed in terms of their implications for maser pumping models and weak-splitting maser polarisation models in Sections 8.2 and 8.3 respectively. The implications of the observed maser morphologies for models of the circumstellar envelope of VY CMa are discussed in Section 8.4. Suggestions for future work are included in each section.

8.1 Data reduction method

As described in Section 5.3 of Chapter 5, several new spectral-line polarimetric data reduction methods were developed for the reduction of the Epoch 2 data set. The new reduction methods include: i) solving for the differential polarisation bandpass phase offset at the reference antenna; ii) incorporating aliasing corrections into the bandpass solution method; iii) the use of a composite template spectrum in the template-fitting amplitude calibration method; iv) incorporating autocorrelation polarisation self-calibration in order to solve for the instrumental polarisation simultaneously with the amplitude gains; and, v) the use of continuum calibrator data to solve for a global amplitude offset between the RCP and LCP systems. Each of these methods was implemented as a new AIPS task or refinement of an existing AIPS task.

The circular polarisation calibration accuracy of the final data reduction method was assessed in Section 5.4, and found to be accurate to within 1%.

These new data reduction methods have only been tested on the VY CMa Epoch 2 data described in this thesis, and a single epoch v=1 J=1-0 SiO maser observation of TX Cam, described in Kemball & Richter (2011), thus far. The methods would benefit from further testing on a wider range of data sets, but show significant promise.

The autocorrelation polarisation self-calibration, in particular, needs broader assessment. The autocorrelation spectra of the Epoch 2 VY CMa data presented in this thesis had very limited emission-free baselines at the ends of the spectra. This was a problem for the autocorrelation model fit, which includes a noise baseline term. It is partly for this reason that the autocorrelation polarisation self-calibration failed for the 86 GHz v=1 J=2-1 data set, where baseline subtraction inaccuracies were most pronounced due to the high SEFD of the VLBA at 86 GHz. Future VLBI observations of VY CMa should therefore be scheduled to include a wider emission-free region around the spectrum.

In addition, autocorrelation polarisation self-calibration should also be tested with Mira variable observations, as these stars display higher integrated linear polarisation than supergiant stars (e.g. Glenn et al. 2003). Higher levels of integrated linear polarisation in the autocorrelation spectra will provide better contraints on the autocorrelation polarisation self-calibration technique.

8.2 SiO maser pumping mechanisms

The morphologies of the Epoch 1 and Epoch 2 SiO maser maps were compared across the v=1 J=1-0, v=2 J=1-0 and v=1 J=2-1 transitions to provide constraints on SiO maser pumping models. The main results of this comparison are as follows,

- The v=2 J=1-0 emission is found almost entirely in a subset v=1 J=1-0 emission regions, consistent with the hydrodynamical models of Gray & Humphreys (2000).
- The Epoch 2 maps display a significant number of coincident v=1 J=1-0 and v=2 J=1-0 SiO maser features. Overlap in SiO maser emission from these two lines is expected under both collisional and radiative pumping models (Alcolea 2004), but has not previously been observed to this extent.
- The v=1 J=2-1 maser emission was weaker than the v=1 J=1-0 maser emission in all but one of six coincident maser features investigated in detail in these observations. This contradicts the Humphreys et al. (2002) model prediction of greater intensity in the v=1 J=2-1 emission in coincident features. The weaker v=1 J=2-1 emission may be explained in the context of a collisional pumping model, where it is indicative of lower densities (Doel et al. 1995).
- The extent of the overlap between the three transitions varies across the circumstellar envelope. This may indicate variable density conditions in the envelope, either on a local or a global scale.

The SiO maser pumping models will benefit from further observational comparisons of the J=1-0 and J=2-1 SiO maser emission towards VY CMa. Due to its extremely high SiO maser luminosity, VY CMa is a good candidate for 86 GHz J=2-1 observations, which suffer from SNR limitations for weaker sources.

8.3 SiO maser polarisation models

Six observational tests of the weak-splitting maser polarisation models were proposed in Chapter 3.4.9. The tests were performed on the Epoch 2 images, in many cases using a subset of six maser features observed to be coincident in two or more of the observed transitions. The test results are summarised as follows:

- No clear ordinal relationship was observed between the magnitude of the v=1 J=1-0 and v=1 J=2-1 fractional linear polarisation of the six coincident features. Assuming comparable saturation of the two lines, the results are most consistent with the Elitzur model, which predicts similar fractional linear polarisation for both transitions (Elitzur 1991).

- The fractional linear polarisation shows a decreasing trend for higher intensity masers. This is consistent with the predictions of anisotropic pumping models (e.g. Nedoluha & Watson 1990a). However, the m-isotropic Watson and Elitzur models cannot be ruled out by this test due to the unknown beaming angle of the masers, making the level of saturation uncertain.

- The fractional linear polarisation is not observed to be stronger closer to the star, which contradicts the predictions of anisotropic pumping models.

- The rotation of the linear polarisation position angle was investigated for two features, F1 and F2 (Figure 7.1), for which this was possible.

  The linear polarisation of F2 was fitted to the GKK linear polarisation function. This feature displayed a $\sim 90°$ EVPA rotation, and the form of the linear polarisation across the feature was broadly consistent with the a transition of the line of sight magnetic field angle across the critical 55° angle. However, the GKK model fit was poor, likely due to the limited number of measured data points across the feature.

  The linear polarisation of F1 shows multiple $\sim 90°$ rotations across the feature. Possible explanations for this behaviour include orientation close to the 55° critical angle, or a helical magnetic field permeating the maser feature.

- The v=1 J=1-0 and v=1 J=2-1 fractional circular polarisation was compared for a single channel in one of the coincident maser features, the only component for which this test was possible. The levels of circular polarisation were found to be the same for both transitions, to within the measured uncertainties. However, the large uncertainty in the v=1 J=2-1 fractional circular polarisation measurement meant that Zeeman circular polarisation cannot be ruled out by this single component test.

- No correlation was found between the fractional circular and linear polarisation of the maser features, and a significant number of maser features are circularly polarised at a level greater than $m_l^2/4$. This is strong evidence against the non-Zeeman circular polarisation mechanism of the Watson model (Wiebe & Watson 1998).

Overall, the tests results are not supportive of non-Zeeman circular polarisation. The most definitive test of Zeeman circular polarisation is the v=1 J=1-0 and v=1 J=2-1 circular polarisation comparison. Unfortunately this test was only possible for a single data point, and the result is inconclusive in the current observations.

Further work is warranted in the area, especially for multi-transition circular polarisation comparison. The calibration innovations discussed in the previous section enable high accuracy circular polarisation measurements, and should be applied to further observations of SiO maser emission towards VY CMa and other sources. This will provide a larger database of coincident maser emission for the observational tests described above.

The development of a software correlator at the VLBA has dramatically increased the spectral resolution of this instrument. This allows high spectral-resolution VLBA observations of SiO maser circular polarisation profiles that will provide further constraints on SiO maser polarisation models, and consequently better estimates of the circumstellar magnetic field.

8.4 VY CMa envelope kinematics

Several images of the J=1-0 SiO maser emission towards VY CMa show a concentration of maser emission to the east and northeast of the star (Miyoshi et al. 1994; Miyoshi 2003; Shibata et al. 2004; Richter et al. 2007; Choi et al. 2008a; Zhang et al. 2012), including the images presented in this thesis. SiO maser emission is variable, with the position of maser features being dependent on favourable local conditions in the envelope. Nonetheless, the persistent eastern concentration of the J=1-0 masers may be consistent with the bipolar envelope morphology proposed for VY CMa by numerous authors, based on observations at other wavelengths (e.g. Yates & Cohen 1994; Richards et al. 1998; Monnier et al. 1999b; Shinnaga et al. 2003; Muller et al. 2007).

Alternatively, the morphology of the maser emission may be the result of many local mass-ejection events, or simply due to chance velocity coherent regions in spherical stellar wind. A recent proper-motion study of v=1 J=1-0 SiO masers towards VY CMa shows a slow quasi-spherical outflow in the maser region (Zhang et al. 2012).

Under the Elitzur Zeeman interpretation, the observed levels of SiO maser circular polarisation imply magnetic fields of a few Gauss in the SiO maser region. If these magnetic field estimates are correct, it is unclear whether they are associated with localised features in the circumstellar envelope, or permeate the entire envelope.

VY CMa is a fascinating source. Many observations over recent years have shown that it's circumstellar envelope is chemically complex (e.g. Ziurys et al. 2007) and host to many small-scale features (e.g. Smith et al. 2001, 2009), postulated to be the result of localised mass-loss. Future observations of VY CMa with the Atacama Large Millimeter Array[1] will allow the circumstellar envelope to be investigated through high-sensitivity intermediate resolution observations of numerous submillimetre spectral lines.

Recent VLBI observations of VY CMa have shown the power of phase referencing to study the proper motion of the masers, and to provide more accurate estimates of the VY CMa position and distance (Choi et al. 2008b; Zhang et al. 2012). Further astrometric monitoring of the VY CMa circumstellar masers with VLBI arrays such as VERA, the VLBA, the EVN[2] and other upcoming trans-continental arrays such as the East Asian VLBI network[3] will provide valuable input to kinematic models of the circumstellar envelope. Technological advances in interferometry, such as software

[1] www.almaobservatory.org
[2] www.evlbi.org
[3] www.miz.nao.ac.jp/en/content/project/east-asia-vlbi-network

correlation, multiple-beam antennas and e-VLBI, can also be harnessed to improve observations of this source.

References

Agudo, I., Thum, C., Wiesemeyer, H., & Krichbaum, T. P. 2010, ApJS, 189, 1

Alcolea, J. 2004, in Proceedings of the 7th EVN Symposium, ed. R. Bachiller, F. Colomer, J.-F. Desmurs, & P. de Vicente (Observatorio Astronomico Nacional), 169

Alcolea, J., Pardo, J. R., Bujarrabal, V., et al. 1999, A&AS, 139, 461

Allen, D. A., Hall, P. J., Norris, R. P., et al. 1989, MNRAS, 236, 363

Aller, H. D., Aller, M. F., & Plotkin, R. M. 2003, Ap&SS, 288, 17

Armandroff, T. E. & Herbst, W. 1981, AJ, 86, 1923

Asensio Ramos, A., Landi Degl'Innocenti, E., & Trujillo Bueno, J. 2005, ApJ, 625, 985

Aurière, M., Donati, J., Konstantinova-Antova, R., et al. 2010, A&A, 516, L2

Aurière, M., Konstantinova-Antova, R., Petit, P., et al. 2008, A&A, 491, 499

Bachiller, R., Fuente, A., Bujarrabal, V., et al. 1997, A&A, 319, 235

Bains, I., Gledhill, T. M., Yates, J. A., & Richards, A. M. S. 2003, MNRAS, 338, 287

Bains, I., Richards, A. M. S., Gledhill, T. M., & Yates, J. A. 2004, MNRAS, 354, 529

Baldwin, J. E., Beckett, M. G., Boysen, R. C., et al. 1996, A&A, 306, L13

Baldwin, J. E., Haniff, C. A., Mackay, C. D., & Warner, P. J. 1986, Nature, 320, 595

Balick, B. & Frank, A. 2002, ARA&A, 40, 439

Barvainis, R., McIntosh, G., & Predmore, C. R. 1987, Nature, 329, 613

Barvainis, R. & Predmore, C. R. 1985, ApJ, 288, 694

Benson, J. M. & Mutel, R. L. 1982, ApJ, 253, 199

Bieging, J. H. 2006, in Astronomical Society of the Pacific Conference Series, Vol. 356, Revealing the Molecular Universe: One Antenna is Never Enough, ed. D. C. Backer, J. M. Moran, & J. L. Turner (Astronomical Society of the Pacific), 149

Bieging, J. H., Chapman, B., & Welch, W. J. 1984, ApJ, 285, 656

Bieging, J. H., Wilner, D., & Thronson, Jr., H. A. 1991, ApJ, 379, 271

Bieniek, R. J. & Green, S. 1983, ApJ, 265, L29

Blackman, E. G. 2009, in IAU Symposium, Vol. 259, Cosmic Magnetic Fields: From Planets, to Stars and Galaxies, ed. K. G. Strassmeier, A. G. Kosovichev, & J. E. Beckman (Cambridge University Press), 35

Blackman, E. G., Frank, A., Markiel, J. A., Thomas, J. H., & Van Horn, H. M. 2001, Nature, 409, 485

Boboltz, D. A., Diamond, P. J., & Kemball, A. J. 1997, ApJ, 487, L147

Boboltz, D. A. J. 1997, PhD thesis, Virginia Polytechnic Institute and State University

Booth, R. S., Diamond, P. J., & Norris, R. P. 1984, in IAU Symposium, Vol. 110, VLBI and Compact Radio Sources, ed. R. Fanti, K. I. Kellermann, & G. Setti (Springer), 313

Born, M. & Wolf, E. 1999, Principles of Optics, 7th edn. (Cambridge University Press)

Bowers, P. F., Claussen, M. J., & Johnston, K. J. 1993, AJ, 105, 284

Bowers, P. F. & Johnston, K. J. 1990, ApJ, 354, 676

Bowers, P. F., Johnston, K. J., & Spencer, J. H. 1983, ApJ, 274, 733

Bracewell, R. N. 1986, The Fourier Transform and its Applications, 2nd edn. (McGraw-Hill Book Company)

Brown, L. F., Roberts, D. H., & Wardle, J. F. C. 1989, AJ, 97, 1522

Brown, R. H. 1968, ARA&A, 6, 13

Buhl, D., Snyder, L. E., Lovas, F. J., & Johnson, D. R. 1974, ApJ, 192, L97

Buhl, D., Snyder, L. E., Lovas, F. J., & Johnson, D. R. 1975, ApJ, 201, L29

Bujarrabal, V. 1994, A&A, 285, 953

Bujarrabal, V., Alcolea, J., Sanchez Contreras, C., & Colomer, F. 1996, A&A, 314, 883

Bujarrabal, V., Fuente, A., & Omont, A. 1994, A&A, 285, 247

Bujarrabal, V. & Nguyen-Q-Rieu, M. 1981, A&A, 102, 65

Buscher, D. F., Baldwin, J. E., Warner, P. J., & Haniff, C. A. 1990, MNRAS, 245, 7P

Cernicharo, J., Alcolea, J., Baudry, A., & Gonzalez-Alfonso, E. 1997, A&A, 319, 607

Cernicharo, J. & Bujarrabal, V. 1992, ApJ, 401, L109

Cernicharo, J., Bujarrabal, V., & Lucas, R. 1991, A&A, 249, L27

Cernicharo, J., Bujarrabal, V., & Santaren, J. L. 1993, ApJ, 407, L33

Chandrasekhar, S. 1960, Radiative Transfer (Dover Publications Inc.)

Chapman, J. M. & Cohen, R. J. 1986, MNRAS, 220, 513

Chapman, J. M., Sivagnanam, P., Cohen, R. J., & Le Squeren, A. M. 1994, MNRAS, 268, 475

Chen, X., Shen, Z., Imai, H., & Kamohara, R. 2006, ApJ, 640, 982

Chen, X. & Shen, Z.-Q. 2008, ApJ, 681, 1574

Chiosi, C. & Maeder, A. 1986, ARA&A, 24, 329

Cho, S. & Ukita, N. 1998, AJ, 116, 2495

Cho, S.-H., Kaifu, N., & Ukita, N. 1996, A&AS, 115, 117

Choi, Y. K., Hirota, T., Honma, M., & Kobayashi, H. 2008a, in Proceedings of the 9th EVN Symposium, 57, http://pos.sissa.it/cgi-bin/reader/conf.cgi?confid=72

Choi, Y. K., Hirota, T., Honma, M., et al. 2008b, PASJ, 60, 1007

Chugai, N. N., Danziger, I. J., & della Valle, M. 1995, MNRAS, 276, 530

Clark, B. C. 1989, in Astronomical Society of the Pacific Conference Series, Vol. 6, Synthesis Imaging in Radio Astronomy, ed. R. A. Perley, F. R. Schwab, & A. H. Bridle (Astronomical Society of the Pacific), 1

Clark, B. G. 1980, A&A, 89, 377

Clark, F. O., Troland, T. H., Pepper, G. H., & Johnson, D. R. 1984, ApJ, 276, 572

Cohen, M. H. 1958, Proceedings of the IRE, 46, 172

Cohen, R. J. 1987, in IAU Symposium, Vol. 122, Circumstellar Matter, ed. I. Appenzeller & C. Jordan (Reidel Publishing Company, Dordrecht), 229

Cohen, R. J., Downs, G., Emerson, R., et al. 1987, MNRAS, 225, 491

Colomer, F., Baudry, A., Graham, D. A., et al. 1996, A&A, 312, 950

Conway, R. G. & Kronberg, P. P. 1969, MNRAS, 142, 11

Cook, A. 1977, Celestial Masers (Cambridge University Press)

Cooke, B. & Elitzur, M. 1985, ApJ, 295, 175

Cornwell, T. & Braun, R. 1989, in Astronomical Society of the Pacific Conference Series, Vol. 6, Synthesis Imaging in Radio Astronomy, ed. R. A. Perley, F. R. Schwab, & A. H. Bridle (Astronomical Society of the Pacific), 167

Cornwell, T. J., Golap, K., & Bhatnagar, S. 2005, in Astronomical Society of the Pacific Conference Series, Vol. 345, From Clark Lake to the Long Wavelength Array: Bill Erickson's Radio Science, ed. N. Kassim, M. Perez, W. Junor, & P. Henning (Astronomical Society of the Pacific), 350

Cornwell, T. J. & Wilkinson, P. N. 1981, MNRAS, 196, 1067

Cotton, W. D. 1993, AJ, 106, 1241

Cotton, W. D. 1995, in Astronomical Society of the Pacific Conference Series, Vol. 82, Very Long Baseline Interferometry and the VLBA, ed. J. A. Zensus, P. J. Diamond, & P. J. Napier (Astronomical Society of the Pacific), 189

Cotton, W. D., Geldzahler, B. J., Marcaide, J. M., et al. 1984, ApJ, 286, 503

Cotton, W. D., Mennesson, B., Diamond, P. J., et al. 2004, A&A, 414, 275

Cotton, W. D., Perrin, G., & Lopez, B. 2008, A&A, 477, 853

Cotton, W. D., Ragland, S., & Danchi, W. C. 2011, ApJ, 736, 96

Cotton, W. D., Ragland, S., Pluzhnik, E., et al. 2009a, ApJ, 704, 170

Cotton, W. D., Ragland, S., Pluzhnik, E. A., et al. 2009b, ApJS, 185, 574

Cotton, W. D., Ragland, S., Pluzhnik, E. A., et al. 2010a, ApJS, 187, 107

Cotton, W. D., Ragland, S., Pluzhnik, E. A., et al. 2010b, ApJS, 188, 506

Cotton, W. D., Vlemmings, W., Mennesson, B., et al. 2006, A&A, 456, 339

Cox, G. G. & Parker, E. A. 1979, MNRAS, 186, 197

Cruzalebes, P., Lopez, B., Bester, M., Gendron, E., & Sams, B. 1998, A&A, 338, 132

D'Addario, L. R. 1989, in Astronomical Society of the Pacific Conference Series, Vol. 6, Synthesis Imaging in Radio Astronomy, ed. R. A. Perley, F. R. Schwab, & A. H. Bridle (Astronomical Society of the Pacific), 59

Danchi, W. C., Bester, M., Degiacomi, C. G., Greenhill, L. J., & Townes, C. H. 1994, AJ, 107, 1469

Davis, J. H., Blair, G. N., van Till, H., & Thaddeus, P. 1974, ApJ, 190, L117

Dayal, A. & Bieging, J. H. 1995, ApJ, 439, 996

De Beck, E., Decin, L., Menten, K. M., et al. 2011, in Astronomical Society of the Pacific Conference Series, Vol. 445, Why Galaxies Care about AGB Stars II: Shining Examples and Common Inhabitants, ed. F. Kerschbaum (Astronomical Society of the Pacific), 317

de Jager, C. 1980, The Brightest Stars (D. Reidel Publishing Company)

Decin, L., Hony, S., de Koter, A., et al. 2006, A&A, 456, 549

Deguchi, S. & Iguchi, T. 1976, PASJ, 28, 307

Deguchi, S. & Watson, W. D. 1986, ApJ, 300, L15

Deguchi, S. & Watson, W. D. 1990, ApJ, 354, 649

Deguchi, S., Watson, W. D., & Western, L. R. 1986, ApJ, 302, 108

Desmurs, J., Bujarrabal, V., Colomer, F., & Alcolea, J. 1999, New Astronomy Reviews, 43, 559

Desmurs, J. F., Bujarrabal, V., Colomer, F., & Alcolea, J. 2000, A&A, 360, 189

Desmurs, J.-F., Soria-Ruiz, R., Colomer, F., et al. 2002, in Proceedings of the 6th EVN Symposium, ed. E. Ros, R. W. Porcas, A. P. Lobanov, & J. A. Zensus (Max-Planck-Institut fuer Radioastronomie (Bonn)), 221

di Benedetto, G. P. & Rabbia, Y. 1987, A&A, 188, 114

Diamond, P. I. 1989, in Astronomical Society of the Pacific Conference Series, Vol. 6, Synthesis Imaging in Radio Astronomy, ed. R. A. Perley, F. R. Schwab, & A. H. Bridle (Astronomical Society of the Pacific), 379

Diamond, P. J. & Kemball, A. J. 1999, in IAU Symposium, Vol. 191, Asymptotic Giant Branch Stars, ed. T. Le Bertre, A. Lebre, & C. Waelkens (Astronomical Society of the Pacific), 195

Diamond, P. J. & Kemball, A. J. 2003, ApJ, 599, 1372

Diamond, P. J., Kemball, A. J., Junor, W., et al. 1994, ApJ, 430, L61

Dinh-v-Trung. 2009a, MNRAS, 396, 2319

Dinh-v-Trung. 2009b, MNRAS, 399, 1495

Doel, R. C., Gray, M. D., Humphreys, E. M. L., Braithwaite, M. F., & Field, D. 1995, A&A, 302, 797

Donati, J., Semel, M., Carter, B. D., Rees, D. E., & Collier Cameron, A. 1997, MNRAS, 291, 658

Dorch, S. B. F. 2004, A&A, 423, 1101

Efstathiou, A. & Rowan-Robinson, M. 1990, MNRAS, 245, 275

Eliasson, B. & Bartlett, J. F. 1969, ApJ, 155, L79

Elitzur, M. 1980, ApJ, 240, 553

Elitzur, M. 1991, ApJ, 370, 407

Elitzur, M. 1992, Astronomical Masers (Kluwer Academic Publishers)

Elitzur, M. 1993, ApJ, 416, 256

Elitzur, M. 1995, ApJ, 440, 345

Elitzur, M. 1996, ApJ, 457, 415

Elitzur, M. 1998, ApJ, 504, 390

Elitzur, M. 2002, in IAU Symposium, Vol. 206, Cosmic Masers: From Proto-Stars to Black Holes, ed. V. Migenes & M. J. Reid (Astronomical Society of the Pacific), 452

Elitzur, M. 2007, in IAU Symposium, Vol. 242, Astrophysical Masers & their Environments, ed. J. M. Chapman & W. A. Baan (Cambridge University Press), 7

Etoka, S. & Diamond, P. 2004, MNRAS, 348, 34

Field, D. & Gray, M. D. 1988, MNRAS, 234, 353

Fieller, E. C. 1932, Biometrika, 24, 428

Fish, V. L. & Reid, M. J. 2007, ApJ, 656, 952

Frank, A. 1995, AJ, 110, 2457

Frank, A., De Marco, O., Blackman, E., & Balick, B. 2007, arXiv:0712.2004

Fransson, C., Chevalier, R. A., Filippenko, A. V., et al. 2002, ApJ, 572, 350

Fu, R., Moullet, A., Patel, N. A., et al. 2011, arXiv:1111.7004

Garcia-Barreto, J. A., Burke, B. F., Reid, M. J., et al. 1988, ApJ, 326, 954

García-Segura, G., López, J. A., & Franco, J. 2005, ApJ, 618, 919

Geballe, T. R., Lacy, J. H., & Beck, S. C. 1979, ApJ, 230, L47

Geballe, T. R. & Townes, C. H. 1974, ApJ, 191, L37

Gezari, D. Y., Labeyrie, A., & Stachnik, R. V. 1972, ApJ, 173, L1

Glenn, J., Jewell, P. R., Fourre, R., & Miaja, L. 2003, ApJ, 588, 478

Goldreich, P. & Keeley, D. A. 1972, ApJ, 174, 517

Goldreich, P., Keeley, D. A., & Kwan, J. Y. 1973, ApJ, 179, 111

Goldreich, P. & Kylafis, N. D. 1981, ApJ, 243, L75

Gómez, Y., Tafoya, D., Anglada, G., et al. 2009, ApJ, 695, 930

Gomez Balboa, A. M. & Lepine, J. R. D. 1986, A&A, 159, 166

Gonidakis, I., Diamond, P. J., & Kemball, A. J. 2010, MNRAS, 406, 395

Gonzalez-Alfonso, E., Alcolea, J., & Cernicharo, J. 1996, A&A, 313, L13

Gray, M. D. 2003, MNRAS, 343, L33

Gray, M. D. & Field, D. 1995, A&A, 298, 243

Gray, M. D. & Humphreys, E. M. L. 2000, New Astronomy, 5, 155

Gray, M. D., Humphreys, E. M. L., & Field, D. 1995a, Ap&SS, 224, 63

Gray, M. D., Humphreys, E. M. L., & Yates, J. A. 1999, MNRAS, 304, 906

Gray, M. D., Ivison, R. J., Yates, J. A., et al. 1995b, MNRAS, 277, L67

Gray, M. D., Wittkowski, M., Scholz, M., et al. 2009, MNRAS, 394, 51

Greaves, J. S. 2002, A&A, 392, L1

Greenhill, L. J., Colomer, F., Moran, J. M., et al. 1995, ApJ, 449, 365

Greisen, E. 1994, AIPS Memo Series, 27

Greisen, E. 2004, AIPS Cookbook, www.aips.nrao.edu/cook.html

Greisen, E. 2009, AIPS Memo Series, 114

Grunhut, J. H., Wade, G. A., Hanes, D. A., & Alecian, E. 2010, MNRAS, 408, 2290

Gustafsson, B., Edvardsson, B., Eriksson, K., et al. 2003, in Astronomical Society of the Pacific Conference Series, Vol. 288, Stellar Atmosphere Modeling, ed. I. Hubeny, D. Mihalas, & K. Werner (Astronomical Society of the Pacific), 331

Högbom, J. A. 1974, A&AS, 15, 417

Habing, H. J. 1996, A&A Rev., 7, 97

Hall, P. J., Allen, D. A., Troup, E. R., Wark, R. M., & Wright, A. E. 1990, MNRAS, 243, 480

Hamaker, J. P. 2000, A&AS, 143, 515

Hamaker, J. P. 2006, A&A, 456, 395

Hamaker, J. P. & Bregman, J. D. 1996, A&AS, 117, 161

Hamaker, J. P., Bregman, J. D., & Sault, R. J. 1996, A&AS, 117, 137

Haniff, C. A., Mackay, C. D., Titterington, D. J., Sivia, D., & Baldwin, J. E. 1987, Nature, 328, 694

Haniff, C. A., Scholz, M., & Tuthill, P. G. 1995, MNRAS, 276, 640

Hartquist, T. W. & Dyson, J. E. 1997, A&A, 319, 589

Harvey, P. J., Booth, R. S., Davies, R. D., McLaughlin, W., & Whittet, D. C. B. 1974, MNRAS, 169, 545

Harwit, M. & Bergin, E. A. 2002, ApJ, 565, L105

Harwit, M., Houde, M., Sonnentrucker, P., et al. 2010, A&A, 521, L51

Harwit, M., Malfait, K., Decin, L., et al. 2001, ApJ, 557, 844

Hayya, J., Armstrong, D., & Gressis, D. 1975, Management Science, 21, 1338

Heger, A., Fryer, C. L., Woosley, S. E., Langer, N., & Hartmann, D. H. 2003, ApJ, 591, 288

Heger, A. & Langer, N. 1998, A&A, 334, 210

Herbig, G. H. 1970, ApJ, 162, 557

Herbig, G. H. 1972, ApJ, 172, 375

Herbig, G. H. 1974, ApJ, 188, 533

Herbig, G. H. & Zappala, R. R. 1970, ApJ, 162, L15

Herman, J. & Habing, H. J. 1985, A&AS, 59, 523

Herpin, F., Baudry, A., Thum, C., Morris, D., & Wiesemeyer, H. 2006, A&A, 450, 667

Hinkley, D. V. 1969, Biometrika, 56, 635

Hoffman, I. M., Goss, W. M., Brogan, C. L., & Claussen, M. J. 2005, ApJ, 620, 257

Hollis, J. M., Boboltz, D. A., Pedelty, J. A., White, S. M., & Forster, J. R. 2001, ApJ, 559, L37

Homan, D. C., Attridge, J. M., & Wardle, J. F. C. 2001, ApJ, 556, 113

Homan, D. C. & Lister, M. L. 2006, AJ, 131, 1262

Homan, D. C. & Wardle, J. F. C. 1999, AJ, 118, 1942

Homan, D. C. & Wardle, J. F. C. 2003, Ap&SS, 288, 29

Humphreys, E. M. L., Gray, M. D., Yates, J. A., & Field, D. 1997, MNRAS, 287, 663

Humphreys, E. M. L., Gray, M. D., Yates, J. A., et al. 1996, MNRAS, 282, 1359

Humphreys, E. M. L., Gray, M. D., Yates, J. A., et al. 2002, A&A, 386, 256

Humphreys, R. M. 1974, ApJ, 188, 75

Humphreys, R. M., Davidson, K., Ruch, G., & Wallerstein, G. 2005, AJ, 129, 492

Humphreys, R. M., Helton, L. A., & Jones, T. J. 2007, AJ, 133, 2716

Hyland, A. R., Becklin, E. E., Frogel, J. A., & Neugebauer, G. 1972, A&A, 16, 204

Hyland, A. R., Becklin, E. E., Neugebauer, G., & Wallerstein, G. 1969, ApJ, 158, 619

Iben, I. & Renzini, A. 1983, ARA&A, 21, 271

Iguchi, S. 2000, PhD thesis, University of Electro-Communications

Iguchi, S., Kawaguchi, N., Murata, Y., et al. 2000, IEICE Trans. Commun., 102

Imai, H., Nakashima, J., Deguchi, S., et al. 2010, PASJ, 62, 431

Imai, H., Obara, K., Diamond, P. J., Omodaka, T., & Sasao, T. 2002, Nature, 417, 829

Ireland, M. J., Tuthill, P. G., Davis, J., & Tango, W. 2005, MNRAS, 361, 337

Jackson, J. M. & Nguyen, Q. 1988, ApJ, 335, L83

Jennison, R. C. 1958, MNRAS, 118, 276

Jewell, P. R., Dickinson, D. F., Snyder, L. E., & Clemens, D. P. 1987, ApJ, 323, 749

Jewell, P. R., Snyder, L. E., Walmsley, C. M., Wilson, T. L., & Gensheimer, P. D. 1991, A&A, 242, 211

Johnston, K. J., Spencer, J. H., & Bowers, P. F. 1985, ApJ, 290, 660

Jones, R. C. 1941, Journal of the Optical Society of America, 31, 488

Jones, T. J., Humphreys, R. M., Gehrz, R. D., et al. 1993, ApJ, 411, 323

Jones, T. J., Humphreys, R. M., Helton, L. A., Gui, C., & Huang, X. 2007, AJ, 133, 2730

Jordan, S., Werner, K., & O'Toole, S. J. 2005, A&A, 432, 273

Josselin, E., Blommaert, J. A. D. L., Groenewegen, M. A. T., Omont, A., & Li, F. L. 2000, A&A, 357, 225

Joy, A. H. 1942, ApJ, 96, 344

Jura, M. & Kleinmann, S. G. 1990, ApJS, 73, 769

Kaifu, N., Buhl, D., & Snyder, L. E. 1975, ApJ, 195, 359

Kamohara, R., Bujarrabal, V., Honma, M., et al. 2010, A&A, 510, A69

Kang, J., Cho, S.-H., Kim, H.-G., et al. 2006, ApJS, 165, 360

Kastner, J. H. & Weintraub, D. A. 1998, AJ, 115, 1592

Kellermann, K. I. & Moran, J. M. 2001, ARA&A, 39, 457

Kemball, A. J. 1992, PhD thesis, Rhodes University

Kemball, A. J. 1999, in Astronomical Society of the Pacific Conference Series, Vol. 180, Synthesis Imaging in Radio Astronomy II, ed. G. B. Taylor, C. L. Carilli, & R. A. Perley (Astronomical Society of the Pacific), 499

Kemball, A. J. & Diamond, P. J. 1993, in Lecture Notes in Physics, Berlin Springer Verlag, Vol. 412, Astrophysical Masers, ed. A. W. Clegg & G. E. Nedoluha (Springer-Verlag), 369

Kemball, A. J. & Diamond, P. J. 1997, ApJ, 481, L111

Kemball, A. J., Diamond, P. J., & Cotton, W. D. 1995, A&AS, 110, 383

Kemball, A. J., Diamond, P. J., Gonidakis, I., et al. 2009, ApJ, 698, 1721

Kemball, A. J., Diamond, P. J., Richter, L., Gonidakis, I., & Xue, R. 2011, ApJ, 743, 69

Kemball, A. J. & Richter, L. 2011, A&A, 533, A26

Kemper, F., Stark, R., Justtanont, K., et al. 2003, A&A, 407, 609

Knapp, G. R., Bowers, P. F., Young, K., & Phillips, T. G. 1995, ApJ, 455, 293

Knowles, S. H., Mayer, C. H., Cheung, A. C., Rank, D. M., & Townes, C. H. 1969, Science, 163, 1055

Kogan, L. 1995, AIPS Memo Series, 9

Konstantinova-Antova, R., Aurière, M., Schröder, K., & Petit, P. 2009, in IAU Symposium, Vol. 259, Cosmic Magnetic Fields: From Planets, to Stars and Galaxies, ed. K. G. Strassmeier, A. G. Kosovichev, & J. E. Beckman (Cambridge University Press), 433

Kukarkin, B. V., Kholopov, P. N., Pskovsky, Y. P., et al. 1971, General Catalogue of Variable Stars, 3rd edn.

Kwan, J. & Scoville, N. 1974, ApJ, 194, L97

Labeyrie, A. 1970, A&A, 6, 85

Labeyrie, A. 1978, ARA&A, 16, 77

Labeyrie, A., Koechlin, L., Bonneau, D., Blazit, A., & Foy, R. 1977, ApJ, 218, L75

Lada, C. J. & Reid, M. J. 1978, ApJ, 219, 95

Lane, A. P. 1982, PhD thesis, University of Massachusetts

Le Sidaner, P. & Le Bertre, T. 1996, A&A, 314, 896

Leppanen, K. J., Zensus, J. A., & Diamond, P. J. 1995, AJ, 110, 2479

Lindqvist, M., Olofsson, H., Lucas, R., et al. 1999, A&A, 351, L1

Lipscy, S. J., Jura, M., & Reid, M. J. 2005, ApJ, 626, 439

Lister, M. L., Aller, H. D., Aller, M. F., et al. 2009, AJ, 137, 3718

Lockett, P. & Elitzur, M. 1992, ApJ, 399, 704

Loup, C., Forveille, T., Omont, A., & Paul, J. F. 1993, A&AS, 99, 291

Lovas, F. J. 1992, Journal of Physical and Chemical Reference Data, 21, 181

Lucas, R. & Guélin, M. 1999, in IAU Symposium, Vol. 191, Asymptotic Giant Branch Stars, ed. T. Le Bertre, A. Lebre, & C. Waelkens (Astronomical Society of the Pacific), 305

Maeder, A. & Meynet, G. 2008, Revista Mexicana de Astronomia y Astrofisica Conference Series, 33, 38

Marshall, C. R., Leahy, D. A., & Kwok, S. 1992, PASP, 104, 397

Martinez, A., Bujarrabal, V., & Alcolea, J. 1988, A&AS, 74, 273

Marvel, K. B. 1996, PhD thesis, New Mexico State University

Masheder, M. R. W., Booth, R. S., & Davies, R. D. 1974, MNRAS, 166, 561

Massey, P., Levesque, E. M., & Plez, B. 2006, ApJ, 646, 1203

Massey, P., Plez, B., Levesque, E. M., et al. 2008, Revista Mexicana de Astronomia y Astrofisica Conference Series, 33, 29

Matsumoto, N., Omodaka, T., Imai, H., et al. 2008, PASJ, 60, 1039

Matt, S., Balick, B., Winglee, R., & Goodson, A. 2000, ApJ, 545, 965

McCarthy, D. W. & Low, F. J. 1975, ApJ, 202, L37

McCarthy, D. W., Low, F. J., & Howell, R. 1977, ApJ, 214, L85

McIntosh, A. C. & Predmore, C. R. 1991, in Astronomical Society of the Pacific Conference Series, Vol. 16, Atoms, Ions and Molecules: New Results in Spectral Line Astrophysics, ed. A. D. Haschick & P. T. P. Ho (Astronomical Society of the Pacific), 83

McIntosh, G. C. & Predmore, C. H. 1996, in Astronomical Society of the Pacific Conference Series, Vol. 97, Polarimetry of the Interstellar Medium, ed. W. G. Roberge & D. C. B. Whittet (Astronomical Society of the Pacific), 207

McIntosh, G. C. & Predmore, C. R. 1993, ApJ, 404, L71

McIntosh, G. C., Predmore, C. R., Moran, J. M., et al. 1989, ApJ, 337, 934

McIntosh, G. C., Predmore, C. R., & Patel, N. A. 1994, ApJ, 428, L29

McIntosh, G. C. & Rislow, B. 2009, ApJ, 692, 154

McKinnon, M. M. 2002, ApJ, 568, 302

McLaren, R. A. & Betz, A. L. 1980, ApJ, 240, L159

Meimon, S., Mugnier, L. M., & Le Besnerais, G. 2009, Journal of the Optical Society of America A, 26, 108

Menten, K. M., Lundgren, A., Belloche, A., Thorwirth, S., & Reid, M. J. 2008, A&A, 477, 185

Menten, K. M. & Melnick, G. J. 1989, ApJ, 341, L91

Menten, K. M. & Melnick, G. J. 1991, ApJ, 377, 647

Menten, K. M., Philipp, S. D., Güsten, R., et al. 2006, A&A, 454, L107

Menten, K. M. & Young, K. 1995, ApJ, 450, L67

Merrill, K. M. & Stein, W. A. 1976, PASP, 88, 285

Michelson, A. A. 1920, ApJ, 51, 257

Michelson, A. A. & Pease, F. G. 1921, ApJ, 53, 249

Middelberg, E. & Bach, U. 2008, Reports on Progress in Physics, 71, 066901

Milam, S. N., Apponi, A. J., Woolf, N. J., & Ziurys, L. M. 2007, ApJ, 668, L131

Milam, S. N., Halfen, D. T., Tenenbaum, E. D., et al. 2008, ApJ, 684, 618

Miyoshi, M. 2003, in ASSL, Vol. 283, Mass-Losing Pulsating Stars and their Circumstellar Matter, ed. Y. Nakada, M. Honma, & M. Seki (Dordrecht: Kluwer Academic Publishers), 303

Miyoshi, M., Matsumoto, K., Kameno, S., Takaba, H., & Iwata, T. 1994, Nature, 371, 395

Monnier, J. D. 2003, Reports on Progress in Physics, 66, 789

Monnier, J. D., Danchi, W. C., Hale, D. S., et al. 2000, ApJ, 543, 861

Monnier, J. D., Geballe, T. R., & Danchi, W. C. 1998, ApJ, 502, 833

Monnier, J. D., Geballe, T. R., & Danchi, W. C. 1999a, ApJ, 521, 261

Monnier, J. D., Traub, W. A., Schloerb, F. P., et al. 2004, ApJ, 602, L57

Monnier, J. D., Tuthill, P. G., Lopez, B., et al. 1999b, ApJ, 512, 351

Moran, J. M. 1998, in Astronomical Society of the Pacific Conference Series, Vol. 144, IAU Colloquium 164: Radio Emission from Galactic and Extragalactic Compact Sources, ed. J. A. Zensus, G. B. Taylor, & J. M. Wrobel (Astronomical Society of the Pacific), 1

Moran, J. M., Ball, J. A., Predmore, C. R., et al. 1979, ApJ, 231, L67

Moran, J. M., Ball, J. A., Yen, J. L., et al. 1977, ApJ, 211, 160

Moran, J. M. & Dhawan, V. 1995, in Astronomical Society of the Pacific Conference Series, Vol. 82, Very Long Baseline Interferometry and the VLBA, ed. J. A. Zensus, P. J. Diamond, & P. J. Napier (Astronomical Society of the Pacific), 161

Moran, J. M., Papadopoulos, G. D., Burke, B. F., et al. 1973, ApJ, 185, 535

Morris, D., Radhakrishnan, V., & Seielstad, G. A. 1964, ApJ, 139, 551

Morris, M. & Bowers, P. F. 1980, AJ, 85, 724

Müller, H. S. P., Schlöder, F., Stutzki, J., & Winnewisser, G. 2005, Journal of Molecular Structure, 742, 215

Muller, S., Dinh-V-Trung, Lim, J., et al. 2007, ApJ, 656, 1109

Napier, P. J. 1994, in IAU Symposium, Vol. 158, Very High Angular Resolution Imaging, ed. J. G. Robertson & W. J. Tango (Kluwer), 117

Napier, P. J. 1995, in Astronomical Society of the Pacific Conference Series, Vol. 82, Very Long Baseline Interferometry and the VLBA, ed. J. A. Zensus, P. J. Diamond, & P. J. Napier (Astronomical Society of the Pacific), 59

Napier, P. J., Thompson, A. R., & Ekers, R. D. 1983, IEEE Proceedings, 71, 1295

Nedoluha, G. E. & Bowers, P. F. 1992, ApJ, 392, 249

Nedoluha, G. E. & Watson, W. D. 1990a, ApJ, 354, 660

Nedoluha, G. E. & Watson, W. D. 1990b, ApJ, 361, L53

Nedoluha, G. E. & Watson, W. D. 1993, in Lecture Notes in Physics, Vol. 412, Astrophysical Masers, ed. A. W. Clegg & G. E. Nedoluha (Springer Berlin / Heidelberg), 47

Nedoluha, G. E. & Watson, W. D. 1994, ApJ, 423, 394

Nercessian, E., Omont, A., Benayoun, J. J., & Guilloteau, S. 1989, A&A, 210, 225

Neufeld, D. A., Feuchtgruber, H., Harwit, M., & Melnick, G. J. 1999, ApJ, 517, L147

Nordhaus, J. & Blackman, E. G. 2006, MNRAS, 370, 2004

Nordhaus, J., Blackman, E. G., & Frank, A. 2007, MNRAS, 376, 599

Norris, R. P., Diamond, P. J., & Booth, R. S. 1982, Nature, 299, 131

Nyman, L.-A., Booth, R. S., Carlstrom, U., et al. 1992, A&AS, 93, 121

Olofsson, H., Rydbeck, O. E. H., Lane, A. P., & Predmore, C. R. 1981, ApJ, 247, L81

Omont, A., Lucas, R., Morris, M., & Guilloteau, S. 1993, A&A, 267, 490

Ott, J., Elias, N., & Kern, J. 2010, CASA User Reference & Cookbook (Release 3.1.0)

Pardo, J. R., Alcolea, J., Bujarrabal, V., et al. 2004, A&A, 424, 145

Pascoli, G. 1997, ApJ, 489, 946

Pawsey, J. L., Payne-Scott, R., & McCready, L. L. 1946, Nature, 157, 158

Pearson, T. J. & Readhead, A. C. S. 1984, ARA&A, 22, 97

Perley, R. & Taylor, G. 2003, The VLA Calibrator Manual, www.vla.nrao.edu/astro/calib/manual

Perley, R. A., Schwab, F. R., & Bridle, A. H., eds. 1989, Astronomical Society of the Pacific Conference Series, Vol. 6, Synthesis imaging in radio astronomy (Astronomical Society of the Pacific)

Perrine, C. D. 1923, PASP, 35, 229

Perryman, M. A. C., Lindegren, L., Kovalevsky, J., et al. 1997, A&A, 323, L49

Phillips, R. B. & Boboltz, D. A. 2000, AJ, 119, 3015

Phillips, R. B., Straughn, A. H., Doeleman, S. S., & Lonsdale, C. J. 2003, ApJ, 588, L105

Phillips, T. G., van Dishoeck, E. F., & Keene, J. 1992, ApJ, 399, 533

Pijpers, F. P., Pardo, J. R., & Bujarrabal, V. 1994, A&A, 286, 501

Plambeck, R. L., Wright, M. C. H., & Rao, R. 2003, ApJ, 594, 911

Pluzhnik, E. A., Ragland, S., LeCoroller, H., et al. 2009, ApJ, 700, 114

Polehampton, E. T., Menten, K. M., van der Tak, F. F. S., & White, G. J. 2010, A&A, 510, A80

Quirrenbach, A. 2009, Experimental Astronomy, 26, 49

Ragland, S., Le Coroller, H., Pluzhnik, E., et al. 2008, ApJ, 679, 746

Rajagopal, J., Menut, J., Wallace, D., et al. 2007, ApJ, 671, 2017

Rausch, E., Kegel, W. H., Tsuji, T., & Piehler, G. 1996, A&A, 315, 533

Readhead, A. C. S., Walker, R. C., Pearson, T. J., & Cohen, M. H. 1980, Nature, 285, 137

Reid, M. J. 1995, in Astronomical Society of the Pacific Conference Series, Vol. 82, Very Long Baseline Interferometry and the VLBA, ed. J. A. Zensus, P. J. Diamond, & P. J. Napier (Astronomical Society of the Pacific), 209

Reid, M. J. 1999, in Astronomical Society of the Pacific Conference Series, Vol. 180, Synthesis Imaging in Radio Astronomy II, ed. G. B. Taylor, C. L. Carilli, & R. A. Perley (Astronomical Society of the Pacific), 481

Reid, M. J. 2002, in IAU Symposium, Vol. 206, Cosmic Masers: From Proto-Stars to Black Holes, ed. V. Migenes & M. J. Reid (Astronomical Society of the Pacific), 506

Reid, M. J. 2007, in IAU Symposium, Vol. 242, Astrophysical Masers & their Environments, ed. J. M. Chapman & W. A. Baan (Cambridge University Press), 522

Reid, M. J., Haschick, A. D., Burke, B. F., et al. 1980, ApJ, 239, 89

Reid, M. J. & Menten, K. M. 1997, ApJ, 476, 327

Reid, M. J. & Moran, J. M. 1981, ARA&A, 19, 231

Reid, M. J., Moran, J. M., Leach, R. W., et al. 1979, ApJ, 227, L89

Reid, M. J. & Muhleman, D. O. 1978, ApJ, 220, 229

Reid, M. J., Muhleman, D. O., Moran, J. M., Johnston, K. J., & Schwartz, P. R. 1977, ApJ, 214, 60

Remijan, A. J., Markwick-Kemper, A., & ALMA Working Group on Spectral Line Frequencies. 2007, Bulletin of the American Astronomical Society, 38, 963

Rhodes, W. T. & Goodman, J. W. 1973, Journal of the Optical Society of America, 63, 647

Richards, A., Bains, I., Bartkiewicz, A., et al. 2008, in Proceedings of the 9th EVN Symposium, 35, http://pos.sissa.it/cgi-bin/reader/conf.cgi?confid=72

Richards, A. M. S., Elitzur, M., & Yates, J. A. 2011, A&A, 525, A56

Richards, A. M. S., Masheder, M. R. W., van Langevelde, H. J., et al. 2004, in Proceedings of the 7th EVN Symposium, ed. R. Bachiller, F. Colomer, J.-F. Desmurs, & P. de Vicente (Observatorio Astronomico Nacional), 209

Richards, A. M. S., Yates, J. A., & Cohen, R. J. 1998, MNRAS, 299, 319

Richter, L. L., Kemball, A. J., & Jonas, J. L. 2007, in IAU Symposium, Vol. 242, Astrophysical Masers & their Environments, ed. J. M. Chapman & W. A. Baan (Cambridge University Press), 328

Richter, L. R. 2005, Master's thesis, Rhodes University

Rioja, M. J., Dodson, R., Kamohara, R., et al. 2008, PASJ, 60, 1031

Roberts, D. H., Potash, R. I., Wardle, J. F. C., Rogers, A. E. E., & Burke, B. F. 1984, in IAU Symposium, Vol. 110, VLBI and Compact Radio Sources, ed. R. Fanti, K. Kellermann, & G. Setti (D. Reidel), 35

Rogstad, D. H. 1968, Applied Optics, 7, 585

Romney, J. D. 2010, Very Long Baseline Array Observational Status Summary

Rosen, B. R., Moran, J. M., Reid, M. J., et al. 1978, ApJ, 222, 132

Rowan-Robinson, M. & Harris, S. 1983, MNRAS, 202, 767

Ryle, M. & Elsmore, B. 1973, MNRAS, 164, 223

Ryle, M. & Hewish, A. 1960, MNRAS, 120, 220

Ryle, M. & Neville, A. C. 1962, MNRAS, 125, 39

Ryle, M. & Vonberg, D. D. 1946, Nature, 158, 339

Sabin, L., Zijlstra, A. A., & Greaves, J. S. 2007, MNRAS, 376, 378

Sahai, R. & Wannier, P. G. 1992, ApJ, 394, 320

Samus, N. N., Durlevich, O. V., & et al. 2009, VizieR Online Data Catalog, 1, 2025

Sarma, A. P., Troland, T. H., Romney, J. D., & Huynh, T. H. 2008, ApJ, 674, 295

Sault, R. J., Hamaker, J. P., & Bregman, J. D. 1996, A&AS, 117, 149

Schlegel, E. M. 1990, MNRAS, 244, 269

Schwab, F. R. & Cotton, W. D. 1983, AJ, 88, 688

Schwarzschild, M. 1975, ApJ, 195, 137

Shibata, K. M., Chung, H., Kameno, S., et al. 2004, PASJ, 56, 475

Shinnaga, H., Claussen, M. J., Lim, J., Dinh-van-Trung, & Tsuboi, M. 2003, in ASSL, Vol. 283, Mass-Losing Pulsating Stars and their Circumstellar Matter, ed. Y. Nakada, M. Honma, & M. Seki (Dordrecht: Kluwer Academic Publishers), 393

Shinnaga, H., Moran, J. M., Young, K. H., & Ho, P. T. P. 2004a, ApJ, 617, L93

Shinnaga, H., Moran, J. M., Young, K. H., & Ho, P. T. P. 2004b, ApJ, 616, L47

Shinnaga, H., Tsuboi, M., & Kasuga, T. 1999, PASJ, 51, 175

Shintani, M., Imai, H., Ando, K., et al. 2008, PASJ, 60, 1077

Smith, N. 2004, MNRAS, 349, L31

Smith, N., Hinkle, K. H., & Ryde, N. 2009, AJ, 137, 3558

Smith, N., Humphreys, R. M., Davidson, K., et al. 2001, AJ, 121, 1111

Snyder, L. E. & Buhl, D. 1974, ApJ, 189, L31

Snyder, L. E. & Buhl, D. 1975, ApJ, 197, 329

Soker, N. 1998, MNRAS, 299, 1242

Soker, N. 2000a, ApJ, 540, 436

Soker, N. 2000b, MNRAS, 312, 217

Soker, N. 2002, MNRAS, 336, 826

Soker, N. & Clayton, G. C. 1999, MNRAS, 307, 993

Soker, N. & Kastner, J. H. 2003, ApJ, 592, 498

Soker, N. & Zoabi, E. 2002, MNRAS, 329, 204

Soria-Ruiz, R., Alcolea, J., Colomer, F., Bujarrabal, V., & Desmurs, J.-F. 2007, A&A, 468, L1

Soria-Ruiz, R., Alcolea, J., Colomer, F., et al. 2004, A&A, 426, 131

Soria-Ruiz, R., Colomer, F., Alcolea, J., et al. 2005, A&A, 432, L39

Soria-Ruiz, R., Colomer, F., Alcolea, J., et al. 2006, in Proceedings of the 8th EVN Symposium, 48, http://pos.sissa.it/cgi-bin/reader/conf.cgi?confid=36

Spencer, J. H., Schwartz, P. R., Winnberg, A., et al. 1981, AJ, 86, 392

Stanek, K. Z., Knapp, G. R., Young, K., & Phillips, T. G. 1995, ApJS, 100, 169

Sudol, J. J., Dyck, H. M., Stencel, R. E., Klebe, D. I., & Creech-Eakman, M. J. 1999, AJ, 117, 1609

Sutton, E. C., Storey, J. W. V., Betz, A. L., Townes, C. H., & Spears, D. L. 1977, ApJ, 217, L97

Swenson, Jr., G. W. & Mathur, N. C. 1968, IEEE Proceedings, 56, 2114

Szomoru, A., van Langevelde, H. J., Verkouter, H., et al. 2006, in Proceedings of the SPIE, Vol. 6267, Ground-based and Airborne Telescopes, ed. L. M. Stepp (SPIE), 62673X

Szymczak, M. & Cohen, R. J. 1997, MNRAS, 288, 945

Szymczak, M., Cohen, R. J., & Richards, A. M. S. 1998, MNRAS, 297, 1151

Szymczak, M., Cohen, R. J., & Richards, A. M. S. 2001, A&A, 371, 1012

Szymczak, M. & Gérard, E. 2004, A&A, 423, 209

Tenenbaum, E. D., Woolf, N. J., & Ziurys, L. M. 2007, ApJ, 666, L29

Tenenbaum, E. D. & Ziurys, L. M. 2009, ApJ, 694, L59

Tenenbaum, E. D. & Ziurys, L. M. 2010, ApJ, 712, L93

Thaddeus, P., Mather, J., Davis, J. H., & Blair, G. N. 1974, ApJ, 192, L33

Thompson, A., Moran, J., & Swenson, G. J. 2001, Interferometry and Synthesis in Radio Astronomy, 2nd edn. (John Wiley and Sons, Inc.)

Thompson, A., Moran, J., & Swenson, G. J. 2004, Interferometry and Synthesis in Radio Astronomy, 2nd edn. (WILEY-VCH Verlag GmbH & Co. KGaA)

Thompson, A. R. 1989, in Astronomical Society of the Pacific Conference Series, Vol. 6, Synthesis Imaging in Radio Astronomy, ed. R. A. Perley, F. R. Schwab, & A. H. Bridle (Astronomical Society of the Pacific), 11

Thompson, A. R. 1995, in Astronomical Society of the Pacific Conference Series, Vol. 82, Very Long Baseline Interferometry and the VLBA, ed. J. A. Zensus, P. J. Diamond, & P. J. Napier (Astronomical Society of the Pacific), 73

Trigilio, C., Umana, G., & Cohen, R. J. 1998, MNRAS, 297, 497

Troland, T. H., Heiles, C., Johnson, D. R., & Clark, F. O. 1979, ApJ, 232, 143

Turner, B. E. 1970, PASP, 82, 996

Tuthill, P. G., Monnier, J. D., Danchi, W. C., & Lopez, B. 2000, ApJ, 543, 284

Ulvestad, J. 2008, Very Long Baseline Array Observational Status Summary

Ulvestad, J., Perley, R., & Chandler, C. 2009, The Very Large Array Observational Status Summary

Van Blerkom, D. & Auer, L. 1976, ApJ, 204, 775

Vitrishchak, V. M., Gabuzda, D. C., Algaba, J. C., et al. 2008, MNRAS, 391, 124

Vlemmings, W., Diamond, P. J., & van Langevelde, H. J. 2001, A&A, 375, L1

Vlemmings, W. H. T. 2007, in IAU Symposium, Vol. 242, Astrophysical Masers & their Environments, ed. J. M. Chapman & W. A. Baan (Cambridge University Press), 37

Vlemmings, W. H. T., Diamond, P. J., & Imai, H. 2006, Nature, 440, 58

Vlemmings, W. H. T., Diamond, P. J., & van Langevelde, H. J. 2002, A&A, 394, 589

Vlemmings, W. H. T. & van Langevelde, H. J. 2008, A&A, 488, 619

Vlemmings, W. H. T., van Langevelde, H. J., & Diamond, P. J. 2005, A&A, 434, 1029

Walker, R. C. 1989, in Astronomical Society of the Pacific Conference Series, Vol. 6, Synthesis Imaging in Radio Astronomy, ed. R. A. Perley, F. R. Schwab, & A. H. Bridle (Astronomical Society of the Pacific), 355

Walker, R. C. 1995, in Astronomical Society of the Pacific Conference Series, Vol. 82, Very Long Baseline Interferometry and the VLBA, ed. J. A. Zensus, P. J. Diamond, & P. J. Napier (Astronomical Society of the Pacific), 133

Walker, R. C., Burke, B. F., Haschick, A. D., et al. 1978, ApJ, 226, 95

Wallerstein, G. 1958, PASP, 70, 479

Wallerstein, G. 1971, ApJ, 169, 195

Wallerstein, G. 1978, The Observatory, 98, 224

Wallerstein, G. 1986, A&A, 164, 101

Wallerstein, G. & Gonzalez, G. 2001, PASP, 113, 954

Wallin, B. K. & Watson, W. D. 1995, ApJ, 445, 465

Wallin, B. K. & Watson, W. D. 1997, ApJ, 481, 832

Wardle, J. F. C. & Kronberg, P. P. 1974, ApJ, 194, 249

Wardle, J. F. C., Roberts, D. H., Potash, R. I., & Rogers, A. E. E. 1986, ApJ, 304, L1

Watson, W. D. 1994, ApJ, 424, L37

Watson, W. D. 2002, in IAU Symposium, Vol. 206, Cosmic Masers: From Proto-Stars to Black Holes, ed. V. Migenes & M. J. Reid (Astronomical Society of the Pacific), 464

Watson, W. D. 2009, in Revista Mexicana de Astronomia y Astrofisica Conference Series, Vol. 36, Magnetic Fields in the Universe II: from Laboratory and Stars to the Primordial Universe, ed. A. Esquivel, J. Franco, G. Garcia-Segura, E. de Gouveia Dal Pino, A. Lazarian, S. Lizano & A. Raga (Instituto de Astronomia), 113

Watson, W. D. & Wyld, H. W. 2001, ApJ, 558, L55

Weaver, H., Williams, D. R. W., Dieter, N. H., & Lum, W. T. 1965, Nature, 208, 29

Weiner, J., Hale, D. D. S., & Townes, C. H. 2003, ApJ, 588, 1064

Weiner, J., Tatebe, K., Hale, D. D. S., et al. 2006, ApJ, 636, 1067

Welch, W. J., Forster, J. R., Dreher, J., et al. 1977, A&A, 59, 379

Wendker, H. J. 1995, A&AS, 109, 177

Western, L. R. & Watson, W. D. 1983a, ApJ, 274, 195

Western, L. R. & Watson, W. D. 1983b, ApJ, 275, 195

Western, L. R. & Watson, W. D. 1983c, ApJ, 268, 849

Western, L. R. & Watson, W. D. 1984, ApJ, 285, 158

White, R. L. & Becker, R. H. 1982, ApJ, 262, 657

White, R. L. & Becker, R. H. 1985, ApJ, 297, 677

Wiebe, D. S. & Watson, W. D. 1998, ApJ, 503, L71

Wiesemeyer, H., Thum, C., Baudry, A., & Herpin, F. 2009, A&A, 498, 801

Wilson, T., Rohlfs, K., & Hüttemeister, S. 2009, Tools of Radio Astronomy, 5th edn. (Springer-Verlag)

Wittkowski, M., Boboltz, D. A., Ohnaka, K., Driebe, T., & Scholz, M. 2007a, in IAU Symposium, Vol. 242, Astrophysical Masers & their Environments, ed. J. M. Chapman & W. A. Baan (Cambridge University Press), 246

Wittkowski, M., Boboltz, D. A., Ohnaka, K., Driebe, T., & Scholz, M. 2007b, A&A, 470, 191

Wittkowski, M., Langer, N., & Weigelt, G. 1998, A&A, 340, L39

Wong, T., Schöier, F. L., Lindqvist, M., & Olofsson, H. 2004, A&A, 413, 241

Woodruff, H. C., Tuthill, P. G., Monnier, J. D., et al. 2008, ApJ, 673, 418

Wright, M. C. H., Carlstrom, J. E., Plambeck, R. L., & Welch, W. J. 1990, AJ, 99, 1299

Wu Zheng, X., Scalise, E. J., & Han, F. 1998, ApJ, 507, 384

Yariv, A. 1982, An Introduction to Theory and Applications of Quantum Mechanics (John Wiley and Sons, Inc.)

Yates, J. A. & Cohen, R. J. 1994, MNRAS, 270, 958

Yates, J. A., Cohen, R. J., & Hills, R. E. 1995, MNRAS, 273, 529

Yi, J., Booth, R. S., & Conway, J. E. 2002, in Proceedings of the 6th EVN Symposium, ed. E. Ros, R. W. Porcas, A. P. Lobanov, & J. A. Zensus (Max-Planck-Institut fuer Radioastronomie (Bonn)), 235

Yi, J., Booth, R. S., Conway, J. E., Diamond, P., & Winnberg, A. 2000, in Proceedings of the 5th EVN Symposium, ed. J. E. Conway, A. G. Polatidis, R. S. Booth, & Y. M. Pihlström (Onsala Space Observatory), 193

Yi, J., Booth, R. S., Conway, J. E., & Diamond, P. J. 2005, A&A, 432, 531

Yuasa, M., Unno, W., & Magono, S. 1999, PASJ, 51, 197

Zensus, J. A., Diamond, P. J., & Napier, P. J., eds. 1995, Astronomical Society of the Pacific Conference Series, Vol. 82, Very Long Baseline Interferometry and the VLBA (Astronomical Society of the Pacific)

Zhang, B., Reid, M. J., Menten, K. M., & Zheng, X. W. 2012, ApJ, 744, 23

Zhou, Z.-P. & Kaifu, N. 1984, A&A, 138, 359

Ziurys, L. M., Milam, S. N., Apponi, A. J., & Woolf, N. J. 2007, Nature, 447, 1094

Ziurys, L. M., Tenenbaum, E. D., Pulliam, R. L., Woolf, N. J., & Milam, S. N. 2009, ApJ, 695, 1604

Zuckerman, B. & Dyck, H. M. 1986, ApJ, 304, 394